Dielectric, Magnetic and Multiferroic Characterization of Nanocomposites based on Spinel and Perovskite Ferrites and Barium Titanate

Thesis submitted to

University of Calicut, Kerala

In partial fulfillment of the requirements for the award of the degree of

DOCTOR OF PHILOSOPHY IN PHYSICS

Under the Faculty of Science

By

Sharon V S

Under the guidance

of

Dr Malini K A

Associate Professor

Post Graduate and Research Department of Physics

Vimala College (Autonomous), Thrissur-680009

Certificate

This is to certify that the thesis entitled “Dielectric, Magnetic and Multiferroic Characterization of Nanocomposites based on Spinel and Perovskite Ferrites and Barium Titanate” submitted to University of Calicut in partial fulfillment of the requirements for the award of the degree of Doctor of Philosophy in Physics under the Faculty of Science, is a record of the authentic work carried out by Ms Sharon V S, at Vimala College (Autonomous), Thrissur, under my guidance. The work presented in this thesis has not been submitted for any degree or diploma of this or any other University and has been found to have no plagiarism using the software approved by the UGC/University.

Declaration

I hereby declare that the dissertation entitled "*Dielectric, Magnetic and Multiferroic Characterization of Nanocomposites based on Spinel and Perovskite Ferrites and Barium Titanate"* submitted to University of Calicut in partial fulfillment of the requirement for the award of the degree of Doctor of Philosophy in Physics is a record of original work done by me under the supervision and guidance of Dr Malini K A, Associate Professor, Post Graduate and Research Department of Physics, Vimala College (Autonomous), Thrissur. It has not formed the basis for the award of any Degree/Diploma/Associateship/ Fellowship or any other similar title to any candidate of any university.

Sharon V S

Acknowledgement

I am deeply indebted to my family, friends, teachers and students for whatever little I was able to achieve in the exciting field of rising science. Many academic institutions and progressive organizations gave me great support to explore a new route in scientific research. This research work is made possible through the help and support from many eminent personalities of my life. I express my sincere gratitude to God Almighty, the nature to allowing me to complete this work. I would like to thank my research supervisor Dr Malini K A, Associate Professor, Post Graduate and Research Department of Physics, Vimala College (Autonomous), Thrissur for her unlimited support and constant encouragement throughout my research work. Her valuable suggestions and advice always helped me to take the right decision at the right time. Her honest criticism and fruitful discussions enriched my knowledge and wisdom in science. She encouraged me to not only grow as a researcher but also as an instructor and as an independent thinker. I express my sincere gratitude to her for allowing me to do this research work.

I would like to express my sincere thanks to Dr Sr Beena Jose, Principal, Vimala College (Autonomous), Thrissur, for giving me the opportunity to pursue my research work at Vimala College (Autonomous). I also thank all teachers, Dr Veena Gopalan E, Dr Mini Krishna K, Dr Aneesh George, Mrs Laveena Varghese, Mr Santhosh P Jose, Dr Dhanya Johnson, Dr Jovia Jose, Dr Regina Jose and Lab assistants in Physics Department. I also thankfully acknowledge the support and guidance of Prof. M R Anantharaman (Rtd), Magnetics lab, Department of Physics CUSAT. I also thank Dr Senoy Thomas, Assistant Professor and Ms Navya, Research scholar at Magnetics Lab CUSAT for the support during my research. I would like to express my sincere thanks to Dr Nandakumar Kalarikkal, Senior Professor Mahatma Gandhi University Kottayam for ME coupling measurements. I would like to express my sincere thanks to Dr Swapna S Nair, Professor, Central University of Kerala and Dr Imaddin A.Al-Omari

Sultan Qaboos University for magnetic measurements. My sincere thanks are also due to Dr Arun K.J, Assistant Professor, Sree Kerala Varma College, Thrissur for ferroelectric measurements. I would also like to express my sincere thanks to Dr Sadasivan Shaji Autonomous University of Nuevo León, San Nicolas de los Garza, Mexico for XPS analysis. Dr Shibu M Eappen, Scientist STIC CUSAT, for XRD analysis. I would like to extend my heartfelt gratitude to Amala Cancer Research Center for In Vitro Cytotoxicity measurements.

I would like to thank Dr Joissy Mathew, Dr Sheena Xavier, Dr Vimala George, Dr Sujatha N V, Ms Jonis V C, Dr Bindhu Christopher, Dr Sr Elia Raine P J, my teachers Department of Physics, St.Xaviers College for Women Aluva.

I should thank my co-researchers Ms Smitha, Ms Vinitha, Ms Rasmi, Ms Haripriya, Ms Rachana and Ms Aswathy for their good company and support during the long hours of experiments. Special words of thanks to the masters students under my mentorship Ms Sneha, Ms Devika and Ms Reshma.

I have no words to express my sincere thanks to all my family members for their continuous support to achieve my goals. I express heartfelt gratitude to my father (Sibi), mother (Rani), brother (Arun), husband (Shinu), father in law (Lazar) and mother in law (Shirley) for their endless care and affection. I express my sincere thanks to my daughter (Irin) for allowing me to continue my work without any hiccups. I would like to thank my entire family and all who took my research as their dreams. Finally I would like to thank all those helped me for the successful completion of the research work. This thesis is a dedication to all my family members and well-wishers.

Sharon V S

PREFACE

Dielectric, Magnetic and Multiferroic Characterization of Nanocomposites based on Spinel and Perovskite Ferrites and Barium Titanate

The thesis is a detailed investigation of multiferroic nanocomposites based on spinel and perovskite ferrites with barium titanate. The thesis comprises two main components: firstly, the synthesis and characterization of ferrites, followed by the studies on nanocomposites formed by integrating these ferrites with barium titanate, each part contributing to a comprehensive understanding of their properties and potential applications.

Chapter 1 of the thesis is the introductory chapter and it starts with the introduction to multiferroic materials. The chapter proceeds with various types of ferroic materials and their properties and concludes with the list of systems under present study and its objectives. **Chapter 2** detail about the various experimental techniques used for synthesis and characterisation of the prepared samples.

Chapter 3 deals with the investigations on zinc-doped nickel ferrite (NZFO) nanoparticles with the general formula $Ni_{1-x}Zn_xFe_2O_4$ (x = 0.0, 0.3, 0.5, 0.7, 1). The focus of this Chapter extends to the synthesis process, as well as the examination of structural, electrical, and magnetic traits using XRD, SEM, EDAX, LCR meter (dielectric studies) and VSM. The structural evaluation is executed through X-ray powder diffraction technique. The morphological assessment of the prepared samples employs scanning electron microscopy (SEM) and Energy Dispersive X-Ray Analysis (EDAX). Additionally, the Chapter provides comprehensive insights into the frequency-dependent dielectric constant and ac conductivity. Furthermore, the impact of zinc doping on the magnetic characteristics of nickel ferrite is also elucidated within this section. The photo degradation studies of zinc doped nickel ferrite and zinc ferrite nanoparticles were evaluated for the degradation of methylene blue dyes under visible light irradiation.

Chapter 4 deals with the synthesis as well as structural, electrical and magnetic characterization of zinc doped cobalt ferrite (CZFO) nanoparticles with general formula, $Co_{1-x}Zn_xFe_2O_4$ (x=0.0, 0.3, 0.5, 0.7, 1). This Chapter delves into the synthesis methodology and conducts a detailed analysis of the structural, electrical, and magnetic characteristics utilizing advanced techniques such as XRD, SEM, EDAX, LCR meter (dielectric studies) and VSM. The photocatalytic and cytotoxicity studies using cobalt ferrite are also detailed in this Chapter.

Chapter 5 discuss the structural, electrical and magnetic characterisation of strontium substituted multiferroic bismuth ferrite (BSFO) nanoparticles with general formula, $Bi_{1-x}Sr_xFeO_3$ (x=0.0, 0.3, 0.5 and 0.7) synthesized by modified sol-gel auto-combustion process. The sharp and strong photoluminescence in the IR region is observed in the samples similar to ZnO, which is reported for the first time. The photo degradation studies of $BiFeO_3$ and $Bi_{0.5}Sr_{0.5}FeO_3$ samples were evaluated for the degradation of methylene blue dyes under visible light irradiation.

Chapter 6 provide the detailed analysis of various multiferroic composites prepared using different ferrites in different ratios. The systems studied include composites of nickel ferrite, nickel zinc ferrite, cobalt ferrite, cobalt zinc ferrite, bismuth ferrite, and bismuth strontium ferrite with barium titanate. The components were taken in different weight ratios of 1:1, 1:2 and 2:1 and the structural, electrical and ferroelectric properties of multiferroic composites are detailed in this Chapter. The structural properties were examined using XRD and XPS techniques, while the electrical properties were investigated through frequency-dependent dielectric constant and ac conductivity analysis. The ferroelectric nature was confirmed through a ferroelectric studies using P-E loop tracer. This Chapter provides some aspects about the various properties leading to different applications of these multiferroic composites.

Chapter 7 deals with the magnetic and multiferroic properties of composites of nickel ferrite and barium titanate ($NiFe_2O_4$-$BaTiO_3$) in the ratio 1:1, 1:2, 2:1 as well as composites of nickel zinc ferrite and barium titanate ($Ni_{1-x}Zn_xFe_2O_4$-$BaTiO_3$) in the ratio 2:1, multiferroic $Co_{1-x}Zn_xFe_2O_4$- $BaTiO_3$ (x=0,0.3,0.5,0.7,1) with the ratio 2:1 samples

and bismuth ferrite and barium titanate in the ratio 2:1 and $Bi_{1-x}Sr_xFeO_3$ – $BaTiO_3$ (x=0.3,0.5,0.7) with the ratio 1:2 and 2:1. prepared by solid-state reaction method.

Chapter 8, which is the last chapter of the thesis gives Summary and Conclusion of the present study. It also gives a brief description of recommendations and scope for future work.

LIST OF PUBLICATIONS

International Journals

- ***Sharon V.S**, Veena Gopalan E, Malini K A, Structural Evolution –Enabled $BiFeO_3$ modulated by strontium doping with enhanced dielectric, optical and superparamagnetic properties by modified sol-gel method, (Chinese Phys. B 32 037504, 2023 https://doi.org/10.1088/1674-1056/ac785b (IF-1.652)*
- ***Sharon V.S**, Veena E. Gopalan, Imaddin A. Al-Omari, K A Malini, Superparamagnetic Nickel Ferrite Nanoparticles Doped with Zinc by Modified Sol–gel Method, Journal of Superconductivity and Novel Magnetism 35:795–804 (2022). https://doi.org/10.1007/s10948-021-06110-7 (IF 1.675)*
- *Haripriya V K, **Sharon V .S** and Malini K A , Tailoring the properties of Ni-Mn based NTC thermistors by Cu and Li addition Physica Scripta 96 (2021) 125728, 6 December 2021. https://doi.org/10.1088/1402-4896/ac379f (IF 3.081)*

Conference Proceedings

- ***Sharon, V S**; Malini, K A; Arun, KJ, Synthesis and characterization of bismuth ferrite-barium titanate nano composites, IOP Conference Series: Materials Science and Engineering 1263 (1), 012028, https://10.1088/1757-899X/1263/1/012028*
- ***Sharon V.S**, Swapna S Nair, Nandakumar Kalarikkal, Malini K A, Multiferroic and magnetic characterization of Nickel Ferrite- Barium Titanate nanocomposites Materials Today: Proceedings, https://doi.org/10.1016/j .matpr. 2023.12.018)*

Presentations

- *Paper presentation on "Multiferroic and magnetic characterization of nickel ferrite-barium titanate nanocomposites" at an International Conference on Science and Technology of Advanced Materials STAM 23 organised by M A College, Kothamangalam during 18-20th April 2023.*

- *Presented a poster on "Synthesis and characterization of bismuth ferrite- barium titanate nano composites" at an international conference ICMPMA 2022 held at fathima matha college on 9-13 may 2022.*

- *Presented a poster on "Synthesis and characterization nickel ferrite- barium titanate nano composites" at an international conference NANOicon 2022 held at CUSAT on jan 11-15 2022.*

- *Presented a poster on "Structural, electrical, optical and magnetic studies of $CoFe_2O_4$ nanoparticles" at a national seminar held at Christ College, Irinjalakuda on 24-25 January 2019.*

- *Presented a poster on "A study on the dielectric, optical and magnetic properties of bismuth ferrite nanoparticles" at an International conference "ICONMAT 2019" held at CUSAT, Cochin on 2-5 January 2019.*

CONTENTS

List of Figures

List of Tables

List of Figures

List of Tables

Chapter 1

INTRODUCTION

Introduction

1.1 Multiferroics

The convergence of magnetism and electricity stands as a pivotal achievement in contemporary physics. Coined by H. Schmid in 1994, the term "multiferroics" describes materials that host two or more coexisting ferroic phases[1]. These phases are defined by four fundamental order parameters: Ferroelectricity, Ferromagnetism, Ferroelasticity, and Ferrotoroidicity, which dictate distinct material behaviors[2].

Ferromagnetic (FM) materials exhibit spontaneous magnetization and spin ordering could be changed by applying an external magnetic field. Correspondingly, ferroelectric (FE) materials show spontaneous polarization changeable by applying an electric field. Until recently, It was once thought that the simultaneous existence of Ferromagnetic and Ferroelectric orders in a single material constituted two separate factors. But in some multiferroic materials, this behaviors are coupled with each other by the magnetoelectric (ME) effect. This effect introduces a new class of substances capable of altering magnetic attributes through electric fields and vice versa, fostering innovation in material design for various applications[3].

Ferroelectric materials are polarization-stable and switchable, while antiferroelectric counterpart's exhibit mutually nullified dipole moments. The ferromagnetic materials have stable spontaneous magnetization that can be altered by an applied magnetic field, whereas antiferromagnetic materials have ordered magnetic moments that completely cancel each other out within each magnetic unit cell. Ferroelastic substances exhibit consistent deformation controllable through stress, and ferrotoroidic materials possess inherent ordered parameters resembling the curl of polarization or magnetization. This potential switchability of ferrotoroidic properties remains an ongoing exploration.

[1] Schmid 2011
[2] Das 2013b
[3] Das 2013a

Only a few compounds show magnetic and electric order parameters simultaneously (Fig 1.1). In 1894 magnetoelectricity was introduced by Pierre Curie. Magnetoelectricity in Cr_2O_3 was experimentally and theoretically proved by Astrow (1959) and Dzyaloshinsky (1960)[4]. However, the limited coupling in these materials impeded their utility, causing a decline in research until NA Hill's theoretical work in 2000 reignited interest[5]. Nanostructured multiferroics, with robust ME coupling and reduced dimensions, find applications in nanoelectronics and spintronics.

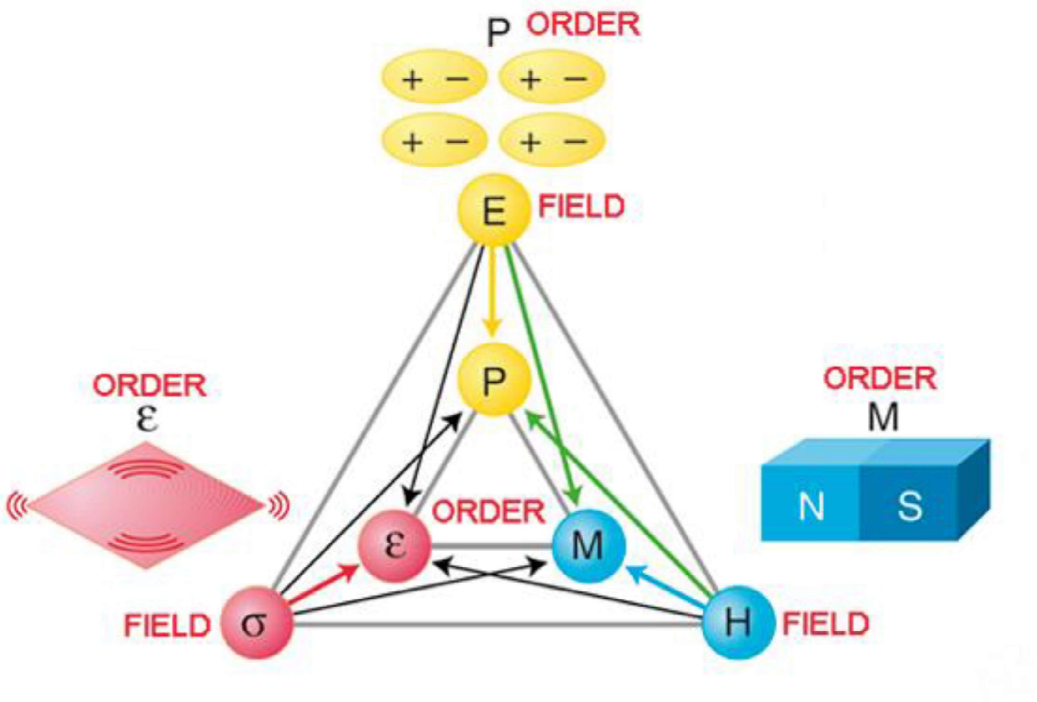

Fig 1.1. Magnetoelectric coupling between different orders and field

Multiferroics are used for the development of a wide range of devices, such as sensors[6], Integrated circuit, data storage memories[7], power generation and in electric transformers[8]. This broad applicability is the motive for creating such a significant interest in this field. It is one of the most important topics in material

[4] Yi et al. 1993
[5] Spaldin & Fiebig 2005
[6] Filippov et al. 2009; Vázquez & Hernando 1996
[7] Li et al. 2006
[8] Wang 2017

science nowadays. Notably, the quest for memory systems has led to exploring multiferroic materials that amalgamate the benefits of magneto-resistance memories (MRAMs) and ferroelectric random access memories (FeRAMs), enabling writing by ferroelectricity and reading by magnetism[9].

1.2 Types of multiferroics

Multiferroic materials segment into two categories according to their components: single-phase and composite multiferroics.

Single-phase Multiferroic Materials

Single-phase multiferroic materials are those materials with coexisting ferroelectric and magnetic ordering. They are divided into two more categories. Type I and Type II multiferroic materials.

The ferroelectricity and magnetism in type-I multiferroics have distinct origins, and there is a relatively weak interaction between them. Furthermore, these materials exhibit ferroelectric and magnetic transitions that occur beyond room temperature and have high spontaneous polarisation values. It is challenging to increase the coupling in these types of multiferroic materials while maintaining their beneficial properties. Conversely, ferroelectricity is only induced in the magnetically ordered state in type-II multiferroics. The difficulty with these materials, in contrast to type-I multiferroics, is to improve the ferroelectric and magnetic behaviour.

Further these materials are classified in to different families based on the origin of ferroelectricity and ferromagnetism[10]. They are

Perovskites

The famous ferroelectric materials are perovskites e.g.$BaTiO_3$, $Pb(ZrTi)O_3$. There are many magnetic materials that possess perovskite structure. On comparing these materials, it can see that ferroelectricity and magnetism in perovskite mutually

[9] Scott 2007
[10] Cane 1999

exclude each other with some exceptions. The transition metal ions in the ferroelectric perovskites have an empty d shell. The transition metal ion's off-center shifts are responsible the ferroelectricity of these materials. The transition metal ion's partially filled d shell is what generates the magnetic.

Bismuth-Based Compounds

Bismuth Ferrite ($BiFeO_3$) possess simultaneous ferromagnetism and ferroelectricity and contain only magnetic ion Fe^{3+} (d^5). This shows that the presence of empty d shell (d^0) is not the enough condition in these materials to be ferroelectric. The stereochemical activity of bismuth lone pairs is the cause of ferroelectricity. In $BiFeO_3$ the origin of ferroelectricity is due to the outer 6s electrons, called dangling bonds, they don't participate in chemical bond and they possess high polarizability. The Fe^{3+} is responsible for the magnetism and dangling bonds are responsible for ferroelectric polarization[11].

Hexagonal Manganites

The multiferroic material with general formula $LnMnO_3$ (where Ln=Y or small rare earth) is in hexagonal structure. The compound $YMnO_3$ is ferroelectric and A-type antiferromagnet. Ferroelectricity in these materials is produce due to the tilting of the MnO_5 polyhedral. These material possess high ferroelectric transition temperature and low Neel temperature[12].

For these materials, ferroelectricity is produced by charge ordering. When an ion with a different valency exists or when there are inequivalent bonds because of the material's structure, the charge ordering in the system can happen. Charge ordering emerges due to formally Mn^{3+} or Mn^{4+} in half-doped manganites such as $P_{1/2}Ca_{1/2}MnO_3$ or $La_{1/2}Ca_{1/2}MnO_3$ where the situation can be realised. In similar manner charge disproportionation at the Ni site results in two inequivalent Ni sites and various Ni-O bond lengths in rare earth (R) Nickelates ($RNiO_3$). Due to the

[11] Cane 1999
[12] Cane 1999

existence of Fe^{2+} and Fe^{3+} ions, Fe_3O_4 and MFe_2O_4 also display this kind of charge ordering[13].

Ferroelectricity due to Magnetic Ordering

There is a significant link between ferroelectricity and magnetism in this family of material systems because the ferroelectricity develops in a magnetically ordered state**.** These materials show small values of polarization (10^{-2} μC/cm^2). This type of multiferroic materials are $TbMnO_3$, $AgCrO_2$, $Ni_3V_2O_6$ and $MnWO_4$, which have been recently discovered. Large magnetoelectric and magnetocapacitance effects in $TbMnO_3$ are related to the magnetic field's switching of electric polarization[14].

Limitations of Single-phase Multiferroic Materials

In single-phase multiferroic materials, the coexistence of ferromagnetism and ferroelectricity is often limited to cryogenic temperatures. Operational complexity arises due to the need for low-temperature investigations. While such materials exhibit weak ME responses, $LiCoPO_4$ stands out with a notable ME coefficient (α_{yx} =30.6 ps m^{-1}). These materials' limitations hinder their practical use in real-world devices.

In summary, the realm of multiferroics encompasses intricate interactions between magnetism and electricity, ranging from single-phase materials with diverse origins of ferroic properties to their composite counterparts. This field's potential applications make it a focal point of modern materials science research[15].

1.3 Multiferroic composite systems

The magneto-electric coupling (ME) of naturally occurring multiferroic single-phase composites is extremely weak and appears below room temperature. These materials are extremely uncommon. So, these materials cannot be used for

[13] Cane 1999
[14] Cane 1999
[15] Lopatin et al. 2011

practical applications. But multiferroic composites that contain both ferroelectric and magnetic phases have large ME coupling above the room temperature and they can be used for industrial applications. In 1972, Suchtelen put forward the theory of product property of two-phase composite materials coming up with the elastic coupling between two phases of different properties. The $BaTiO_3$- $CoFe_2O_4$ composites developed at Philips laboratory possess a large ME coupling ($\frac{\partial E}{\partial H} = 0.13\ \mathrm{V/cm.Oe}$) at room temperature. For these nanocomposites, the ME effect obtained was hundred times larger than single-phase multiferroics. They prepared the composites by the technique of unidirectional solidification of eutectic compositions. But this technique is very complex and due to this the research becomes inactive for 20 years. The Newnham's and others have[16] prepared the nanocomposites of ferrites with barium titanate by a very cost-effective and simple method. After this, various composites were discovered. The ME composites are classified into five categories: bulk ceramic composites, nanostructured and composite thin films, three-phase ME composites, two-phase ME composites made of piezoelectric materials and magnetic alloys. ME composites find use in energy harvesters, ME transformers, gyrators, magnetic sensors, memory devices, electrically tunable microwave magnetic devices, and more[17].

1.4 Microscopic origin of Ferroelectricity and Ferromagnetism

In perovskite (ABO_3) multiferroic materials, ferroelectricity and ferromagnetism are coupled with each other. The fundamental cause of magnetism in multiferroics closely resembles that of all magnets. It is mostly attributed to localised electrons that are mostly present in transition metal or rare-earth ion partially filled d or f subshells. These localized electrons harbor spin or magnetic moments that interact through exchange mechanisms, leading to magnetic alignment. In ferroelectric material a distorted asymmetric crystal structure is necessary for FE polarization but for ferromagnetism symmetric structure is necessary. Scholars have deduced that there exist multiple tiny sources of ferroelectricity, and thus, distinct

[16] Bichurin et al. 2011; Lopatin et al. 2011
[17] Wang 2017

kinds of multiferroics can be produced. According to reports, the traditional mechanism for ferroelectricity in perovskite compounds involves off-centering of the d^0 electrons at the B-site. Therefore, the atoms that move off centre to generate the electric dipole moment and the atoms that carry the magnetic moment should be different in order for ferroelectricity and magnetism to coexist in a single phase. There is still scope for more research on multiferroics with various forms of magnetism. This might theoretically be achieved via either an alternative (non-d-electron) mechanism for magnetism or an alternative mechanism for ferroelectricity; however, only the latter approach has been considered. For instance, in $PbTiO_3$ (PTO), the influence of Pb lone-pair is dominant, but in $BaTiO_3$ (BTO), the centre of Ti ions plays a crucial role in ferroelectricity. The most popular method of achieving multiferroism in magnetic perovskite-structure oxides and related materials is to use the stereochemical activity of the lone pair on the big (A-site) cation to produce ferroelectricity while maintaining the magnetic properties of the tiny (B-site) cation[18].

1.5 Magnetoelectric effect in multiferroics

In multiferroic materials, the electric field and magnetic field are coupled. In normal situations, the electric and magnetic fields are not intrinsically coupled. This coupling is very important in designing property of the materials. The magnetoelectric property can be explained by Landau-theory,

The free energy is given by

$$F(E,H) = F_0 - P_i^s E_i - M_i^s H_i - \frac{1}{2}\varepsilon_0 \varepsilon_{ij} E_i E_j - \frac{1}{2}\,\mu_0\,\mu_{ij} H_i H_j - \alpha_{ij}\, E_i H_j - \frac{1}{2}\,\beta_{ijk} E_i\, H_j H_k - \frac{1}{2}\,\gamma_{ijk} H_i\, E_j E_k - \cdots\cdots \quad (1.1)$$

where P_i^s and M_i^s represent spontaneous polarization and magnetization respectively and $\hat{\varepsilon}$ and $\hat{\mu}$ represent electric and magnetic susceptibilities.

Differentiation of 1.1 with respect of E gives the polarization

[18] Liou et al. 1999

$$P_i(E,H) = -\frac{\partial F}{\partial E_i} = P_i^S + \varepsilon_0 \varepsilon_{ij} E_j + \alpha_{ij} H_j + \frac{1}{2}\beta_{ijk} H_j H_k + \gamma_{ijk} H_i\, E_j - \cdots \quad (1.2)$$

Differentiation of 1.1 with respect of H gives the magnetization

$$M_i(E,H) = -\frac{\partial F}{\partial H_i} = M_i^S + \mu_0 \mu_{ij} H_j + \alpha_{ij} E_i + \beta_{ijk} E_i\, H_j + \frac{1}{2}\gamma_{ijk} E_j E_k - \cdots \quad (1.3)$$

The tensor $\hat{\alpha}$ describes the induction of electric polarization on the application of the magnetic field or vice versa and represents the linear ME effect, while, tensors $\hat{\beta}$ and $\hat{\gamma}$ describe the higher order ME effect.

Furthermore, the α_{ij} tensor is bounded by the geometric mean of ε_{ij} and μ_{ij}

$$\alpha_{ij}{}^2 < \varepsilon_0 \mu_0 \varepsilon_{ii} \mu_{jj}$$

This suggests that multiferroic material which is ferroelectric and ferromagnetic, is likely to show large ME effect due to the fact that ferroelectric and ferromagnetic materials often (but not always) exhibit high permittivity and permeability, respectively.

1.6 Magnetic Properties

Hans Christian Oersted a Danish Physicist found that when an electric field flows through a wire then the magnetic field is created. This result shows a connection between electricity and magnetism. The reason for the magnetism is the orbital and spin motion associated with an electron. The minute current that arises because of this motion can create magnetic dipoles. When we apply a magnetic field the medium will be magnetically polarized[19].

The magnetization M is given by

$$M = \sum_{volume} m_i \quad (1.5)$$

[19] Blundell 2001

Magnetization is defined as M, the magnetic moment per unit volume. The magnetic susceptibility is defined as the ratio of magnetization (M) to magnetic field strength (H).

$$\chi = \frac{M}{H} \tag{1.6}$$

H represents the magnetic field's strength. B is a material's magnetic flux density or magnetic induction.

$$B = \mu_0(H + M) = \mu_0 H(1 + \frac{M}{H}) \tag{1.7}$$

From equation 1.6

$$B = \mu_0 H(1 + \chi) \tag{1.8}$$

Here $\mu_0 = 4\pi \times 10^{-7} Hm^{-1}$ is the permeability of free space,

$\mu = \mu_0(1 + \chi)$

$$B = \mu H \tag{1.9}$$

The M-H curve or magnetization curve is given in Figure 1.2

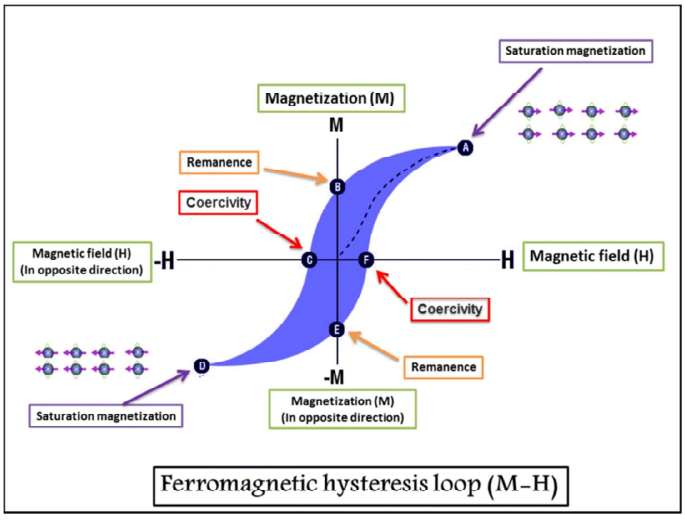

Fig 1.2 M-H curve of a ferromagnetic material

The saturation magnetization M_S is defined as the magnetization at highest value of H, where at the point 'A' the magnetization becomes constant. After saturation, the value of H is reduced to zero, then it reaches the 'B' where the magnetic field is zero and the magnetic induction is not zero. The retained magnetic induction is known as the retentivity of the material. The magnetic induction becomes zero with a further decrease in the applied field. The point 'C' in the figure is denoted as the coercivity of the material, it is defined as the negative field applied to bring the magnetic induction to zero. When we increase the magnetic field in the negative direction, the magnetization once more gets saturated in the opposite direction 'D'. When the field is again reduced to zero, then obtained residual magnetization 'E'. The point 'F' is reached with the increasing magnetic field in the positive direction where the magnetization is zero.

There are two types of magnetic materials: *soft magnetic materials and hard magnetic materials*. Temporary magnets are made of soft magnetic materials, which are readily magnetised or demagnetized[20]. Their coercivity and retentivity are low. The area covered by the hysteresis loop will be small. For the soft magnets, the susceptibility and permeability are high and also eddy current loss is less. The core of transformers, generators and stators are made of these soft magnets. Hard magnetic materials are used in permanent magnets because they are difficult to demagnetize[21]. The hysteresis loop area and the hysteresis loss are large for hard magnets. For hard magnetic materials, the eddy current loss, coercivity and retentivity values are high. Hard magnetic materials are used in the application of loudspeakers, motors, telephone receivers, etc. Magnetism is divided into five major types depending on the interaction of the material with the magnetic field. They are diamagnetism, paramagnetism, ferromagnetism, antiferromagnetism and ferrimagnetism[22].

[20] *Elements of Materials Science and Engineering (Addison-Wesley Series in Metallurgy & Materials Engineering)*
[21] *Elements of Materials Science and Engineering (Addison-Wesley Series in Metallurgy & Materials Engineering)*.
[22] Blundell 2001

1.6.1 Diamagnetism

Diamagnetism is the most common form of magnetism. The atom of a diamagnetic substance has no net magnetic moment, which means the atoms do not possess unpaired electrons and the orbital shells are filled. In the presence of a non-uniform magnetic field, a diamagnetic material shift from the stronger to the weaker part of the magnetic field. In the presence of a magnetic field, the direction of magnetization is opposite to the field and it drops its magnetization once the field is removed.

In Langevin's theory, magnetic susceptibility is defined as,

$$\chi = -\frac{Nz^{2}}{mc^{2}} < r^{2} > \tag{1.10}$$

where N is the number of atoms per unit volume, c is the speed of light, z is the number of electrons within the atom, and m is the mass of the electron and $< r^{2} >$ is denoted as the mean square distance of the electron from the nucleus. Diamagnetic material has negative susceptibility and is also temperature independent. Diamond, gold, copper, mercury, silver, tin, and zinc are also the examples of diamagnetic materials.

1.6.2 Paramagnetism

Paramagnetism is magnetism related to atoms or molecules that carry unpaired electrons. In the absence of an external magnetic field, the atoms are orientated randomly, resulting in zero net magnetization. However, when an external magnetic field is applied, the arrangement of the atomic moments in the direction of the applied magnetic field results in positive susceptibility and positive magnetization.

For paramagnetic materials, the magnetization is expressed as,

$$M = C\left(\frac{H}{T}\right) \tag{1.11}$$

where C is defined as the Curie constant, H is the magnetic field strength, T the temperature

Susceptibility of a paramagnetic material is defined as

$$\chi = \frac{C}{T} \tag{1.12}$$

So, the paramagnetic materials possess small and positive susceptibility and it is inversely proportional to the temperature. The paramagnetic materials are aluminum, chromium, copper sulphate, palladium, manganese, tungsten, etc.

1.6.3 Ferromagnetism

A ferromagnetic substance has a net magnetic moment while there is no external magnetic field. The strong interaction between the individual atoms or electrons causes the parallel alignment of the magnetic moments; this is the reason for the net magnetic moment. This interaction results in areas of magnetism called domains. By the application of external field, the dipoles in the domain get aligned. The energy required to reorient the domains from a magnetised to a demagnetized condition is known as hysteresis. The magnetization of ferromagnetic materials occurs spontaneously, that is, without the presence of an external field. There is a critical temperature below which the spontaneous magnetization occurs (θ). Spontaneous magnetization is because of the interaction between the magnetic ions. The ferromagnetic material becomes paramagnetic above Curie temperature due to the spin alignment because of the thermal effects. The Curie-Weiss law determines a ferromagnetic material's susceptibility, and its value is high and positive.

$$\chi = \frac{C}{T-\theta} \tag{1.13}$$

1.6.4 Antiferromagnetism

The individual magnetic moments in a domain are antiparallel for antiferromagnetism. Because the nearby magnetic moments cancel each other out, in the absence of an external magnetic field, there is no net magnetization. However, a

tiny magnetization is created when an external magnetic field is introduced, and it grows as temperature rises. Similar to the Curie temperature in ferromagnetic materials, Neel temperature (T_N) is for antiferromagnetic materials. Above Neel temperature, antiparallel alignment is disturbed and it comes back to a paramagnetic state. Ionic compounds like sulphides, chlorides, and oxides are examples of antiferromagnetic substances.

1.6.5 Ferrimagnetism

The magnetic oxides of iron namely ferrites exhibit ferrimagnetism. Ferrimagnetism is similar to antiferromagnetism in the opposite dipoles being not equal. The net magnetization is not zero, because the dipoles do not cancel each other. Above Curie temperature, they show paramagnetism and possess spontaneous magnetization. The ferrites, Yittirium Iron Garnet (YIG) are examples of ferrimagnetic materials. Figure 1.3 shows the various types of magnetism.

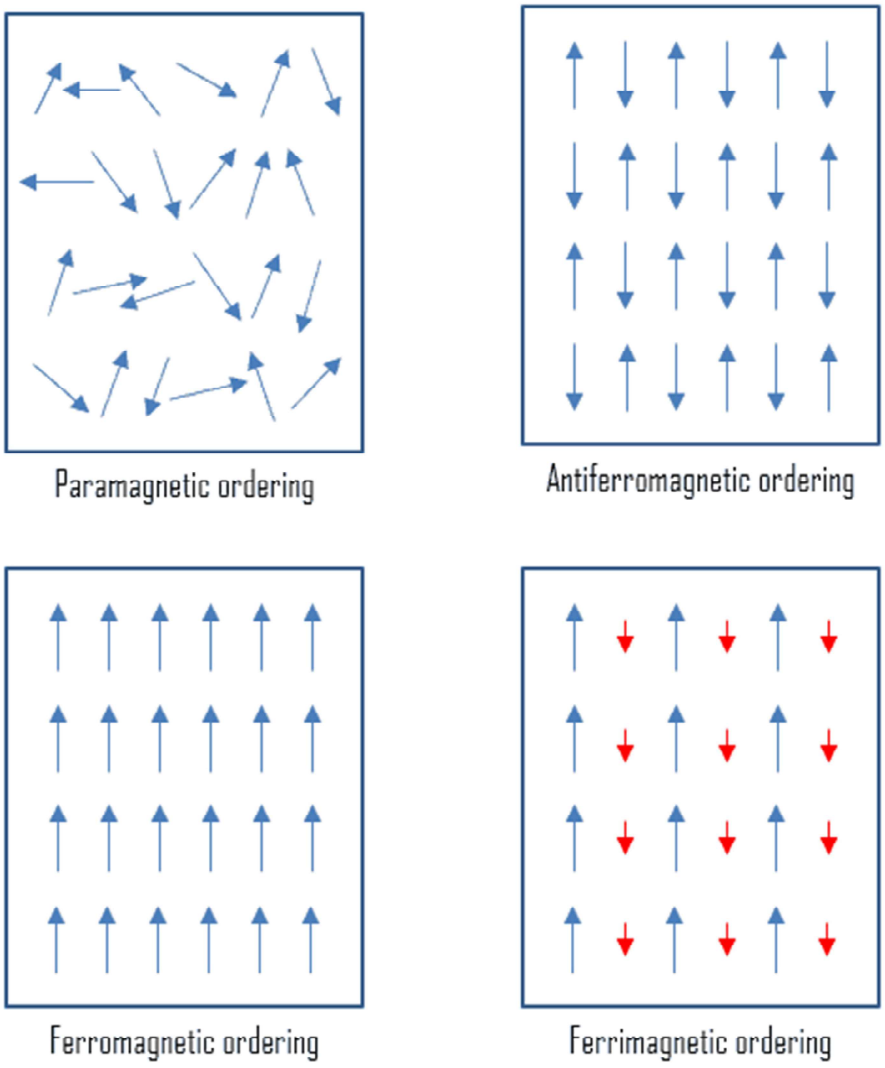

Fig.1.3. Types of magnetism

1.6.6 Nano Magnetism

The nanoparticles have at least one of their dimensions in the nanoscale, their magnetic properties are called Nanomagnetism. Nanomagnetism adds coercive force, ultrafine magnetic anisotropy, superparamagnetism, and giant magnetic resistance[23]. The magnetic properties of nanoparticles can be changed by altering their shape,

[23] Liou et al. 1999

structure, size, or composition. The properties of nanoparticles turn on with their composition, size, the shape of the particle, etc[24].

Magnetic nanoparticles have gained great attention in applications such as high-frequency electronics, permanent magnets, etc. The magnetic properties of nanoparticles are significantly influenced by their finite size and surface effects. The internal and surface chemical and magnetic structures, as well as the symmetry breaking of the crystal structure at each particle's boundary, all have an impact on the surface effects[25].

1.6.7 Super-paramagnetism

Super-paramagnetism shown by the nanoparticles is related to their magnetic anisotropy[26].

According to the Stoner-Wohlfarth hypothesis, the energy-related per particle in an identical single domain particle is approximately as,

$$E_A = kv \sin^2\theta \qquad (1.14)$$

In this case, θ indicates the angle formed by the nanoparticles' easy direction and magnetization direction, v is the volume of the nanoparticles, and k is the magnetocrystalline anisotropy constant. Easy direction is the favorite direction in which each particle acquires an ordered magnetic moment when the temperature is below the Curie temperature. E_A is the energy that generates from the angular momentum of its orbital motion in the crystal lattice and the magnetic coupling of the electron spin. The product of magnetic anisotropy and the volume, that is, kv becomes closest to the thermal activation (k_BT), when the size of the nanoparticles is below the threshold value. Here k_B represents the Boltzman constant. Even in the absence of an applied field, thermal energy fluctuation will control the anisotropic forces one by one that can move easily axis[27]. The anisotropy thermal energy

[24] Das 2013b
[25] Kodama 1999; *Magnetic Nanoparticles - Google Books* n.d.
[26] Bedanta & Kleemann 2008
[27] Néel 1949

interaction results in properties similar to that of a paramagnetic material, but possesses a large magnetic moment represented by m=Msv, which is very high of the order of thousands of Bohr magnetons. When we apply the field, the magnetic moment (Msv) tends to align with the field. This phenomenon is known as superparamagnetism. But in the case of paramagnetism thermal activation energy (k_BT) will restrict the alignment of magnetic moments. The direction of magnetization fluctuates instead of keeping a fixed direction in the case superparamagnetic relaxation process.

Neel's theory provides the superparamagnetic relaxation period, which is the mean interval between magnetization direction reorientations

$$\tau = \tau_0 \exp(\frac{kV}{k_B T}) \quad (1.15)$$

Where τ_0 represents the relaxation time constant and T is the temperature. Blocking temperature (T_B) is the temperature at which magnetic anistropic energy exceeds the thermal activation energy and the nanoparticle set off superparamagnetically relaxed.

The blocking temperature T_B is given by,

$$T_B = \frac{KV}{k_B} \ln(\frac{\tau_m}{\tau}) \quad (1.16)$$

when $T < T_B$, the system is going to be in a blocked state and show hysteresis. When $T > T_B$, the system is going to be superparamagnetic, where the hysteresis vanishes and thermal equilibrium comes to happen. At the temperature below T_B, the magnetic moment is obstructed by anisotropy but for temperature above T_B it seems to be superparamagnetic. So the property of the superparamagnetism is the absence of hysteresis, and as a consequence of this remanence and coercivity disappear. The main difference between classical paramagnetism and superparamagnetism is the magnetic saturation attained with a weak field for nanoparticles. This is because the particle moment ($\mu \sim 10^4\ \mu_B$) is a greater value compared to the atomic moment value $\mu_{atm} \sim 10\ \mu_B$.

1.7 Ferroelectricity.

Piezoelectricity was discovered in the eighteenth and nineteenth century as a result of research on the pyroelectric effect. In 1920, Vaiasek first observed the first ferroelectric crystal sodium potassium tartrate tetrahydrate ($NaKC_4H_4C_6$-$4H_2O$) also known as Rochelle salt[28]. The creation of domain structures with differentially oriented polarization in virgin ferroelectric single crystals, which resulted in a zero-net polarization and very tiny pyroelectric and piezoelectric responses, is primarily responsible for the much later discovery of ferroelectrics. By observing a hysteresis effect in the electric field polarization curve, Vaiasek identified ferroelectricity. This was achieved by pinpointing a Curie temperature (Tc) and noting an incredibly large dielectric and piezoelectric response in and near the ferroelectric temperature region of the Rochelle salt crystal. These effects are similar to corresponding effects in ferromagnetism in many ways. Having been discovered in 1945, barium titanate ($BaTiO_3$) is the first ferroelectric substance having a perovskite structure.

Compared to other ferroelectric materials, $BaTiO_3$, KH_2PO_4 (KDP) and Rochelle salt are important because of the cubic center-symmetric perovskite structure which is highly symmetric above the Curie temperature. It has five atoms per unit cell. It is ferroelectric at room temperature. It is chemically and mechanically very stable. $BaTiO_3$ is the most extensively studied ferroelectric material. Ferroelectric behavior at a microscopic level is explained by the lattice dynamics theory.

1.7.1 General properties of ferroelectric materials

1.7.1.1 Crystal symmetry

Seven separate crystal systems can be used to classify the whole variety of crystals: triclinic, monoclinic, orthorhombic, tetragonal, cubic, trigonal, and hexagonal [29]. Based on their specific symmetry patterns, these systems can be further classified into 32-point groups, as shown in Figure 1.4. Among these, 11 are

[28] Valasek 1921
[29] Goldschmidt 1926

centrosymmetric, meaning they possess a central point of symmetry. Consequently, these centrosymmetric crystals cannot exhibit any spontaneous polarization properties[30]. Cubic 432, one of the 21 non-centrosymmetric point groups that are still present, possess symmetry components that inhibit polar features. The remaining 20 point groups incorporate one or more polar axes (as outlined in Table 1.1), thereby showcasing various polar phenomena such as ferroelectricity, pyroelectricity, and piezoelectricity.

Table 1.1. Classification of crystals on the basis of symmetry

Crystal class	**Centro symmetric Point groups**		**Non-centrosymmetric Point groups**				
			Polar		**Non-polar**		
Cubic	m3	m3m	none	none	432	-3m	23
Tetragonal	4 or m	4 or mmm	4	4mm	-4	-42m	22
Orthorhombic	mmm		mm2		222		
Hexagonal	6 or m	6 or mmm	6	6mm	-6	-62m	622
Trigonal	-3	-3m	3	3m	32		
Monoclinic	2 or m		2	m	none		
Triclinic	-1		1		none		
Total Number	11 groups		10 groups		11 groups		

[30] Shannon & IUCr 1976

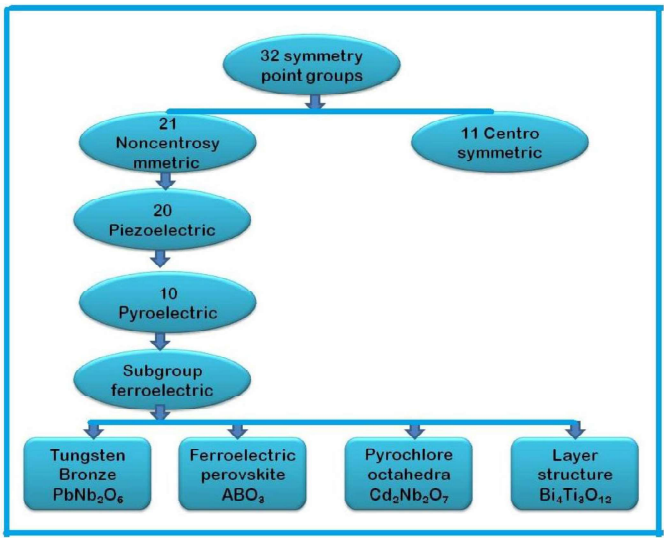

Fig 1.4. Classification of electro-ceramics

A crystal with spontaneous polarization that has the ability to reverse its orientation in response to an electric field is said to possess ferroelectricity[31]. Since the depolarization field that results from the spontaneous polarization (charge distribution) can be offset by the flow of free charge within the crystal and in the surrounding medium or by twinning (domain formation), the spontaneous polarization is typically not detectable by charges on the crystal's surface[32]. To enable the reversal of polarization by the electric field, ferroelectricity necessitates that the crystal have at least two identical orientational states for polarization in the absence of the electric field. Only at a specific temperature, known as the Curie temperature (Tc), can ferroelectricity be seen; above this point, spontaneous polarization ceases to occur and the randomising impact of thermal energy (kT) becomes dominant. It is said that the phase is in the paraelectric condition when it exists above Tc.

Piezoelectricity is the property of a crystal that shows electrical polarization caused by stress[33]. Otherwise, when an electric field is applied, the strain will be produced in the crystal and the material experiences stretch or compression

[31] *Handbook of Advanced Dielectric, Piezoelectric and Ferroelectric Materials ... - Google Books* n.d.
[32] Kalinin et al. 2018
[33] Paufler 1986

depending on the orientation of the field with the polarization in the crystal. Ten of the twenty kinds of piezoelectric crystals have a distinct polar axis. Since these crystals exhibit spontaneous polarization (electric moment per unit volume), they are known as polar crystals. Temperature affects the spontaneous polarization strength in pyroelectric materials. All the 10 polar crystals belong to the pyroelectric.

1.7.1.2 Spontaneous polarization

In ferroelectric materials, spontaneous polarization happens even when there is no external electric field. When the temperature is raised, an increase in thermal energy prompts the dipoles to reorient themselves. Consequently, the level of spontaneous polarization becomes dependent on temperature. As the temperature rises, the spontaneous polarization diminishes, and it reaches zero above the Curie temperature[34]. In a crystal structure, alterations in temperature can moderately adjust the positions of atoms, leading to the generation of voltage. This phenomenon is referred to as the pyroelectric effect[35]. A subclass of pyroelectric crystals is ferroelectric crystals, in which an electric field can be applied to change the direction of spontaneous polarization. While all crystals exhibiting ferroelectric properties are inherently piezoelectric and pyroelectric, the reverse relationship may not always hold true.

1.7.1.3 Ferroelectric Domains and Hysteresis loop

In the absence of an applied electric field, spontaneous polarization occurs in several equivalent directions, when the temperature of a ferroelectric crystal is decreased towards its Curie temperature, or T_C. The adjacent parts of the crystal align themselves along all these analogous directions to reach a state of lowest energy. The regions where dipoles are oriented uniformly in a single direction are referred to as ferroelectric domains. The interfaces separating these adjacent domains are termed domain walls or domain boundaries. Consequently, due to the deviation from the regular lattice arrangement in these domain walls, a distinct amount of energy is associated with them, termed the domain wall energy.

[34] Nan et al. 2008
[35] Van Run et al. 1974

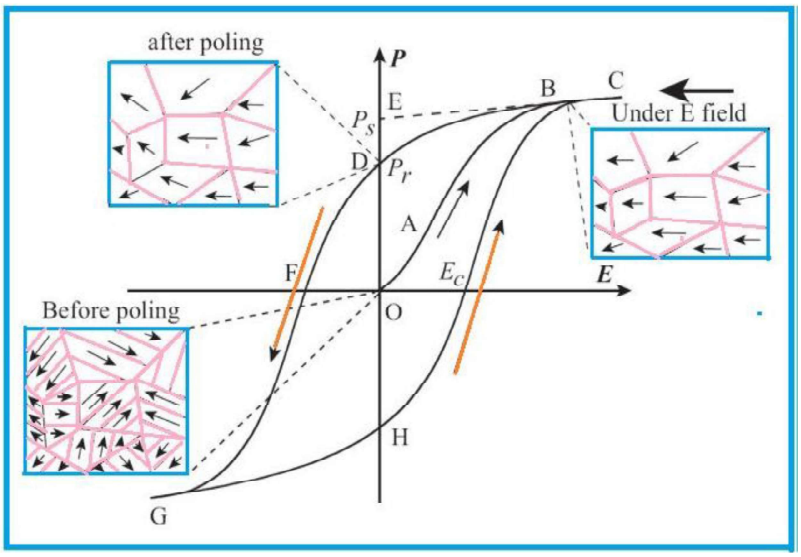

Fig 1.5. The variation of applied field E and resulting polarization P

$BaTiO_3$ and other ferroelectric single crystals exhibit intricate domain configurations[36]. The formation of domains in ferroelectric materials is governed by the minimization of free energy. In the case of barium titanate, above the Curie temperature (130°C), the lattice unit cells undergo some degree of deformation due to the structural phase transition. This leads to a slight distortion in the crystallite, brought about by the altered lattice cells[37]. In ceramics, the grains are interconnected by their neighboring grains across all three dimensions. As a result, they can only flex to a limited extent through the collective movement of adjacent grains. In order to maintain the overall shape of the grain, it either retains mechanical twinning (domains) or experiences high internal stress through deformation to alleviate these stresses[38]. Ferroelectric materials consist of regions characterized by uniform polarization, referred to as ferroelectric domains. These domains are demarcated by interfaces known as domain walls. Within a given domain, the dipoles are uniformly aligned in a specific direction. Multi-ferroelectric domains are formed while a single ferroelectric crystal grows. By applying strong electric fields, the motion of domain walls can lead to the formation of a single domain. This process, termed domain

[36] Van Run et al. 1974
[37] Van Den Boomgaard et al. 1976
[38] Priya et al. 2007

switching, involves the reversal of polarization within a domain due to the influence of a high electric field[39]. A defining attribute of ferroelectric materials is their capability to alter the polarization direction in response to an applied electric field. This characteristic gives rise to a hysteresis in their behavior.

1.8 Dielectric properties

The word 'dielectric material' refers to materials that are good electrical insulators and also polarizable. When an electric field is applied these materials do not conduct electric current but they are not inert to the electric field (E). On application of electric field, there occurs a slight shift in the charged particles within the materials, and the materials gain an electric dipole moment (P). The definition of polarization is the dipole moment per unit volume. Polarization rises in tandem with an increase in the electric field[40]. Two categories of dielectric materials exist: polar and non-polar dielectric materials[41].

The centres of positive and negative charges within the nucleus of non-polar dielectric materials coincide. This alignment results in atoms or molecules lacking a permanent dipole moment. Examples include H_2, N_2, He and Ne. Dielectric materials stemming from non-polar molecules are termed non-polar dielectrics. These materials, in the absence of an external electric field, do not exhibit any net polarization.

Conversely, in polar dielectric materials, the centers of positive and negative charges are not superimposed within the nucleus. Instead, these charges experience a slight but measurable displacement from one another. This leads to the presence of a permanent dipole moment and a resultant net polarization. Examples of such materials include H_2O, N_2O etc. In the presence of an external electric field, these molecules possess both an inherent permanent dipole moment and an induced electric dipole moment. In the absence of an electric field, the intrinsic polarity of one molecule cancels out the polarity of another. When an external electric field is

[39] Priya et al. 2007
[40] Rosenberg 1992
[41] *Physics of dielectric materials: Tareev, Boris Mikhaìlʹlovich: Amazon.com: Books* n.d.

applied, the dipoles align themselves in the direction of the field. Polar dielectric materials can be further categorized into *linear and nonlinear dielectrics*.

When an external electric field is introduced, the polarization of materials with linear dielectrics increases linearly. The polarization likewise diminishes to zero with zero applied field. These materials do not possess saturation polarization (P_{sat}) nor coercive field (E_c). The polarization P and the electric displacement D in linear dielectrics are closely correlated with the applied electric field's intensity (E).

$$D = \varepsilon_0 \varepsilon_r \mathrm{E} \qquad \text{and} \quad P = \varepsilon_0 \chi_e \mathrm{E} \tag{1.17}$$

ε_0 is the free space permittivity =8.854×10^{-12} F/m, χ_e is the dielectric susceptibility, and ε_r is the relative dielectric constant.

The capacitance C is given by

$$C = \varepsilon_0 \varepsilon_r \frac{A}{d} \tag{1.18}$$

For a linear dielectric, the capacitance of a capacitor does not depend upon the applied voltage (V).

In *nonlinear dielectrics*, the electric polarization is a nonlinear function of the electric field. In nonlinear dielectrics, the most important materials are ferroelectric materials. Because of the spontaneously polarised regions known as "domains," these materials exhibit spontaneous polarization (Ps) even in the absence of an applied electric field.

1.8.1 Dielectric Polarization

Upon the application of an external field, dielectric materials undergo polarization. An electric dipole moment emerges when electrically charged particles in the dielectric substance align, causing this polarization (P)[42]. A material is considered polarized when the positive and negative charges within it are displaced relative to each other[43]. Dielectric materials can be represented using two vector

[42] *Physics of Dielectric Materials - B. Tareev - Google Books* n.d.
[43] Colclaser & Diehl-Nagle 1985

quantities: the first is the intensity of the applied electric field (E), and the second is the polarization (P), as depicted in Figure 1.6. In a dielectric, the magnitude of polarization (P) is defined as the response to an external electric field. When no external electric field is present, the dielectric exhibits a zero electric dipole moment because the centers of positive and negative charges coincide [44].

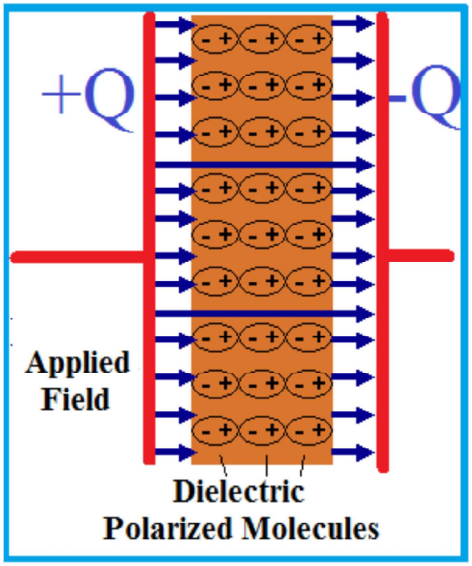

Fig 1.6. Dielectric polarization inside capacitors under an electric field[45]

On application of an external field the centers of positive and negative charges move apart and the dielectric attains a non-zero dipole moment. The total dipole moment is calculated by the molecule's vector polarization.

The polarization can be expressed as

$$P = \frac{\sum p}{V} \tag{1.19}$$

$\sum p$ is the sum of electric dipole moment and V is the volume.

The electric displacement vector (D) can also be used to explain the macroscopic behavior of dielectrics under static or low-frequency conditions.

[44] Kasap 2006
[45] *Ferroelectric Devices - Kenji Uchino - Google Books* n.d.

Dielectric capacitors can accumulate more electric charge than an air-filled capacitor. The electric charge stored per unit area is defined as electric displacement D which is connected to electric field E as [46].

$$D = \varepsilon_r \, \varepsilon_0 E \tag{1.20}$$

$$D = \varepsilon_0 E + \mathrm{P} \tag{1.21}$$

Comparing 1.20 and 1.21 we get

$$P = \varepsilon_0 E(\varepsilon_r - 1) = \chi_e \varepsilon_0 E \tag{1.22}$$

ε_0 is the free space permittivity, ε_r is the dielectric constant or relative permittivity. χ_e or $(\varepsilon_r - 1)$ is called dielectric susceptibility. Permittivity is the macroscopic explanation of the properties of a dielectric, which is associated with the polarization of a material[47]. Macroscopically, polarization (P) is characterized as the density of bound charges per unit area on the surface of a material. When the polarizing constituents within a solid are closely arranged, this arrangement gives rise to dipoles in response to the field [48]. The induced polarization is associated with the effective field experienced by individual molecules, which can differ from the applied field (E)[49]. Electric field along a dielectric is not a constant, but it is determined by the charge on the plates and the orientation of the dipoles. The total field E_{loc} is the actual field induced by a molecule in the dielectric.

The polarization is proportional to the local field E_{loc}

$$P = \chi_e \varepsilon_0 E_{loc} \tag{1.23}$$

E_{loc} induced by the dielectric increases with polarization

$$E_{loc} = E_{ex} + \frac{P}{3\varepsilon_0} \tag{1.24}$$

[46] Buchanan 1986
[47] Anderson & Leaver 1969
[48] *Introduction to Solid State Physics Charles Kittel* 2005
[49] Y. Xu 1991

The induced polarization in molecules is connected with the local field and alternately depends on the external field.

$$P_{induced} \propto E_{loc} \Rightarrow P_{induced} = \alpha E_{loc} \quad (1.25)$$

α is the polarizability. The polarizability is explained as the average dipole moment induced in a unit volume to the local electric field. Polarizability shows the properties of an individual atom or molecule of a dielectric. Dielectric polarizability is a macroscopic electric parameter[50]. The polarization of the dielectric containing N atoms per unit volume is given by,

$$P = N\alpha E_{loc} \quad (1.26)$$

From equation (1.22) , (1.24) and (1.26) we can obtain the Clausius-Mossotti equation, which shows the relation between dielectric permittivity ε_r and polarizability α[51].

$$\frac{(\varepsilon_r - 1)}{(\varepsilon_r + 2)} = \frac{N\alpha}{3\varepsilon_0} \quad (1.27)$$

This formula consists of macroscopic and microscopic quantities.

The total polarization is the sum of the several polarizations namely space charge, electronic, dipolar, and ionic polarization. Total polarization depends upon each type of polarization and also the frequency of the applied external electric field[52] rather than the type of material.

If we apply a reverse electric field, the dipoles can reverse their alignment. The polarization reversal also occur for the dipoles in dielectric material and hence the total polarizability and relative permittivity also changes upon the reversal of the dipoles. In the case of high frequency electric field, the dipoles cannot follow the oscillating electric field, so the switching of polarization is delayed with the applied electric field.

[50] Bell Telephone Laboratories. & Baker 1970
[51] *Introduction to Solid State Physics Charles Kittel* 2005
[52] Y. Xu 1991

This is the reason for the decrease in polarization and also electric permittivity of a material. This stage is called the relaxation stage and the frequency is called relaxation frequency. The frequency exceeds the relaxation frequency dipoles cannot reorient with the applied electric field and the polarization mechanism is on a descend.

1.8.2 Types of Polarization

There are four types of polarization as shown in Figure (1.7) and (1.8) and they are

(1) **Electronic polarization**

Materials made of all-dielectric exhibit this kind of polarization. An atom's nucleus moves towards the negative electrode when an external electric field is applied to it. This is due to the electrons in the atom experiencing a small displacement in the direction of the positive electrode. This displacement results in the atoms acquiring a dipole moment ($\mu=\alpha.E$), where α represents the electronic polarizability of the atom. However, once the applied electric field is removed, both the nuclei and the atom's electrons return to their original positions, causing the polarization to dissipate. Due to the minute nature of charge displacement, the contribution of electronic polarization to the overall polarization is comparatively small in comparison to other polarization mechanisms[53]. Electronic polarization is observable in response to alternating fields with frequencies reaching up to 10^{15} Hz, which surpasses the frequency of visible light[54]. Additionally, this type of polarization is influenced by temperature variations.

(2) **Orientation or Dipolar polarization**

The orientation polarization is dominant than electronic polarization due to the potential for higher charge displacement in relatively larger molecules compared to the separation between the nucleus and electrons in individual atoms. In this type

[53] Moreau et al. 1971
[54] Foster 1960

of polarization reorientation of permanent dipoles occurs. The permanent dipoles are arranged randomly when no external electric field is applied. However, the dipoles align themselves in the direction of an external electric field that is applied. The large degree of polarization is due to the considerable distance between the centers of the opposite charges in a permanent dipole. The dipolar polarization happens in solids and liquids which consist of asymmetric molecules with permanent dipole moments. The dipolar polarization accompanies the alternate electric field up to GHz frequencies.

The dipolar polarizability is defined as

$$\alpha_d = \frac{\alpha_{do}}{1+j\omega} \tag{1.28}$$

α_{do} is the low frequency polarizability and τ is the time required for the orientation process.

(3) Space charge polarization

The space charge polarization takes place because of the charged defects produced by the thermal deformation in the fabrication process. A large number of defects exist in a crystal because of the presence of impurities and dislocations. If we apply an external electric field, free charge carriers moving through the crystal may be trapped by such defects. The consequence of this accumulation of charges induces their image charges to generate a net dipole moment. This is called interfacial polarization or space-charge polarization. The relaxation frequency is in the range 100Hz to 1kHz[55]. In some cases, it is increased up to 100kHz.

[55] *Introduction to Solid State Physics Charles Kittel* 2005

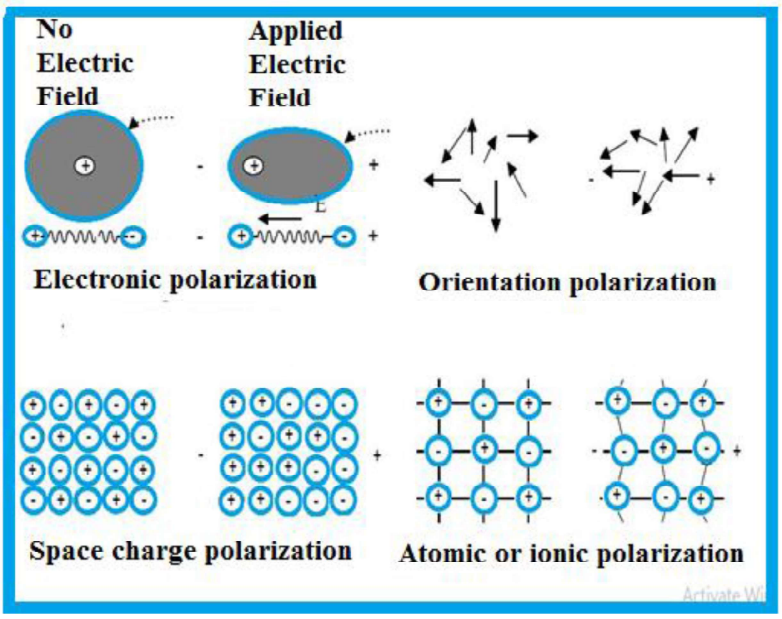

Fig 1.7. Types of polarization mechanism

(4) Ionic polarization

In ionic materials, the ions are shifted from their equilibrium position on application of external field and this is called ionic polarization. Up until the ionic bonding forces stop the process, the ions are moved in opposite directions. α_i is denoted as ionic polarizability. Ionic polarization continues up to a frequency range of 10^{13}Hz in the IR region

So all these polarisabilities contribute to the total polarizabilty,

$$\alpha_{tot}=\alpha_e+\alpha_i+\alpha_d+\alpha_s \quad (1.29)$$

α_{tot} : total polarizabilty

α_e: electronic polarization

α_d: dipolar polarization

α_s: space charge polarization

α_i: ionic charge polarization

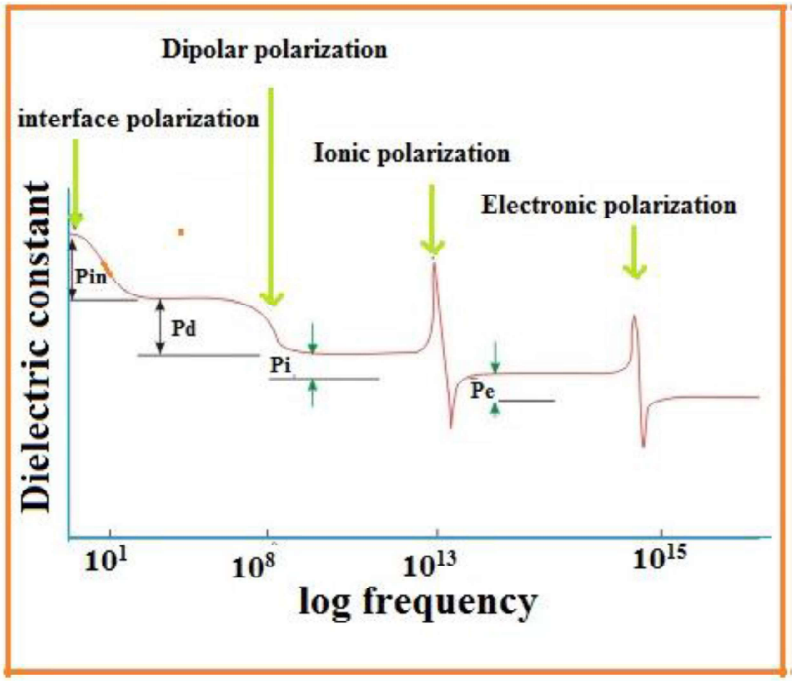

Fig 1.8. Frequency dependence of polarization

1.8.3 Effect of frequency on polarization process

When we apply an electric field, polarization occur as a function of time, as per the relation.

$$P_t = P_{max}(1-e^{\frac{t}{t_\tau}}) \quad (1.30)$$

P_t = Polarization at any time t

t_τ= The relaxation time for a particular polarization process

P_{max}= Maximum polarization when the external field is applied for a long time

When t=t_τ , the equation becomes

$$P_t = P_{max}(1-e) = 0.63\ P_{max} \quad (1.31)$$

The relaxation time is described as the time for the polarization to attain 63% of the maximum polarization.

(a) The change in the electron cloud of the relevant nucleus is what causes the electrical polarization. It can change quickly with varying frequencies. Therefore, it is a fast process that is not affected up to a frequency range about 10^{15} Hz as shown in Figure 1.8.

(b) Because the displaced ions are somewhat heavier than the electrons, ionic polarisation occurs more slowly than electronic polarization. The frequency of lattice vibration is in the range of 10^{13} Hz. If we apply an electric field of frequency 10^{15}Hz, the time needed for one vibration will be a hundred times larger than the period of the applied field, so there is no ionic polarization after the frequency range of 10^{13}Hz as shown in Figure 1.8.

(c) Compared to ionic polarization, dipolar polarization occurs more slowly. The permanent molecular dipoles are aligned in a particular direction which causes the increase in the dielectric loss. The relaxation time is of the order of 10^{-6}s. If the relaxation time is greater than the field oscillation period, the orientational polarization will not take place. It is more common in the audio frequency range and can increase up to the frequency range of 10^{6} Hz in solid materials.

(d) Space charge polarization process is very slow, and it takes place because of the ion migration at lower frequencies that normally extend up to a few kHz.

1.8.4 Dielectric constant

Dielectric constant

The degree of polarizability and storage capacity of charge is defined by the term dielectric constant. A capacitor may store more charge if a dielectric substance is placed in between its plates. The formula links the dielectric constant to the capacitance of a capacitor dielectric material[56].

$$C_0 = \frac{A}{d}\varepsilon_0 \qquad (1.32)$$

[56] Kasap 2006

$$C = C\varepsilon_r \tag{1.33}$$

C and C_0 is the capacitance with and without dielectric respectively. ε_r : permittivity of the dielectric medium. A: Area of the plate. d : thickness of a capacitor.

The low relative permittivity materials are used for electrical insulation applications, and high relative permittivity materials are used in charge storage capacitors.

1.9 Systems under present study

The present study consists of two parts. First part is the synthesis and characterization of spinel and perovskite ferrites. The second part is the synthesis and characterization of composites based on these ferrites and barium titanate. The basic systems under study in the thesis are nickel zinc ferrite and cobalt zinc ferrite as two spinel ferrite phases, and bismuth strontium ferrite as the perovskite ferrites phase.

1.10 Ferrites

Ferrites, which falls under the category of ferromagnetic materials have iron as the main metallic component[57]. These materials exhibit a hard and brittle nature and appear in shades of black or dark grey. The distinctive magnetic properties of the ferrites result from the interactions between the metallic ions positioned in specific arrangements relative to oxygen ions within a crystal structure of the oxide. They find application in various technologies, including transformers, loudspeakers, switches, phase shifters, and more. Ferrites can be categorized into three main types: spinel type, Garnet type, and Magnetoplumbite [58].

[57] Foster 1960
[58] Bammannavar et al. 2008

1.10.1 Spinel ferrite

Spinel ferrites belongs to the cubic crystal system and possess space group Fd-3m. They have the cubic structure with the general formula, MFe_2O_4 where M is a divalent metal ion like Mn, Zn, Co, Cu, or a mixture of these. The smallest cell of a spinel lattice possesses eight molecules of MFe_2O_4. The FCC lattice is established with the larger oxygen ions. Tetrahedral (A) and octahedral (B) sites, which are surrounded by four and six oxygen ions, respectively, are the main interstitial sites. Figure 1.9 indicates the tetrahedral and octahedral coordination of A and B site cations.

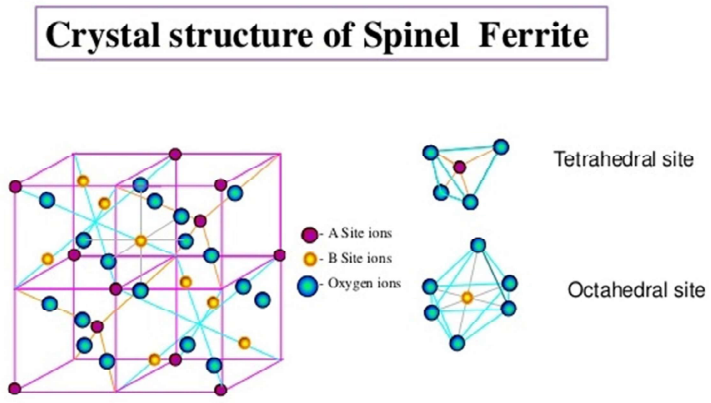

Fig 1.9. crystal structure of spinel ferrite

32 oxygen anions, 64 tetrahedral sites, and 32 octahedral sites make up the unit cell of a spinel structure; however, only 8 and 16 of these sites, respectively, are used with metal ions[59]. The locations of the tetrahedral and octahedral sites are independent of cations character and all the time same. But Madelung energy and ionic radii of the cations also decide the distribution of the cations in the spinel ferrites. There are four groups into which the spinel ferrites are divided: normal, spinel, inverse spinel, and random spinel. According to the cation distribution in the tetrahedral site (A) and octahedral site(B). The cation distribution is generally defined as $(M_{\delta}^{2+}Fe_{1-\delta}^{3+})[M_{1-\delta}^{2+}Fe_{1+\delta}^{3+}]O_4$, inside square bracket represents the cations

[59] Craik n.d.

occupied in the octahedral sites and for elemets outside this, the bracket represents the tetrahedral sites. The general formula $[M^{2+}]_{\text{tetra}}[Fe_2^{3+}]_{\text{oct}}O_4$ where δ=1 for normal spinel ferrite. The octahedral sites are occupied by trivalent cations, whereas the tetrahedral sites are occupied by divalent cations. When an inverse spinel structure has δ=0, the divalent cations solely occupy the octahedral sites, whereas the trivalent cations are equally distributed in both tetrahedral and octahedral locations. The inverse spinel has the general formula $Fe^{3+}[M^{2+}Fe^{3+}]O_4$. The intermediate cation distribution is given as $[B_{0.67}A_{0.33}]_{\text{tet}}[A_{0.67}B_{1.33}]_{\text{oct}}O_4$ with δ=1/3 for random distribution. $ZnFe_2O_4$ shows normal spinel ferrite but $NiFe_2O_4$ and $CoFe_2O_4$ show inverse spinel structure. The nature of the sample and the preparation techniques influence the degree of inversion[60]. The physical properties of the spinel depend upon the degree of inversion[61].

We can permit the arrival of a wide variety of cations into the spinel structure because it is a very stable structure. The arrangement of metal ions in the A and B sites is controlled by the factors like static energy, ionic radius, and electronic configuration. Octahedral sites are bigger than tetrahedral sites in size. Since divalent ions are bigger than trivalent ions, the trivalent ions are occupied in the tetrahedral sites which favors inverse structure. Ni^{2+}, Co^{2+} ions prefer octahedral sites because their charge distribution fit in the octahedral site[62].

Compared to ferrites made of metal, spinel ferrites are less dense. Although their tensile strength is lower, they have a great compressive strength. They can be sculpted into shapes but cannot be rolled or coiled into thin sheets. Although they can withstand moisture and salt, they are vulnerable to strong acids. Spinel ferrites are appropriate for the memory cores of digital computers and microwave guides due to their high electrical resistance, high coercive field, high saturation magnetization, high permeability, and low dielectric losses (shown in Fig. 1.10).

[60] Foster 1960
[61] Barkatt 1996
[62] Foster 1960

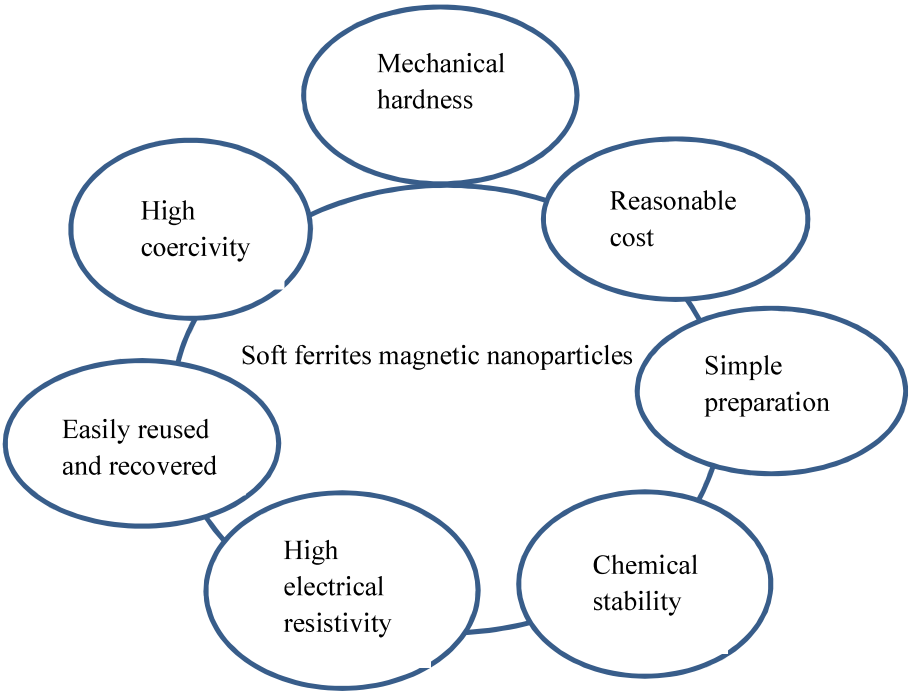

Fig 1.10 Properties of Spinel ferrites

Spinel ferrites have received attention recently in a variety of fields, including communications, automation, audio and video equipment, home appliances, and industrial technology. The demand for magnetic materials, especially those based on ferrite-based compounds, is currently very high in the electronic sectors. However, as high-frequency applications become more prevalent, conventional approaches to reducing eddy current losses, including using iron cores, proved to be cost-effective. Additionally, power supply companies demand decreased power conversion energy losses while retaining sufficient initial permeability. The most widely used ferrite is Mn-Zn ferrite, which is suited for use in transformers, deflection yoke rings, magnetic recording heads, transducers, and other devices due to its low magnetic loss, higher saturation magnetization, and permeability. Here we have studied two spinel ferrite systems namely, nickel zinc ferrite and cobalt zinc ferrite.

1.10.2 Nickel Zinc ferrite ($Ni_{1-x}Zn_xFe_2O_4$)

Soft magnetic Ni-Zn ferrite nanoparticles are useful for high-frequency applications because to their high saturation magnetization, high electrical resistance, and high magnetic permeability. The metal ions occupying the A and B sites together determine the net magnetic moment in spinel ferrite. When ferromagnetic iron ions, zinc ions, and nickel ions coexist in nickel-zinc ferrites, the outcome is a maximum magnetic moment that makes these Ni-Zn ferrites suitable for a variety of uses. Soft ferrimagnetic materials, nickel-zinc ferrites have good corrosion resistance, low dielectric constant, low magnetic coercivity, considerable eddy-current loss in the high-frequency band, and extraordinarily high resistivity. The microstructure and magnetic characteristics of these ferrites are greatly influenced by the amount of constituent metal oxides, impurities, or doping levels, the sintering environment, and the preparation method. Because Ni-Zn ferrites are easy to make and may be used for a wide range of purposes, they are consequently attractive materials from a business perspective[63].

1.10.3 Cobalt Zinc ferrite ($Co_{1-x}Zn_xFe_2O_4$)

Cobalt zinc Ferrite ($Co_{1-x}Zn_xFe_2O_4$) belong to hard ferromagnetic material with a higher Curie temperature ($T_C \sim 520^0C$), moderate saturation magnetization (80 emu/g), large magneto-crystalline anisotropy constant (270×10^3 - 90×10^3 Jm^{-3}) and large coercivity. $CoFe_2O_4$ is a member of the AB_2O_4-type spinel family, where A, B, and O stand for divalent, trivalent cations, and oxygen anion, respectively. It possess an inverse spinel structure, where Co^{2+} cations hold at octahedral sites and Fe^{3+} cations are occupied at both the tetrahedral site and the octahedral site and it is represented as $[Co_\delta Fe_{1-\delta}][Co_{1-\delta}Fe_{1+\delta}]O_4$. The distribution of A and B cations in the FCC oxygen sub-lattices is being carried out by an inversion factor of δ. The difference in the actual dispersion of the cations at A and B positions in spinel ferrites depends on the length of the link because the super-exchange interaction in the Fe^{3+} (A-site) – Fe^{3+} (B-site) ions is typically different from the Co^{2+} (A-site)-

[63] Punia et al. 2021

Fe^{3+} (B-site) interactions. $Co_{1-x}Zn_xFe_2O_4$ is one of the most promising materials for use in medical applications, such as microwave devices, data storage, magneto-optic sensors, electronic devices, medical diagnostics, magnetic medication delivery, and data storage. Since Zn^{2+} ions, which are nonmagnetic, are present in zinc ferrite, it is a very significant soft magnetic material.

The utilization of nano zinc ferrite in the electronics industry is expanding rapidly owing to its combination of low coercivity, minimal dielectric loss, and heightened magnetic permeability. These are the materials with exceptional chemical and physical characteristics and are also thermally stable semiconductor materials. The uses for zinc ferrites include as catalysts in photocatalysis, in MRI, gas sensors, temperature stabilisers, pigments, actuators, and others. It also exhibits excellent mechanical hardness, ease of synthesis, wear resistance, electrical insulation, chemical, and thermal stability. Cobalt Ferrite is a good option to create a magneto-electric composite material because of its effective magnetization parameters and higher magneto-crystalline anisotropy value[64].

1.10.4 Bismuth Strontium Ferrite ($Bi_{1-x}Sr_xFeO_3$)

Since the 1960s, Bismuth ferrite ($BiFeO_3$) has been thoroughly investigated as a multiferroic material that exhibits both antiferromagnetic and ferroelectric order characteristics coexisting in one phase at the same time. Researchers have shown great interest in $BiFeO_3$ due to its room temperature coexistence of ferroelectric and magnetic orders, making it valuable for applications like nonvolatile memories and nanoelectronic products[65]. Due to its high ferroelectric polarization, it is the most researched multiferroic material (~100 $\mu C/cm^2$) with a high Curie temperature of ~1103K and G-type antiferromagnetism with a high Neel temperature of ~673K. The perovskite structure of $BiFeO_3$ is rhombohedral and has space group R3c[66]. The $BiFeO_3$ has unit cell lattice parameter $a_{rhombohedral}$ =3.965Å and a rhombohedral angle,

[64] Bammannavar et al. 2008
[65] Wang 2017
[66] Moreau et al. 1971

α is 89.3^0-89.4^0 at room temperature[67]. Additionally, the unit cell has a hexagonal form with the perovskite cube's diagonals running parallel to the c axis, specifically [001]hexagonal ‖ [111]pseudo cubic. $a_{hexagonal}$ =5.58Å and $c_{hexagonal}$ =13.89Å are the reported lattice parameters[68]. For the ideal cubic structure, the rotation angle of the oxygen octahedral has to be 0^0, but in the case of bismuth ferrite, it is ω=11^0-14^0 around the polar [111]pseudo cubic axis[69]. The oxygen octahedra is deformed by the change in rotation angle, which modifies the Fe-O-Fe bond angle (θ=154^0 to 156^0). Oxygen octahedra is defined by the Gold Schmid tolerance factor(t) described as[70].

$$t = {(r_{Bi} + r_0)}\Big/{(r_{Fe} + r_0)^{1/2}} \quad . \tag{1.34}$$

In $BiFeO_3$, the bismuth ion has eightfold coordination, and iron has sixfold coordination and high spin and also has t=0.88[71]. Due to the t value being less than 1. The oxygen octahedra deform to fit into small unit cells. Figure 1.11 shows the crystal structure of bismuth ferrite.

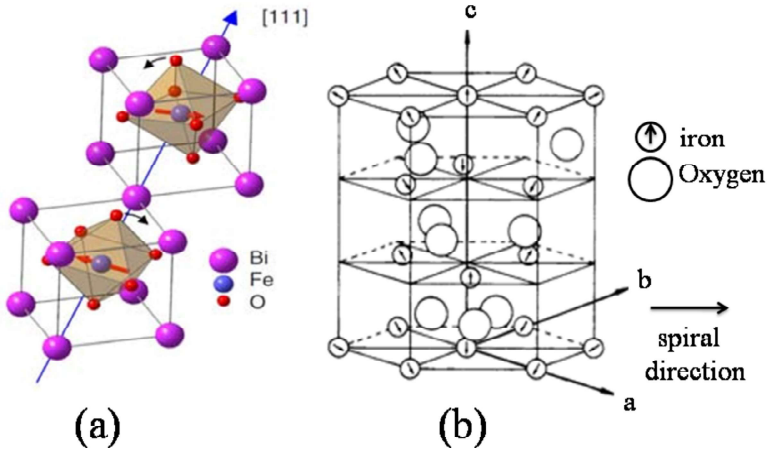

Fig 1.11: (a) Crystal structure of bulk $BiFeO_3$ [72](b) The part of $BiFeO_3$ lattice with only iron and oxygen ions[73]. The arrow indicate the Fe^{3+} moment direction.

[67] Kubel & Schmid 1990
[68] Bucci et al. 1972
[69] Kubel & Schmid 1990; Moreau et al. 1971
[70] Goldschmidt 1926
[71] Shannon & IUCr 1976
[72] Lubk et al. 2009

In bulk $BiFeO_3$, ferroelectric polarization aligns with the diagonals of the perovskite unit cell, specifically along the pseudo-cubic [111]c direction. The polarization arises from the rearrangement of Bi, Fe, and O atoms relative to each other. Early measurements showed relatively small polarization (~6.1 μCcm^{-2}) due to impurities and measurement limitations, but recent studies on single crystals and thin films demonstrate a spontaneous polarization of approximately 100 μCcm^{-2}. $BiFeO_3$'s G-type antiferromagnetic nature involves ferromagnetic coupling within the same (111) planes and antiferromagnetic coupling between adjacent (111) planes. The hexagonal description of the spin structure of $BiFeO_3$ is displayed in Figure 1.11b. The unique spin cycloid pattern in the antiferromagnetic ordering introduces a long repeat distance and a specific propagation vector. The cycloid has a very long repeat distance (62–64 nm), and the direction of propagation is [110][74].

1.11 Perovskite oxides as ferroelectric phase

Among the preceding ferroelectric materials, the perovskite oxides, barium titanate in the general formula ABO_3 is widely used as a ferroelectric phase in multiferroic composites. With the oxygen available at the face centres and the larger cations (A) at the corners and the smaller cations (B) in the centre, the ABO_3 structure has a basic cubic unit cell. The unit cell is built up of a corner—linked network of oxygen octahedra with B ions engaged in the interstices set up by the linked octahedral. These materials' spontaneous polarization results from the B cations' off-center shift with respect to the oxygen[75]. In $BaTiO_3$, Ba ions are occupied in the A-site and Ti ions are occupied in B-site. Below Curie temperature (T_C) it possesses a ferroelectric phase with a tetragonal structure and above Curie temperature, it possesses a cubic structure with a paraelectric phase (Fig1.12) Due to its piezoelectric, dielectric, and ferroelectric properties it find application in the capacitor, microwave devices, and transducers, etc.

[73] Sosnowska et al. 1982
[74] Lebeugle et al. 2008
[75] Roy & Majumder 2012

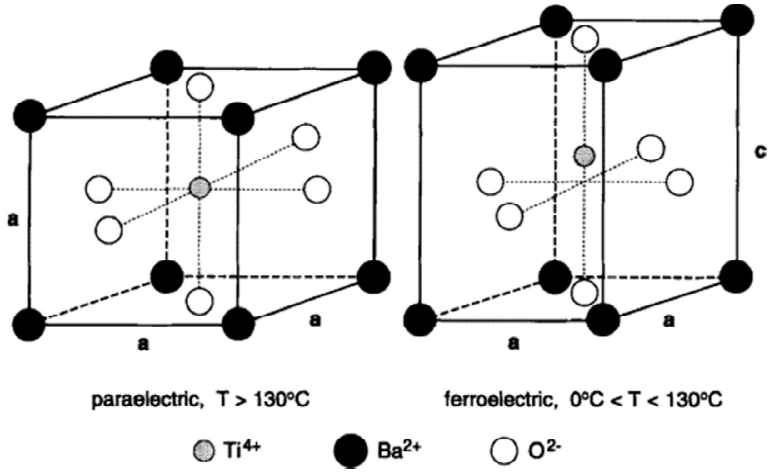

Fig 1.12 Structure of barium titanate

1.12 Motivation and objectives of the thesis

As the search for highly insulating single-phase magnetoelectric multiferroics with potential for functioning at higher temperatures becomes more intense, the integration of such materials into technological applications like ferroelectric and magnetic devices is still a challenge. Achieving higher levels of magnetism and extending operational temperatures beyond room temperature are essential requisites. For instance, a desirable objective involves amalgamating the advantageous electrical characteristics for writing data with the non-resettable magnetic properties for reading data in a magnetoelectric random access memory, thereby capitalizing on the strengths of both magnetic and ferroelectric random access memory technologies.

However, the current magnetism exhibited by multiferroics is insufficient for efficient practical read operations. Furthermore, the magneto-electric effect, which allows qualities to be converted from magnetic to electric, is usually limited to insulators and frequently does not meet application requirements. To render multiferroics feasible for practical devices, maintaining their ferroelectric behavior while simultaneously enhancing their magnetic properties is imperative. Among naturallyoccurring single-phase multiferroics, only $BiFeO_3$ demonstrates magnetoelectric coupling at room temperature. Nevertheless, this coupling is exceptionally weak, rendering it impractical for use in real-world device applications.

The objective of this thesis is to synthesize multiferroic composites comprising ferrites with barium titanate to enhance the multiferroic properties of composites. The linear magnetoelectric effect in $BiFeO_3$ is attributed to its crystalline structure, but it diminishes in pure $BiFeO_3$ due to its spatially modulated spiral structure leading to zero net magnetism, which also hinders ferroelectric polarization. Additionally, $BiFeO_3$ often exhibits excellent electrical conductivity due to Fe state shifting and the presence of oxygen vacancies. However, synthesizing pure phase $BiFeO_3$ ceramics is challenging due to the narrow temperature range required for phase stabilization.

Researchers have explored various strategies to overcome these challenges, such as employing different synthesis techniques, partially substituting analogous ions (e.g., rare-earth, transition metal, and alkaline earth) for Fe^{3+} and Bi^{3+} in the $BiFeO_3$ lattice, and combining $BiFeO_3$ solid solutions with other perovskites. By adjusting stoichiometry, substituting ions at specific sites, forming solid solutions, and optimizing temperature and pressure conditions, it is possible to disrupt the spin cycloidal structure, thereby enhancing magnetoelectric properties and reducing electrical leakage in the $BiFeO_3$ system.

Motivated by these considerations, our study focuses on synthesizing and investigating the structural, microstructural, and magnetoelectric properties of Ni-Zn and Co-Zn ferrites, as well as strontium-substituted bismuth ferrite systems incorporated into barium titanate to form multiferroic composites. This research is innovative as it explores Ni-Zn and Co-Zn ferrites within a multiferroic composite, an area with limited prior exploration.

Unlike single-phase materials, multiferroic composites exhibit improved magnetoelectric response at temperatures above ambient. This response is influenced by various properties such as electric, dielectric, and magnetic characteristics. Furthermore, a comprehensive understanding of both pure phase and composite properties is crucial for specific device applications, as they significantly affect device performance.

Importantly, many high-performance multiferroic composites reported in the literature contain materials with high lead content, posing environmental and health risks. Therefore, the development of lead-free multiferroic composites exhibiting significant magnetoelectric behavior while being environmentally safe is of paramount importance.

To address this, our current thesis work focuses on creating lead-free multiferroic composites that integrate ferrites as the magnetic phase and pure $BaTiO_3$ as the ferroelectric phase. The first part of the thesis involves making ferrites, while the second part deals with synthesising and characterising barium titanate-based nanocomposites. The main objectives of the thesis include

- ✓ Structural, Dielectric, Magnetic and optical characterization of zinc substituted nickel ferrite samples $Ni_{1-x}Zn_xFe_2O_4$ (x=0, 0.3, 0.5, 0.7 and 1)
- ✓ Structural, Dielectric, Magnetic and optical characterization of zinc substituted cobalt ferrite samples $Co_{1-x}Zn_xFe_2O_4$ (x=0, 0.3, 0.5, 0.7 and 1)
- ✓ Structural, Dielectric, Magnetic and optical characterization of strontium substituted bismuth ferrite samples $Bi_{1-x}Sr_xFeO_3$ (x=0, 0.3, 0.5 and 0.7)
- ✓ Synthesize and structural, electrical, magnetic and multiferroic characterisation of nickel zinc ferrite and barium titanate nanocomposites ($Ni_{1-x}Zn_xFe_2O_4$:$BaTiO_3$ (1:1, 1:2, 2:1 ratio)
- ✓ Synthesize and structural, electrical, magnetic and multiferroic characterisation of cobalt zinc ferrite and barium titanate nanocomposites ($Co_{1-x}Zn_xFe_2O_4$:$BaTiO_3$ (2:1 ratio)
- ✓ Synthesize and structural, electrical, magnetic and multiferroic characterisation of strontium substituted bismuth ferrite and barium titanate nanocomposites ($Bi_{1-x}Sr_xFeO_3$:$BaTiO_3$ (1:2 and 2:1 ratio)
- ✓ Interpreting and understanding the results based on various potential mechanisms.

The thrust of this research is to advance our understanding of these novel materials and contribute to the development of enhanced multiferroic composites that can be harnessed for practical applications while maintaining environmental sustainability.

1.13 Literature Review

Single phase materials possess low ME response which limits the application in this field and alternative methods were used to overcome the limitation[76]. The concept of "product property was put forward by Van Suchtelen in 1972 [77] in two-phase nanocomposite materials. After that, the product property was explained by the scientists at Philips research laboratory who experimentally proved this on the composite system of $BaTiO_3$-$CoFe_2O_4$ nanocomposites prepared by the unidirectional solidification[78].This system possesses a voltage coefficient is two times larger than the value obtained by the single-phase materials at room temperature[79]. In nanocomposites, the elastic coupling interaction between the two materials causes the ME coupling. The ME value obtained for the composite systems is very large but the preparation technique is more complex including the critical control over the composition and other processing parameters [80].

In the 1990s the nanocomposites of $BaTiO_3$ or $Pb(Zr,Ti)O_3$ with ferrites were synthesized by the conventional sintering method[81]. In this technique, the synthesized samples of the two phases are mixed and made into pellets that are sintered at relevant temperatures. The synthesis technique is easier compared with the solidification technique but due to the large number of variables involved in this process such as grain size and crystallinity of the two phases and the sintering temperature, the properties of the composites can be found to be widespread[82]. However, to realize the ME coupling between the constituent phases of the

[76] Nan et al. 2008
[77] Nan et al. 2008
[78] Van Den Boomgaard et al. 1974; Van Run et al. 1974
[79] Van Den Boomgaard et al. 1976
[80] Priya et al. 2007
[81] Lopatin et al. 2011
[82] van den Boomgaard & Born 1978

composites by various techniques such as microchemical approaches[83] and Green's function technique[84] emerged. By Green's function approach, a large value of ME coupling was theoretically predicted in 2001 in $Tb_{1-x}Dy_xFe_2$ (Terfenol-D) as a magnetic phase [85] which proved to be the ground breaking development and then, subsequently demonstrated experimentally[86]. Thereafter, a large number of multiferroic composites with different connectivity schemes have been synthesized and their multiferroic properties are investigated in detail. Many of the above nanocomposites were prepared using PZT, PZN-PT, and PMN-PT it is very hazardous to human health, and these materials containing lead are also banned in industrial applications[87]. So in our thesis, we synthesized the nanocomposites based on barium titanate. After that large number of multiferroic nanocomposites was prepared some of them are given in below.

$BaTiO_3$ is the most popular ferroelectric material[88]. $BaTiO_3$ is the ferroelectric phase in many composite systems, and it is the subject of extensive investigation, to modify the material's properties by changing its constituent parts for a specific purpose. Similarly, the magnetic phase can also be modified by substitution. Some of the investigated composite systems are $Ba_{0.8}Pb_{0.2}Ti_{0.8}Zr_{0.2}O_3$-$Ni_{0.8}Cu_{0.2}Fe_2O_4$[89].$(0.5Ba(Zr_{0.2}Ti_{0.8})O_3$- $0.5(Ba_{0.7}Ca_{0.3})TiO_3$-$CoFe_2O_4$[90], $BaZr_{0.08}Ti_{0.92}O_3$-$Co_{1.2-y}Mn_yFe_{1.8}O_4$,[91] $Ba_{0.6}Sr_{0.4}TiO_3$- $Ni_{0.2}Cu_{0.2}Zn_{0.62}O$ $(Fe_2O_3)_{0.98}$,[92] $BaTiO_3$-$Co_{0.6}Zn_{0.4}Fe_{1.7}Mn_{0.3}O_4$[93]. Patankar et al. have calculated the dielectric, ac conductivity and ME coupling studies of composite systems $BaTiO_3$ with

[83] Benveniste 1995; Huang & Kuo 1998
[84] Nan 1994
[85] Nan et al. 2001
[86] Dong et al. 2003; Ryu et al. 2001
[87] Leontsev & Eitel 2010
[88] Van Den Boomgaard et al. 1976
[89] Kanamadi, Seeta Rama Raju, et al. 2009
[90] Rani et al. 2014
[91] Kambale, Shaikh, Kolekar, et al. 2010
[92] Su et al. 2010
[93] Gupta & Chatterjee 2013

$MnFe_{1.8}Cr_{0.2}O_4$[94] and $CuFe_{1.6}Cr_{0.4}O_4$ [95]and $Ba_{0.8}Pb_{0.2}TiO_3$ with $Ni_{0.5}Co_{0.5}Fe_2O_4$[96] $MnFe_{2-x}Cr_xO_4$ and $CuFe_{2-x}Cr_xO_4$[97].

Similar research was also done by the researchers[98]. We can see that for most of the nanocomposites the ME coefficient value was maximum for the content of the Magnetic phase[99]. This behavior can be explained by the resistance network. Patil et al. [100] explain the dependence of ME output and dc resistivity of the (x)$NiFe_2O_4$-(1-x) $Ba_{0.9}Sr_{0.1}TiO_3$composites it is found that both dc resistivity and ME coupling decrease with the ferrite content from x=0.15 to 0.45 Yu et al. [101]studied on the (1-x) $BaTiO_3$-(x) $(Ni_{0.3}Zn_{0.7})Fe_{2.1}O_4$ composites and observed a sharp decrease in the resistivity of the composites from $10^8\Omega$cm to $10^4\Omega$cm as ferrite phase increases. This gives the idea that the current leakage is one of the limiting factors to getting the large ME signal in the composites so it should be minimized. The solution to the problem was good dispersion of the magnetic phase in the matrix of the ferroelectric phase and an increase in the resistivity of the magnetic phase. The composites the value of ME coefficient for different synthesis techniques such as spark plasma sintering(SPS)[102] hot pressing[103] and microwave sintering [104]are used to improve ME coupling of the composites. Spark plasma sintered (0.75)$BaTiO_3$-(0.25) $BaFe_{12}O_9$ composite system shows improved ferroelectric and magnetic properties compared to the conventional sintered (CS) sample[105]. The ME output for SPS is 2.95 mV/cm Oe compared to CS sample (1.45 (mV/cm Oe)). Some of barium titanate based composites are given below.

[94] Patankar et al. 2001
[95] *(PDF) AC conductivity and magnetoelectric effect in CuFe 1.6Cr 0.4O 4–BaTiO 3 composite ceramics | Kota Venkata Sivakumar and Kota Venkata Siva Kumar - Academia.edu* n.d.
[96] Patankar et al. 2005
[97] Patankar et al. 2006
[98] Kambale, Shaikh, Bhosale, et al. 2010; Kanamadi, Kim, et al. 2009
[99] S. Srinivas et al. 2006; S. Srinivas & Yu Li 2005
[100] D. R. Patil & Chougule 2009
[101] Yu & Ang 2002
[102] Ghosh et al. 2012
[103] Srinivasan et al. 2004
[104] Katlakunta et al. 2014
[105] A. Srinivas et al. 2013

$BaTiO_3$-$CoFe_2O_4$ nanocomposites were prepared by Molten-salt synthesis method with the value α_E = 17.04 (mV/cm Oe)[106]. $BaTiO_3$-$La_{0.7}Sr_{0.3}MnO_3$ core shell nanostructure synthesized by sol-gel method with the value of α_E = 15.6 (mV/cm Oe)[107]. $Ba_{1-x}Sr_xTiO_3$-$La_{0.67}Sr_{0.33}MnO_3$ nanocomposites were prepared by hydroxide co-precipitation route with the value of α_E = 15.51(mV/cmOe)[108]. $BaZr_{0.08}Ti_{0.92}O_3$-$NiFe_{1.9}Mn_{0.1}O_4$ were prepared by conventional ceramic method with the value of α_E = 1.18(mV/cm Oe)[109]. $BaSr_{0.02}TiO_3$-$CoFe_2O_4$ nanocomposites were prepared by solid state reaction method with the value of α_E = 0.761(mV/cm Oe)[110]. $Ba_{1-x}Sr_xTiO_3$-$Co_{0.9}Ni_{0.1}Fe_{2-x}Mn_xO_4$ nanocomposites were prepared by Hydroxide-co-precipitation route followed by ceramic processing approach with the value of α_E =5.57(mV/cm Oe)[111]. $BaTiO_3$ – (0.5) $CoFe_2O_4$ nanocomposites were prepared by conventional solid state reaction method with the value of α_E = 15.6 (mV/cm Oe)[112].

$Ba_{0.5}Sr_{0.5}Zr_{0.5}Ti_{0.5}O_3$–(0.2) $Ni_{0.12}Mg_{0.18}Cu_{0.2}Zn_{0.5}Fe_2O_4$ nanocomposites were prepared by conventional solid state reaction method with the value of α_E = 0.60 (mV/cm Oe)[113]. $BaTiO_3$ – $La_{0.7}Ba_{0.3}MnO_3$ nanocomposites of trilayer were prepared by co-firing method with the value of α_E = 0.55 (mV/cm Oe)[114]. $BaTiO_3$ – $NiFe_2O_4$ multilayer were prepared by sintering method with the value of α_E = 18 (mV/cm Oe)[115]. [0.65$BiFeO_3$ -0.35$BaTiO_3$] –$BiY_2Fe_5O_{12}$ nanocomposites of bilayer were prepared by co-firing method with the value of α_E = 0.87 (mV/cm Oe)[116]. The literature review concludes that the multiferroic nanocomposites are fabricated and studied by various researchers.

[106] Nie et al. 2009
[107] Nayek et al. 2013
[108] Sutar et al. 2014
[109] Kambale, Shaikh, Bhosale, et al. 2010
[110] Kanamadi, Kim, et al. 2009
[111] Sutar et al. 2012
[112] Agarwal et al. 2012
[113] Rahaman et al. 2014
[114] Clabel H. et al. 2014
[115] D. Patil et al. 2011
[116] Yang et al. 2015

References

AC conductivity and magnetoelectric effect in CuFe 1.6Cr 0.4O 4–BaTiO 3 composite ceramics | Kota Venkata Sivakumar and Kota Venkata Siva Kumar - Academia.edu. (n.d.). Retrieved August 9, 2022, from https://www.academia.edu/7741949/AC_conductivity_and_magnetoelectric_effect_in_CuFe_1_6Cr_0_4O_4_BaTiO_3_composite_ceramics

Agarwal, S., Caltun, O. F., & Sreenivas, K. (2012). Magneto electric effects in BaTiO 3-CoFe 2O 4 bulk composites. *Solid State Communications*, *152*(21), 1951–1955. https://doi.org/10.1016/j.ssc.2012.08.002

Anderson, J. C. (Joseph C., & Leaver, K. D. (Keith D. (1969). *Materials science*. 276.

Bammannavar, B. K., Naik, L. R., & Chougule, B. K. (2008). Studies on dielectric and magnetic properties of (x) Ni0.2 Co0.8 Fe2 O4 + (1-x) barium lead zirconate titanate magnetoelectric composites. *Journal of Applied Physics*, *104*(6), 0–8. https://doi.org/10.1063/1.2986470

Barkatt, A. (1996). Magnetic Ceramics By Raul Valenzuela (National University of Mexico). Cambridge University Press: Cambridge, U.K. 1994. xix + 312 pp. $79.95. ISBN 0-521-36485-X. *Journal of the American Chemical Society*, *118*(4), 5–6. https://doi.org/10.1021/JA945153Z

Bedanta, S., & Kleemann, W. (2008). Supermagnetism. *Journal of Physics D: Applied Physics*, *42*(1), 013001. https://doi.org/10.1088/0022-3727/ 42/ 1/013001

Bell Telephone Laboratories., & Baker, D. (1970). *Physical design of electronic systems.* Prentice-Hall.

Benveniste, Y. (1995). Magnetoelectric effect in fibrous composites with piezoelectric and piezomagnetic phases. *Physical Review B*, *51*(22), 16424. https://doi.org/10.1103/PhysRevB.51.16424

Bichurin, M. I., Kornev, I. A., Petrov, V. M., & Lisnevskaya, I. V. (2011). Investigation of magnetoelectric interaction in composite. *Http://Dx.Doi.Org/10.1080/00150199708222209*, *204*(1–4), 289–297. https:// doi.org/10.1080/00150199708222209

Blundell, S. (2001). *Magnetism in Condensed Matter: Paperback: Stephen Blundell - Oxford University Press*. 256. http://ukcatalogue.oup.com/ product/ 9780198505914.do

Bucci, J. D., Robertson, B. K., James, W. J., & IUCr. (1972). The precision determination of the lattice parameters and the coefficients of thermal expansion of BiFeO3. *Urn:Issn:0021-8898*, *5*(3), 187–191. https:// doi.org/ 10.1107/S0021889872009173

Buchanan, R. C. (1986). *Ceramic materials for electronics : processing, properties, and applications*. 481.

Cane, P. (1999). Chapter 1: Introduction. *Atiyah's Accidents, Compensation and the Law*, 3–21.

Clabel H., J. L., Zabotto, F. L., Nogueira, I. C., Schio, P., Garcia, D., De Lima, O. F., Leite, E. R., Moreira, F. M. A., & Cardoso, C. A. (2014). Magnetoelectric properties of laminated La0.7Ba 0.3MnO3-BaTiO3 ceramic composites. *Journal of Magnetism and Magnetic Materials*, *364*, 18–23. https://doi.org/10.1016/j.jmmm.2014.04.014

Colclaser, R. A., & Diehl-Nagle, S. (1985). *Materials and devices for electrical engineers and physicists*. 284.

Craik, D. J. (Derek J. . (n.d.). *Magnetic oxides,*.

Das, R. (2013a). *Study of Magnetic, Ferroelectric and Magnetoelectric properties in bulk and nanostructured Multiferroics Physics (Experimental)*.

Das, R. (2013b). *Study of Magnetic , Ferroelectric and Magnetoelectric properties in bulk and nanostructured Multiferroics University of Calcutta*. *September*.

Dong, S., Cheng, J., Li, J. F., & Viehland, D. (2003). Enhanced magnetoelectric effects in laminate composites of Terfenol-D/Pb(Zr,Ti)O 3 under resonant drive. *Applied Physics Letters*, *83*(23), 4812–4814. https://doi.org/ 10.1063/1.1631756

Elements of Materials Science and Engineering (Addison-Wesley Series in Metallurgy & Materials Engineering). Retrieved May 6, 2022

Ferroelectric Devices - Kenji Uchino - Google Books. (n.d.). Retrieved April 2, 2022

Filippov, Y. P., Ihas, G. G., & Vainberg, V. V. (2009). Magnetoresistance of TVO temperature sensor at T<1 K. *Review of Scientific Instruments*, *80*(9), 094902. https://doi.org/10.1063/1.3193718

Foster, L. S. (1960). Ferrites (Smit, J.; Wijn, H. P. J.). *Journal of Chemical Education*, *37*(7), 380–380. https://doi.org/10.1021/ED037P380.3

Ghosh, D., Han, H., Nino, J. C., Subhash, G., & Jones, J. L. (2012). Synthesis of BaTiO3-20wt%CoFe2O4 Nanocomposites via Spark Plasma Sintering. *Journal of the American Ceramic Society*, *95*(8), 2504–2509. https:// doi.org/10.1111/J.1551-2916.2012.05221.X

Goldschmidt, V. M. (1926). Die Gesetze der Krystallochemie. *Naturwissenschaften 1926 14:21*, *14*(21), 477–485. https://doi.org/10.1007/BF01507527

Gupta, A., & Chatterjee, R. (2013). Dielectric and magnetoelectric properties of BaTiO3–Co0.6Zn0.4Fe1.7Mn0.3O4 composite. *Journal of the European Ceramic Society*, *33*(5), 1017–1022. https://doi.org/10.1016/J. JEURCERA MSOC.2012.11.003

Handbook of Advanced Dielectric, Piezoelectric and Ferroelectric Materials .Google Books. (n.d.). Retrieved May 2, 2022

Huang, J. H., & Kuo, W. S. (1998). The analysis of piezoelectric/piezomagnetic composite materials containing ellipsoidal inclusions. *Journal of Applied Physics*, *81*(3), 1378. https://doi.org/10.1063/1.363874

Introduction to Solid State Physics Charles Kittel. (2005).

Kalinin, S. V., Kim, Y., Fong, D. D., & Morozovska, A. N. (2018). Surface-screening mechanisms in ferroelectric thin films and their effect on polarization dynamics and domain structures. *Reports on Progress in Physics*, *81*(3). https://doi.org/10.1088/1361-6633/AA915A

Kambale, R. C., Shaikh, P. A., Bhosale, C. H., Rajpure, K. Y., & Kolekar, Y. D. (2010). Studies on magnetic, dielectric and magnetoelectric behavior of (x) NiFe1.9Mn0.1O4 and (1 − x) BaZr0.08Ti0.92O3 magnetoelectric composites. *Journal of Alloys and Compounds*, *489*(1), 310–315. https://doi.org/10.1016/J.JALLCOM.2009.09.080

Kambale, R. C., Shaikh, P. A., Kolekar, Y. D., Bhosale, C. H., & Rajpure, K. Y. (2010). Studies on dielectric and magnetoelectric behavior of 25% CMFO ferrite and 75% BZT ferroelectric multiferroic magnetoelectric composites. *Materials Letters*, *64*(4), 520–523. https://doi.org/10.1016/J. MATLET. 2009.11.064

Kanamadi, C. M., Kim, J. S., Yang, H. K., Moon, B. K., Choi, B. C., & Jeong, J. H. (2009). Magnetoelectric effect and complex impedance analysis of (x)CoFe2O4 + (1 − x)Ba0.8Sr0.2TiO3 multiferroics. *Journal of Alloys and Compounds*, *481*(1–2), 781–785. https://doi.org/10.1016/ J.JALLCOM. 2009.03.085

Kanamadi, C. M., Seeta Rama Raju, G., Yang, H. K., Choi, B. C., & Jeong, J. H. (2009). Conduction mechanism and magnetic properties of (x) Ni0. 8Cu0.2Fe2O4 + (1 − x)Ba0.8Pb0.2Ti0.8Zr0.2O3 multiferroics. *Journal of Alloys and Compounds*, *479*(1–2), 807–811. https://doi.org/ 10. 1016/J. JALLCOM.2009.01.053

Kasap, S. O. (Safa O. . (2006). *Principles of electronic materials and devices*.

Katlakunta, S., Raju, P., Meena, S. S., Srinath, S., Sandhya, R., Kuruva, P., & Murthy, S. R. (2014). Multiferroic properties of microwave sintered BaTiO3–SrFe12O19 composites. *Physica B: Condensed Matter*, *448*, 323–326. https://doi.org/10.1016/J.PHYSB.2014.04.073

Kodama, R. H. (1999). Magnetic nanoparticles. *Journal of Magnetism and Magnetic Materials*, *200*(1–3), 359–372. https://doi.org/10.1016/S0304-8853(99)00347-9

Kubel, F., & Schmid, H. (1990). Structure of a ferroelectric and ferroelastic monodomain crystal of the perovskite BiFeO3. *Urn:Issn:0108-7681*, *46*(6), 698–702. https://doi.org/10.1107/S0108768190006887

Lebeugle, D., Colson, D., Forget, A., Viret, M., Bataille, A. M., & Gukasov, A. (2008). Electric-field-induced spin flop in BiFeO3 single crystals at room temperature. *Physical Review Letters*, *100*(22), 227602. https://doi.org/10.1103/PHYSREVLETT.100.227602/FIGURES/4/MEDIUM

Leontsev, S. O., & Eitel, R. E. (2010). Progress in engineering high strain lead-free piezoelectric ceramics.,*11*(4), 13. https://doi.org/10.1088/1468-6996/11/4/044302

Li, X., Terabe, K., Hatano, H., Zeng, H., & Kitamura, K. (2006). Domain patterning thin crystalline ferroelectric film with focused ion beam for nonlinear photonic integrated circuits. *Journal of Applied Physics*, *100*(10). https://doi.org/10.1063/1.2374935

Liou, S. H., Huang, S., Klimek, E., Kirby, R. D., & Yao, Y. D. (1999). Enhancement of coercivity in nanometer-size CoPt crystallites. *Journal of Applied Physics*, *85*(8), 4334. https://doi.org/10.1063/1.370359

Lopatin, S., Lopatina, I., & Lisnevskaya, I. (2011). Magnetoelectric PZT/ferrite composite material. *Http://Dx.Doi.Org/10.1080/00150199408245091*, *162*(1), 63–68. https://doi.org/10.1080/00150199408245091

Lubk, A., Gemming, S., & Spaldin, N. A. (2009). First-principles study of ferroelectric domain walls in multiferroic bismuth ferrite. *Physical Review B - Condensed Matter and Materials Physics*, *80*(10), 104110. https://doi.org/10.1103/PHYSREVB.80.104110/FIGURES/11/MEDIUM

Magnetic Nanoparticles - Google Books. (n.d.). Retrieved May 20, 2022

Moreau, J. M., Michel, C., Gerson, R., & James, W. J. (1971). Ferroelectric BiFeO3 X-ray and neutron diffraction study. *Journal of Physics and Chemistry of Solids*, *32*(6), 1315–1320. https://doi.org/10.1016/S0022-3697(71)80189-0

Nan, C. W. (1994). Magnetoelectric effect in composites of piezoelectric and piezomagnetic phases. *Physical Review B*, *50*(9), 6082. https://doi.org/10.1103/PhysRevB.50.6082

Nan, C. W., Bichurin, M. I., Dong, S., Viehland, D., & Srinivasan, G. (2008). Multiferroic magnetoelectric composites: Historical perspective, status, and future directions. *Journal of Applied Physics*, *103*(3). https://doi.org/10.1063/1.2836410

Nan, C. W., Li, M., & Huang, J. H. (2001). Calculations of giant magnetoelectric effects in ferroic composites of rare-earth–iron alloys and ferroelectric polymers. *Physical Review B*, *63*(14), 144415. https://doi. org/10.1103/ PhysRevB.63.144415

Nayek, C., Sahoo, K. K., & Murugavel, P. (2013). Magnetoelectric effect in La0.7Sr0.3MnO3–BaTiO3 core–shell nanocomposite. *Materials Research Bulletin*, *48*(3), 1308–1311. https://doi.org/10.1016/J. MATERRESBULL. 2012.12.043

Néel, L. (1949). Les propriétés magnétiques du sesquioxyde de Fer rhomboédrique. *Comptes Rendus Hebdomadaires Des Seances De L Academie Des Sciences*, *228*(1), 64–66. https://hal.archives-ouvertes.fr/hal-02878470

Nie, J., Xu, G., Yang, Y., & Cheng, C. (2009). Strong magnetoelectric coupling in CoFe2O4–BaTiO3 composites prepared by molten-salt synthesis method. *Materials Chemistry and Physics*, *115*(1), 400–403. https://doi.org/10.1016/J. MATCHEMPHYS.2008.12.011

Patankar, K. K., Dombale, P. D., Mathe, V. L., Patil, S. A., & Patil, R. N. (2001). AC conductivity and magnetoelectric effect in MnFe1.8Cr0.2O4-BaTiO3 composites. *Materials Science and Engineering B: Solid-State Materials for Advanced Technology*, *87*(1), 53–58. https://doi.org/10.1016/S0921-5107(01)00695-X

Patankar, K. K., Joshi, S. S., & Chougule, B. K. (2005). Dielectric behaviour in magnetoelectric composites. *Physics Letters A*, *346*(5–6), 337–341. https://doi.org/10.1016/J.PHYSLETA.2005.06.099

Patankar, K. K., Mathe, V. L., Patil, R. N., & Chougule, B. K. (2006). Structural analysis, magnetic properties and magnetoelectric effect in piezomagnetic–piezoelectric composites. *Materials Chemistry and Physics*, *96*(2–3), 197–200. https://doi.org/10.1016/J.MATCHEMPHYS.2005.07.009

Patil, D., Kim, J. H., Chai, Y. S., Nam, J. H., Cho, J. H., Kim, B. I., & Kim, K. H. (2011). Large longitudinal magnetoelectric coupling in NiFe2O 4-BaTiO3 laminates. *Applied Physics Express*, *4*(7), 23–25. https://doi.org/ 10.1143/ APEX.4.073001

Patil, D. R., & Chougule, B. K. (2009). Effect of resistivity on magnetoelectric effect in (x)NiFe2O4–(1−x)Ba0.9Sr0.1TiO3 ME composites. *Journal of Alloys and Compounds*, *1–2*(470), 531–535. https://doi.org/10. 1016/ J.JALLCOM. 2008.03.006

Paufler, P. (1986). J. F. Nye. Physical Properties of Crystals. Clarendon Press — Oxford. First published in paperback with corrections and new material 1985. XVII + 329 p. £ 15.00. ISBN 0-19-851165-5. *Crystal Research and Technology*, *21*(12), 1508–1508. https://doi.org/10.1002/CRAT.2170211204

Physics of dielectric materials: Tareev, Boris MikhaiÌ†lovich: Amazon.com: Books. (n.d.). Retrieved March 28, 2022, from https://www.amazon.com/ Physics-dielectric-materials-MikhaiÌ†lovich-Tareev/dp/B0007AOBIA

Physics of Dielectric Materials - B. Tareev - Google Books. (n.d.). Retrieved April 2, 2022, from https://books.google.co. in/books/ about/ Physics_ of_ Dielectric_Materials.

Priya, S., Islam, R., Dong, S., & Viehland, D. (2007). Recent advancements in magnetoelectric particulate and laminate composites. *Journal of Electroceramics*, *19*(1), 147–164. https://doi.org/10.1007/S10832-007-9042-5

Punia, P., Bharti, M. K., Chalia, S., Dhar, R., Ravelo, B., Thakur, P., & Thakur, A. (2021). Recent advances in synthesis, characterization, and applications of nanoparticles for contaminated water treatment- A review. *Ceramics International*, *47*(2), 1526–1550. https://doi.org/10.1016/ J.CERAMINT. 2020.09.050

Rahaman, M. D., Saha, S. K., Ahmed, T. N., Saha, D. K., & Hossain, A. K. M. A. (2014). Magnetoelectric effect of (1−x) Ba0.5Sr0.5Zr0.5Ti0.5O3+(x) Ni0.12Mg0.18Cu0.2Zn0.5Fe2O4 composites. *Journal of Magnetism and Magnetic Materials*, *371*, 112–120. https://doi.org/10.1016/ J.JMMM. 2014.07.025

Rani, J., Yadav, K. L., & Prakash, S. (2014). Dielectric and magnetic properties of xCoFe2O4–(1 − x)[0.5Ba(Zr0.2Ti0.8)O3–0.5(Ba0.7Ca0.3)TiO3] composites. *Materials Research Bulletin*, *60*, 367–375. https://doi.org/ 10. 1016/ J.MATERRESBULL.2014.09.013

Rosenberg, H. M. (Harold M. (1992). *The solid state : an introduction to the physics of solids for students of physics, materials science, and engineering*. 315.

Roy, S., & Majumder, S. B. (2012). Recent advances in multiferroic thin films and composites. *Journal of Alloys and Compounds*, *538*, 153–159. https://doi.org/10.1016/J.JALLCOM.2012.05.125

Ryu, J., Priya, S., Vázquez Carazo, A., Uchino, K., & Kim, H. E. (2001). Effect of the Magnetostrictive Layer on Magnetoelectric Properties in Lead Zirconate Titanate/Terfenol-D Laminate Composites. *Journal of the American Ceramic Society*, *84*(12), 2905–2908. https://doi.org/10.1111/J.1151-2916. 2001. TB01113.X

Schmid, H. (2011). Multi-ferroic magnetoelectrics. *Http://Dx.Doi.Org/ 10.1080/ 00150199408245120*, *162*(1), 317–338. https://doi.org/10. 1080/ 001501 99408245120

Scott, J. F. (2007). Multiferroic memories. *Nature Materials 2007 6:4*, *6*(4), 256–257. https://doi.org/10.1038/nmat1868

Shannon, R. D., & IUCr. (1976). Revised effective ionic radii and systematic studies of interatomic distances in halides and chalcogenides. *Urn:Issn:0567-7394*, *32*(5), 751–767. https://doi.org/10.1107/S0567739476001551

Sosnowska, I., Neumaier, T. P., & Steichele, E. (1982). Spiral magnetic ordering in bismuth ferrite. *Journal of Physics C: Solid State Physics*, *15*(23), 4835. https://doi.org/10.1088/0022-3719/15/23/020

Spaldin, N. A., & Fiebig, M. (2005). The renaissance of magnetoelectric multiferroics. In *Science* (Vol. 309, Issue 5733, pp. 391–392). https://doi.org/10.1126/science.1113357

Srinivas, A., Raja, M., Sivaprahasam, D., & Saravanan, P. (2013). Enhanced ferroelectricity and magnetoelectricity in 0.75BaTiO3-0.25BaFe12O19 by spark plasma sintering. *Processing and Application of Ceramics*, *7*(1), 29–35. https://doi.org/10.2298/PAC1301029S

Srinivas, S., Li, J. Y., Zhou, Y. C., & Soh, A. K. (2006). The effective magnetoelectroelastic moduli of matrix-based multiferroic composites. *Journal of Applied Physics*, *99*(4), 043905. https://doi.org/10.1063/1.2173035

Srinivas, S., & Yu Li, J. (2005). *The effective magnetoelectric coefficients of polycrystalline multiferroic composites*. https://doi.org/ 10.1016/j. actamat. 2005.05.014

Srinivasan, G., Devreugd, C. P., Flattery, C. S., Laletsin, V. M., & Paddubnaya, N. (2004). Magnetoelectric interactions in hot-pressed nickel zinc ferrite and lead zirconante titanate composites. *Applied Physics Letters*, *85*(13), 2550. https://doi.org/10.1063/1.1795365

Su, L. na, Liu, P., He, Y., Zhou, J. ping, Cao, L., Liu, C., & Zhang, H. wu. (2010). Electrical and magnetic properties of low-temperature sintered xBa0.6Sr0.4TiO3 + (1 − x)Ni0.2Cu0.2Zn0.62O(Fe2O3)0.98 composite ceramics. *Journal of Alloys and Compounds*, *494*(1–2), 330–335. https://doi.org/10.1016/J.JALLCOM.2010.01.029

Sutar, M. M., Jigajeni, S. R., Tarale, A. N., Kulkarni, S. B., & Joshi, P. B. (2014). Magnetoelectric and magnetodielectric effect in BST–LSMO ferromagnetic/ferroelectric composites. *Journal of Materials Science: Materials in Electronics 2014 25:9*, *25*(9), 3771–3778. https://doi.org/10.1007/S10854-014-2088-7

Sutar, M. M., Tarale, A. N., Jigajeni, S. R., Kulkarni, S. B., Reddy, V. R., & Joshi, P. B. (2012). Magnetoelectric and magnetodielectric effect in Ba1−xSrxTiO3 and Co0.9Ni0.1Fe2−xMnxO4 composites. *Solid State Sciences*, *14*(8), 1064–1070. https://doi.org/10.1016/J.SOLIDSTATESCIENCES.2012.05.016

Valasek, J. (1921). Piezo-Electric and Allied Phenomena in Rochelle Salt. *Physical Review*, *17*(4), 475. https://doi.org/10.1103/PhysRev.17.475

van den Boomgaard, J., & Born, R. A. J. (1978). A sintered magnetoelectric composite material BaTiO3-Ni(Co, Mn) Fe2O4. *Journal of Materials Science*, *13*(7), 1538–1548. https://doi.org/10.1007/BF00553210

Van Den Boomgaard, J., Terrell, D. R., Born, R. A. J., & Giller, H. F. J. I. (1974). An in situ grown eutectic magnetoelectric composite material. *Journal of Materials Science 1974 9:10*, *9*(10), 1705–1709. https://doi.org/10.1007/BF00540770

Van Den Boomgaard, J., Van Run, A. M. J. G., & Van Suchtelen, J. (1976). Magnetoelectricity in Piezoelectric—Magnetostrictive Composites. *Ferroelectrics*, *10*(1), 295–298. https://doi.org/10.1080/00150197608241997

Van Run, A. M. J. G., Terrell, D. R., & Scholing, J. H. (1974). An in situ grown eutectic magnetoelectric composite material. *Journal of Materials Science 1974 9:10*, *9*(10), 1710–1714. https://doi.org/10.1007/BF00540771

Vázquez, M., & Hernando, A. (1996). A soft magnetic wire for sensor applications. *Journal of Physics D: Applied Physics*, *29*(4), 939. https://doi.org/10.1088/0022-3727/29/4/001

Wang, J. (2017). *Multiferroic materials : properties, techniques, and applications*.

Y. Xu. (1991). Ferroelectric Materials and Their Applications - 1st Edition. *North Holland*. https:// www. elsevier. com/ books/ ferroelectric-materials-and-their-applications/xu/978-0-444-88354-4

Yang, H., Zhang, G., & Han, N. (2015). Enhanced ferroelectric and magnetoelectric properties of the laminated 0.65BiFeO3-0. 35BaTiO3/ BiY2Fe5O12 composite. *Materials Letters*, *145*, 91–94. https://doi.org/10.1016/j. matlet. 2015.01.077

Yi, L., Buttner, G., Usadel, K. D., & Yao, K. L. (1993). Quantum Heisenberg spin glass with Dzyaloshinskii-Moriya interactions. *Physical Review B*, *47*(1), 254. https://doi.org/10.1103/PhysRevB.47.254

Yu, Z., & Ang, C. (2002). Electrical and magnetic properties of BaTiO3−(Ni0.3Zn0.7)Fe2.1O4 composites. *Journal of Materials Science: Materials in Electronics 2002 13:4*, *13*(4), 193–196. https://doi.org/10. 1023/A:1014819731557

Chapter 2

EXPERIMENTAL TECHNIQUES AND MATERIALS

Experimental Techniques and Materials

This chapter provide a comprehensive overview of the experimental methods employed to synthesize, characterize and manipulate multiferroic composites. Multiferroicity is a complex and intriguing phenomenon that emerges from the intricate interplay of various structural, magnetic, and electronic factors. Therefore, the experimental exploration of multiferroic materials necessitates a diverse set of techniques and methodologies to unveil their underlying properties and the mechanisms governing their behavior. This chapter discusses the tools and theories used for evaluating the structural, electrical, magnetic and multiferroic properties of various materials as well as their synthesis procedures.

2.1 Introduction

Several experimental approaches and procedures have been employed in this work to synthesize and characterize the samples. Numerous characteristics of nanomaterials have been thoroughly researched, including their structural/microstructural, dielectric, electrical, magnetic, magneto-electric and optical characteristics. Diffraction analysis has been used to determine the spatial configurations of atoms in various materials. The primary purpose of the non-destructive scanning electron microscope (SEM) is to study the surface morphology of materials. The materials' shape, chemical composition, grain distribution, and grain boundary are all revealed by the interaction of high-energy electron beams with the materials. One of the most effective methods available for providing the elemental analysis of the materials is energy dispersive analysis of X-rays, or EDAX. Using the LCR meter (HP 4285A), the dielectric characteristics have been investigated as a function of frequency. The key properties of dielectric materials that affect their applicability for different applications are their dielectric constant, and ac conductivity. In the current work, a vibrating sample magnetometer was used to evaluate the magnetic properties of prepared materials. Using a (M-H) hysteresis loop, the produced materials' magnetic characteristics were examined. Using UV-VIS-NIR spectroscopy, one of the most potent non-destructive and sensitive method for characterizing the materials' optical characteristics. This chapter also depicts the materials and methods used for ferroelectric properties.

2.2 Preparation of nanoparticles

Synthesis methods of materials play a vital role in their physical behaviour and hence appropriate methods is to be opted for specific applications. There are two categories for the different methods utilised in the synthesis of nanoparticles: top-down and bottom-up. Using cutting, etching, and breaking, bulk material is broken down into nanosized particles using the top-down technique. Examples of Top-down methods are laser ablation, high-energy ball milling, sputtering, etc. The Bottom-up approach involves synthesising nanoparticles from the bottom up, atom by atom, molecule by

molecule, and cluster by cluster. Examples of bottom-up methods are a sol-gel method, chemical co-precipitation, etc. Various chemical and physical methods such as plasma deposition, chemical vapor deposition, microwave irradiation, pulsed laser method, hydrothermal reaction, sol-gel technique, coprecipitation, etc are used for the synthesis of nanoparticles[1]. Out of these synthesis techniques, the sol-gel method is a very easy and cost-effective technique at low temperatures[2].

2.2.1 Modified sol-gel method

Citric acid is the primary ingredient of the Sol-gel method, a wet chemical process used to prepare ferrites. To obtain the appropriate solution, the stoichiometric amount of metal nitrates is weighed and dissolved separately in deionized water. The metal nitrate solution is mixed with citric acid in a 1:1 molar ratio. After that, solutions are combined and heated to 80^0 C for 30 minutes while being continuously stirred. After that, it is moved to a hot plate and heated to a high temperature where it evaporates to create a dark, viscous resin. Resin undergoes auto-combustion when heated continuously, producing brown colour samples as a result.

During the course of this study, $Ni_{1-x}Zn_xFe_2O_4$ (x=0.0,0.3,0.5,0.7,1), $Co_{1-x}Zn_xFe_2O_4$ (x=0.0,0.3,0.5,0.7,1) and $Bi_{1-x}Sr_xFeO_3$ (x=0.0,0.3,0.5,0.7), nanoparticles are prepared by modified Sol-gel method. Precursors used for the synthesis of $Ni_{1-x}Zn_xFe_2O_4$ nanoparticles are analytic grade $Ni(NO_3)_2.6H_2O$ (Nickel nitrate), $Zn(NO_3)_2.6H_2O$ (Zinc nitrate), $Fe(NO_3)_3.9H_2O$ (Iron nitrate), and $C_6H_8O_7$ (Citric acid). For the synthesis of $Co_{1-x}Zn_xFe_2O_4$ nanoparticles analytic grade $Co(NO_3)_2.6H_2O$ (Cobalt nitrate), $Zn(NO_3)_2.6H_2O$ (Zinc nitrate), $Fe(NO_3)_3.9H_2O$ (Iron nitrate), and $C_6H_8O_7$ (Citric acid) are used. $Bi_{1-x}Sr_xFeO_3$ nanoparticles were prepared from analytic grade Bismuth nitrate ($Bi(NO_3)_3.5H_2O$), Strontium nitrate ($Sr(NO_3)_2.6H_2O$), Iron nitrate ($Fe(NO_3)_3.9H_2O$), and Citric acid ($C_6H_8O_7$) were used. All the chemicals were of purity >98% and were purchased from Merck.

[1] Liu & Fu 2007; Mishra et al. 2006
[2] Jacob et al. 2012

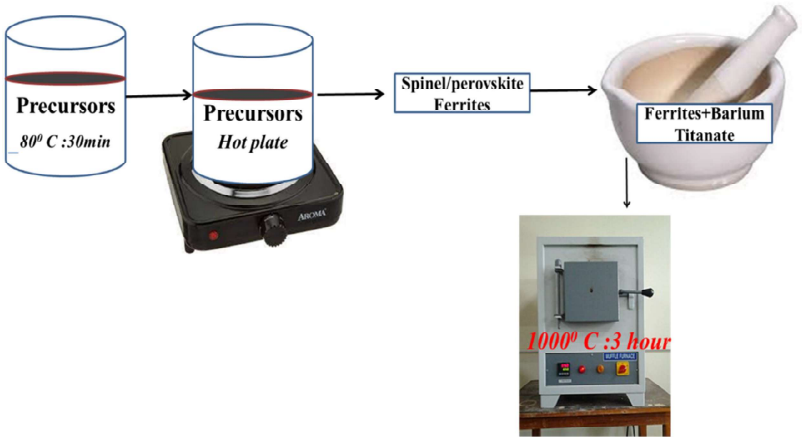

Fig 2.1: Schematic representation of modified sol-gel method

The ferroelectric phase $BaTiO_3$ with a tetragonal structure was directly purchased from Nano Research Elements. Composite samples are prepared via solid-state reaction approach. Various samples prepared include composites of nickel ferrite with barium titanate with various weight propositions namely (NFO: BTO and $Ni_{1-x}Zn_xFe_2O_4$- $BaTiO_3$ (x=0.3, 0.5, 0.7, 1). Using the same solid state reaction method cobalt ferrite and barium titanate ($Co_{1-x}Zn_xFe_2O_4$- $BaTiO_3$ (x=0, 0.3, 0.5, 0.7, 1)) composites as well as $BiFeO_3$-$BaTiO_3$ (BF: BTO) and $Bi_{1-x}Sr_xFeO_3$ - $BaTiO_3$ (x=0.3, 0.5, 0.7) composites are also prepared.

The required amounts of the components of magnetic phase and barium titanate were taken in various weight ratios. Next, these were thoroughly combined with acetone serving as a medium, using a mortar and pestle. After three hours of annealing at 1000°C, the samples were gradually cooled to room temperature.

2.3 Structural characterization

Structural characterization is used to find the size, shape, surface morphology, etc. X-ray Diffraction (XRD), Scanning Electron Microscope (SEM), Energy-dispersive X-ray spectroscopy (EDAX), and X-ray photoelectron spectroscopy (XPS) are among the techniques used for structural characterization.

2.3.1 X-ray Diffractometer (XRD)

An efficient non-destructive method for determining the phase and crystal structure of materials with crystallite sizes larger than 5 nm is powder X-ray diffraction (PXRD)[3]. A regular and periodic arrangement of atoms or molecules, or a combination of atoms and molecules, makes up crystalline materials. One type of electromagnetic wave that has a wavelength of around 1Å and a size comparable to interplanar spacing is X-rays. In the X-ray diffraction technique, X-ray e.g. CuKα radiations (λ = 1.5418 Å) are elastically dispersed from the atom through the electron. In a polycrystalline or powder substance, the crystals are arranged randomly. As soon as an X-ray beam strikes the materials, a variety of plane orientations are orientated to satisfy Bragg's diffraction requirements and produce a crisp diffraction pattern[4].

X-ray diffractometer works on the principle of Bragg's law

$$n\lambda = 2d \sin\theta \tag{2.1}$$

In this case, d indicates the distance between the diffraction planes, θ the angle of the incident X-rays, and n the order of diffraction. λ stands for the wavelength of the incident beam.

[3] *Amazon.in* n.d.; *Solid State Chemistry and its Applications - Anthony R. West - Google Books* n.d.
[4] Tanner et al. 2001

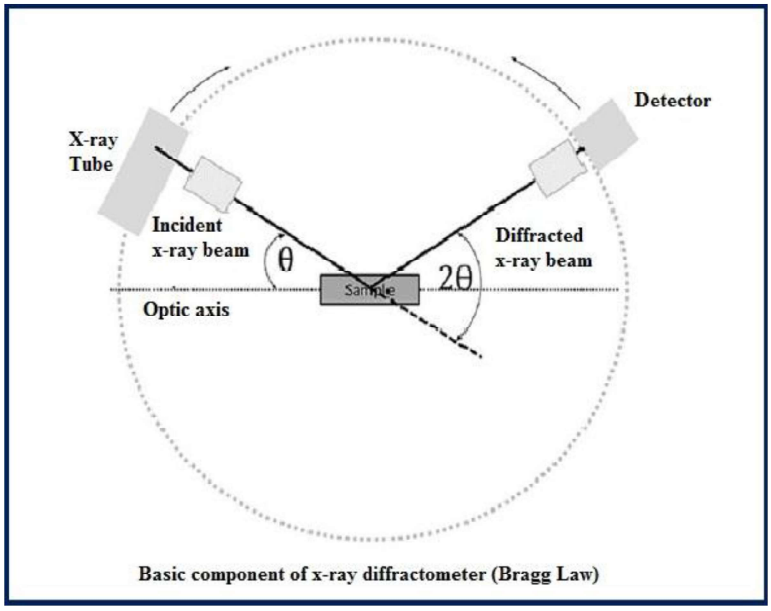

Fig 2.2 Schematic diagram of the diffractometer [5]

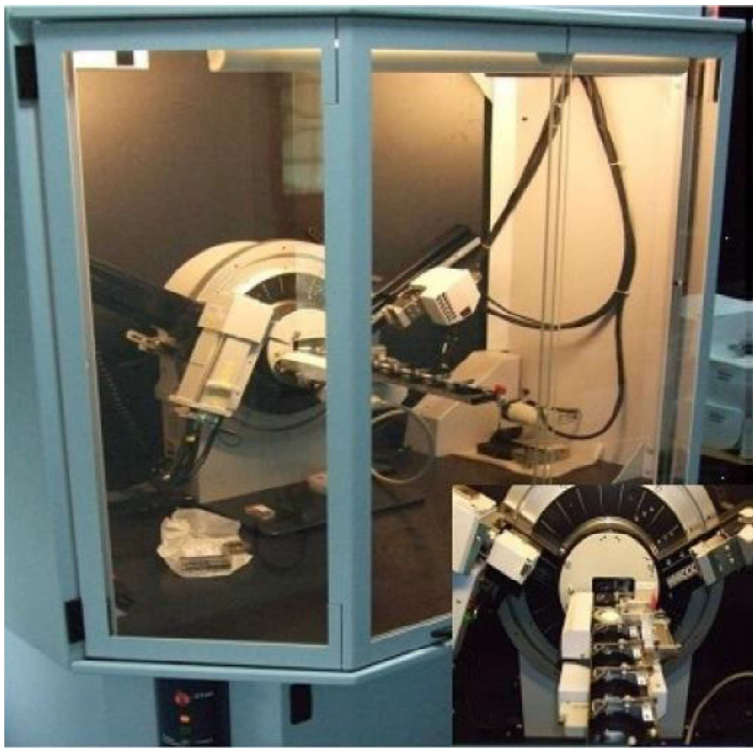

Fig 2.3 Powder X-ray diffractometer [6]

[5] *Elements of X-Ray Diffraction Book Online at Low Prices in India | Elements of X-Ray Diffraction Reviews & Ratings - Amazon* n.d.

A beam of monochromatic X-ray is admitted to hitting on the sample and it will be scattered in different directions by different planes of the crystal. The differential beams from different planes are recorded by the recorder and the plot of $\frac{I}{I_0}$ versus 2θ is obtained.

2.3.1.1 Line Broadening in XRD

The width of the diffraction peak increases when the crystallite size reduces to below a certain limit (<100nm). The line broadening of the peaks is used for the calculation of grain size. The instrumental effect, crystallite size, and microstrain are the three factors that influence the diffraction line broadening. The total full width at half maximum (FWHM) can be defined as,

$$\beta_{exp}=\beta_{inst}+\beta_{size}+\beta_{strain} \quad (2.2)$$

β_{exp} is defined as the experimentally measured FWHM, β_{inst} is defined as the FWHM due to instrument. β_{size} is defined as the FWHM due to crystallite size and β_{strain} is defined as the FWHM induced by the strain.

The instrumental Broadening occurs due to the slit width imperfections in the focusing X-ray beam and the undetermined Kα1 and Kα2 peaks[7]. The consequence of the instrumental broadening can be removed by running a standard stress-free sample under the same circumstances and subtracting the effect of broadening from the line broadening obtained for the test sample.

Suppose that the sample is strain-free and there is no effect of the instrumental broadening then the size generated broadening can be defined as,

$$\beta(2\theta) = \frac{0.9\lambda}{D\cos\theta} \quad (2.3)$$

where θ is the diffraction angle, D is the average crystallite size, and λ is the X-ray wavelength. We can use the Debye-Scherrer equation to calculate the crystallite size if we remove the broadening effects because of the strain and instrumental parameters.

[6] *Elements of X-Ray Diffraction Book Online at Low Prices in India | Elements of X-Ray Diffraction Reviews & Ratings - Amazon* n.d.
[7] Warren 1969

2.3.1.2 Structural phase identification

The materials are mainly composed of either single or multi-phases. The uniqueness of the diffraction patterns of each phase may be used for the identification of the phase. The materials possess the same chemical composition but they can have different structural phases, and hence can have different diffraction patterns. The observed experimental diffraction pattern is analyzed with the JCPDS [Joint Committee on Powder Diffraction Standards] files. The crystalline materials that possess the same chemical formula with various crystal structures can be evaluated by the 2θ versus intensity (I) plot which is acquired from the diffractometer. The quantity present in the compounds has the responsibility for the intensity of the peaks. The integral intensity of diffraction peak (hkl) from a phase (α) is calculated from the equation (2.4)

$$I_\alpha(hkl) = \frac{k_\alpha(hkl) * X_\alpha}{\rho_\alpha * (\frac{\mu}{\rho})_m} \quad (2.4)$$

where X_α and ρ_α represents the weight and mass fraction of phase α, $K_{\alpha(hkl)}$ is a constant for a given phase α and $(\frac{\mu}{\rho})_m$ gives mass absorption coefficient of compound.

2.3.1.3 Determination of lattice parameter

Crystals possess a large number of parallel planes of equal distance of 'd' apart. For the cubic structure lattice constant a given by

$$a = d(h^2+k^2+l^2)^{1/2} \quad (2.5)$$

where a=lattice constant, d=inter planar distance and (h,k,l) are the miller indices

The lattice parameters of the rhombohedral perovskite structure samples can be calculated using the formula,

$$d = \frac{a}{\sqrt{\frac{4(h^2+k^2+hk)}{3} + \frac{a^2l^2}{c^2}}} \quad (2.6)$$

$$d = \frac{1}{\sqrt{\frac{h^2}{a^2} + \frac{k^2}{b^2} + \frac{l^2}{c^2}}} \quad (2.7)$$

The lattice parameters of the tetragonal samples can be calculated using the formula,

$$\frac{1}{d^2} = \frac{(h^2+k^2)}{a^2}+\frac{l^2}{c^2} \quad (2.8)$$

where a=lattice constant, d=inter planar distance and (h,k,l) are the miller indices

2.3.1.4 X-ray density

X-ray density is calculated using the formula

$$\rho_x=\frac{8M}{Na^3} \quad (2.9)$$

where a denotes the lattice constant, M is the sample's molecular mass, and N is the Avogadro's number.

2.3.1.5 Rietveld refinement method

The Rietveld refinement method, which is used to characterise crystalline materials, was created by Hugo M. Rietveld[8]. We used the theoretical line profile to be refined to utilize the least square approach till up to it matches the measured profile. The Rietveld refinement is used for the refinement of their parameters mainly peak shape function, profile parameters, and structural parameters. The sample (defects, domain size, stress/strain) and the instrument (radiation source, slit size), both dependent on 2θ, are contained in the peak shape function. Refinement parameters contain unit cell parameters, peak symmetry of the Bragg's peak, and FWHM. Structural parameters include the type, position, and occupancy of atoms in a crystal. The Rietveld refining method is initiated using XRD and the structure knowledge. At least one hundred cycles are needed to fit a structure with a moderate level of complexity. The final profile and the R (Reliability) numbers can be used to evaluate the refinement's quality[9].

The R factors are defined as,

R pattern $$R_p=\frac{\sum|y_i(obs)-y_i(calc)|}{\sum y_i(obs)} \quad (2.10)$$

R weighted pattern as,

[8] Rietveld & IUCr 1969
[9] Toby 2006

$$R_{wp}=\left\{\frac{\sum w_i[y_i(obs)-y_i(calc)]^2}{\sum w_i\ (y_i(obs))^2}\right\}^{1/2} \quad (2.11)$$

Statistically expected R of value R_{exp} as,

$$R_{wp}=\left\{\frac{N-P+C}{\sum w_i\ (y_i(obs))^2}\right\}^{1/2} \quad (2.12)$$

where N denotes the number of observations, P denotes the number of parameters, and C denotes the number of refinement constraints.

The goodness of fit is given by

$$Reduced\ \chi^2=\left(\frac{R_{wp}}{R_{exp}}\right)^2 \quad (2.13)$$

The quality of fit is judged from the goodness of fit (χ^2) and R values namely R_P and R_{WP}. The value of χ^2 must be close to one and the values of R_P and R_{WP} must be close to 10% for a good fit[10]. Full-proof software were used for the Rietveld refinment . The Pseudo void, a blend of Cauchyian and Gaussian functions, is the most realistic peak shape function utilized in the Rietveld structure refinement software.

2.3.2 X-ray photoelectron spectroscopy (XPS)

The most popular technique for a material's surface chemistry that includes the determination of the elemental composition, chemical state, electronic configuration of a material's constituent elements, and empirical formula is called X-ray photoelectron spectroscopy (XPS). Generally speaking, X-rays from electron emission guns are used to irradiate solid surfaces in order to produce an X-ray beam, which is then followed by a monochromator producing an X-ray photon. When an X-ray photon is absorbed by the sample, a photoelectron will be released from its surface. The photon energy that is emitted onto the surface of the sample determines the electron's kinetic and binding energies. Counting the ejected electrons across a range of electron kinetic energy yields a photoelectron spectrum. The elemental identity, chemical state, and quantity of a detected element can be determined and measured using the binding energy and

[10] Gomes et al. 2005

intensity of a photoelectron peak in an XPS spectrum. There is no need for time-consuming sample preparation because XPS analysis employs the synthesized sample directly for analysis.

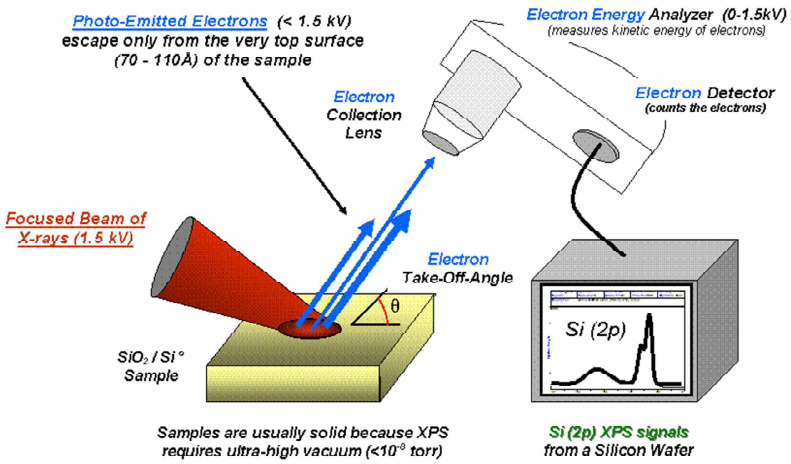

Fig 2.4 Basic components of a monochromatic XPS system

Typically, specialised software like CASAXPS, Igor Pro, Unifit software, XPSPEAK41, etc. is used to do the data analysis. It is useful to obtain the fitted high-resolution XPS spectra because many researchers have used Origin software to fit their XPS spectra. In addition, the XPS technique can be used to analyse the metal oxide lattice structure's contaminants. Here, we analysed the data using the XPSPEAK41 programme.

2.3.3 Scanning Electron Microscope (SEM)

For the last few years, electron microscopy has gained much importance in imaging. The microscope's resolving power is limited by the lens's numerical aperture and the electrons' wavelength. However, a high-energy focused electron beam is employed in scanning electron microscopes to produce images with a high magnification of up to 10,000x. SEM data provides information about surface morphology. SEM contains an electron gun at the top of a microscope. The electrons produced by this electron gun move through a vacuum and are then concentrated by the electromagnetic fields and lenses to fall on the sample. The sample surface is scanned

by the electrons in a raster manner[11]. When an electron beam falls on our sample some of them are scattered and some out of them pass through the sample. The secondary electrons, Auger electrons, and X-rays are produced by the elastic scattering. The back scattered electrons and the secondary electrons are used for the imaging in SEM. The image is shown in Figure 2.5.

Fig 2.5 SEM machine used for the measurement(Jeol 6390LA/ OXFORD XMX N)

The secondary electrons which depend on surface topography and give topographic images with higher depth of field and great magnification. The amount of elements in the sample determines the intensity of backscattered electrons, which provides information on the elemental composition[12]. In this work, the morphology of the prepared samples was studied using Jeol 6390LA/ OXFORD XMX N.

[11] *Magnetic Nanomaterials - Google Books* n.d.
[12] "Handb. Microsc. Nanotechnol." 2005; *Scanning Electron Microscopy and X-Ray Microanalysis: Third Edition eBook : Goldstein, Joseph, Newbury, Dale E., Joy, David C., Lyman, Charles E., Echlin, Patrick, Lifshin, Eric, Sawyer, Linda, Michael, J.R.: Amazon.in: Kindle Store* n.d.

2.3.4 Energy Dispersive Analysis (EDAX)

To analyze the composition, the X-ray energy dispersive analysis (EDAX) method has been carried out using Jeol 6390LA/ OXFORD XMX N. It is a flexible method available for the analysis and examination of the microstructural features of the surface of materials. The EDAX method is employed to investigate the chemical composition of microstructural characteristics through both qualitative and quantitative assessment. X-ray energy dispersive analysis (EDAX) spectrometer is used to study the composition working based on Mosley law. Theorem states that when the emitter's atomic number increases, the wavelength of any given line decreases. An element's concentration in our sample can be determined by focusing on the energy or frequency of a specific X-ray, which determines the material's properties.

2.4 Dielectric measurements

2.4.1 Dielectric parameters

The dielectric permittivity or dielectric constant (ε' or ε_r) is the ratio of the field's strength in a vacuum to its strength in a medium with an identical charge distribution. The dielectric constant of material shows the ability to store electrical energy. It depends upon various factors like orientation, frequency of the applied field, grain size, temperature, and molecular structure of the material[13]. Here, the HP 4285A LCR metre is used to analyse the dielectric readings of the sample pellets in the 100kHz–5MHz frequency range at room temperature. The picture of HP 4285A LCR meter is shown in Figure 2.6.

[13] BROCKMAN & WHITE 1971

Fig 2.6 HP 4285A LCR meter

The dielectric constant of nanoparticles are calculated using the formula

$$\varepsilon = \frac{Cd}{\varepsilon_0 A} \tag{2.14}$$

where A is the cross-sectional area of the samples in metres, ε_0 is the permittivity of the open space, C is the capacitance, and d is the thickness of the pellets.

For an alternating electric field, the dielectric constant is given by (2.15)

$$\varepsilon^* = \varepsilon' - \varepsilon'' \tag{2.15}$$

where ε' is defined as the real part of dielectric constant and in phase with applied field and ε'' is defined as the imaginary part of dielectric constant, which is 90^0 out of phase with applied field and is create by either resistive leakage or dielectric absorption

2.4.2 AC Conductivity

For a parallel plate capacitor AC Conductivity,

$$\sigma_{ac} = \frac{J}{E} \tag{2.16}$$

where J is defined as the current density and E is the field density, E can be defined as

$$E = \frac{D}{\varepsilon} = \frac{V}{d} \tag{2.17}$$

where ε is the material's complex permittivity and D is the dipole charges' displacement vector. The thickness of the pellet is represented by d, and the potential difference between the two ends of the capacitor's pellet is described as V.

Current density $J = \frac{dq}{dt}$ (2.18)

By Maxwell's equation $q = \frac{Q}{A} = \frac{V\varepsilon}{d}$ (2.19)

where Q is defined as the charge in coulombs due to potential difference of V volts

$$J = \frac{dq}{dt} = \frac{d}{dt}\left(\frac{V\varepsilon}{d}\right) = \frac{\varepsilon}{d}\frac{dV}{dt} \tag{2.20}$$

$$J = \frac{\varepsilon}{d} V_0 j\omega \tag{2.21}$$

As V=$V_0 \exp(j\omega t)$

Substituting in equation (2.16), (2.17) and (2.21)

Now $\sigma_{ac} = \frac{J}{E}$

Hence $\sigma_{ac} = \varepsilon j\omega$ (2.22)

If ε' is a complex quantity, $\varepsilon = \varepsilon' - j\varepsilon''$

$\sigma_{ac} = (\varepsilon' - j\varepsilon'')\, j\omega$

$$\sigma_{ac} = \varepsilon'\, j\omega + \boldsymbol{\omega}\varepsilon'' \tag{2.23}$$

Consider σ_{ac} is a real quantity,

$$\sigma_{ac} = \boldsymbol{\omega}\varepsilon'' \tag{2.24}$$

where, ε''=$\varepsilon' tan\delta$

Hence σ_{ac}=2πf$\varepsilon' tan\delta$ (2.25)

Thus AC conductivity can be calculated from the dielectric constant and tanδ values for a particular frequency[14].

2.4.3 Cole-Cole plots

The Debye equation for dielectric dispersion is given by

$$\varepsilon^* - \varepsilon_\infty = \frac{(\varepsilon_s - \varepsilon_\infty)}{(1+j\omega\tau)} \quad (2.26)$$

The complex permittivity is represented by ε^*, the static and optical dielectric constants at limiting frequencies are represented by ε_s and ε_∞ respectively, ω=2πf$_{max}$ and the relaxation period is represented by τ. In this instance, the centre of the semicircular Cole-Cole plots is on the real axis. A deviation from perfect Debye behaviour is observed for the materials with dielectric dispersion, because various relaxation times may exist [15]. According to K.S. and R.H. Cole, permittivity in this situation complies with the empirical equation[16].

$$\varepsilon^* - \varepsilon_\alpha = \frac{(\varepsilon_s - \varepsilon_\alpha)}{1 + (j\omega\tau_0)^{1-\alpha}} \quad (2.27)$$

where α is the spreading factor of the actual relaxation time τ about its mean value τ_0, and τ_0 is the average relaxation time. The range of α is 0-1. A Cole-Cole plot illustrates the plot of ε″ at a given frequency against ε′ at the same frequency in the complex plane. The Cole-Cole plot for a dielectric with α=0 or single relaxation time is a semicircle; for α>0, the plot is a circular arc with its centre located below the real axis. The preceding equation reduces to Debye's equation for α = 0. The expression for the highest value of the imaginary component of permittivity can be used to calculate the spreading factor α[17].

$$\varepsilon''_{max} = \frac{(\varepsilon_s - \varepsilon_\infty)(tan[(1-\alpha)\pi/4}{2} \quad (2.28)$$

[14] *Physics of dielectric materials: Tareev, Boris Mikhaĭlovich: Amazon.com: Books* n.d.; Soohoo 1960
[15] *Dielectric relaxation [by] Vera V. Daniel. (Book, 1967) [WorldCat.org]* n.d.; Sagar et al. 2006
[16] S et al. 2022
[17] S et al. 2022

The equation can be utilised to get the mean value of τ_0

$$\frac{(\varepsilon_0-\varepsilon')^2+\varepsilon''^2}{(\varepsilon'-\varepsilon_\infty)^2+\varepsilon''^2} = (j\omega\tau_0)^{2(1-\alpha)} \quad (2.29)$$

The molecular relaxation time was computed by changing the value of τ_0 in the equation

$$\tau = [(2\varepsilon_s + \varepsilon_\infty)/3\varepsilon_s]\tau_0 \quad (2.30)^{18}.$$

2.5 Magnetic characterization technique

Vibrating Sample Magnetometer (VSM)

The samples' magnetic behaviour is examined using a vibrating sample magnetometer (VSM). The magnetic characteristics of the material at various temperatures and the variations in magnetic properties as a function of temperature with various applied fields are also investigated using a VSM. The operation of VSM is based on Faraday's law, which states that when there is a change in the flux associated with a coil, an electromagnetic field (emf) will be formed [19].

$$V = -N_0\left(\frac{d\Phi}{dt}\right) \quad (2.31)$$

Since B=Φ/A

$$V = -N_0 A\left(\frac{dB}{dt}\right) \quad (2.32)$$

where A is the cross sectional area, B is represent the magnetic flux density that is magnetic flux passes through the coil, N_0 is defined as the number of turns $\frac{d\Phi}{dt}$ is defined as the rate of flux change.

In the VSM instrument, the sample is put in the sample holder, which is placed between the pole pieces of an electromagnet. The sample holder is attached to a transducer. The transducer transfers sinusoidal AC signals into sinusoidal vertical vibrations and the sample goes for a sinusoidal motion in a uniform magnetic field. To

[18] Sagar et al. 2006
[19] Foner 1959

gather the signals created by the motion of the sample, the coil is stacked over the magnet's pole piece. The AC signal generated is proportional to the vibrational amplitude, frequency, and magnitude of the moment induced. The signal of a particular vibration frequency is a response to the oscillator where it is differentiated with the drive signal to continue a constant drive output. This signal is a phase regulator that radiates out as a reference signal after passing through a signal demodulator. The signal that comes from the pick-up coil is also amplified and buffered and given to the demodulator. The pick-up coil signal is simultaneously demodulated with respect to the reference signal by the demodulator, producing a DC analogue signal that is only dependent on the magnetic moment. The result gives the relation between magnetic moment (M) with the function of field (H). The low-temperature measurements were done with the cryogenic setup connected with the sample. The hysteresis loop is used to calculate the saturation magnetization (Ms), coercive field (H_C), remanence (M_r), and the squareness ratio (M_r/ M_S).

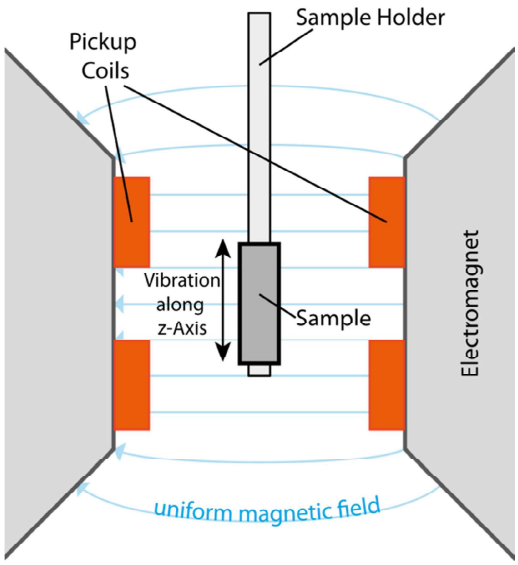

Fig 2.7. Illustration of Vibrating Sample Magnetometer and Quantum Design Physical Property Measurement System (PPMS)

2.6 Ferroelectric Measurements

The ferroelectric properties of the prepared samples are studied by polarization (P) vs Electric field (E) loop at room temperature. The ferroelectric hysteresis loop is measured using the modified Sawyer-Tower circuit[20]. The schematic diagram of ferroelectric measurements is shown in Figure 2.8. In the circuit C_x is represented as the ferroelectric sample to be measured, C_1 represents the standard capacitor of well-defined capacitance which is connected in series with C_x and C_x is independent of the applied voltage. U_{ac} is defined as the sinusoidal voltage applied to the measuring circuit.

[20] Sinha 1965

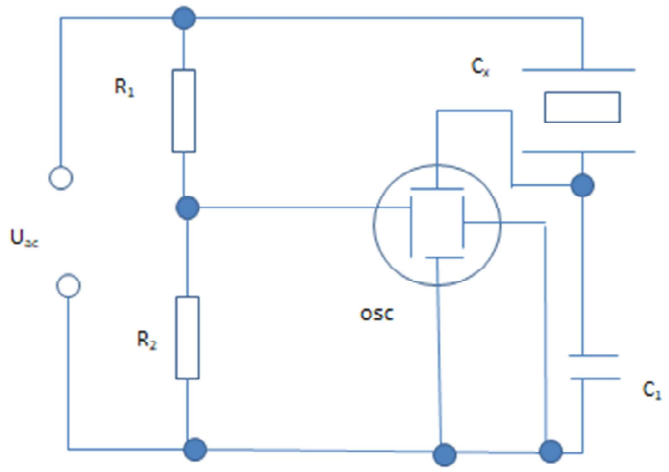

Fig 2.8. Schematic diagram of the modified Sawyer-Tower circuit[21]

For showing the hysteresis loop at the oscilloscope, the voltage at the y-channel must be proportional to the electric polarization of the sample, and the voltage at the x-channel is proportional to the electric field inside the sample. The input impedance is not taken into account because it is high enough as compared to all impedance and resistance of the circuit. The voltage between the voltage dividers R_1 and R_2at the oscilloscope's x-channel is proportional to the supply voltage U_0. When $C_1 >> C_x$, the voltage drop at C_1 is probably neglected. As a consequence of this, the voltage U_x at C_x is nearly equal to U_{ac}. Because of the link between voltage and electric field strength, the voltage at the x-channel most likely chooses the measurement for the electric field inside sample C_x.

The polarization of sample C_x is proportional to the voltage at the y-channel. This can be recognized by two capacitors connected in series that must be the same charge. In the circuit, C_x and C_1 are in series connections, so the same current will always flow through them. It is known that at any one time, C_1 and C_x both have the same charge. Given the proportionality between voltage and charge, the capacitor C_x's charge is measured by the voltage at C_1

[21] Sinha 1965

The produced samples' polarisation (P) vs. electric field (E) loops were monitored in the current study.

Fig 2.9. Photograph of P-E loop tracer

2.7 Magnetoelectric (ME) Measurements

2.7.1 ME Coefficient

The ME effect is the induction of either magnetization or electric polarization by the introduction of either a magnetic field or an electric field. The ME effect in multiferroic composites is based on the product property, produced by the coupling interaction between the constituent phases of the composites, specifically the ferroelectric and magnetic phases. The strength of the ME coupling is described by the electric field produced across the sample by the application of magnetic field i.e. ME coefficient (α_E) is defined by,

$$\alpha_E = \frac{dE}{dH} = \frac{dV}{dH \times t} \tag{2.33}$$

where V is the voltage created across the sample when a magnetic field is applied, and t is the sample's thickness. The sample is electrically poled using the dc poling equipment (Figure 2.10) prior to ME testing. The sample is heated above the Curie temperature (T_C) for electric poling, and then is allowed to cool to ambient temperature while being surrounded by an electric field. To make the sample

piezoelectrically active, the ferroelectric phase's domains must be aligned with one another via electric poling.

Fig 2.10. Photograph of the DC poling system

The dynamic technique is used to calculate the ME coupling in this study. This method involves superimposing an ac magnetic field on top of the dc magnetic field while measuring the ME voltage that is generated. The schematic diagram of the experimental setup used for the measurement of ME coefficient is explained in Figure 2.11. The electromagnets are used to produce the dc magnetic field by a dc power supply. Additionally, a dc magnetic field has an ac magnetic field superimposed on it. The Helmholtz coils use a function generator to create the ac magnetic field. Using a multimeter to measure the driving current, one may compute the amplitude of the applied ac magnetic field.

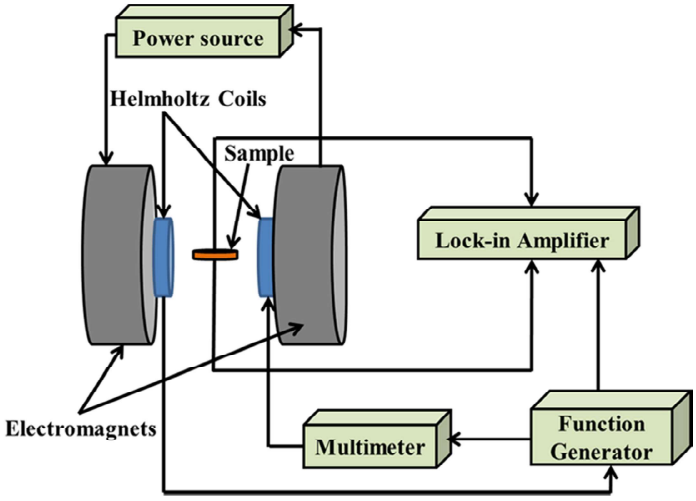

Fig 2.11 Schematic illustration of experimental setup for ME measurement

For ME calculation, the sample is placed between the electromagnets as shown in Figure 2.11. Magnetostriction causes a sample's magnetic phase to change when a magnetic field is applied. An induced voltage is created when the resultant strain is transmitted to the ferroelectric phase of the sample and results in stress. The lock-in amplifier measures the induced voltage. The ME coefficient can also be measured in both longitudinal and transverse directions. While in transverse mode, the direction of polarization is perpendicular to the magnetic field, it is parallel to the magnetic field in longitudinal mode[22].

2.8 UV-Vis Spectrophotometer

The absorption/reflectance spectroscopy in the UV-Vis range is called ultraviolet-visible spectroscopy. The UV-Vis spectrophotometer operates according to the following theory: it measures the light's intensity (I) after it passes through a sample and contrasts it with the light's intensity (I_0) prior to the material being incident. The transmittance value is I/ I_0 usually denoted as (%T).

[22] Wang et al. 2010

The absorbance A is given by the relation[23].

$$A = -\log(\%T) \tag{2.34}$$

According to the Beer-Lambert equation, ε or molar absorptivity constant is directly proportional to the concentration of the absorbing substance in the solution and route length.

$$A = \varepsilon cl \tag{2.35}$$

Two single-beam spectrophotometers and a double-beam spectrophotometer make up the UV spectrophotometer. Since all light goes through the sample when using a single-beam spectrophotometer, light must be eliminated in order to estimate the incident light intensity of the sample. The single-beam spectrophotometer is very cheaper than the double-beam spectrophotometer and this system wants a minimum number of parts and is less complicated. The double beam spectrophotometer includes a light source (tungsten light source or deuterium arc lamp), a sample holder (a transparent cell is named a cuvette with an internal width of 1cm), a diffraction grating or a prism to distinguish between the different wavelengths of light, and a detector (a photodiode array, a photodiode, photomultiplier tube). Figure 2.12 shows the optical ray diagram of the UV Spectrophotometer.

[23] *Optical Processes in Semiconductors - Jacques I. Pankove - Google Books* n.d.

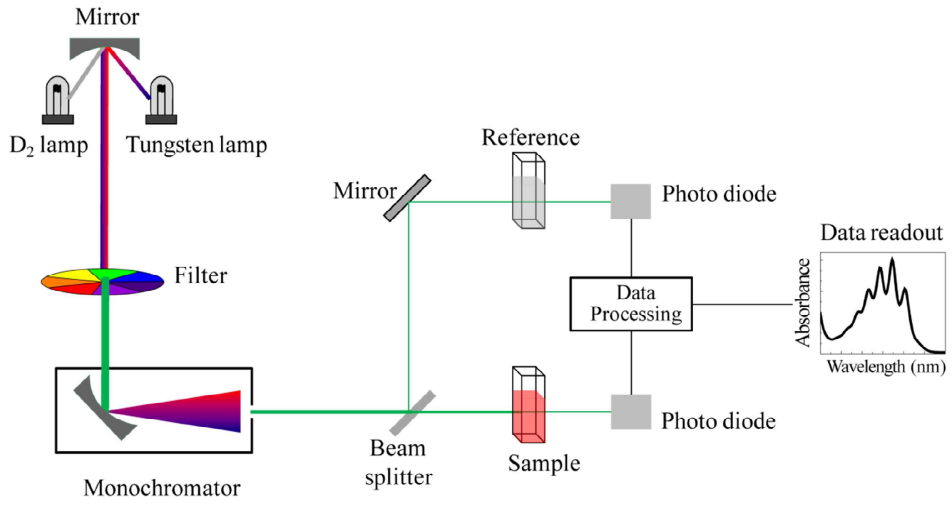

Fig 2.12 Optical ray diagram of UV-Vis Spectrophotometer

In a double-beam spectrophotometer, the monochromator prism or diffraction grating is used for the separation of the beam from the source into a single wavelength. To divide the single wavelength into beams with similar intensities, a half-mirrored apparatus is employed. One beam travels through the sample and serves as a sample beam. The next beam performs as a reference beam and transmits through another cuvette possessing only the solvent. The intensity of a beam that goes through the sample(I) and the intensity of the reference beam(I_0) detected by the detector and the intensities are compared. The scanning range of UV-Visible spectrophotometer is 200nm-800nm. The absorption coefficient near the band edge is defined as the[24].

$$\alpha = \frac{A(h\nu - E_g)^n}{h\nu} \qquad (2.36)$$

where A denoted as a constant, and E_g denoted as the band gap, and αhν =0 and $E_g = h\nu$

[24] Tauc 1974

The graph between $(\alpha h\nu)^{1/n}$ and $h\nu$ is known as the Tauc's plot. From the Tauc plot, the value of band gap of a material is estimated at α=0. If the transition is direct n=1/2, and for allowed indirect transition n=2, n=3/2 for forbidden direct transition, and n=3 for forbidden indirect transition. UV Spectrophotometer (Model No: UV 2600) - SHIMADZU used for the measurement. Figure 2.13 shows the image of UV Spectrophotometer (Model No: UV 2600).

Fig 2.13 The image of UV Spectrophotometer (Model No: UV 2600)

2.9 Photoluminescence Spectroscopy (PL)

Photoluminescence spectroscopy commonly known as (PL) is a technique in which light or photons falling on any matter stimulates photon emission. The PL studies are used for the investigation of optical characteristics and electronic structure of the material and it is contact-less and non-destructive. Figure 2.14 displays a schematic diagram of photoluminescence spectroscopy.

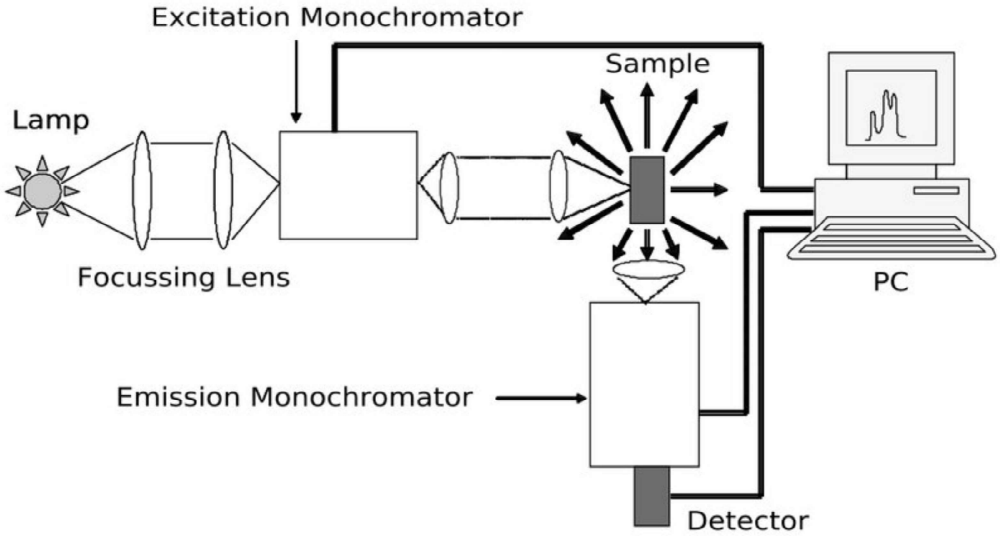

Fig 2.14. Schematic diagram of photoluminescence spectrophotometer

It is used for the characterization of inorganic and organic materials in the form of gas, liquid, and solid[25]. In the theory of photoluminescence, a higher an energy laser beam (light of sufficient energy) falls into the sample and is absorbed by the material, and transfers excess energy causing photoexcitation. The excess energy is eliminated from the sample by luminescence or photon emission. We refer to this glow as photoluminescence. When a material is photoexcited, its electrons migrate in the permitted excited state. Through the radiative or nonradiative process, the electrons return to their ground state by emitting excess energy. The energy difference between the excited and ground states is equivalent to the energy of light released (photoluminescence). The proportional contribution of the radiative process is correlated with the amount of light emitted[26]. The photoluminescence emission (PL) and photoluminescence excitation were studied using Spectro-fluorophotometer (Model No: RF 5301 PC)- SHIMADZU was shown in the Figure given below.

[25] Mohamed et al. 2020
[26] *Physical Methods in Chemistry and Nano Science : Andrew R. Barron : Free Download, Borrow, and Streaming : Internet Archive* n.d.

Fig 2.15 Digital photograph of Spectro-fluorophotometer (Model No: RF 5301 PC) - SHIMADZU

2.10 Photocatalytic studies

A photocatalyst is a substance that absorbs light and increases its energy level. It then transfers this energy to a substance that is reacting to cause a chemical reaction. Photocatalyst are defined as materials which decomposes detrimental substance under the sunlight containing UV rays. In the presence of a photocatalyst, light, and water, photocatalysis produces a potent oxidation agent that breaks down any organic substance into carbon dioxide and water. When solar light has enough photon energy to match or exceed the photocatalyst's band gap energy, the photocatalysts absorb the light and produce pairs of electrons and holes. In order to go through a redox reaction, the produced electron-hole pairs move to the photocatalyst's surface.

But many of these pairs of holes and electrons recombine to release energy as heat and light. While the holes in the photocatalyst's valence band attack the methylene blue dye and some of the holes also react with water to produce hydroxyl radicals, which in turn powerfully oxidise the methylene blue dye, the unrecombined electrons are excited to the photocatalyst's conduction band. However, in the presence of a photocatalyst and light, the excited electrons attack the oxygen again to generate superoxide anion radicals, which also break down the methylene blue dye into carbon

dioxide, water, and other less harmful or non-toxic compounds. The light intensity and the kind of catalyst that is utilised determine the photocatalyst's efficiency.

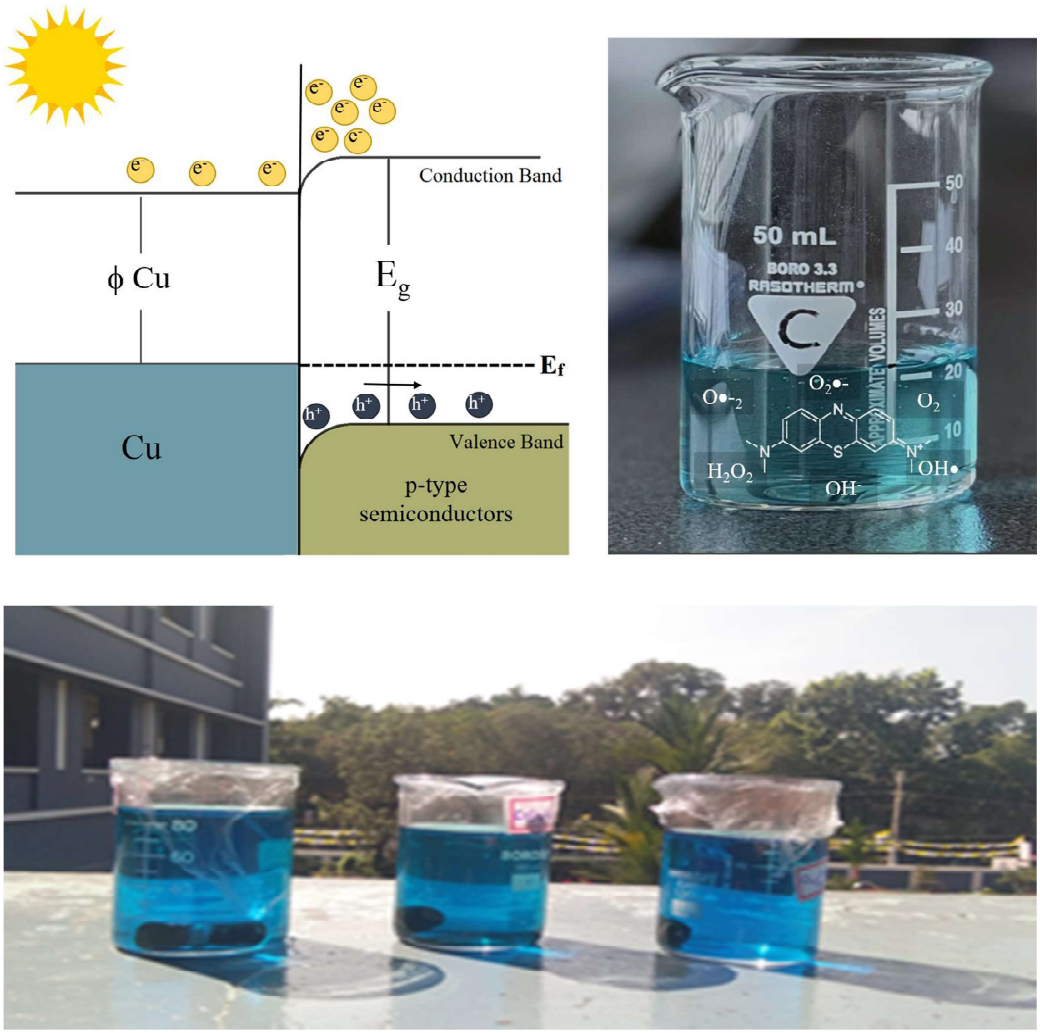

Fig 2.16 Sunlight-Driven Photocatalytic Degradation of Methylene Blue

Different processes occur when photocatalyst absorbs UV radiation from sunlight or a light source. These processes can be summed up in four key steps. (1) An electron-hole pair is produced by light absorption ; (2) separation of excited charge; (3) electron and hole transport to the photocatalyst surface; and (4) use of surface charges for redox reaction. This cycle keeps going as long as there is light. A significant fraction of electron-hole pairs recombine at the third stage, either on the surface or at the surface locations. The energy that was captured is released during recombination

either as heat (nonradiative recombination) or as light (radiative emission). Different redox processes may be facilitated by the long-lasting photogenerated charges on the surface; the specifics of these reactions will depend on the accepter or donor characteristics of the surface-absorbed species.

The dye degradation efficiency of these magnetic materials was studied by sunlight irradiation and subsequent recording of the absorption spectra. The scheme or procedure adopted for the solution preparation for the photocatalysis studies are given in Figure 2.16. For the preparation of methylene blue solution for the degradation studies using ferrite 0.004g of methylene blue was dissolved in 500ml of distilled water. 0.1g of ferrite was weighed and added to 20 ml of prepared methylene blue solution kept in a beaker covered using Aluminium foil and stirred it using magnetic stirrer for 15 minutes. These samples were kept on the ultrasonicator for 15 minutes. Then it is kept undisturbed for 16 hours and the absorption spectrum was taken for the dark condition using UV-Visible spectrophotometer on the next day. Thereafter it was exposed to sunlight for 60 min; again the measure of amount of visible light absorbed by the sample was studied using UV-Visible Spectrophotometer. We continued it for the next 4 hours and after each hour UV spectrum were recorded (Figure 2.16).

2.11 In Vitro Cytotoxicity

Heat is used in oncothermia, a type of cancer treatment, to shrink tumours. In the presence of an alternating magnetic field (AMF), magnetic nanoparticles (MNPs) have the ability to transform electromagnetic energy into heat energy. In addition to traditional treatments, unconventional therapies like hyperthermia are also in high demand. With the fewest possible side effects, hyperthermia is a unique form of therapeutic treatment in which extreme temperatures (between 41 and 45^0 C) are used to locally eradicate cancer cells. Consequently, a prospective area of use for magnetic nanoparticle research is the transport of drugs induced by hyperthermia. The use of ferromagnetic and superparamagnetic nanoparticles in hyperthermia is possible due to their ability to produce local heating in the presence of an external alternating current (ac) magnetic field. Cobalt ferrite is ferromagnetic in nature. More heat can be produced under an ac magnetic field than a superparamagnetic particle under the same field

because of its enormous hysteresis loop area[27]. The assessment of surviving and/or growing mammalian cells is necessary for many biological tests. There are various ways to accomplish this, e.g., counting cells that include/exclude a dye, measuring released, Cr-labeled protein after cell lysis etc.

Idealistically, a colorimetric assay for living cells should use a colourless substrate that can only be altered into a coloured result by other living cells dead cells or tissue culture medium are not allowed to do this. Tetrazolium salts are good candidates for this job since they can gauge different dehydrogenase enzymes' levels of activity. Only living cells can undergo the process because the tetrazolium ring is cleaved there. We have created a quick colorimetric assay that measures only living cells and can be read on an ELISA reader. It is based on the tetrazolium salt MTT (3-(4,5-dimethylthiazol-2-yl)-2,5-diphenyl tetrazolium bromide). This test is adaptable and quantitative, and it represents a considerable improvement over existing methods for a number of widely used proliferation and cytotoxicity assays[28].

With Dalton's Lymphoma Ascites cells (DLA), the produced nanoparticles' short-term in vitro cytotoxicity was investigated. For the investigation, tumour cells that were extracted from the peritoneal cavity of mice that carried tumours were employed. Three rounds of phosphate buffered saline (PBS) or normal cell line washing were performed on the tumour cells that emerged from the peritoneal cavity of mice that carried the tumour. Trypan blue exclusion was utilised to determine the vitality of the cells. Tubes holding various concentrations of the test substances were filled with a suspension of viable cells ($1*10^6$ cells in 0.1 ml), and the volume was increased to 1 ml using phosphate buffered cell line (PBS). There was only cell suspension in the control tube. The array mixture was incubated at 37^0C for three hours. After adding 0.1 ml of 1% trypan blue to the additional cell solution, it was stored for two to three minutes before being placed into a hemocytometer. Trypan blue dye is taken up by dead cells, but it is not taken up by living cells. Separate counts were made for the number of stained and unstained cells.

[27] Dey et al. 2018
[28] Mosmann 1983

The National Centre for Cell Sciences in Pune, India provided the mouse breast cancer cell line (C127I), which was cultured in DMEM media with 10% foetal bovine serum, 100 µg/mL penicillin, and 100 µg/mL streptomycin as supplements. The cell line was maintained at 37 °C in an incubator with 5% CO_2. The media was replaced every third day when the cells were passaged at 80–90% confluency. Using the MTT (3-(4,5-Dimethylthiazol-2-yl)-2,5-Diphenyltetrazolium Bromide) assay, the cytotoxicity of the test materials was assessed.

In a 24 well plate, $1x10^5$ cells/mL were planted with full growth media (DMEM) and allowed to adhere and proliferate. After the medium reached 80% confluency, fresh media was added with varying sample concentrations (0-100 µg/mL) and incubated for a full day. The medium was once more changed out with new medium at the conclusion of the incubation period. Following the addition of 40 µL of 5 mg/mL MTT, each well was incubated for 4 hours. After dissolving the formazan crystals in dimethyl sulfoxide, the absorbance was measured in an ELISA microplate reader (BioTek, USA) at 570 nm.

Rat spleen cells were used to investigate the test compound's short-term in vitro cytotoxicity. Using carbon dioxide anaesthesia, the rat was slaughtered for this purpose, and the spleen tissue was removed. After that, it was broken up into a single cell suspension in antibiotic-containing RPMI complete medium and filtered through mesh cloth. After three rounds of washing, the recovered cells were suspended in a predetermined volume of RPMI complete media with antibiotics and then tallied. Tubes holding different concentrations of the test chemical were filled with viable cell suspension ($1X10^6$cells in 0.lml), and the volume was increased to l ml using RPMI medium. Only cell suspension (no additions) was present in the control tubes. For three hours, these tubes were incubated at 37^0C. After the incubation period, the cell suspension in the tubes was combined with 0.1 % trypan blue, allowed to stand for two to three minutes, and then put into a hemocytometer. Trypan blue dye is taken up by dead cells, but it is not taken up by living cells. A different count was made of the labelled cells.

References

Amazon.in. (n.d.). Retrieved June 13, 2022

BROCKMAN, F. G., & WHITE, R. P. (1971). Nickel-Zinc Ferrites: III, Dielectric Properties of Stoichiometric Nickel-Zinc Ferrites*. *Journal of the American Ceramic Society*, *54*(4), 183–185. https://doi.org/10.1111/J.1151-2916. 1971. TB12259.X

Dey, C., Ghosh, A., Ahir, M., Ghosh, A., & Goswami, M. M. (2018). Improvement of Anticancer Drug Release by Cobalt Ferrite Magnetic Nanoparticles through Combined pH and Temperature Responsive Technique. *ChemPhysChem*, *19*(21), 2872–2878. https://doi.org/10.1002/cphc.201800535

Dielectric relaxation [by] Vera V. Daniel. (Book, 1967) [WorldCat.org]. (n.d.). Retrieved March 3, 2021, from https://www.worldcat.org/title/dielectric-relaxation-by-vera-v-daniel/oclc/859841181

Elements of X-Ray Diffraction Book Online at Low Prices in India | Elements of X-Ray Diffraction Reviews & Ratings - Amazon. (n.d.). Retrieved June 16, 2022

Foner, S. (1959). Versatile and Sensitive Vibrating-Sample Magnetometer*. *THE REVIEW OF SCIENTIFIC INSTRUMENTS*, *30*(7). http://rsi.aip.org/ about/ rights_and_permissions

Gomes, J. A., Sousa, M. H., Tourinho, F. A., Mestnik-Filho, J., Itri, R., & Depeyrot, J. (2005). Rietveld structure refinement of the cation distribution in ferrite fine particles studied by X-ray powder diffraction. *Journal of Magnetism and Magnetic Materials*, *289*, 184–187. https://doi.org/10.1016/ J.JMMM. 2004.11.053

Handbook of Microscopy for Nanotechnology. (2005). *Handbook of Microscopy for Nanotechnology*. https://doi.org/10.1007/1-4020-8006-9

Jacob, B. P., Thankachan, S., Xavier, S., & Mohammed, E. M. (2012). Dielectric behavior and AC conductivity of Tb3+ doped Ni0.4Zn0.6Fe2O4 nanoparticles. *Journal of Alloys and Compounds*, *541*, 29–35. https://doi.org/10.1016/ J.JALLCOM.2012.07.033

Liu, X. M., & Fu, S. Y. (2007). Synthesis of nanocrystalline Zn0.5Mn0.5Fe2O4 via in situ polymerization technique. *Journal of Magnetism and Magnetic Materials*, *308*(1), 61–64. https://doi.org/10.1016/J.JMMM.2006.05.003

Magnetic Nanomaterials - Google Books. (n.d.). Retrieved June 18, 2022

Mishra, S., Karak, N., Kundu, T. K., Das, D., Maity, N., & Chakravorty, D. (2006). Nanocrystalline nickel ferrites prepared by doping with niobium ions. *Materials Letters*, *60*(9–10), 1111–1115. https://doi.org/10.1016/J.MATLET.2005.10.085

Mohamed, M. A., Mohd Hir, Z. A., Wan Mokthar, W. N. A., & Osman, N. S. (2020). Features of metal oxide colloidal nanocrystal characterization. In *Colloidal Metal Oxide Nanoparticles*. Elsevier Inc. https://doi.org/10.1016/b978-0-12-813357-6.00008-5

Mosmann, T. (1983). Rapid colorimetric assay for cellular growth and survival: application to proliferation and cytotoxicity assays. *Journal of Immunological Methods*, *65*(1–2), 55–63. https://doi.org/10.1016/0022-1759(83)90303-4

Optical Processes in Semiconductors - Jacques I. Pankove - Google Books. (n.d.). Retrieved June 25, 2022

Physical Methods in Chemistry and Nano Science : Andrew R. Barron : Free Download, Borrow, and Streaming : Internet Archive. (n.d.). Retrieved June 25, 2022, from https://archive.org/details/ost-chemistry-col10699

Physics of dielectric materials: Tareev, Boris MikhaiÌ†lovich: Amazon.com: Books. (n.d.). Retrieved March 28, 2022, from https://www.amazon.com/Physics-dielectric-materials-MikhaiÌ†lovich-Tareev/dp/B0007AOBIA

Rietveld, H. M., & IUCr. (1969). A profile refinement method for nuclear and magnetic structures. *Urn:Issn:0021-8898*, *2*(2), 65–71. https://doi.org/ 10.1107/ S0021889869006558

S, S. V., E, V. G., & A, M. K. (2022). Structural Evolution–Enabled BiFeO 3 modulated by strontium doping with enhanced dielectric, optical and superparamagnetic properties by modified sol-gel method . *Chinese Physics B*, *32*. https://doi.org/10.1088/1674-1056/ac785b

Sagar, S., Saravanan, S., Suresh Kumar, S., Venkatachalam, S., & Anantharaman, M. R. (2006). Evidence for the existence of multiple equilibrium states in cobalt phthalocyanine tetramer: A study by dielectric spectroscopy. *Journal of Physics D: Applied Physics*, *39*(8), 1678–1683. https://doi.org/10.1088/0022-3727/39/8/030

Scanning Electron Microscopy and X-Ray Microanalysis: Third Edition eBook : Goldstein, Joseph, Newbury, Dale E., Joy, David C., Lyman, Charles E., Echlin, Patrick, Lifshin, Eric, Sawyer, Linda, Michael, J.R.: Amazon.in: Kindle Store. (n.d.). Retrieved June 18, 2022

Sinha, J. K. (1965). Modified Sawyer and Tower circuit for the investigation of ferroelectric samples. *Journal of Scientific Instruments*, *42*(9), 696–698. https://doi.org/10.1088/0950-7671/42/9/308

Solid State Chemistry and its Applications - Anthony R. West - Google Books. (n.d.). Retrieved June 13, 2022

Soohoo, R. (1960). *Theory and application of ferrites.* Prentice-Hall.

Tanner, B. K., Hase, T. P. A., Clarke, J., Pape, I., Li-Bassi, A., & Fulthorpe, B. D. (2001). High resolution X-ray scattering from nanotechnology materials. *Applied Surface Science*, *182*(3–4), 202–208. https://doi.org/10.1016/S0169-4332(01)00424-X

Tauc, J. (1974). *Amorphous and Liquid Semiconductors*.

Toby, B. H. (2006). R factors in Rietveld analysis: How good is good enough? *Powder Diffraction*, *21*(1), 67–70. https://doi.org/10.1154/1.2179804

Wang, Y., Hu, J., Lin, Y., & Nan, C. W. (2010). Multiferroic magnetoelectric composite nanostructures. *NPG Asia Materials*, *2*(2), 61–68. https://doi.org/10.1038/asiamat.2010.32

Warren, B. E. (Bertram E. (1969). *X-ray diffraction*. 381.

Chapter 3

STRUCTURAL, ELECTRICAL, MAGNETIC AND OPTICAL STUDIES ON ZINC DOPED NICKEL FERRITE NANOPARTICLES

STRUCTURAL, ELECTRICAL, MAGNETIC AND OPTICAL STUDIES ON ZINC DOPED NICKEL FERRITE NANOPARTICLES

This Chapter deals with the investigations on zinc-doped nickel ferrite (NFO) nanoparticles with the general formula $Ni_{1-x}Zn_xFe_2O_4$ (x = 0.0, 0.3, 0.5, 0.7, 1). These nanoparticles were prepared using a modified Sol-gel auto-combustion process. The focus of this chapter extends to the synthesis process, as well as the examination of structural, electrical, and magnetic traits. The structural evaluation is executed through X-ray powder diffraction technique. The morphological assessment of the prepared samples employs scanning electron microscopy (SEM) and Energy Dispersive X-Ray Analysis (EDAX). Additionally, the chapter provides comprehensive insights into the frequency-dependent dielectric constant and ac conductivity. Furthermore, the impact of zinc doping on the magnetic characteristics of nickel ferrite is also elucidated within this section. The photo degradation studies of zinc doped nickel ferrite and zinc ferrite nanoparticles were evaluated for the degradation of methylene blue dyes under visible light irradiation.

Part of this chapter have been published in

Superparamagnetic Nickel ferrite nanoparticles doped with zinc by modified Sol–gel method, Sharon V.S, Veena E. Gopalan, Imaddin A. Al-Omari, K A Malini, Journal of Superconductivity and Novel Magnetism 35:795–804 (2022). https://doi. org/ 10. 1007/s10948-021-06110-7 (IF 1.675)

3.1 Introduction

Magnetic materials in the nano-dimension exhibit distinct properties and have many technological applications in biomedical, magnetic storage, magnetic refrigeration devices, etc[1]. Researchers have been interested in magnetic nanoparticles due to their practical uses as well as their fundamental understanding of the amazing features, like superparamagnetism and surface spin effects, that they exhibit in the nanometric regime [2].

In recent years, researchers have shown immense interest on transition metal ferrite MFe_2O_4, because of the superior physical properties and their potential application in magnetic devices. Due to the electrical and magnetic properties, ferrites are the most important material in technological applications[3]. These materials have high-frequency applications owing to their high permeability and permittivity[4]. Nano-sized spinel ferrites are used in microwave absorbers, targeted drug delivery, biotechnology and magnetic fluids, etc[5]. Among them, nickel-zinc ferrites have great importance because of their high saturation magnetization and low coercivity. Ni-Zn ferrite has an inverse spinel structure with tetrahedral sites occupied by Zn^{2+} and Fe^{3+} ions and the octahedral sites occupied by Ni^{2+} and Fe^{3+} ions and has moderate saturation magnetization and mechanical hardness[6]. The properties of spinel ferrites are greatly influenced by the type of dopants used, the chemical composition and the synthesis process, etc[7]. This chapter of our research, reports the impact of zinc substitution on the structural, dielectric, and magnetic characteristics of nickel ferrite nanoparticles ($Ni_{1-x}Zn_xFe_2O_4$ (x=0.0,0.3,0.5,0.7,1)) prepared using a modified sol-gel auto combustion process[8]. It also reports the photocatalytic activity of nickel-zinc ferrite nanoparticles. The prepared samples are identified as NFO, NZFO-0.3, NZFO-0.5, NZFO-0.7, and ZFO, respectively, for zinc contents of x=0, 0.3, 0.5, 0.7, and 1. The

[1] A. A. Khan et al. 2017; V.S et al. 2022
[2] Kurmude et al. 2014; V.S et al. 2022
[3] *Effect of Zinc doping on Structural and Magnetic Properties of NiFe 2O4 Nanoparticles* n.d.
[4] Bener et al. 2009; Bener 2012; Brunzell et al. 2008; V.S et al. 2022
[5] Association 2009; Jones et al. 2003; Kotseva et al. 2001; V.S et al. 2022
[6] Schuster et al. 2004; V.S et al. 2022
[7] *Effect of Zinc doping on Structural and Magnetic Properties of NiFe 2O4 Nanoparticles* n.d.
[8] V.S et al. 2022

benefit of this process is that it produces uniform and ultrafine powder easily and cost effectively[9].

3.2 Synthesis

Nickel ferrite (NFO) nanoparticles and zinc doped nickel ferrite (NZFO) nanoparticles ($Ni_{1-x}Zn_xFe_2O_4$ (x=0.0,0.3,0.5,0.7,1)) were synthesized by modified sol-gel auto-combustion method. Precursors used for the synthesize of $Ni_{1-x}Zn_xFe_2O_4$ nanoparticles were analytic grade $Ni(NO_3)_2.6H_2O$ (Nickel nitrate), $Zn(NO_3)_2.6H_2O$ (Zinc nitrate), $Fe(NO_3)_3.9H_2O$ (Iron nitrate), and $C_6H_8O_7$ (Citric acid). Preparation methods are detailed in Section 2.2.1 of Chapter 2[10]. The produced powder samples were made into pellets of 12mm diameter by a hydraulic press at a pressure 0.53± 0.003Mpa. The pellets were then sintered for 4 hours at 900^0C for the dielectric measurements[11].

3.3 Results and Discussion

3.3.1 X-ray diffraction analysis

The prepared samples $Ni_{1-x}Zn_xFe_2O_4$ (x=0.0,0.3,0.5,0.7,1) were examined utilising Cu-Kα radiation and Brucker AXS D8 X-ray diffractometer for X-ray diffraction(with $\lambda = 1.5405Å$). Using the Debye-Scherrer formula, the size of the crystallite was determined.

$$D = \frac{0.9\lambda}{\beta \cos\theta} \qquad (3.1)$$

where β is full-width at half-maxima of the strongest intensity diffraction peak, λ is the wavelength of the radiation and θ is the angle of the strongest characteristic peak.

The lattice parameters of the samples were calculated using the formula[12]

[9] Sivakumar et al. 2011; V.S et al. 2022
[10] V.S et al. 2022
[11] V.S et al. 2022
[12] V.S et al. 2022

$$a = d(h^2+k^2+l^2)^{1/2} \quad (3.2)^{13}$$

where a=lattice constant, d=inter planar distance and (h,k,l) are the miller indices The formula was used to compute the X-ray density D_X

$$D_X = \frac{8M}{Na^3} \quad (3.3)$$

where a is the lattice constant, N is Avogadro's number, and M is the molecular weight. The following formula was used to get the dislocation density:

$$\Sigma = \frac{1}{D^2} \quad (3.4)^{14}$$

where D is grain size (determined using Scherrer's equation)

In spinel ferrites ($(A^{2+})[B^{3+}]_2O_4$), the cation distribution between tetrahedral and octahedral sites can be denoted by $(A^{2+}_{\delta}\ B^{3+}_{1-\delta})[A^{2+}_{1-\delta}\ B^{3+}_{1+\delta}]O_4$ here δ represents the degree of inversion. δ=0 for the inverse spinel and 1 for typical ferrites. Because δ in mixed spinel ferrite ranges from 0 to 1, divalent and trivalent ions are present in the tetrahedral and octahedral locations. Zinc doped nickel ferrite have inverse spinel structure with Fe^{3+} and Zn^{2+} ions on tetrahedral A- site Ni^{2+} and Fe^{3+} on octahedral B-site. So the distribution of cations can be represented as shown in Eq.3.5[15]

$$(Zn^{2+}_{x}Fe^{3+}_{1-x})(Ni^{2+}_{1-x}Fe^{3+}_{1+x})O^{2-}_{4} \quad (3.5)$$

The following formula was used to get the radii of the tetrahedral and octahedral sites:

$$r_A = [C_{Zn}r(Zn^{2+})+C_{Fe}\ r(Fe^{3+})] \quad (3.6)^{16}$$

$$r_B = \frac{1}{2}[C_{Ni}\ r(Ni^{2+})+C_{Fe}\ r(Fe^{+3})] \quad (3.7)^{17}$$

where, $r(Fe^{3+})$, $r(Zn^{2+})$, and $r(Ni^{2+})$ represent the ionic radii of iron, zinc and nickel ions respectively. C_{Fe}, C_{Zn} and C_{Ni} represent the concentration of iron, zinc and nickel respectively.

Using the following formula, the theoretical lattice constant was determined:

[13] Krishna et al. 2012
[14] Majid et al. 2018
[15] V.S et al. 2022
[16] Lin et al. 2018
[17] Lin et al. 2018

$$a_{th}=\frac{8}{3\sqrt{3}}[(r_A + R_0)+(r_B + R_0)] \quad (3.8)^{18}$$

a_{th} is the theoretical value of lattice constant, r_A , r_B , R_0 radii of A-site and B-site(tetrahedral and octahedral sites) and oxygen atom[19].

The degree to which the A site species occupy the cubo-octahedral gaps made by the B site octahedra is indicated by the tolerance factor. It is also considered as a measure of stability of crystal structure. The following formula was used to get the tolerance factor:

$$T=\frac{1}{\sqrt{3}}\left(\frac{r_A+R_0}{r_B+R_0}\right)+\frac{1}{\sqrt{2}}\left(\frac{R_0}{r_A+R_0}\right) \quad (3.9)\ ^{20}$$

Figure 3.1 represents the XRD pattern of $Ni_{1-x}Zn_xFe_2O_4$ (x=0.0, 0.3, 0.5, 0.7, 1) samples. The XRD patterns confirm the emergence of a single-phase cubic spinel structure for doped and un-doped nickel ferrite. This indicates that auto combustion method can be successfully used to produce pure crystalline particles. The presence of planes (220), (311), (222), (400), (422), (511), and (440) in the XRD pattern confirms the cubic spinel structure with no impurity peaks for all samples (JCPDS card no: 10-0325). The XRD pattern demonstrates that the synthesized materials have crystallite sizes in the nanoscale range due to the broadening of major peaks[21].

[18] Lin et al. 2018
[19] V.S et al. 2022
[20] Majid et al. 2018; V.S et al. 2022
[21] V.S et al. 2022

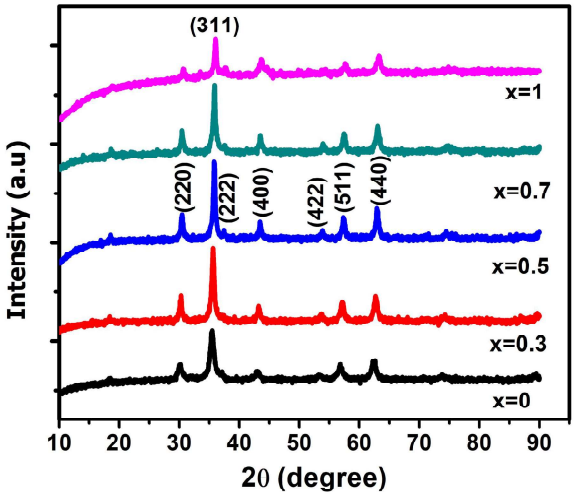

Fig 3.1 X-ray diffractograms of all the samples $Ni_{1-x}Zn_xFe_2O_4$ (x=0.0, 0.3, 0.5, 0.7, 1)

The calculated values of various structural parameters of $Ni_{1-x}Zn_xFe_2O_4$ nanoparticles are tabulated in Table 3.1. The findings show that, in the nickel ferrite samples, the increasing zinc concentration causes the lattice constant 'a' to increase from 8.269Å to 8.452Å. Lattice constant value show that the produced nanoparticles are cubic spinel structured[22]. The theoretically computed and the experimentally obtained lattice constants of nickel ferrite are in excellent agreement with the earlier reported results[23]. The ionic radii of Ni^{2+} ($0.71A^0$) and Fe^{3+} ($0.63A^0$) are small compared to the ionic radius of Zn^{2+} ($0.74A^0$). Since in $Ni_{1-x}Zn_xFe_2O_4$, Ni^{2+} and Fe^{3+} ions of smaller ionic radius are replaced by larger Zn^{2+} ions, the lattice constant increases. The lattice constant has a linear effect on the unit cell volume, which also increases with the amount of Zn^{2+} in obedience to Vegard's law. The lattice expands without changing its symmetry, as evidenced by the lattice constant value. The X-ray density values obtained for $ZnFe_2O_4$ is smaller than nickel-zinc ferrite. D_x and the lattice constant have an inverse relationship, and when x increases, we see a drop in X-ray density[24].

[22] Ameer et al. 2015
[23] Dhole 2016
[24] V.S et al. 2022

Table 3.1. Structural date from XRD for Zn doped nickel ferrite samples

Composition (x)	**Crystallite size(D) nm**	**Lattice constant a_{exp} (A^0)**	**Lattice constant a_{th} (A^0)**	**Unit cell volume $(A^0)^3$**	**X-ray density D_X (g cm^{-3})**
0	9	8.269	8.319	565.40	5.51
0.3	12	8.311	8.347	574.06	5.46
0.5	13	8.377	8.367	587.84	5.37
0.7	13	8.385	8.386	589.53	5.39
1	17	8.452	8.408	603.77	5.30

Equation 3.4 is also used to compute the dislocation density value for various concentrations, and the results are shown in Table 3.2. It is found that size grows, dislocation density reduces, and packing factor increases as zinc concentration increases. The relationships indicated in Eqs. 3.6 and 3.7, respectively, are used to compute the radii of the cations in the tetrahedral and octahedral sites. The calculated values of r_A and r_B are shown in Table 3.2. On comparing cation radii r_A and r_B, it is observed that the value of lattice constant (a) increased with x, as the increase in the value of r_A is more than the decrease in the value of r_B with x. The theoretical lattice constant is calculated using cationic radii values of A and B sites by Eq.3.8 and is tabulated in Table 3.1. It is observed that the calculated value of lattice constant from experimental data agrees well with the theoretical value[25]. The slight deviation of a_{th} from a_{exp} may be because of the assumption of rigid spherical geometry of cations and anions in spinel ferrites[26]. The tolerance factor is calculated using Eq.3.9 and tabulated in Table 3.2. The tolerance factor (T) for $Ni_{1-x}Zn_xFe_2O_4$ ferrites at different concentration of Zn ions values are ~1, which indicate the cubic spinel structure of ferrites[27].

[25] Majid et al. 2018
[26] Sharma & Singhal 2013
[27] Majid et al. 2018; V.S et al. 2022

Table 3.2. Dislocation density, packing fraction, radii of tetrahedral and octahedral sites and Tolerance factor for $Ni_{1-x}Zn_xFe_2O_4$ (x=0.0,0.3,0.5,0.7,1) samples.

Composition (x)	Dislocation density(σ) (10^{-3} nm^{-2})	Packing fraction(P)	r_A (Å)	r_B (Å)	T
0	12.32	36.18	0.645	0.677	1.108
0.3	6.25	50.39	0.673	0.667	1.111
0.5	5.96	51.80	0.692	0.661	1.112
0.7	5.92	52.20	0.711	0.654	1.332
1	3.48	67.30	0.740	0.645	1.117

The XRD patterns are refined using Rietveld refinement. The Rietveld refinement revealed that the space group of ferrite systems belongs to *Fd3m*. The best-fitting parameters indicate that the prepared samples are of better quality and refinements of samples are successful. The refinement analysis was conducted using the FullProf suit programme. Figure 3.2 a-e shows the XRD diffractograms that where refined using the Rietveld refinement[28].

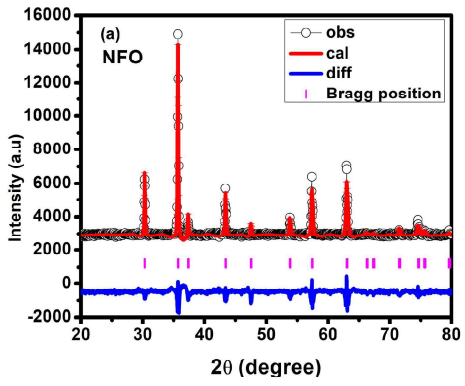

(a)

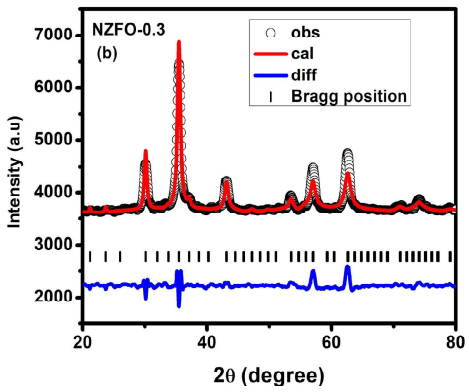

(b)

[28] V.S et al. 2022

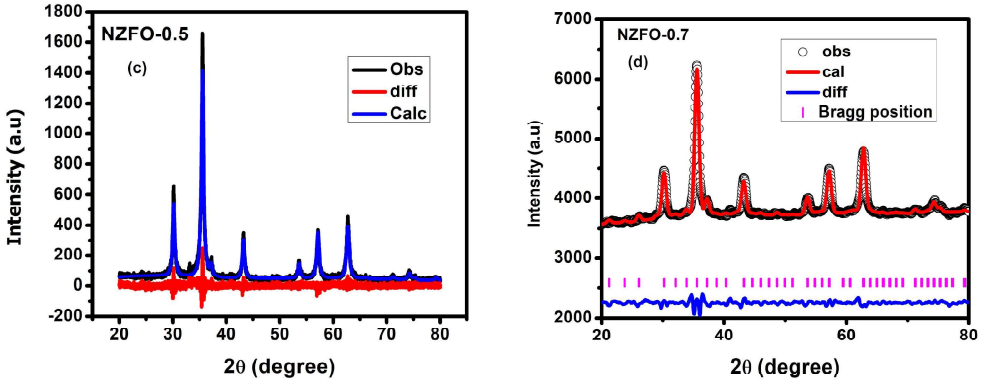

(c) (d)

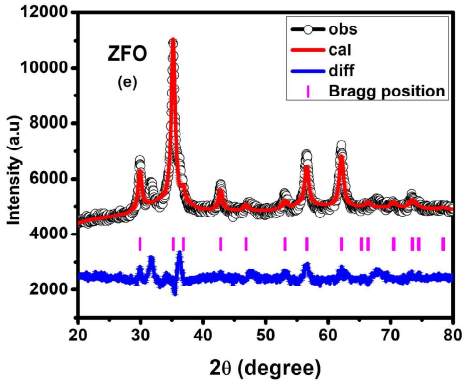

(e)

Fig 3.2 Rietveld refinement data for (a) NFO (b) NZFO-0.3 (c) NZFO-0.5 (d) NZFO-0.7 (e) ZFO samples

For structural analysis, the atomic positions of Ni^{2+} and Fe^{3+} in tetrahedral (A) and octahedral (B) sites for nickel ferrite nanoparticles are simulated using VESTA software and are shown in Figure 3.3. The atomic positions of Ni^{2+} and Zn^{2+} in tetrahedral (A) and octahedral (B) sites for composition x=0.5 are also shown in Figure 3.3[29].

[29] V.S et al. 2022

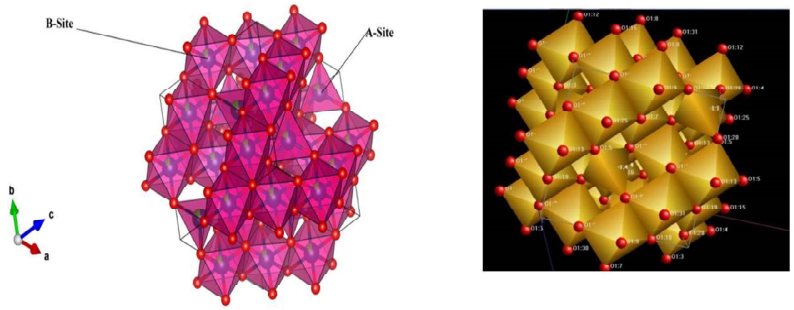

(a) (b)

Fig 3.3 (a) Atomic positions of Ni^{2+} and Fe^{3+} in the tetrahedral and octahedral sites for $NiFe_2O_4$ nano ferrite. (b) Atomic positions of Ni^{2+} and Zn^{2+} in tetrahedral and octahedral sites for NZFO-0.5 nano ferrite.

3.3.2 Morphological studies and Elemental Analysis

The morphology of the NZFO-0.5 nanoparticle was analyzed by using scanning electron microscope (SEM). The SEM image provide the surface morphology of the $Ni_{0.5}Zn_{0.5}Fe_2O_4$ nanoparticles. The SEM image of the NZFO-0.5 nanoparticles are shown in Figure 3.4, which shows how well the nanoparticles are agglomerated. The interaction between magnetic nanoparticles is thought to be the cause of the particle aggregation[30].

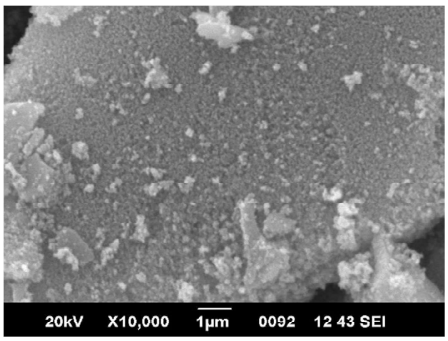

Fig. 3.4 The SEM image of the NZFO-0.5 sample

EDAX spectrum analysis was done in order to verify the stoichiometry of NZFO-0.5 nanoparticles, and is shown in Figure 3.5. The EDAX confirmed the homogenous mixing of Fe, Ni, Zn, and O atoms in the NZFO-0.5 sample[31].

[30] Kesavamoorthi et al. 2016; V.S et al. 2022
[31] Dubey et al. 2019; V.S et al. 2022

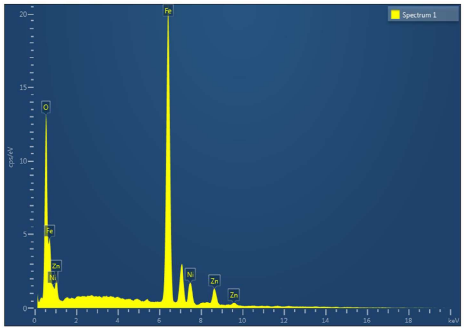

Fig. 3.5 EDAX spectrum of NZFO-0.5 nanopowder

3.3.3 Electrical properties

3.3.3.1 Variation of dielectric constant with frequency

HP 4285 LCR meter was used to measure the change of samples' ac conductivity and dielectric constant (ε) at room temperature for the frequency between 100 kHz to 5 MHz.

The formula used to determine the dielectric constant and ac conductivity for the prepared samples given in Section 2.4.1 of Chapter 2[32].

Figure 3.6 illustrates the dielectric constant variation with frequency. Dielectric constant values for different samples at lower frequencies are found to be in the range of 5-45 for 100 kHz. The dielectric constant is found to decrease with increasing frequency. Spinel ferrites typically exhibit the reduction in dielectric constant with frequency. The dielectric constant aberrance with frequency is explained by Maxwell Wagner type interfacial polarization and space charge polarization[33] agreeing on Koop's phenomenological theory[34].

In nano ferrites, the extending grains separated by weak amorphous grain boundaries form the non-homogeneous dielectric structure which causes space charge polarization [35]. The electron-exchange in Fe^{2+} and Fe^{3+} ions generating electric field is

[32] V.S et al. 2022
[33] Spies et al. 1992
[34] Ashtar et al. 2016; Meaz et al. 2003; V.S et al. 2022
[35] Ashtar et al. 2016; Soosen Samuel et al. 2011

the cause of dielectric polarization[36]. The relaxation time is the time taken by the dielectric material to return to their original equilibrium state after being perturbed by an external electric field[37]. To line up with their axis along the applied electric field, each dielectric substance requires a limited amount of time. As frequency increases, a point reaches when the charge carriers do not align with the applied external electric field, so polarization cannot reach the saturation value and also does not follow the alternating electric field. This is the reason for the fast decrease in dielectric constant with frequency at larger frequencies[38]. All the samples show high value dielectric constant and these materials can be used in gate dielectrics, capacitor dielectrics and photoelectrochemical cells, etc[39].

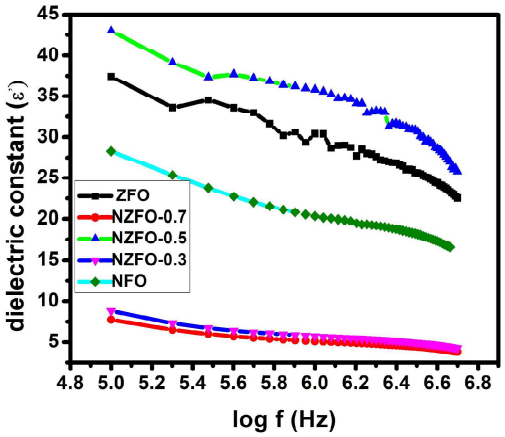

Fig 3.6 Variation of dielectric constant with frequency

The stable d-shell configuration in Fe^{3+} ion creates a spherical symmetry of the charged electron cloud. But the Fe^{2+} ions have extra electrons which perturb the symmetry of the charged electron cloud. So, the presence of Fe^{2+} ions in the ferrite sample is the motive for the increase in polarization and hence permittivity. But few Fe^{2+} ions were replaced by the dopant zinc and the dielectric permittivity changes drastically[40]. From Figure 3.6 it is also clear that the dielectric constant is maximum for

[36] Sonia et al. 2018
[37] Jun et al. 2005
[38] Hussain et al. 2013
[39] Singh & Ulrich 1999; V.S et al. 2022
[40] Chandamma et al. 2017

x=0.5, the highest dispersion is due to the existence of available Fe^{2+} ions at the octahedral sites. The sample x=0.5 contains a large concentration of ferrous ions at octahedral sites in comparison with other samples. The sample x=0.5 has maximum polarization which increases the permittivity due to electron transfer between Fe^{2+}/Fe^{3+} ions[41]. Another intriguing finding is that the dielectric constant for x=0.3 and x=0.7 at all frequencies is essentially comparable. The substitution by zinc may change the distribution of Fe^{2+} and Fe^{3+} ions which may appear as a change in hoping and hence the dielectric constant. Reports suggest that substitution with tetravalent cations like Ti^{4+} and Mn^{4+} can also change the dielectric constant marginally[42]. The wide range of low frequency dielectric constant values of the prepared samples point towards its use as tunable dielectric materials[43].

3.3.3.2 Variation of ac conductivity with frequency

Frequency variation of ac conductivity of Ni-Zn ferrites nanoparticles is studied and is represented in Figure 3.7. It is evident that as applied field frequency rises, carrier hopping also rises, leading to an increase in conductivity[44].

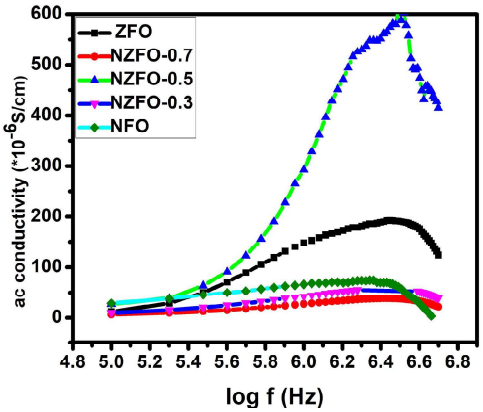

Fig 3.7. Variation of ac conductivity with frequency

The increase in ac conductivity with frequency is based on Koop's model. According to Koop's model, low-frequency conductivity is because of the grain

[41] S. B. Khan et al. 2019
[42] Patil et al. 2021
[43] V.S et al. 2022
[44] V.S et al. 2022

boundaries, and in the higher frequencies is due to conducting grains. Because of high density, the interfacial states in the nano-system can act as charge carriers due to ionization and can also act as conduction centers for the transfer of charge carriers. When the applied field increases ac conductivity also increases. The variation in ac conductivity can be attributed to the low- and high-frequency zones. In low-frequency regions, the grain boundaries are more active so that the probability density of charge carriers hopping is smaller, whereas in the high-frequency region, conducting grains are more energetic which encourages the charge carrier hopping[45]. Figure 3.8 illustrates how dielectric constant and ac conductivity varies with composition. The maximum value of ac conductivity is obtained for x=0.5 and samples with x=0.3 and 0.7 recorded almost identical values for ac conductivity[46]. The dielectric constant is also found to be maximum for x=0.5.

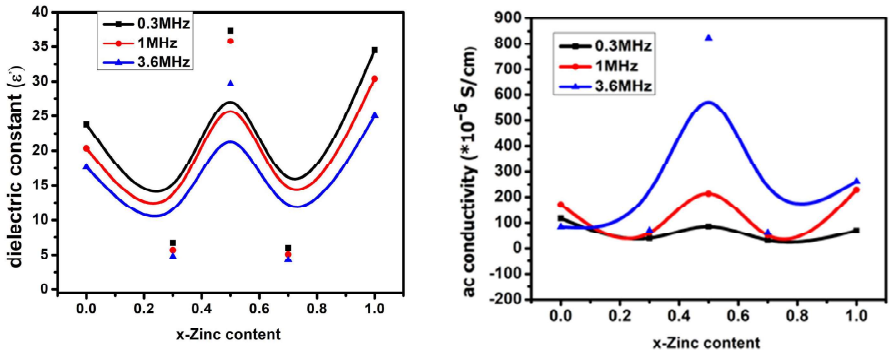

Fig 3.8 Variation of dielectric constant and ac conductivity with Zn content in NFO samples

3.3.4 Magnetic Properties

Magnetic properties of the samples $Ni_{1-x}Zn_xFe_2O_4$ (x=0.0, 0.3, 0.5, 0.7, 1) were studied using a VSM in a Physical Properties Measurement System (PPMS) from Quantum Design at two temperatures 5K and 300K (SQU, Sultanate of Oman). The magnetic moment and magneto-crystalline anisotropic constant (K) were calculated by the given equations 3.10 and 3.11.

[45] Ahmad et al. 2016
[46] V.S et al. 2022

$$n_B^e = \frac{M.M_S}{N_A \mu_B} \quad (3.10)$$

$$H_C = \frac{0.96K}{M_S} \quad (3.11)[47]$$

where M is molecular weight, M_s is the saturation magnetization, $N_A * \mu_B$ is a constant which is equal to 5585, H_C is coercivity, n_B^e is the magnetic moment and K is the anisotropic constant.

The value of Yafet and Kittel(Y-K) angle were calculated using the formula for the net experimental magnetic moment n_B^e expressed in the units of Bohr magneton

$$n_B^e = M_B \cos \alpha_{YK} - M_A \quad (3.12)$$

here, M_A and M_B are the magnetic moment on the A site and B sites respectively.

The magnetic behavior of samples $Ni_{1-x}Zn_xFe_2O_4$ (x=0.0, 0.3, 0.5, 0.7, 1) at two temperatures namely 5K and 300K are shown in Figure 3.9a, 3.9b and 3.9c. For all samples, the magnetization of ferromagnetic materials increases with the applied field and reaches its maximum value namely the saturation magnetization. It has been established that zinc doping has a significant impact on the magnetic characteristics of nickel ferrite nanoparticles. This is because of the cationic stoichiometry and their occupancy in the particular sites[48]. In pure zinc ferrite, the reported values of saturation magnetization is found to be very low and zero value remanence magnetization suggests the antiferromagnetic behavior of the sample below Neel temperature[49]. Although zinc ferrite crystallizes in normal spinel structure where Zn occupying tetrahedral site, the net magnetization may be due to the occupation of some amount of zinc in the octahedral site, shifting the Fe ions to the tetrahedral sites. For ultrafine particles the surface interaction dominates and can result in spin canting and freezing which manifests as variations in magnetic properties[50].

[47] Bhaskaran et al. 2021
[48] Kurmude et al. 2014; V.S et al. 2022
[49] Kurmude et al. 2014
[50] V.S et al. 2022

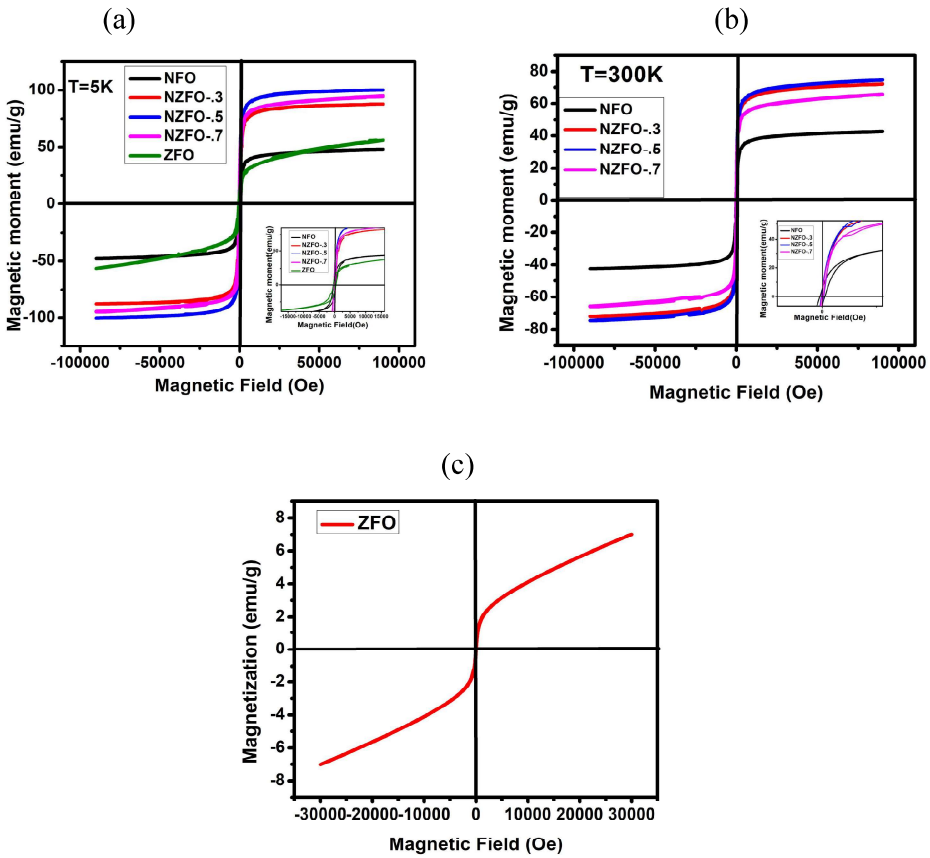

Fig 3.9 (a)M-H curve for $Ni_{1-x}Zn_xFe_2O_4$ (x=0.0,0.3,0.5,0.7,1) at 5K (b) M-H curve for $Ni_{1-x}Zn_xFe_2O_4$ (x=0.0,0.3,0.5,0.7) at 300K (c) $ZnFe_2O_4$ at 300K respectively

Equation 3.10 is used to compute the magnetic moment values, and equation 3.11 is used to get the anisotropy constant. The saturation magnetization value rises with x, reaches a maximum, and then falls, as shown by the magnetization curves. Tables 3.3 provide the magnetic parameters that were measured and computed from the VSM studies[51].

The fluctuation of the magnetic moment caused by the doping of zinc in nickel ferrite is depicted in Figure 3.10. Similar reports are available in the literature[52].

[51] V.S et al. 2022
[52] Kurmude et al. 2014

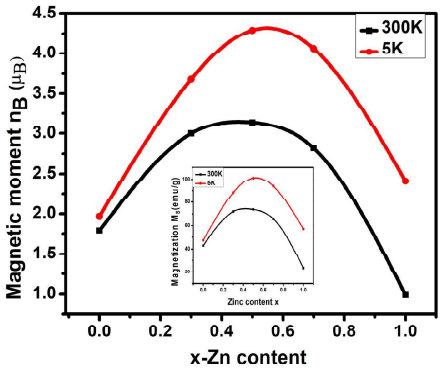

Fig 3.10 Variation of saturation magnetization and magnetic moment for NZF with x

In our samples, it is observed that the saturation magnetization increases from 42.84 to 74 emu/g up to x=0.5 and then decreases for higher values of x and recorded a value of 7.06 emu/g for x=1. The variation of saturation magnetization could be explained by Neel's two-sublattice collinear model according to which the magnetic moment is the vector sum of lattice magnetic moments of {(A) and [B]} sublattices[53]. In nickel-zinc ferrite, the Zn^{2+} ions are located at the tetrahedral (A) site and Ni^{2+} ions are at the octahedral (B) site. When we substitute the diamagnetic Zn^{2+} ions, then the concentration of Fe^{3+} ions in tetrahedral (A) site is diluted by the Zn^{2+} ions so the net magnetization and magnetic moment increase.

After certain value, the magnetic moment decreases with increasing zinc concentration which cannot be explained by Neel's collinear two-sublattice model. Yafet and Kittel's 1952 introduction of the three-sublattice model provides an explanation for this[54]. The B sublattice is split into two sublattices, B_1 and B_2, according to the Y-K model. Both sublattices have equal magnitude and are oppositely canted at the same angle (Y-K angle) with respect to net magnetization at 0K. Then the three sublattices (A, B_1 and B_2) have triangular spin arrangements which become more relevant with increasing zinc concentration. The presence of canted spin and the magnetic moment's behaviour as the zinc content increases are determined by the Y-K angle. The value of the Y-K angle is calculated using equation 3.12 and tabulated in

[53] Iyer et al. 2009
[54] Mazen & Abu-Elsaad 2012

Table 3.3. The Y-K angle is found to increase with zinc concentration and finally extrapolates to 88.25 for pure zinc ferrite. When the higher concentration of nickel ions is replaced by zinc ions the magnetic ions in the tetrahedral site decrease and the A-B interaction weakens and the B-B interaction become stronger. As a result, the B-site's spin cant in relation to the A-site's spin direction. This is the reason for the decrease in the value of magnetic moment for x>0.5[55]. Except for pure nickel ferrite, nickel ferrite nanoparticles in this investigation exhibit a Y-K kind of magnetic ordering. Similar results are also available in some research works[56].

Table 3.3 shows the results of the magnetization measurements at 300K. As expected, the magnetization values are higher at lower temperatures. The increased magnetization values for all of the samples when compared to the reported magnetization values is another intriguing finding. The saturation magnetization of zinc ferrite prepared using this method is higher than the previously reported values[57].

Table 3.3. Observed magnetic parameters for $Ni_{1-x}Zn_xFe_2O_4$

Zn content in sample (x)	M_s (emu/g)	M_r (emu/g)	M_r/M_S	H_C (Oe)	K (erg/g)	Magnetic moment n_B (μ_B)	α_{YK}
0	42.84	5.43	0.13	106.42	4748	1.79	0
0.3	71	3.66	0.05	46.43	3433	3	34.63
0.5	74	3.66	0.04	46.43	3578	3.14	48.43
0.7	66	1	0.01	22.43	1542	2.82	61.65
1	7.06	0.124	0.02	4.17	30.6	0.304	88.25

Figure 3.11 displays the magnetic coercivity and anisotropic constant for each sample. At 300K, the coercivity drops from 106.42 Oe as zinc content is increased and pure zinc ferrite has a coercivity of 4.17Oe. The coercivity depends upon average grain

[55] Topkaya et al. 2013
[56] Mahmood et al. 2022; Rana et al. 2003; V.S et al. 2022
[57] V.S et al. 2022

size D, anisotropic constant, and several other factors[58]. Zinc ferrite has a lower coercivity than nickel ferrite. It is observed that as zinc content increases, grain size increases and coercivity decreases. Literature reports also point towards the inverse relation between grain size and coercivity[59].

The ratio M_r /M_s measures the M-H hysteresis loop's squareness; a low value denotes isotropic nature[60]. It is a crucial characteristic of a material that is dependent on anisotropy; it is useful to determine the direction of the closest easy axis of magnetization; and this value is in excellent agreement with the values that have been previously published[61]. As zinc concentration rises, the coercive field and remanent magnetization both decrease, indicating superparamagnetic behaviour. The samples' estimated crystallite size of 20 nm supports the formation of the superparamagnetic phase. Many similar reports can be found throughout in the literature[62].

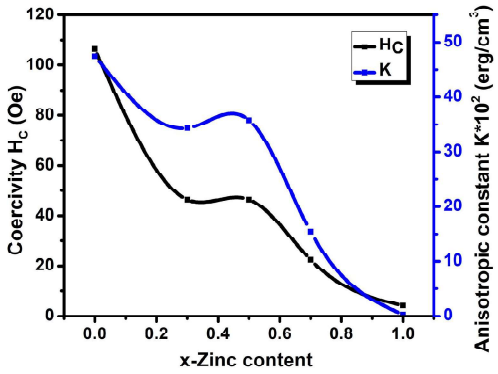

Fig 3.11 Variation of coercive field, anisotropic constant with zinc content for $Ni_{1-x}Zn_xFe_2O_4$ (x=0.0, 0.3, 0.5, 0.7, 1) at 300k

[58] M. H. R. Khan & Hossain 2012
[59] Gabal et al. 2012; V.S et al. 2022
[60] Rhaman et al. 2020
[61] Kurmude et al. 2014
[62] Kurmude et al. 2014; Nath et al. 2004; V.S et al. 2022

3.3.5 Photocatalytic Activity Studies

The photocatalytic activity of the set of nickel zinc ferrite samples was evaluated by studying the degradation of methylene blue (MB) dye under sunlight irradiation. Figure 3.12 shows the absorption spectra of the MB solution containing the sample as photocatalyst from 200 to 750 nm with time step of 60 min. The preparation methods are given in section 2.10 of Chapter 2.

Photocatalytic degradation of MB dye was carried out using zinc doped nickel ferrite samples as photocatalysts under solar radiation. The MB solution is a bright blue solution in the initial condition. With longer irradiation times when photocatalysts were present, a consistent colour decrease was seen. According to Beer Lambert's law, dye concentration and absorbance maxima are directly correlated. The MB dye solution's time-dependent absorption spectra in the presence of ferrite are displayed in Figure 3.12. The MB blue solution has the absorbance peak at 664 nm and the secondary peaks at 610 nm and 290 nm. The intensity of absorbance peak was found to decrease with increasing irradiation time without change in shape or position. The elimination of chromophoric group is the reason for the decrease in the intensity at 664 nm. That no other chromophore molecule was created as a by-product was proven by the absence of any other further peaks in the UV-VIS spectra [63].

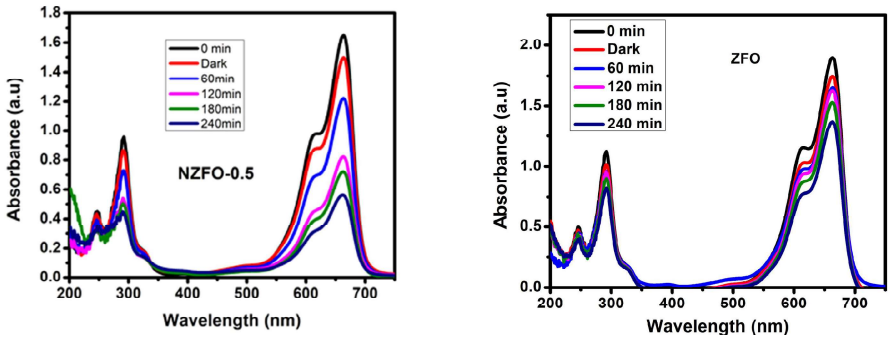

Fig 3.12 Time-dependent absorption spectra of the MB dye solution under visible light for NZFO-0.5 and ZFO samples.

[63] N et al. 2023

The degradation of MB can be defined by the degradation efficiency, $(C_0\text{-}C)/C_0$, where C is the dye's change in concentration at predetermined intervals of time, and C_0 is the initial dye concentration at time t = 0. This can also be expressed in terms of absorbance as $(A_0\text{-}A)/A_0$ where A is the absorbance of the MB solution containing the sample after photocatalytic degradation.

Percentage dye degradation was studied for NZFO-0.5 and ZFO and is plotted in Figure 3.13. The recombination of photo-induced e^-/h^+ pairs limits the photocatalytic activity of zinc ferrite. The inhibition of e^-/h^+ pairs recombination and the production of Fermi energy levels below the conduction band are the causes of the increasing photodegradation in NZFO-0.5. The degradation percentage is calculated using the equation $(\frac{C_0-C}{C_0}) * 100$. Here, C_0 is equivalent to the dye's starting absorbance (A_0) at time t = 0, and C represents the dye's change in absorbance (A) at predetermined time intervals. Table 3.4 gives the dye degradation percentage which leads to following inference.

The maximum degradation of NZFO-0.5 and ZFO after 240 minutes exposure are 66% and 28% respectively. The results indicate that by doping nickel in zinc ferrite we can improve the photocatalytic activity. The modification/enhancement of the magnetic properties with nickel content in zinc ferrite is very well studied and hence this will be added advantage of tailoring the properties for various applications[64].

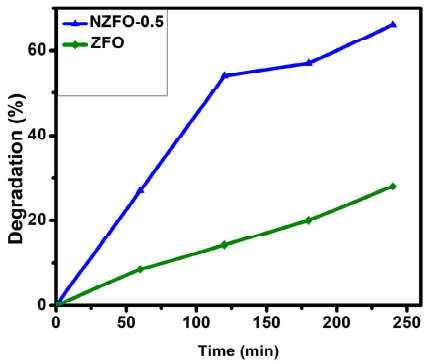

Fig 3.13 Photocatalytic activity for samples.

[64] Madhukara Naik et al. 2019

Table 3.4: Dye Degradation percentage for $Ni_{1-x}Zn_xFe_2O_4$

Time of irradiation in minutes	Degradation percentage	
	NZFO-0.5	ZFO
0	11	0
60	27	8.42
120	54	14.2
180	57	20
240	**66**	**28**

3.3.5.1 Kinetic Study of Photodegradation

Using the Langmuir-Hinshelwood model, the kinetic performance of ferrites for MB degradation was computed and fitted. The rate constant of MB photodegradation as seen in Figure 3.14 is explained by this hypothesis which shows the chemical kinetics for the degradation of MB dye fits pseudo-first order kinetic model.

$$\ln\frac{c_0}{c_t} = kt \qquad (3.13)$$

The slope of the linear fit plot of $\ln\frac{c_0}{c_t}$ vs irradiation time gives degradation rate constant. All graphs of $\ln\frac{c_0}{c_t}$ vs time were fitted linearly and the fitted curves are given in Figure 3.14. Slope of the linear fit was obtained and these are called the rate constant are tabulated in Table 3.5.

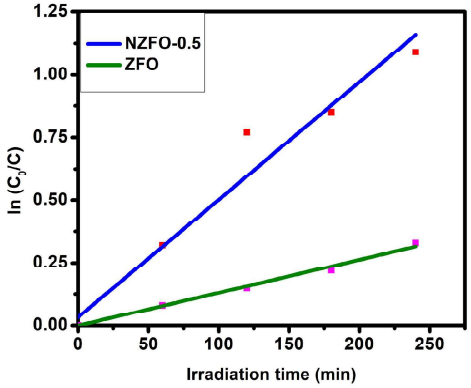

Fig 3.14 Linear fit of Kinetic plot

Table 3.5: Rate constant of MB dye in the presence of NZFO samples as photocatalyst

Sample	Rate constant ($k*10^{-2}$ min^{-1})
NZFO-0.5	0.45
ZFO	0.13

Under visible light irradiation, doped samples exhibit superior photocatalytic activity compared to pure zinc ferrite, with nickel-zinc ferrite showing higher activity than pure zinc ferrite. However, after reaching an optimal limit, the photocatalyst's efficiency declines due to the rapid recombination of electron-hole (e^-/h^+) pairs. This increased recombination leads to a reduction in photodegradation efficiency. Additionally, during the photocatalytic process, greater structural deformation occurs in doped samples compared to pure ferrites.[65]

3.4. Conclusions

Nickel ferrite $Ni_{1-x}Zn_xFe_2O_4$ (x=0.0, 0.3, 0.5, 0.7, 1) nanoparticles are prepared by modified Sol-gel auto-combustion method. It is a quick, inexpensive, and simple method. We carefully analysed the structural, dielectric, and magnetic properties of all samples and how they vary with the degree of zinc doping. XRD analysis shows that the produced samples have a cubic spinel structure with a Fd-3m space group, crystallite sizes in the range of 9 nm to 16 nm, and a minor fluctuation in the lattice constant (8.269 to 8.452 Å) with zinc content. The structural characteristics (lattice constant, density, dislocation density, radii of tetra and octahedral sites, and tolerance factor) alter as Zn concentration rises. The homogeneous mixing of Ni, Zn, Fe, and O atoms was confirmed by the EDAX spectrum. According to the dielectric studies, frequency increase resulted in a drop in the dielectric constant. The undoped nickel ferrite sample has a dielectric constant of roughly 29, but the dielectric constant can be changed by doping with zinc. For all samples, a high value of the dielectric constant was found, in comparison to the literature (R Singh et al) and this can be used for gate and capacitor dielectric applications.

[65] Madhukara Naik et al. 2019

Magnetization studies of all NZFO samples show that remanent magnetization and coercive field decreases with increasing zinc concentration. The coercivity and magnetisation values confirms the soft magnetic nature of the prepared samples. The low squareness ratio (M_r/M_s) of all samples indicate that they are less anisotropic containing a large fraction of superparamagnetic nanoparticles and show pronounced spin canting effects. As a result, nickel ferrites' magnetic and dielectric properties can be changed using the very straightforward, cost-effective technique of zinc doping. This will make it easier to customize materials for different uses. Thus, these materials hold promise for applications using magnetic devices in the future.

The degradation of methylene blue under sunlight in the presence of catalyst NZFO samples are investigated by studying the absorption intensities of the solution containing the photocatalysts after exposure to sunlight for known durations. The time of irradiation was varied and a maximum time of 240 minutes exposure to sunlight was given to all samples. This indicates that nickel zinc ferrite can act as an efficient photocatalyst. Zinc ferrite has least activity as far as dye degradation is concerned. It showed a degradation rate of 28% even after 240 minutes exposure to sunlight. Nickel ferrite nanoparticles are efficient photocatalytic semiconductor in comparison to the literature (Madhukara Naik et al) for degradation of organic pollutants because after dye degradation the catalyst can be removed easily by using a magnetic field.

References

Ahmad, R., Hussain Gul, I., Zarrar, M., Anwar, H., Khan Niazi, M. B., & Khan, A. (2016). Improved electrical properties of cadmium substituted cobalt ferrites nano-particles for microwave application. *Journal of Magnetism and Magnetic Materials*, *405*, 28–35. https://doi.org/10.1016/j.jmmm.2015.12.019

Ameer, S., Gul, I. H., Mahmood, N., & Mujahid, M. (2015). Synthesis, characterization and optical properties of in situ ZnFe2O4 functionalized rGO nano hybrids through modified solvothermal approach. *Optical Materials*, *45*(45), 69–75. https://doi.org/10.1016/j.optmat.2015.02.035

Ashtar, M., Munir, A., Anis-Ur-Rehman, M., & Maqsood, A. (2016). Effect of chromium substitution on the dielectric properties of mixed Ni-Zn ferrite prepared by WOWS sol-gel technique. *Materials Research Bulletin*, *79*, 14–21. https://doi.org/10.1016/j.materresbull.2016.02.044

Association, A. D. (2009). Standards of medical care in diabetes-2009. In *Diabetes Care* (Vol. 32, Issue SUPPL. 1, pp. S13–S61). American Diabetes Association. https://doi.org/10.2337/dc09-S013

Bener, A. (2012). Association between psychological distress and gastrointestinal symptoms in diabetes mellitus. *World Journal of Diabetes*, *3*(6), 123. https://doi.org/10.4239/wjd.v3.i6.123

Bener, A., Zirie, M., Janahi, I. M., Al-Hamaq, A. O. A. A., Musallam, M., & Wareham, N. J. (2009). Prevalence of diagnosed and undiagnosed diabetes mellitus and its risk factors in a population-based study of Qatar. *Diabetes Research and Clinical Practice*, *84*(1), 99–106. https://doi.org/10.1016/j.diabres.2009.02.003

Bhaskaran, S., Al-omari, I. A., & Gopalan, E. V. (2021). On the enhanced coercive field and anisotropy observed in cobalt substituted copper ferrite nanoparticles prepared by a modified sol-gel method. *Journal of Alloys and Compounds*, *884*, 161095. https://doi.org/10.1016/j.jallcom.2021.161095

Brunzell, J. D., Davidson, M., Furberg, C. D., Goldberg, R. B., Howard, B. V., Stein, J. H., Witztum, J. L., & Kirkman, M. S. (2008). Lipoprotein management in patients with cardiometabolic risk: Consensus statement from the American diabetes association and the american college of cardiology foundation. In *Diabetes Care* (Vol. 31, Issue 4, pp. 811–822). Diabetes Care. https://doi.org/10.2337/dc08-9018

Chandamma, N., Manohara, B. M., Ujjinappa, B. S., Shankarmurthy, G. J., & Santhosh Kumar, M. V. (2017). Structural and electrical properties of Zinc doped Nickel ferrites nanoparticles prepared via facile combustion technique. *Journal of Alloys and Compounds*, *702*, 479–488. https://doi.org/10.1016/j.jallcom.2016.12.392

Dhole, V. V. (2016). STRUCTURAL AND MAGNETIC PROPERTIES OF NICKEL FERRITE NANOPARTICLES BY WET CHEMICAL CO-PRECIPITATION TECHNIQUE Vithal Vinayak Dhole. *Ijesrt*, *5*(11), 3–6. http://www.ijesrt.xn--com-1ea

Dubey, H. K., Verma, C., Rai, S., Kumar, A., & Lahiri, P. (2019). Notes Synthesis, characterization and properties of nickel based zinc ferrite nanoparticles. *Indian Journal of Chemistry*, *58*, 454–458.

Effect of Zinc doping on Structural and Magnetic Properties of NiFe 2O4 Nanoparticles. (n.d.). Retrieved March 16, 2021, from https://1library.net/document/zkk4dnez-effect-zinc-doping-structural-magnetic-properties-nife-nanoparticles.html

Gabal, M. A., El-Shishtawy, R. M., & Al Angari, Y. M. (2012). Structural and magnetic properties of nano-crystalline NiZn ferrites synthesized using egg-white precursor. *Journal of Magnetism and Magnetic Materials*, *324*(14), 2258–2264. https://doi.org/10.1016/j.jmmm.2012.02.112

Hussain, T., Siddiqi, S. A., Atiq, S., & Awan, M. S. (2013). Induced modifications in the properties of Sr doped BiFeO3 multiferroics. *Progress in Natural Science: Materials International*, *23*(5), 487–492. https://doi.org/10.1016/j. pnsc. 2013. 09.004

Iyer, R., Desai, R., & Upadhyay, R. V. (2009). Low temperature synthesis of nanosized mn1-xznxfe2o4 ferrites and their characterizations. *Bulletin of Materials Science*, *32*(2), 141–147. https://doi.org/10.1007/s12034-009-0021-0

Jones, P. H., Davidson, M. H., Stein, E. A., Bays, H. E., McKenney, J. M., Miller, E., Cain, V. A., & Blasetto, J. W. (2003). Comparison of the efficacy and safety of rosuvastatin versus atorvastatin, simvastatin, and pravastatin across doses (STELLAR* trial). *American Journal of Cardiology*, *92*(2), 152–160. https:// doi.org/10.1016/S0002-9149(03)00530-7

Jun, Y. K., Moon, W. T., Chang, C. M., Kim, H. S., Ryu, H. S., Kim, J. W., Kim, K. H., & Hong, S. H. (2005). Effects of Nb-doping on electric and magnetic properties in multi-ferroic BiFeO3 ceramics. *Solid State Communications*, *135*(1–2), 133–137. https://doi.org/10.1016/j.ssc.2005.03.038

Kesavamoorthi, R., Vigneshwaran, A. N., Sanyal, V., & Ramachandra Raja, C. (2016). Synthesis and characterization of nickel ferrite nanoparticles by sol - Gel auto combustion method. *Journal of Chemical and Pharmaceutical Sciences*, *9*(1), 160–162.

Khan, A. A., Hira, U., Iqbal, Z., Usman, M., & Sher, F. (2017). Structural, magnetic and magnetocaloric properties of CoFe2−xMoxO4 ($0.0 \leq x \leq 0.3$) ferrites. *Ceramics International*, *9*(43), 7088–7093. https://doi.org/10.1016/J. CERAMINT. 2017. 02.139

Khan, M. H. R., & Hossain, A. K. M. A. (2012). Reentrant spin glass behavior and large initial permeability of Co 0.5-xMnxZn0.5Fe2O4. *Journal of Magnetism and Magnetic Materials*, *324*(4), 550–558. https://doi.org/10.1016/j.jmmm.2011.08.039

Khan, S. B., Irfan, S., & Lee, S. L. (2019). Influence of Zn+2 doping on ni-based nanoferrites; (Ni1−x ZnxFe2O4). *Nanomaterials*, *9*(7). https://doi.org/ 10.3390/ nano9071024

Kotseva, K., Wood, D. A., De Backer, G., De Bacquer, D., Pyöräla, K., & Keil, U. (2001). Lifestyle and risk factor management and use of drug therapies in coronary patients from 15 countries: Principal results from EUROASPIRE II Euro Heart Survey Programme. *European Heart Journal*, *22*(7), 554–572. https:// doi.org/ 10.1053/euhj.2001.2610

Krishna, K. R., Kumar, K. V., & Ravinder, D. (2012). Structural and Electrical Conductivity Studies in Nickel-Zinc Ferrite. *Advances in Materials Physics and Chemistry*, *02*(03), 185–191. https://doi.org/10.4236/ampc.2012.23028

Kurmude, D. V., Kale, C. M., Aghav, P. S., Shengule, D. R., & Jadhav, K. M. (2014). Superparamagnetic behavior of zinc-substituted nickel ferrite nanoparticles and its effect on mossbauer and magnetic parameters. *Journal of Superconductivity and Novel Magnetism*, *27*(8), 1889–1897. https://doi.org/10.1007/s10948-014-2535-y

Lin, Q., Xu, J., Yang, F., Lin, J., Yang, H., & He, Y. (2018). Magnetic and Mössbauer spectroscopy studies of zinc-substituted cobalt ferrites prepared by the sol-gel method. *Materials*, *11*(10), 1–12. https://doi.org/10.3390/ma11101799

Madhukara Naik, M., Bhojya Naik, H. S., Nagaraju, G., Vinuth, M., Vinu, K., & Viswanath, R. (2019). Green synthesis of zinc doped cobalt ferrite nanoparticles: Structural, optical, photocatalytic and antibacterial studies. *Nano-Structures and Nano-Objects*, *19*, 100322. https://doi.org/10.1016/j.nanoso.2019.100322

Mahmood, A., Maqsood, A., & Abdi, A. (2022). Effect of manganese doping on the structural, mechanical, optical, and magnetic properties of zinc ferrite nanoparticles. *Physica Scripta*, *97*(6), 65707. https://doi.org/10.1088/1402-4896/ac6f2a

Majid, F., Rauf, J., Ata, S., Bibi, I., Yameen, M., & Iqbal, M. (2018). Hydrothermal Synthesis of Zinc Doped Nickel Ferrites: Evaluation of Structural, Magnetic and Dielectric Properties. *Zeitschrift Fur Physikalische Chemie*. https:// doi.org/ 10.1515/zpch-2018-1305

Mazen, S. A., & Abu-Elsaad, N. I. (2012). Structural and some magnetic properties of manganese-substituted lithium ferrites. *Journal of Magnetism and Magnetic Materials*, *324*(20), 3366–3373. https://doi.org/10.1016/J.JMMM.2012.05.056

Meaz, T. M., Attia, S. M., & Abo El Ata, A. M. (2003). Effect of tetravalent titanium ions substitution on the dielectric properties of Co-Zn ferrites. *Journal of Magnetism and Magnetic Materials*, *257*(2–3), 296–305. https:// doi.org/ 10.1016/S0304-8853(02)01212-X

N, A., Philip, R. S., & Mathew, M. (2023). Photocatalytic activities of SnS thin films deposited at room temperature. *Applied Surface Science Advances*, *13*(September 2022), 100374. https://doi.org/10.1016/j.apsadv.2023.100374

Nath, B. K., Chakrabarti, P. K., Das, S., Kumar, U., Mukhopadhyay, P. K., & Das, D. (2004). Mössbauer, X-ray diffraction and AC susceptibility studies on nanoparticles of zinc substituted magnesium ferrite. *European Physical Journal B*, *39*(4), 417–425. https://doi.org/10.1140/epjb/e2004-00212-0

Patil, B. A., Kounsalye, J. S., Humbe, A. V., & Kokate, R. D. (2021). Structural, magnetic, dielectric and hyperfine interaction studies of titanium (Ti4+)-substituted nickel ferrite (Ni1+xTixFe2−2xO4) nanoparticles. *Journal of Materials Science: Materials in Electronics*, *32*(4), 4556–4567. https://doi.org/10.1007/s10854-020-05197-3

Rana, M. U., Misbah-ul-Islam, & Abbas, T. (2003). Magnetic interactions in Cu-substituted manganese ferrites. *Solid State Communications*, *126*(3), 129–133. https://doi.org/10.1016/S0038-1098(02)00908-0

Rhaman, M. M., Matin, M. A., Hossain, M. N., Khan, M. N. I., Hakim, M. A., & Islam, M. F. (2020). Ferromagnetic, electric, and ferroelectric properties of samarium and cobalt co-doped bismuth ferrite nanoparticles. *Journal of Physics and Chemistry of Solids*, *147*(July 2019), 109607. https://doi.org/10.1016/j.jpcs.2020.109607

Schuster, H., Barter, P. J., Stender, S., Cheung, R. C., Bonnet, J., Morrell, J. M., Watkins, C., Kallend, D., & Raza, A. (2004). Effects of switching statins on achievement of lipid goals: Measuring Effective Reductions in Cholesterol Using Rosuvastatin Therapy (MERCURY I) study. *American Heart Journal*, *147*(4), 705–712. https://doi.org/10.1016/j.ahj.2003.10.004

Sharma, R., & Singhal, S. (2013). Structural, magnetic and electrical properties of zinc doped nickel ferrite and their application in photo catalytic degradation of methylene blue. *Physica B: Condensed Matter*, *414*, 83–90. https://doi.org/10.1016/j.physb.2013.01.015

Singh, R., & Ulrich, R. K. (1999). High and low dielectric constant materials. *Electrochemical Society Interface*, *8*(2), 26–30.

Sivakumar, P., Ramesh, R., Ramanand, A., Ponnusamy, S., & Muthamizhchelvan, C. (2011). Synthesis and characterization of nickel ferrite magnetic nanoparticles. *Materials Research Bulletin*, *46*(12), 2208–2211. https://doi.org/10.1016/j.materresbull.2011.09.009

Sonia, M. M. L., Anand, S., Vinosel, V. M., Janifer, M. A., Pauline, S., & Manikandan, A. (2018). Effect of lattice strain on structure, morphology and magneto-dielectric properties of spinel NiGdxFe2−xO4 ferrite nano-crystallites synthesized by sol-gel route. *Journal of Magnetism and Magnetic Materials*, *466*, 238–251. https://doi.org/10.1016/j.jmmm.2018.07.017

Soosen Samuel, M., Koshy, J., Chandran, A., & George, K. C. (2011). Dielectric behavior and transport properties of ZnO nanorods. *Physica B: Condensed Matter*, *406*(15–16), 3023–3029. https://doi.org/10.1016/j.physb.2011.04.070

Spies, W., Maller, A., Linkemann, J., Frank, A., Wagner, M., Kozhuharov, C., Franzke, B., Beckert, K., Bosch, F., Eickhoff, H., Jung, M., Klepper, O., König, W., Mokler, P. H., Moshammer, R., Nolden, F., Schaaf, U., Spädtke, P., Steck, M., … Badnell, N. R. (1992). Dielectronic and radiative recombination of lithiumlike gold. *Physical Review Letters*, *69*(19), 2768–2771. https://doi.org/10.1103/ PhysRevLett. 69.2768

Topkaya, R., Baykal, A., & Demir, A. (2013). Yafet-Kittel-type magnetic order in Zn-substituted cobalt ferrite nanoparticles with uniaxial anisotropy. *Journal of Nanoparticle Research*, *15*(1). https://doi.org/10.1007/s11051-012-1359-6

V.S, S., Gopalan, V. E., Al-Omari, I. A., & Malini, K. A. (2022). Superparamagnetic Nickel Ferrite Nanoparticles Doped with Zinc by Modified Sol–gel Method. *Journal of Superconductivity and Novel Magnetism 2021*, 1–10. https://doi. org/10.1007/S10948-021-06110-7

Chapter 4

STRUCTURAL, ELECTRICAL AND MAGNETIC STUDIES ON ZINC DOPED COBALT FERRITE NANOPARTICLES

STRUCTURAL, ELECTRICAL AND MAGNETIC STUDIES ON ZINC DOPED COBALT FERRITE NANOPARTICLES

The synthesis as well as structural, electrical and magnetic characterization of zinc doped cobalt ferrite (CFO) nanoparticles with general formula, $Co_{1-x}Zn_xFe_2O_4$ (x=0.0,0.3,0.5,0.7,1) is discussed in this Chapter. The samples have been synthesized by modified Sol-gel auto-combustion process. The technique known as X-ray powder diffraction is used to perform the structural analysis. Energy Dispersive X-Ray Analysis (EDAX) and scanning electron microscopy (SEM) are used to perform morphological evaluations on the generated samples. Studies have been conducted on ac conductivity and frequency-dependent dielectric constant. The effects of zinc doping on the magnetic properties of cobalt ferrite had been studied in detail. The photo degradation studies of cobalt ferrite zinc doped and cobalt ferrite nanoparticles were evaluated for the degradation of methylene blue dyes under visible light irradiation. Cytotoxicity studies on cobalt ferrite nanoparticles are also presented in this Chapter.

4.1 Introduction

Cobalt ferrite has attracted a lot of attention among nano-ferrites[1]. The spinel structure of cobalt ferrite is represented by the formula AB_2O_4, in which site A is a tetrahedral site and B is an octahedral site. It may be inverse spinel or mixed spinel cobalt ferrite, depending on the distribution of the metal cations (Fe and Co) at the octahedral and tetrahedral sites. Cobalt ferrite is categorised as a hard magnet due to its strong coercivity and moderate magnetism. Due to its significant magnetic coercivity value and excellent physical and chemical stability, it has been used in a variety of applications. These include torque sensors, ferrofluids, medical diagnostics, magneto-mechanical systems, and high-density magnetic storage materials.

In the present studies, we report the preparation of Zn-doped cobalt ferrite ($Co_{1-x}Zn_xFe_2O_4$ (x=0.0, 0.3, 0.5, 0.7, 1)) samples by modified sol-gel method. The prepared samples are labelled as CFO, CZFO-0.3, CZFO-0.5, CZFO-0.7 and ZFO for zinc content x=0, 0.3, 0.5 0.7 and 1 respectively. The structural studies of the prepared samples were done using XRD and Rietveld refinement. The morphological studies were done using SEM and EDAX. The dielectric, magnetic and photocatalytic properties of cobalt ferrite zinc doped samples were also evaluated.

4.2 Synthesis

Zinc doped cobalt ferrite nanoparticles ($Co_{1-x}Zn_xFe_2O_4$ (x=0.0, 0.3, 0.5, 0.7, 1)) (CZFO) were prepared by modified Sol-gel method. Materials used for the synthesize of $Co_{1-x}Zn_xFe_2O_4$ nanoparticles were analytic grade $Co(NO_3)_2.6H_2O$ (Cobalt nitrate), $Zn(NO_3)_2.6H_2O$ (Zinc nitrate), $Fe(NO_3)_3.9H_2O$ (Iron nitrate), and $C_6H_8O_7$ (Citric acid). Details of preparation are given in Section 2.2.1. The powder samples were annealed at 800^0C for 3 hours. The resulting powder samples were compressed into 12 mm-diameter pellets using a hydraulic press operating at 0.53 ± 0.003 MPa of pressure. The pellets were then sintered for 4 hours at 900^0C for the dielectric measurements.

[1] Sugimoto 1999

4.3 Results and Discussion

4.3.1 X-ray diffraction analysis

Structural characterization of $Co_{1-x}Zn_xFe_2O_4$ (x=0.0, 0.3, 0.5, 0.7, 1) samples were done using XRD on Brucker AXS D8 X-Ray diffractometer. Crystallite size was obtained by employing the Debye- Scherrer formula.

$$D = \frac{0.9\lambda}{\beta \cos\theta} \quad (4.1)$$

where β represents the full-width at half-maxima of the strongest intensity diffraction peak, λ represents the wavelength of the radiation and θ represents the angle of the strongest characteristic peak.

The lattice parameters of the prepared samples were obtained using the formula

$$a = d(h^2+k^2 + l^2)^{1/2} \quad (4.2)^2$$

where 'a' represents the lattice constant, 'd' represents the inter planar distance and (h,k,l) are the miller indices. The unit cell volume is given by $V_{cell}=a^3$ since a=b=c and $\alpha=\beta=\gamma=90^0$ for cubic spinel.

X-ray density D_X was obtained using

$$D_X = \frac{8M}{Na^3} \quad (4.3)$$

where M represents the molecular weight, N represents the Avogadro's number, 'a' represent the lattice constant.

The spinel structure which can be expressed as

$$(Zn^{2+}{}_xFe^{3+}{}_{1-x})[Co^{2+}{}_{1-x}Fe^{3+}{}_{1+x}]O^{2-}{}_4 \quad (4.4)$$

The Zn^{2+} and Fe^{3+} ions are in tetrahedral A-site and Co^{2+} and Fe^{3+} ions are in octahedral B-site.

The radii of tetrahedral (A) and octahedral (B) sites were obtained using the formula,

[2] Krishna et al. 2012

$$r_A = [x\ r(Zn^{2+}) + (1-x)\ r(Fe^{3+})] \quad (4.5)$$

$$r_B = \frac{1}{2}[(1-x)\ r(Co^{2+}) + (1+x)\ r(Fe^{+3})] \quad (4.6)$$

where, $r(Fe^{3+})$, $r(Zn^{2+})$, and $r(Co^{2+})$ represent the ionic radii of iron, zinc and cobalt ions respectively and x represent the concentration of zinc.

Theoretical lattice constant was obtained using the formula,

$$a_{th} = \frac{8}{3\sqrt{3}}[(r_A + R_0) + \sqrt{3}\,(r_B + R_0)] \quad (4.7)$$

a_{th} represents the theoretical value of lattice constant, r_A, r_B, R_0 radii of A-site (tetrahedral), B-site (octahedral sites) and oxygen atom.

Using the following formula, the tolerance factor was determined:

$$T = \frac{1}{\sqrt{3}}\left(\frac{r_A + R_0}{r_B + R_0}\right) + \frac{1}{\sqrt{2}}\left(\frac{R_0}{r_A + R_0}\right) \quad (4.8)$$

The dislocation density was calculated using the formula,

$$\Sigma = \frac{1}{D^2} \quad (4.9)$$

where D is grain size (determined using Scherrer's equation)

The X-ray diffraction (XRD) patterns of Zn^{2+} doped cobalt ferrite nanoparticles prepared by modified sol-gel process is shown in Figure 4.1. The reflection planes (220), (311), (400), (422), (511), and (440) of the produced nanoparticles indicate their single-phase nature, with the distinctive peak corresponding to plane (311) indicating the creation of cubic phase [JCPDS Card No.22-1086]. There are no additional peaks corresponding to the impurity phases. Addition of zinc causes dopant induced distortion and it decreases the molecular concentration on crystal surface. This restricts the crystal growth and effects the cation occupancy. Also the greater bond energy Co^{2+}-O^{2-} as compared with Zn^{2+}-O^{2-} could be the reason for the decrease in particle size with increasing zinc concentration[3].

[3] Lin et al. 2018

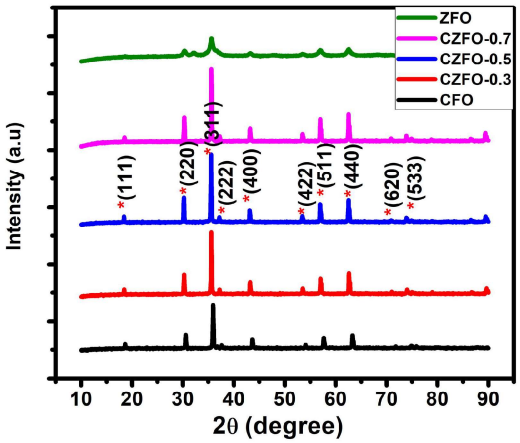

Fig 4.1: XRD pattern of $Co_{1-x}Zn_xFe_2O_4$ (x=0, 0.3, 0.5, 0.7, 1)

As a result of the rise in Zn^{2+} content, the lattice expanded without changing its symmetry. When Co^{2+} ion is replaced by Zn^{2+} ions the lattice parameter is increased from 8.33 Å to 8.45 Å as listed in Table 4.1. The lattice constant increase may be because of the greater the ionic radius Zn^{2+} (0.74Å) compared to Co^{2+} (0.72Å) ions. Zinc ion has the tetrahedral (A-site) preference, but the cobalt ions prefer to occupy the octahedral B-site in $Co_{1-x}Zn_xFe_2O_4$ ferrite. We can calculate the theoretical lattice constant using equation 4.7. The differential site occupancy of cobalt ions can be used to explain the discrepancy between observed and theoretical lattice constants. However, the theoretical lattice constant and experimental lattice constant all increase with zinc concentration are tabulated in Table 4.1[4]. The X-ray density for different samples are also calculated and tabulated in Table 4.1 and are in very good agreement with the previously reported values[5]. Even though the atomic weight of zinc is higher than cobalt, a decrease in X-ray density is observed with zinc doping which is because of the increase in lattice constant[6].

Equation 4.9 is also used to compute the dislocation density value for various concentrations, and the results are shown in Table 4.2. It is found that size decreases, dislocation density increases, and packing factor decreases as zinc concentration

[4] Topkaya et al. 2013
[5] Supriya et al. 2018
[6] Topkaya et al. 2013

increases. The tolerance factor is calculated using Eq.4.8 and tabulated in Table 4.2. The tolerance factor (T) for $Co_{1-x}Zn_xFe_2O_4$ ferrites at different concentration of Zn ions values are ~1, which indicate the cubic spinel structure of ferrites[7].

Table 4.1. X-ray diffraction studies of Zn doped cobalt ferrite at various zinc content.

Composition (x)	Crystallite size(D) nm	Lattice constant a_{exp} (Å)	Lattice constant a_{th} (Å)	Unit cell volume (Å)^3	X-ray density D_X (g cm^{-3})
0	52	8.330	8.362	578.00	5.39
0.3	39	8.409	8.375	594.61	5.28
0.5	40	8.419	8.385	596.73	5.30
0.7	36	8.435	8.394	600.14	5.31
1	17	8.452	8.408	603.77	5.30

Table 4.2. Dislocation density, packing fraction, radii of tetrahedral and octahedral sites and Tolerance factor for $Co_{1-x}Zn_xFe_2O_4$ (x=0.0, 0.3, 0.5, 0.7, 1) samples.

Composition (x)	Dislocation density(σ) (10^{-4} nm^{-2})	Packing fraction(P)	r_A (Å)	r_B (Å)	T
0	3.63	209	0.645	0.682	1.10
0.3	6.51	154	0.673	0.671	1.10
0.5	6.10	160	0.692	0.663	1.11
0.7	7.7	143	0.711	0.656	1.11
1	34.7	67	0.74	0.645	1.11

The cobalt ferrite and zinc doped samples' space group is confirmed to be the Fd3m space group by the Rietveld refinement of the X-Ray Diffractograms. The synthesized samples are of higher quality, as shown by the best-fitting parameters, and the refinement was therefore successful. Using the Full-Prof suit programme, the

[7] V.S et al. 2022

refinement analysis was performed. Rietveld refinement was used to calculate the lattice parameters. Figure 4.2 displays the XRD diffractogram that was improved using the Rietveld refinement on all samples.

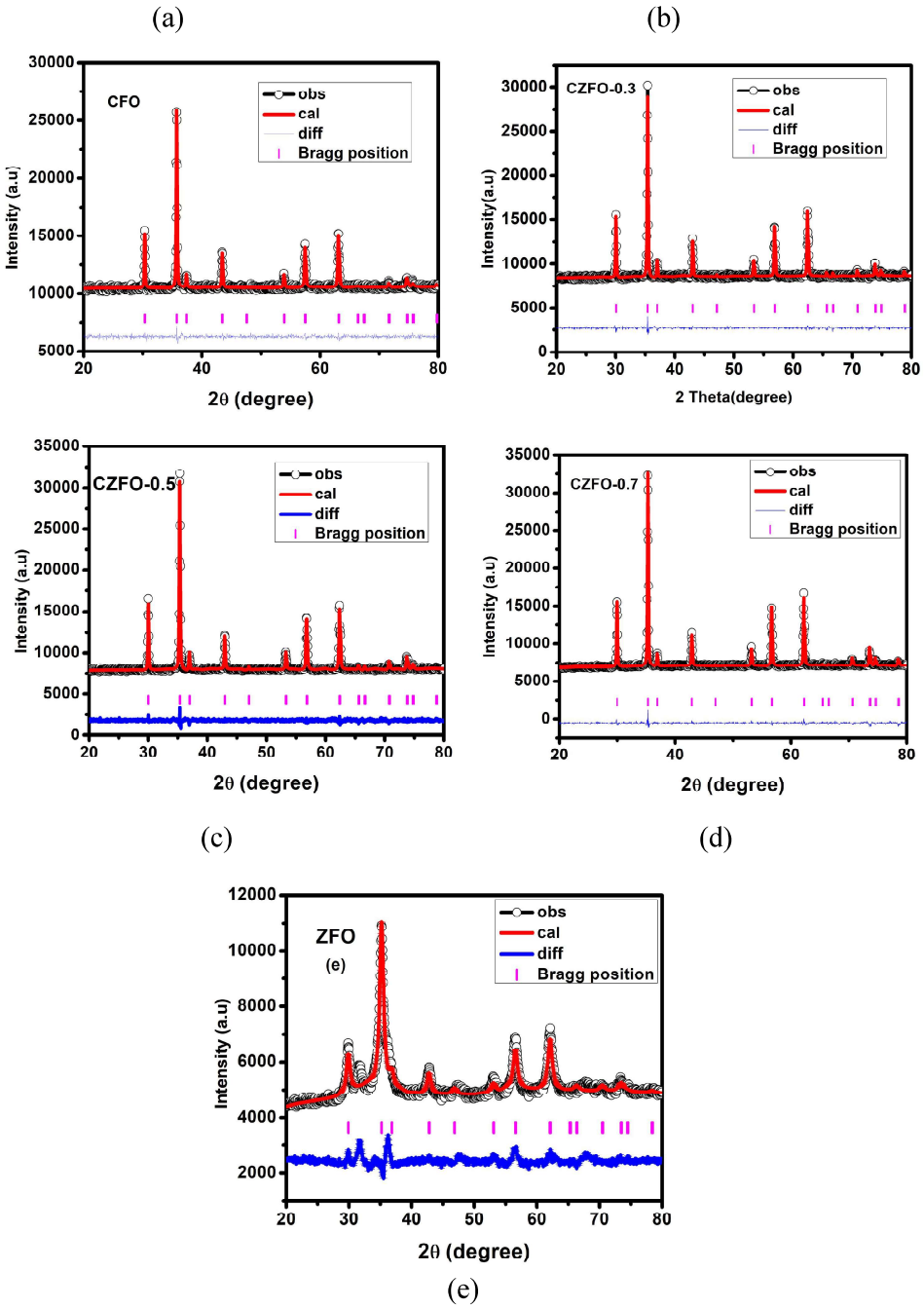

Fig 4.2 Rietveld refinement data for (a) CFO (b) CZFO-0.3 (c) CZFO-0.5 (d) CZFO-0.7 (e) ZFO samples

Figure 4.3 illustrates the Co^{2+} and Fe^{3+} atomic locations for cobalt ferrite nanoparticles in the tetrahedral (A) and octahedral (B) sites using the VESTA programme.

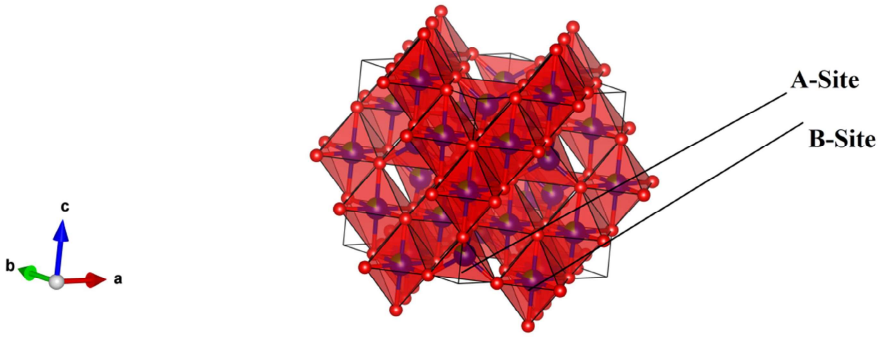

Fig 4.3. Atomic positions of Co^{2+} and Fe^{3+} in the tetrahedral and octahedral sites for $CoFe_2O_4$ nanoferrite.

4.3.2 Morphological and Compositional analysis

The surface morphology of the CZFO-0.5 nano ferrite samples were carried out using a high-resolution scanning electron microscope (SEM). SEM pictures of the CZFO-0.5 nanoparticles in Figure 4.4 demonstrate their excellent agglomeration. The agglomeration is because of the magnetic dipole-dipole interaction[8]. The image shows the sample is well crystallized[9].

[8] Andhare et al. 2020
[9] Iqbal et al. 2019

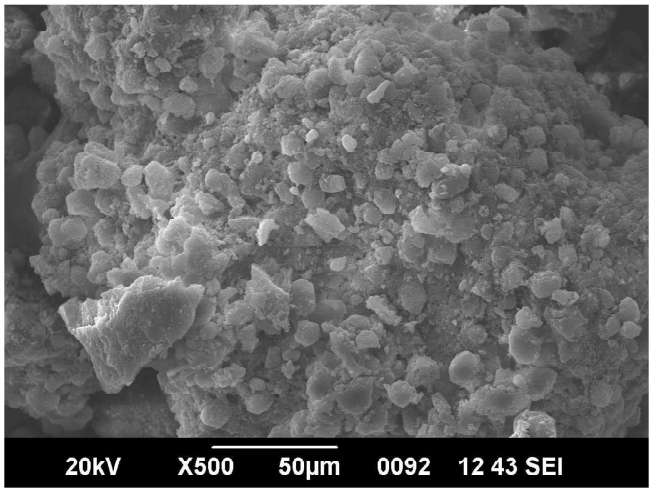

Fig 4.4. The SEM image of the CZFO-0.5 sample

Elemental analysis on the CZFO-0.5 sample was performed using EDAX which is depicted in Figure 4.5. The values obtained from the EDAX investigation are 0.2576 and 0.2693, respectively, whereas the expected stoichiometric ratio of Co: Fe and Zn: Fe is 0.25. It is evident that the predicted stoichiometry and the expected values correspond well.

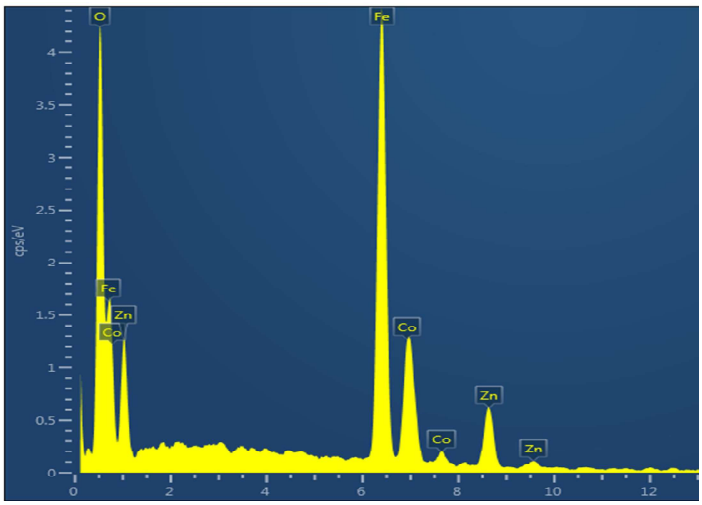

Fig 4.5.EDAX spectrum of CZFO-0.5 sample

4.3.3 Electrical properties

4.3.3.1 Variation of dielectric constant with frequency

HP 4285 LCR meter was used to measure the change of samples' ac conductivity and dielectric constant (έ) with frequency in the range 100 kHz to 5 MHz at room temperature.

The formulae used to determine the dielectric constant and ac conductivity for the prepared samples are given in Section 2.4.1 of Chapter 2.

The relationship between the dielectric constant and frequency is seen in Figure 4.6. The dielectric constant is high at low frequencies and decreases with increasing frequency for all samples. The dielectric dispersion is a normal behavior representing the Maxwell-Wagner type of interfacial polarization agreeing on Koop's phenomenological theory. The preparation method, doping level, grain size, structural uniformity, density, etc. affects the dielectric characteristics. Ferrites have conducting grains and grain boundaries of poor conductivities. At first when we apply the electric field, the electrons try to align with the field and collide with the grain boundaries and this along with hopping process produces polarization. But beyond a frequency, Fe^{2+}/Fe^{3+} ion electron exchange is not field-dependent as it needs a finite time to arrange along the field direction and this is the reason for the decrease in polarization and hence the dielectric constant[10].

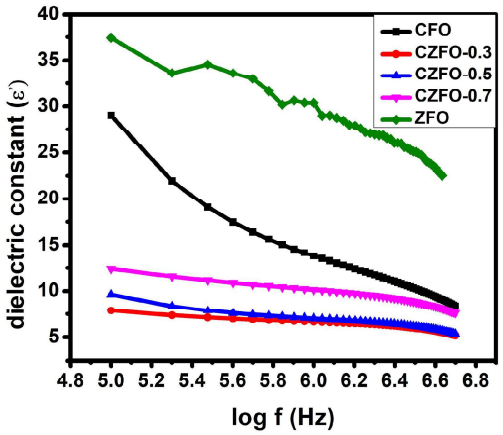

Fig 4.6. Change of dielectric constant with frequency for the nanoparticles $Co_{1-x}Zn_xFe_2O_4$ (x=0.0, 0.3, 0.5, 0.7, 1)

[10] Hossain et al. 2018

Following the substitution of zinc, the dielectric constant value initially declines but subsequently increases with zinc concentration, reaching its highest value for pure zinc ferrite. The measured dielectric constant for all samples in present study is less than the previously reported values[11]. The as-prepared $Co_{1-x}Zn_xFe_2O_4$ samples are promising candidates for technological applications such as gate dielectrics, capacitor dielectrics, and epitaxial dielectrics, etc[12].

4.3.3.2 Variation of ac conductivity with frequency

Figure 4.7 indicate room temperature variation of ac conductivity with frequency. The ac conductivity increases as the frequency increases. The cobalt ferrite has highly conducting grains separated by low conductivity grain boundaries. Because the grain boundaries are more active at lower frequencies, there is less electron hopping and less conductivity. Higher frequencies cause grains to be more energetic, which causes electrons to pass over grain borders. This enhances electron hopping and raises the ac conductivity. The Figure 4.7 also shows the decrease in ac conductivity with the increasing zinc substitution which is because of the decrease in the ratio of Fe^{2+}/Fe^{3+} ions which attribute to the decrement in electron hopping.

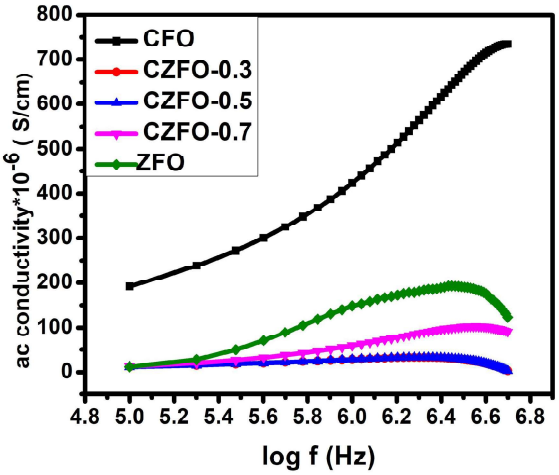

Fig 4.7. Variation of ac conductivity with frequency for the nanoparticles $Co_{1-x}Zn_xFe_2O_4$ (x=0.0, 0.3, 0.5, 0.7, 1)

[11] Andhare et al. 2020
[12] Singh & Ulrich 1999

Figure 4.8 illustrates the variation of dielectric constant and ac conductivity with composition. The dielectric constant is maximum for zinc ferrite whereas the ac conductivity is maximum for cobalt ferrite.

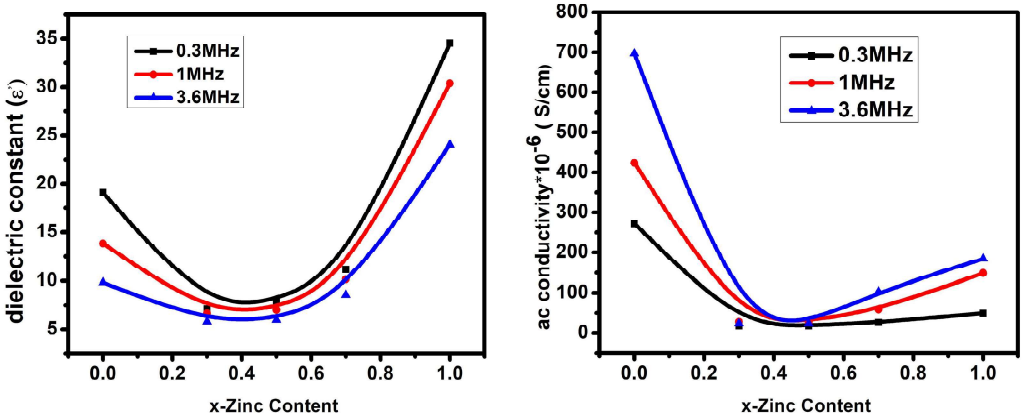

Fig 4.8. Variation of dielectric constant and ac conductivity with Zn content in CFO samples

4.3.4 Magnetic Properties

At temperatures 300K, the magnetic characteristics of the samples $Co_{1-x}Zn_xFe_2O_4$ (x=0.0, 0.3, 0.5, 0.7, 1) were assessed using a VSM in a Physical Property Measurement System (PPMS) from Quantum Design. Equations 4.10 is used to get the magneto-crystalline anisotropic constant (K).

$$H_C = \frac{0.96K}{M_S} \tag{4.10}$$

M_S stands for saturation magnetization and H_C is the coercivity.

The experimental magnetic moment is calculated using the equation 4.11.

$$n_B^e = \frac{M.M_S}{N_A \mu_B} \tag{4.11}$$

where M is molecular weight, M_s is the saturation magnetization, $N_A * \mu_B$ is a constant which is equal to 5585[13].

The value of Yafet and Kittel(Y-K) angle have been calculated using the formula 4.12.

$$n_B^e = M_B \cos \alpha_{YK} - M_A \qquad (4.12)$$

Here, M_A and M_B are the Bohr magneton on the A and B sites, respectively, and n_B^e is the experimental magnetic moment represented in Bohr magneton units.

Figure 4.9 displays the magnetic hysteresis (M-H) loops of the produced nanoparticles. $CoFe_2O_4$ exhibits ferromagnetic behaviour in the hysteresis loop, and doping with zinc ions modifies the magnetic characteristics to some extent. Table 4.3 presents the results of calculations and tabulations of magnetic properties, including saturation magnetization (M_s), remanent magnetization (M_r), coercivity (H_c), and magnetic moment (n_B).

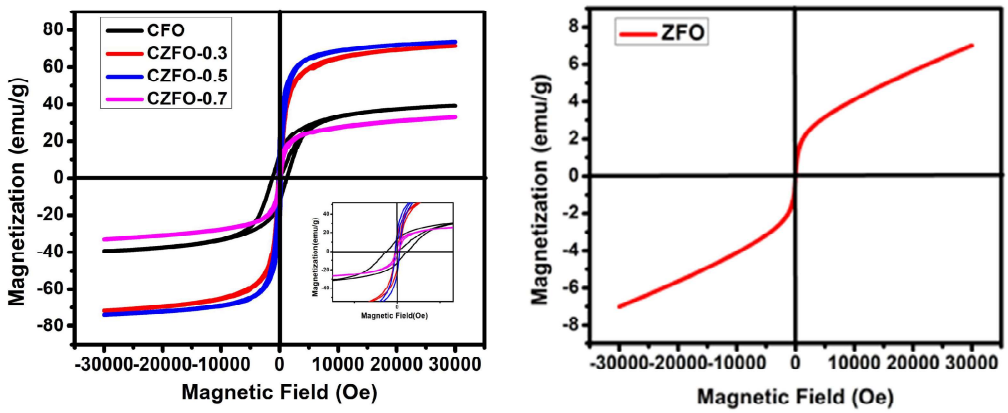

Fig 4.9. M-H curve for all $Co_{1-x}Zn_xFe_2O_4$ (x=0.0, 0.3, 0.5, 0.7, 1) samples

[13] Topkaya et al. 2013

Table 4.3. Observed magnetic parameters of the samples

Zn content (x)	M_S (emu/g)	M_r (emu/g)	M_r/M_S	H_c (Oe)	K (erg/g)	Magnetic moment n_B (μ_B)	α_{YK}
0	38.5	12.77	0.33	1209	48485	1.61	0
0.3	71.07	15.55	0.21	230	17027	3	34.63
0.5	73.72	19.51	0.26	219	16817	3.13	48.52
0.7	32.27	2.59	0.08	89	2991	1.38	71.54
1	7.06	0.124	0.02	4.17	30.66	0.304	88.25

Figure 4.10 depicts the fluctuation of saturation and remanent magnetization with zinc content. The Ms value first increases from 38.5 emu/g to 73.72 emu/g up to x=0.5 and then decreases with the zinc content increase. Neel's two-sublattice model explains the initial increase in magnetic moment up to x=0.5. The saturation magnetization value is found to be higher than the reported values for CZFO-0.3 and CZFO-0.5 samples[14]. The difference in saturation magnetization with zinc content is explained on the basis of the interaction between the ions in the tetrahedral (A) site and octahedral (B) site. The zinc ions and also Fe^{3+} ions have a tendency to occupy the tetrahedral (A) site compared to the octahedral (B) site. When the zinc ion with zero magnetic moments, is introduced into the system it pushes Fe^{3+} ions at the tetrahedral (A) site to the octahedral (B) site and the Zn^{2+} ions occupy at A-site[15]. This is the reason for increasing magnetization up to x=0.5. Then, because zinc ions are present, the A-site's magnetic moment drops and also the magnetic moment of the B-site increases due to the presence of Fe^{3+} ions. Then the total magnetization M_{oct}-M_{tet} of the CZFO samples increases on the basis of A-B super-exchange interaction. Similar results are reported by many authors[16]. Beyond x=0.5, the saturation magnetization decreases from

[14] Andhare et al. 2020
[15] Upadhyay et al. 2004
[16] Mahmood et al. 2022; Topkaya et al. 2013

73.72 emu/g to 7.06 emu/g[17]. This decrease in magnetic moment with increasing zinc concentration cannot be explained by Neel's collinear two-sublattice model. Yafet and Kittel's 1952 introduction of the three-sublattice model provides an explanation for this[18]. When x>0.5 i.e at higher concentration of zinc ions, the magnetic ions in the tetrahedral site decrease and the the strength of the B-B super-exchange connection increases while the A-B super-exchange interaction decreases. As a result, the B-site's random spin canting with respect to the A-site's spin direction occurs. This is the reason for the decrease in the value of magnetic moment for the value of x>0.5[19].

In accordance with the Y-K model, the B sublattice is split into two equal-magnitude sublattices, B_1 and B_2, which are both oppositely canted at the same angle with respect to net magnetization at 0K. Then the two sublattices have triangular spin arrangements which become more relevant with increasing zinc concentration. The presence of canted spin and the magnetic moment's behaviour as zinc content increases are determined by the Y-K angle. The value of the Y-K angle is calculated using equation 4.12 and tabulated in Table 4.3. The Y-K angle is found to increase with zinc concentration and becomes 88.25 for pure zinc ferrite. For x>0.5 the triangular spin arrangement on B-site leads to a decrease in saturation magnetization. An rise in frustration and randomness is observed, which greatly differs from the Neel-type collinear magnetic order. Cobalt ferrite nanoparticles in this study exhibit a Y-K type of magnetic ordering, with the exception of pure cobalt ferrite. Similar results are also available in some research works[20].

The magnetic ions at the A and B sub-lattices, which show super exchange interactions mediated by oxygen ions, are the main source of the magnetic order in spinel ferrites. According to Neel's two-sub-lattice model of ferrimagnetism, the ions' magnetic moments at the A and B sub-lattices have collinear spins and are not parallel. An increase in inter-sub-lattice interaction causes super-exchange (A-B) interactions between the magnetic ions over the A and B sub-lattices. According to Neel's collinear

[17] Topkaya et al. 2013
[18] Mazen & Abu-Elsaad 2012
[19] Topkaya et al. 2013
[20] Mahmood et al. 2022; Rana et al. 2003

two-sub lattice model, M_S rises with Zn^{2+} content. The Y-K angle can be used to study the presence of canted spin configuration and the behaviour of the magnetic moments as the Zn^{2+} content increases. When non-collinear spin structures are present at B-sites, B-B interactions increases while A-B interactions decreases, implies that the Neel two-sub-lattices model is not suitable to explain the magnetization behaviour of the $Co_{1-x}Zn_xFe_2O_4$ nanocrystalline system. The preference for the triangular spin configurations at B-site is evident from the increase in canted spin angles, or Y-K angles , which is observed with the doping of Zn^{2+}concentrations. Consequently, there was a decrease in exchange contacts (A-B) and canted-spin configurations were seen in all of the samples.

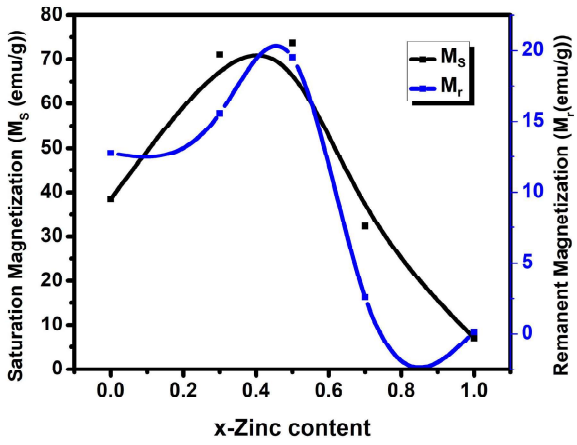

Fig 4.10. Saturation magnetization and remanent magnetization with zinc content

The nanocrystalline structure is confirmed by the M-H plot, which displays a high coercivity value. Equation 4.10 was utilised to compute the coercivity. Figure 4.10 demonstrates how coercivity falls down as zinc content rises. This is due to the substitution of non-magnetic zinc ions on cobalt ferrite, which is magnetic. The A-B magnetic interaction decreases due to the substitution of nonmagnetic zinc[21].

[21] Prabagar et al. 2021

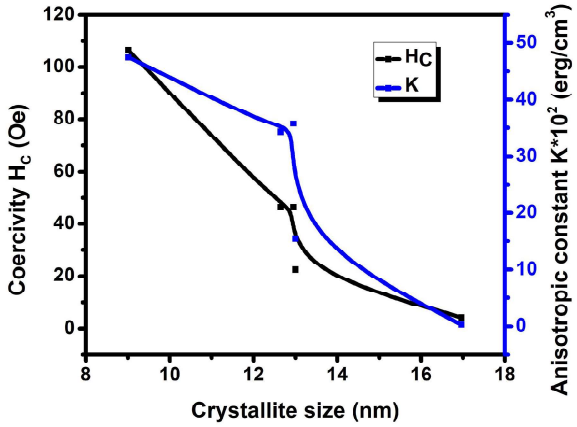

Fig 4.11. Coercivity and anisotropic with zinc content

Figure 4.12 shows the zero-cooled (ZFC) and field-cooled (FC) magnetization curves of $Co_{0.3}Zn_{0.7}Fe_2O_4$ samples in the temperature range of 50-300K.

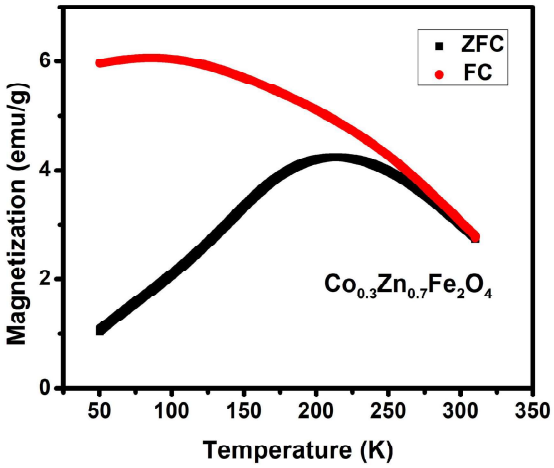

Fig 4.12. Zero-Cooled (ZFC) and Field-Cooled (FC) curves of $Co_{0.3}Zn_{0.7}Fe_2O_4$ samples

The sample was first cooled down in the absence of an external magnetic field, and then its magnetization (M_{ZFC}) was measured as it heated to 300K. Then the CZFO-0.7 sample was cooled down and then the magnetization (M_{FC}) was recorded during heating up to 300K. M_{ZFC} rises with temperature and reaches its maximum value at a particular temperature known as the blocking temperature (T_B). The M_{ZFC} falls with rising temperature above T_B. This is the specific feature of superparamagnetic behavior. The value of T_B for the sample is around 210K.

The value of the remanent magnetization and coercive field of CZFO-0.7 and ZFO nanoparticles indicate its superparamagnetic nature. The M_r/M_S is found to be decreasing with increasing zinc concentration and it is found to be nearly zero for x=0.7 and 1. This is explained by decreasing magnetic anisotropy with increasing zinc concentration. Stoner-Wohlfarth model explains non-interacting 3D random particle have M_r/M_S value is 0.832 for cubic anisotropy and 0.5 for uniaxial anisotropy. The reduced remanent magnetization for all samples gives agreement with uniaxial anisotropy[22].

4.3.5 Photocatalytic Activity Studies

The photocatalytic activity of the set of cobalt ferrite and zinc doped cobalt ferrite samples are evaluated by the degradation of methylene blue (MB) dye under sunlight irradiation. Figure 4.13 shows the absorption spectra of the MB solution containing the sample as photocatalyst from 200 to 750 nm with time step of 60 min. The preparation methods are given in section 2.10 of Chapter 2.

A steady drop in the color was found with increasing irradiation time for the MB solution which is original blue colored, with the presence of photocatalysts. According to Beer Lambert's law, dye concentration and absorbance maxima are directly correlated. Time-dependent absorption spectra of the MB dye solution are displayed in Figure 4.13 with CZFO-0.7 and CFO had the absorbance peaks at 664 nm and the secondary peaks at 610 nm and 290 nm. The intensity of absorbance peak was found to decrease with increasing irradiation time without change in shape or position. The elimination of chromophoric group is the reason for the decrease in the intensity at 664 nm. That no additional chromophore molecule was created as a byproduct was proven by the absence of additional peaks in the UV-VIS spectra[23].

[22] Stoner 1948
[23] N et al. 2023

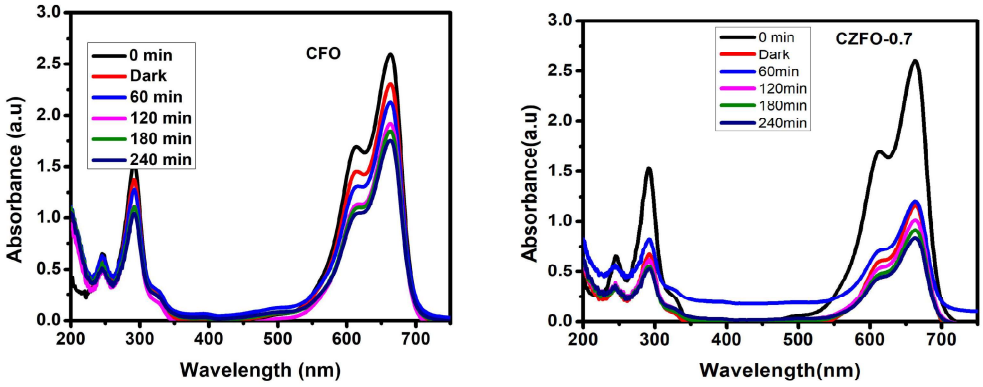

Fig 4.13 Time-dependent absorption spectra of the MB dye solution under visible light for CFO and CZFO-0.7.

The degradation of MB can be defined by the degradation efficiency, $(C_0\text{-}C)/C_0$, where C is the change in dye's concentration at predetermined intervals of time, and C_0 is the initial dye concentration at time t = 0. This can also be expressed in terms of absorbance as $(A_0\text{-}A)/A_0$ where A is the absorbance of the MB solution containing the sample after photocatalytic degradation.

Percentage dye degradation was studied for all the catalysts and is plotted in Figure 4.14. The recombination of photo-induced e^-/h^+ pairs limits the photocatalytic activity of cobalt ferrite. To avoid recombination rate of cobalt ferrite attempts are made to dope with Zn^{2+} ions for improve photocatalytic activity. The inhibition of e^-/h^+ pairs recombination and the creation of Fermi energy levels below the conduction band are the causes of the increasing photodegradation. The degradation percentage is calculated using the equation $(\frac{c_0-c}{c_0}) * 100$. Here, C_0 represents the dye's starting absorbance (A_0) at time t = 0, and C represents the change in dye's absorbance (A) at predetermined time intervals. The dye degradation percentage of all the samples under the present study is also given in Table 4.4. From the table the following inference can be obtained. The degradation of CFO and CZFO-0.7 reached 33% and 68% respectively. It is also evident that the zinc doping has effect on the catalytic activity of cobalt ferrite.

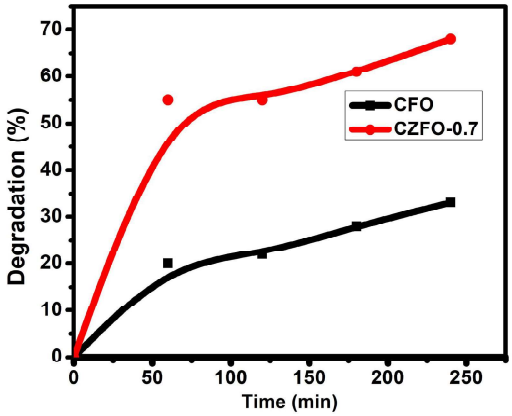

Fig 4.14 Photocatalytic activity for samples.

Table 4.4. Dye Degradation percentage for the CFO and CZFO-0.7 samples

Time of irradiation in minutes	CFO	CZFO-0.7
0	0	0
60	20	55
120	22	55
180	28	61
240	**33**	**68**

4.3.5.1 Kinetic Study of Photodegradation

Using the Langmuir-Hinshelwood model, the kinetic performance of CZFO samples for MB degradation was computed and fitted. This model fits the pseudo-first order kinetic model, which explains the rate constant of MB photodegradation as shown in Figure 4.15, which depicts the chemical kinetics for MB dye degradation.

$$\ln\frac{c_0}{c_t} = kt \qquad (4.13)$$

The slope of the linear fit plot of $\ln\frac{c_0}{c_t}$ v/s irradiation time gives degradation rate constant. All graphs of $\ln\frac{c_0}{c_t}$ v/s time were fitted linearly and the fitted curves are given

in Figure 4.15. Slope of the linear fit called the rate constant was obtained and is tabulated in Table 4.5. Under visible light irradiation, the photocatalytic activity for doped samples shows superior activity when compared to pure cobalt ferrite. The photocatalytic activity increases with doping. Efficiency of photocatalyst decreases because of the fast recombination of e^-/h^+ pairs after reaching its optimal limit. After crossing the optical limit of zinc doping the space charge barrier become greater. Hence recombination of photo-generated e^-/h^+ pairs become more easier this is the reason for the efficiency of photodegradation decreases. In the photocatalytic process deformation generated is more for doped samples compared to pure cobalt ferrite[24].

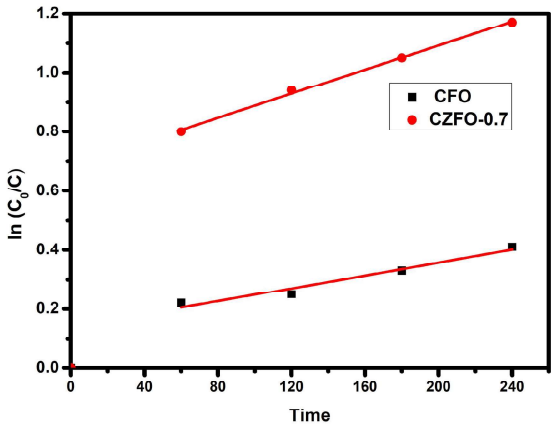

Fig 4.15 Kinetic plots and Linear fit for dye degradation by CFO and CZFO-0.7.

Table 4.5. Rate constant of MB dye in the presence of CZFO samples as photocatalyst

Sample	Rate constant ($k*10^{-2}$ min^{-1})
CFO	0.10
CZFO0.7	0.20

4.3.6 In Vitro Cytotoxicity

Using Dalton's Lymphoma Ascites cells (DLA), the short-term in vitro cytotoxicity of the produced cobalt ferrite nanoparticles was investigated. For the investigation, tumour cells that were extracted from the peritoneal cavity of mice that

[24] Madhukara Naik et al. 2019

carried tumours were employed. Three rounds of phosphate buffered saline (PBS) or normal cell line washing were performed on the tumour cells that emerged from the peritoneal cavity of mice that carried the tumour. Trypan blue exclusion was utilised to determine the vitality of the cells.Tubes holding various concentrations of the test substances were filled with a suspension of viable cells ($1*10^6$ cells in 0.1 ml), and the volume was increased to 1 ml using phosphate buffered cell line (PBS). There was only cell suspension in the control tube. The array mixture was incubated at 37^0C for three hours. After adding 0.1 ml of 1% trypan blue to the additional cell solution, it was stored for two to three minutes before being placed into a hemocytometer. Trypan blue dye is taken up by dead cells, but it is not taken up by living cells. Separate counts were made of the number of stained and unstained cells. The fluctuation of cancer cell cytotoxicity (%) with sample concentration is shown in Figure 4.16. The substance exhibits around 41.5% cytotoxicity against tumour cells at 200 µg/mL, making it a biocompatible anti-cancer medication.

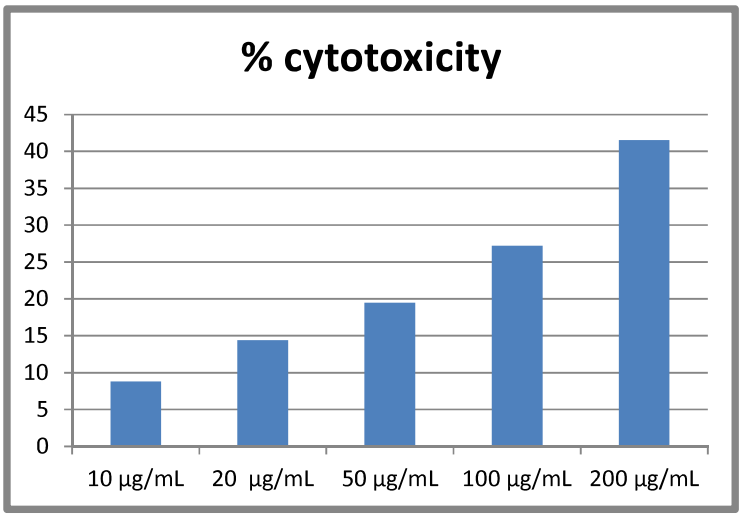

Fig 4.16. % cytotoxicity as a function of cobalt ferrite concentration.

The effect of ($CoFe_2O_4$) NPs on C127I breast cancer cells lines (Fig 4.17) indicated that exposure of the breast cell lines to $CoFe_2O_4$ NPs led to a marginal decrease in the cell viability and the relative cell viability reached 21.41 %. The National Centre for Cell Sciences in Pune, India provided the mouse breast cancer cell line (C127I), which was cultured in DMEM media with 10% foetal bovine serum, 100

µg/mL penicillin, and 100 µg/mL streptomycin as supplements. The cell line was maintained at 37 °C in an incubator with 5% CO_2. The media was replaced every third day when the cells were passaged at 80–90% confluency. Using the MTT (3-(4,5-Dimethylthiazol-2-yl)-2,5-Diphenyltetrazolium Bromide) assay, the cytotoxicity of the test materials was assessed.

In a 24 well plate, $1x10^5$ cells/mL were planted with full growth media (DMEM) and allowed to adhere and proliferate. After the medium reached 80% confluency, fresh media was added with varying sample concentrations (0-100 µg/mL) and incubated for a full day. The medium was once more changed out with new medium at the conclusion of the incubation period. Following the addition of 40 µL of 5 mg/mL MTT, each well was incubated for 4 hours. After dissolving the formazan crystals in dimethyl sulfoxide, the absorbance was measured in an ELISA microplate reader (BioTek, USA) at 570 nm.

The percentage viability was calculated using the formula; Figure 4.18 represents the percentage of inhibition with the vehicle control.

$$\%\ viability\ = \frac{Ab\ of\ sample}{Ab\ of\ control} \times 100 \qquad (4.14)$$

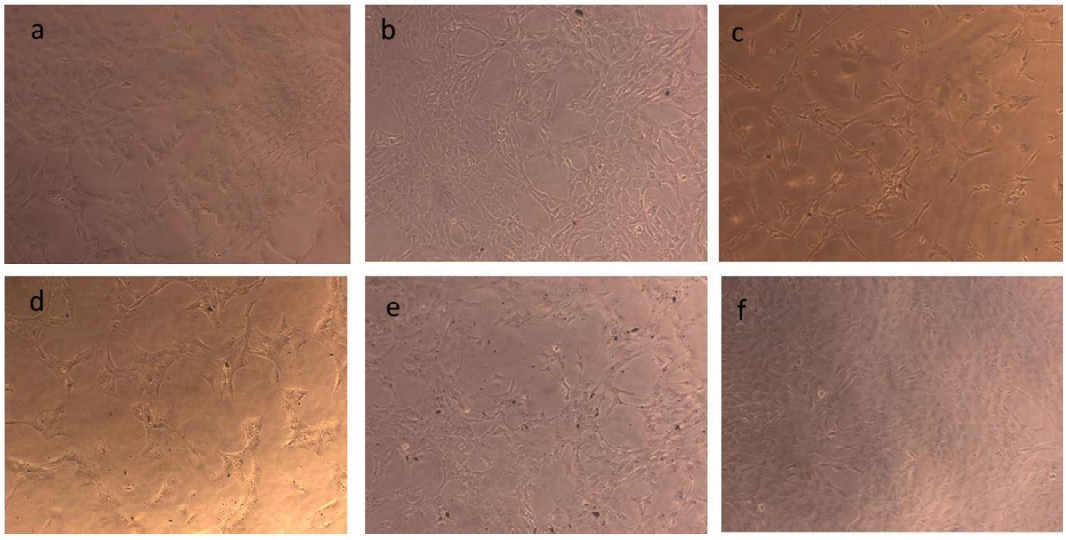

Fig 4.17: Photos of C127I breast cancer cells (a) control (b) after incubation with 6.25 μg/mL ($CoFe_2O_4$) NPs by optical microscope, (c) 12.5 μg/mL ($CoFe_2O_4$) NPs ,(d) 25 μg/mL ($CoFe_2O_4$) NPs ,(e) 50 μg/mL ($CoFe_2O_4$) NPs and (f) Vehicle control.

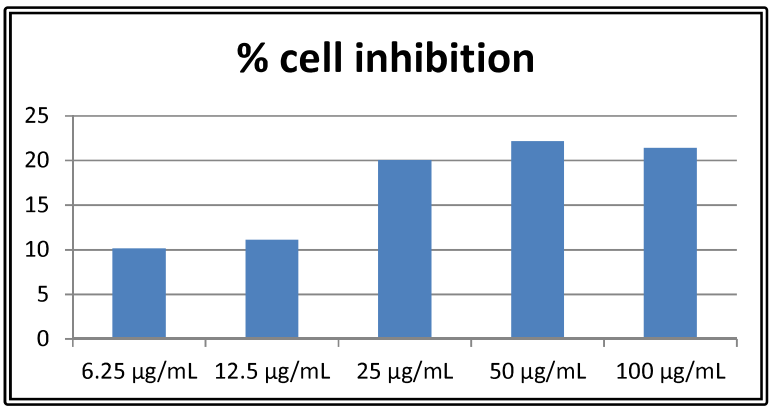

Fig 4.18: Evaluation of inhibition using cobalt ferrite NPs

It is well documented that the effect of a compound on tumor cells is mainly due to their oxidative stress effects. Tumor cells may, however, be dependent on a certain amount of hydrogen peroxide and the deficiency of hydrogen peroxide may resulted in cell cycle arrest or apoptosis of these cells (Loo, 2003). Horev-Azaria et al. (2013) found, in keeping with the present findings, that the survivability of cell-lines towards ($CoFe_2O_4$) NPs may be mostly ascribed to their capacity to interact with NPs in the event of either the NPs' adsorption to the cell surface or their uptake by the cells. Furthermore, Nel et al. (2006) stated that the most significant mechanism of NPs-induced hazardous effects is oxidative stress, which is characterised as the imbalance between antioxidant defences and the generation of reactive oxygen species (ROS) or reactive nitrogen species (RNS). Horev-Azaria et al. (2013) discovered a strong linear relationship between the quantity of reactive oxygen species (ROS) produced after being exposed to ($CoFe_2O_4$) NPs and the toxicity of the NPs. According to earlier research, NPs have the ability to produce ROS, deplete natural antioxidant reserves, interfere with mitochondrial activity, and cause oxidative damage to lipids and DNA (Moller et al., 2010). As a result, NPs-induced ROS activation boosts the antioxidant defence response elements. If damage continues, the protective systems trigger intracellular signalling triggered by NF-κB and protein kinase, which releases pro-inflammatory cytokines, matrix metalloproteinase, and chemokines, ultimately leading to apoptosis (Shubayev and Pisanic, 2009)[25].

[25] Mosmann 1983

Rat spleen cells were used to investigate the test compound's short-term in vitro cytotoxicity. Using carbon dioxide anaesthesia, the spleen tissue of the rat was taken. After that, it was broken up into a single cell suspension in antibiotic-containing RPMI complete medium and filtered through mesh cloth. After three rounds of washing, the recovered cells were suspended in a predetermined volume of RPMI complete media with antibiotics and then tallied. Tubes holding different concentrations of the test chemical were filled with viable cell suspension ($1X10^6$cells in 0.lml), and the volume was increased to l ml using RPMI medium. Only cell suspension (no additions) was present in the control tubes. For three hours, these tubes were incubated at 37^0C. After the incubation period, the cell suspension in the tubes was combined with 0.1 % trypan blue, allowed to stand for two to three minutes, and then put into a hemocytometer. Trypan blue dye is taken up by dead cells, but it is not taken up by living cells. A different count was made of the labelled cells.

$$\%\ cytotoxicity\ = \frac{No.of\ dead\ cells}{No.of\ live\ cells + No.of\ dead\ cells} * 100 \qquad (4.15)$$

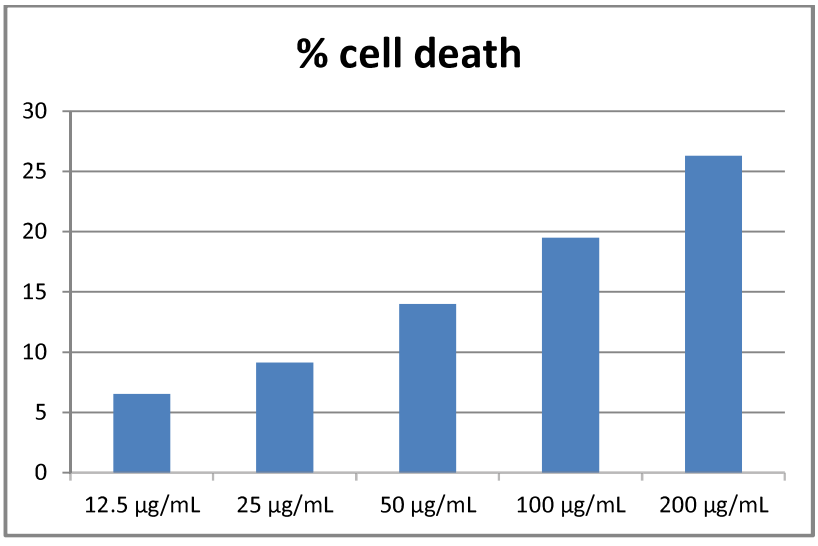

Fig 4.19: % cell death using cobalt ferrite NPs

4.4. Conclusions

$Co_{1-x}Zn_xFe_2O_4$ (x=0.0,0.3,0.5,0.7,1) nanoparticles have been successfully prepared by modified sol-gel method, with citric acid as fuel. With increasing zinc content, samples showed a drop in crystallite size and an increase in lattice parameter, which is explained by the sizes of the component ions. Rietveld refinement established that the samples synthesized have a cubic spinel structure with *an Fd-3m* space group and small variation in the lattice constant (8.33Å to 8.45Å) with the increasing the zinc concentration. The frequency-dependent dielectric response can be explained by the Maxwell-Wagner two-layer model hypothesis. All samples showed a high value for the dielectric constant, which can be applied to capacitor dielectrics, gate dielectrics, and epitaxial dielectrics. At 300K, the magnetic characteristics were investigated. The increasing of saturation magnetization up to x=0.5 was explained by Neel's collinear two-sublattice model and then decreasing was explained using three-sublattice model of Yafet and Kittel. The coercive field and Mr/M_s continuously decreased with increasing Zn concentration. The ZFC-FC curve and hysteresis loops of CZFO-0.7 indicate the superparamagnetic behavior. The lower value Mr/M_s shows the uniaxial anisotropy and this material can be used for biomedical applications. The degradation of methylene blue under sunlight in the presence of catalyst CZFO samples are investigated by studying the absorption intensities of the solution containing the photocatalysts after exposure to sunlight for known durations. The time of irradiation was varied and a maximum time of 240 minutes exposure to sunlight was given to all samples. This indicates that cobalt zinc ferrite can act as an efficient photocatalyst and also the advantage of using these as photocatalyst is that after dye degradation the catalyst can be removed easily by using a magnetic field. The cytotoxicity studies confirm that cobalt ferrite nanoparticles have potential cytotoxic activity.

References

Andhare, D. D., Patade, S. R., Kounsalye, J. S., & Jadhav, K. M. (2020). Effect of Zn doping on structural, magnetic and optical properties of cobalt ferrite nanoparticles synthesized via. Co-precipitation method. *Physica B: Condensed Matter*, *583*. https://doi.org/10.1016/j.physb.2020.412051

Hossain, M. S., Alam, M. B., Shahjahan, M., Begum, M. H. A., Hossain, M. M., Islam, S., Khatun, N., Hossain, M., Alam, M. S., & Al-Mamun, M. (2018). Synthesis, structural investigation, dielectric and magnetic properties of Zn2+-doped cobalt ferrite by the sol-gel technique. *Journal of Advanced Dielectrics*, *8*(4), 2–7. https://doi.org/10.1142/S2010135X18500303

Iqbal, S., Fakhar-e-Alam, M., Atif, M., Amin, N., Alimgeer, K. S., Ali, A., Aqrab-ul-Ahmad, Hanif, A., & Aslam Farooq, W. (2019). Structural, morphological, antimicrobial, and in vitro photodynamic therapeutic assessments of novel Zn+2-substituted cobalt ferrite nanoparticles. *Results in Physics*, *15*(July), 102529. https://doi.org/10.1016/j.rinp.2019.102529

Krishna, K. R., Kumar, K. V., & Ravinder, D. (2012). Structural and Electrical Conductivity Studies in Nickel-Zinc Ferrite. *Advances in Materials Physics and Chemistry*, *02*(03), 185–191. https://doi.org/10.4236/ampc.2012.23028

Lin, Q., Xu, J., Yang, F., Lin, J., Yang, H., & He, Y. (2018). Magnetic and Mössbauer spectroscopy studies of zinc-substituted cobalt ferrites prepared by the sol-gel method. *Materials*, *11*(10), 1–12. https://doi.org/10.3390/ma11101799

Madhukara Naik, M., Bhojya Naik, H. S., Nagaraju, G., Vinuth, M., Vinu, K., & Viswanath, R. (2019). Green synthesis of zinc doped cobalt ferrite nanoparticles: Structural, optical, photocatalytic and antibacterial studies. *Nano-Structures and Nano-Objects*, *19*, 100322. https://doi.org/10.1016/j.nanoso.2019.100322

Mahmood, A., Maqsood, A., & Abdi, A. (2022). Effect of manganese doping on the structural, mechanical, optical, and magnetic properties of zinc ferrite nanoparticles. *Physica Scripta*, *97*(6), 65707. https://doi.org/10.1088/1402-4896/ac6f2a

Mazen, S. A., & Abu-Elsaad, N. I. (2012). Structural and some magnetic properties of manganese-substituted lithium ferrites. *Journal of Magnetism and Magnetic Materials*, *324*(20), 3366–3373. https://doi.org/10.1016/J.JMMM.2012.05.056

Mosmann, T. (1983). Rapid colorimetric assay for cellular growth and survival: application to proliferation and cytotoxicity assays. *Journal of Immunological Methods*, *65*(1–2), 55–63. https://doi.org/10.1016/0022-1759(83)90303-4

N, A., Philip, R. S., & Mathew, M. (2023). Photocatalytic activities of SnS thin films deposited at room temperature. *Applied Surface Science Advances*, *13*(September 2022), 100374. https://doi.org/10.1016/j.apsadv.2023.100374

Prabagar, C. J., Anand, S., Janifer, M. A., & Pauline, S. (2021). Structural and magnetic properties of Mn doped cobalt ferrite nanoparticles synthesized by Sol-Gel auto combustion method. *Materials Today: Proceedings*, *47*(July), 2013–2019. https://doi.org/10.1016/j.matpr.2021.04.209

Rana, M. U., Misbah-ul-Islam, & Abbas, T. (2003). Magnetic interactions in Cu-substituted manganese ferrites. *Solid State Communications*, *126*(3), 129–133. https://doi.org/10.1016/S0038-1098(02)00908-0

Singh, R., & Ulrich, R. K. (1999). High and low dielectric constant materials. *Electrochemical Society Interface*, *8*(2), 26–30.

Stoner, B. E. C. (1948). *A M E C H A N IS M O F M A G N E T IC H Y S T E R E S IS IN*. *826*(May), 599–642.

Sugimoto, M. (1999). The Past, Present, and Future of Ferrites. *Journal of the American Ceramic Society*, *82*(2), 269–280. https://doi.org/10.1111/j.1551-2916.1999.tb20058.x

Supriya, S., Kumar, S., & Kar, M. (2018). Band gap engineering of zinc substituted cobalt ferrite for optoelectronic applications. *2017 IEEE 12th Nanotechnology Materials and Devices Conference, NMDC 2017*, *2018*-*Janua*(October), 33–34. https://doi.org/10.1109/NMDC.2017.8350491

Topkaya, R., Baykal, A., & Demir, A. (2013). Yafet-Kittel-type magnetic order in Zn-substituted cobalt ferrite nanoparticles with uniaxial anisotropy. *Journal of Nanoparticle Research*, *15*(1). https://doi.org/10.1007/s11051-012-1359-6

Upadhyay, C., Verma, H. C., & Anand, S. (2004). Cation distribution in nanosized Ni-Zn ferrites. *Journal of Applied Physics*, *95*(10), 5746–5751. https:// doi.org/10.1063/1.1699501

V.S, S., Gopalan, V. E., Al-Omari, I. A., & Malini, K. A. (2022). Superparamagnetic Nickel Ferrite Nanoparticles Doped with Zinc by Modified Sol–gel Method. *Journal of Superconductivity and Novel Magnetism 2021*, 1–10. https://doi.org/10.1007/S10948-021-06110-7

Chapter 5

STRUCTURAL, ELECTRICAL, MAGNETIC AND OPTICAL STUDIES ON STRONTIUM DOPED BISMUTH FERRITE NANOPARTICLES

STRUCTURAL, ELECTRICAL, MAGNETIC AND OPTICAL STUDIES ON STRONTIUM DOPED BISMUTH FERRITE NANOPARTICLES

This chapter essentially discuss the structural, electrical and magnetic characterisation of strontium substituted multiferroic bismuth ferrite (BFO) nanoparticles with general formula, $Bi_{1-x}Sr_xFeO_3$ (x=0.0,0.3,0.5 and 0.7) synthesized by modified sol-gel auto-combustion process. The structural analysis is carried out by X-ray powder diffraction technique. Morphological analyses of the prepared samples are carried out using scanning electron microscopy (SEM). Frequency-dependent dielectric constant and ac conductivity have been studied. The effects of strontium substitution on the magnetic properties of bismuth ferrite have also been studied in detail. The sharp and strong photoluminescence in the IR region is observed in the samples similar to ZnO, which is reported for the first time. The photo degradation studies of $BiFeO_3$ and $Bi_{0.5}Sr_{0.5}FeO_3$ samples were evaluated for the degradation of methylene blue dyes under visible light irradiation.

Part of this chapter have been published in

Structural Evolution –Enabled $BiFeO_3$ modulated by strontium doping with enhanced dielectric, optical and superparamagnetic properties by modified sol-gel method. Sharon V.S, Veena Gopalan E, Malini K A (Chinese Phys. B 32 037504, 2023 https://doi.org/10.1088/1674-1056/ac785b (IF-1.652)

5.1 Introduction

Bismuth ferrite $BiFeO_3$ (BFO) is an environmentally friendly material and is a notable member of the multiferroic family in which both ferroelectricity and anti-ferromagnetism coexist[1]. BFO has a deformed perovskite structure that is rhombohedral and has the space group R3c at room temperature[2]. Despite its high conductivity and antiferromagnetic nature due to charge defects[3], BFO has limited utility in various devices owing to weak magnetoelectricity caused by its spatially periodic nonhomogeneous spin structure. Weak magnetism is due to the spin cycloid magnetic moment and the reduction of Fe^{3+} to Fe^{2+} which results the creation of oxygen vacancies contribute to leakage current. For minimizing this leakage current the substitution of rare earth and transitional metal atoms is attempted at the bismuth ferrite A and B sites. Therefore, introducing dopants can enhance its potential[4], and the synthesis procedure significantly influences the magnetic and structural properties of $BiFeO_3$ nanoparticles. Recent investigations have also shown that BFO is an excellent visible light responsive photo-catalytic material due to its band gap of 2 eV and remarkable chemical stability.

Several reports have shown that suitable alkaline earth metal substitution in BFO can notably improve its physical properties. By substituting cations at the Bi site, one can enhance the properties of BFO. Many scientists have utilized rare earth metal and alkaline earth metal ions (such as Mg, Ca, Ba, Sr, etc.) to enhance the multiferroic properties of BFO[5]. Strontium (Sr) is a suitable choice for substitution at the bismuth site due to its close ionic radius to that of bismuth (1.18 Å and 1.03 Å, respectively). This substitution leads to a charge imbalance that can be compensated through the creation of oxygen vacancies. The oxygen vacancies are created as a

[1] Khomchenko et al. 2008
[2] Soibam & Devadatta Mani 2018
[3] Ahlawat et al. 2014
[4] Costa et al. 2014
[5] Anju et al. 2017; Hussain et al. 2013

result of Sr^{2+} doping to overcome charge discrepancy[6] of Fe^{3+} and Fe^{5+}, and partial transformation of Fe^{3+} to Fe^{4+}.

Synthesizing pure BFO without impurities is a challenging task. This chapter focuses on the synthesis of strontium-substituted bismuth ferrite nanoparticles and examines the effect of Sr^{2+} on their structural, electrical, magnetic, optical and photocatalytic properties. The prepared samples are labeled as BFO, BSFO-0.3, BSFO-0.5, and BSFO-0.7, corresponding to $BiFeO_3$, $Bi_{0.7}Sr_{0.3}FeO_3$, $Bi_{0.5}Sr_{0.5}FeO_3$, and $Bi_{0.3}Sr_{0.7}FeO_3$, respectively.

5.2 Synthesis

Bismuth ferrite (BFO) nanoparticles and strontium doped bismuth ferrite nanoparticles (BSFO) ($Bi_{1-x}Sr_xFeO_3$ (x=0.0, 0.3, 0.5, 0.7)) were synthesized by modified Sol-gel auto-combustion method. Precursors used for the synthesize $Bi_{1-x}Sr_xFeO_3$ nanoparticles were analytic grade bismuth nitrate, strontium nitrate, iron nitrate, and citric acid. Details of preparation technique are provided in Section 2.2.1. The impurity content was minimized by the leaching with nitric acid and washing the samples several times with distilled water. The prepared powder samples were mixed with 3% PVA and pressed into pellets of 12mm diameter by a hydraulic press. Then the pellets were sintered at 900^0C for 4 hours for the further studies.

5.3 Results and Discussion

5.3.1 X-ray diffraction analysis

The prepared samples were characterized by XRD on a Brucker AXS D8 X - Ray diffractometer using Cu-Kα radiation. The XRD pattern of $Bi_{1-x}Sr_xFeO_3$ series is depicted in Figure 5.1. The most intense peaks were matched with the PCPDF file (86-1518). The XRD pattern confirms the formation of a rhombohedral perovskite R-3c structure of bismuth ferrite. A secondary phase of bismuth ferrite $Bi_2Fe_4O_9$ is also present in the sample. The result is in very good agreement with the previously

[6] Ahlawat et al. 2014; Hegab et al. 2017

reported papers[7]. The X-ray diffractograms reveal that for samples x=0.3 and 0.5, the two peaks at 2θ value 31.4^0 and 32.25^0 are merged in to single peak at 2θ value 32.83^0 , This indicate a structural transformation from rhombohedral to cubic phase (space group, Pm-3m) which agrees with the previously reported results[8]. This may be due to the presence of Sr^{2+} cation that compensates for the evaporation of Bi^{3+} cation during the preparation (Pm-3m). The XRD pattern of BSFO-0.7 in Figure 5.1 shows that all peaks are marked to cubic space with the Fd3m space group. The diffraction peaks correspond to (220), (311), (400), (422), (511), and (440) crystal planes exhibited by the face-centered cubic crystal and are in good agreement with JCPDS-00-001-1121. The Bi^{3+} ions contains $6s^2$ lone pair electrons (Bi:[Xe] $4f^{14}5d^{10}6s^26p^3$). This polarized lone pair in bismuth ferrite causes the displacement of Bi^{3+} from its centro-symmetric position, and forming rhombohedral structure with space group R-3c. With the substitution of Sr^{2+} ions, this polar displacement can be suppressed by the emergence of oxygen vacancies whereby the lone pair electrons are directed into the vacancies. This leads to the development of a more symmetric environment around Bi^{3+} leading to cubic structure(Pm- 3m)[9].

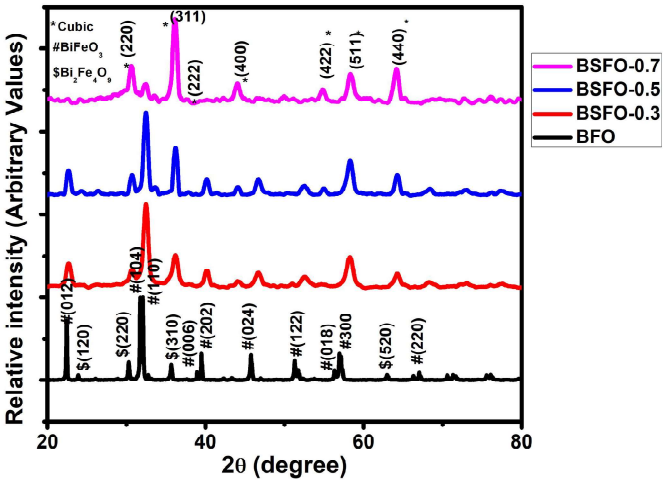

Fig 5.1 X-ray diffractograms of all the samples

[7] Ahmad et al. 2016
[8] Ma et al. 2022
[9] Hegab et al. 2015; S et al. 2022

The average crystallite sizes of the samples were obtained by Scherrer's formula given in Section 2.3.1[10].

The crystallite size calculated for the samples BFO, BSFO-0.3, BSFO-0.5 and BSFO-0.7 were 48.39nm, 10.03nm, 13.23nm, and 13.10 nm respectively. The variation of crystallite size with strontium content is shown in Figure 5.2. From the XRD pattern, lattice parameters for the synthesized samples were also calculated and tabulated in Table 5.1.

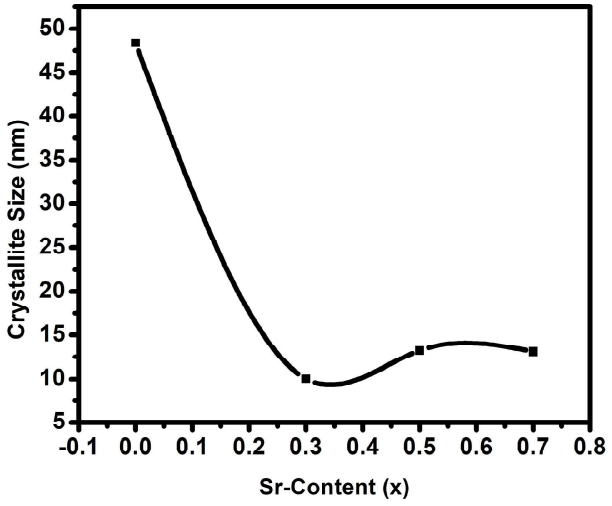

Fig 5.2 . Variation of crystallite size with Sr-content for all the samples

Table 5.1. Structural parameters of $Bi_{1-x}Sr_xFeO_3$ samples.

X	Space group	a=b=[Å]	c[Å]	V[Å^3]	X-ray density D_X (g cm^{-3})	Crystallite size (nm)
0	R-3c	5.51	13.8	362.03	11.47	48
0.3	Pm-3m	3.97	3.97	62.57	58.68	10
0.5	Pm-3m	3.97	3.97	62.57	53.53	13
0.7	Fd-3m	8.38	8.38	588.48	5.14	13

[10] Hussain et al. 2013

5.3.2 Microstructure Analysis

The morphology of the BFO nanoparticles was studied by using high resolution scanning electron microscope (SEM) and Energy Dispersive Spectroscopy(EDS). The SEM gives the information about the surface morphology of $BiFeO_3$ nanoparticles. SEM pictures of the BFO nanoparticles in Figure 5.3 demonstrate their excellent agglomeration. The agglomeration is because of the magnetic dipole-dipole interaction[11]. The image shows the sample is well crystallized[12]. Elemental analysis on the BFO sample was carried out using EDAX, which is shown in Figure 5.3. The expected stoichiometric ratio of Bi: Fe and Bi: O is 1 and 0.33, whereas the values obtained from the EDAX investigation are 0.75 and 0.30, respectively. It is evident that the predicted stoichiometry and the expected values correspond well.

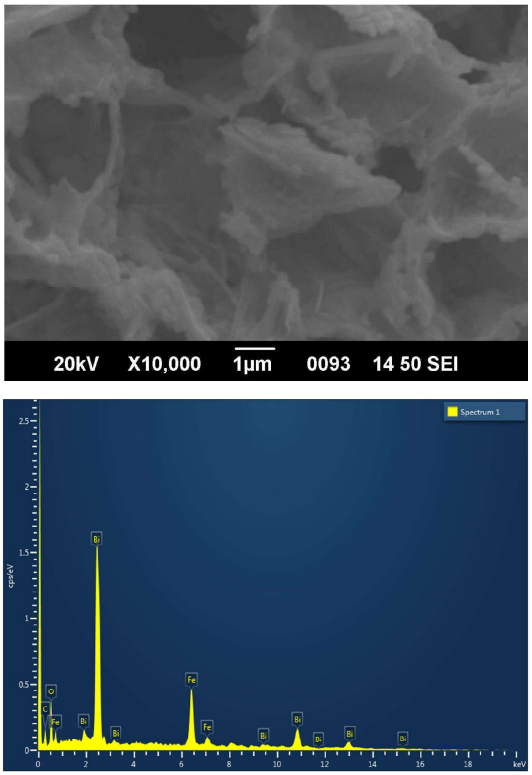

Fig 5.3 SEM and EDS image of BFO nanoparticles

[11] Andhare et al. 2020
[12] Iqbal et al. 2019

5.3.3 Electrical properties

5.3.3.1 Dielectric dispersion

HP 4285A LCR meter was used to measure the change of samples' ac conductivity and dielectric constant (ε) with frequency in the range 100 kHz to 5MHz at room temperature.

The formula used to determine the dielectric constant and ac conductivity for the prepared samples given in Section 2.4.1 of Chapter 2.

The variation of dielectric constant with frequency for the prepared samples is given in Figure 5.4. It is observed that the dielectric constant decreases with increasing frequency which is due to dielectric relaxation. According to Koop's theory, dielectric material has a double layer structure with one conducting and one insulating layer and the dielectric relaxation is because of orientational polarization[13]. The decreasing dielectric constant with frequency is also linked with the hopping of electrons from Fe^{2+} to Fe^{3+} ions.

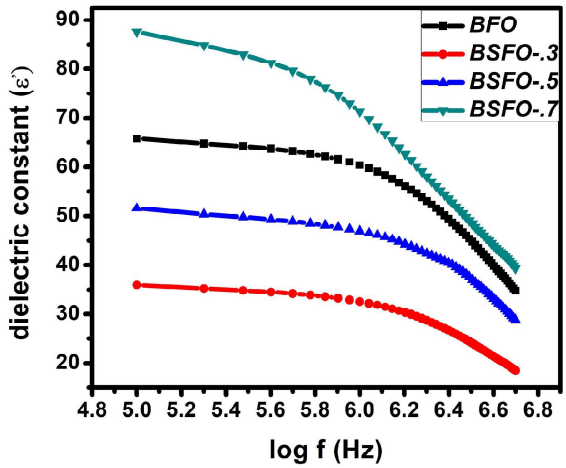

Fig 5.4: Variations of dielectric constant with frequency

Each dielectric material requires a finite time to align with its axis along the applied electric field. As frequency increases, a point reaches when the charge

[13] S et al. 2022

carriers do not align with the applied external electric field, so polarization cannot reach the saturation value and also does not follow the alternating electric field. This is the reason for the fast decrease in dielectric constant with frequency at larger frequencies[14]. In this research, the maximum value obtained for dielectric constant at low frequency is greater than the reported value of Sr doped bismuth ferrite[15]. All the samples possess a high dielectric constant value (~35-90) and hence are used in gate dielectrics and photoelectrochemical cells. Thus, these materials are important for technological applications[16].

5.3.3.2 Cole-Cole representation of dielectric data

The Debye equation for dielectric dispersion is given by

$$\varepsilon^* - \varepsilon_\infty = \frac{(\varepsilon_s - \varepsilon_\infty)}{(1+j\omega\tau)} \quad (5.1)$$

ε^* is the complex permittivity ε_s and ε_∞ are the values at limiting frequencies, i.e. the static dielectric constant and optical dielectric constant, $\omega=2\pi f_{max}$ and τ is the relaxation time. The Cole-Cole plots, in this case, are semicircular with the center on the real axis. For the materials possessing dielectric dispersion, a variation from ideal Debye behavior is observed, as there is the possibility of the existence of multiple relaxation times [17]. K.S Cole and R.H Cole suggested that in such case permittivity follows the empirical equation[18].

$$\varepsilon^* - \varepsilon_\alpha = \frac{(\varepsilon_s - \varepsilon_\alpha)}{1 + (j\omega\tau_0)^{1-\alpha}} \quad (5.2)$$

where τ_0 is the average relaxation time and α is the spreading factor of actual relaxation time τ about its mean value τ_0 and α lies in the range 0-1. A plot of ε″ for a certain frequency against ε′ at the same frequency in the complex plane is represented as a Cole-Cole plot. For α =0, the above equation reduces to Debye′s equation, for a dielectric with α=0 or single relaxation time the Cole-Cole plot is a

[14] Hussain et al. 2013
[15] Hussain et al. 2013
[16] S et al. 2022; Singh & Ulrich 1999
[17] *Dielectric relaxation [by] Vera V. Daniel. (Book, 1967) [WorldCat.org]* n.d.; Sagar et al. 2006
[18] S et al. 2022

semicircle, for α>0 the plot is a circular arc with its center lying below the real axis. The spreading factor α can be calculated from the expression for a maximum value of the imaginary part of permittivity[19].

$$\varepsilon''_{max} = \frac{(\varepsilon_s - \varepsilon_\infty)(tan[(1-\alpha)\pi/4}{2} \quad (5.3)$$

The average value of τ_0 can be calculated from the equation

$$\frac{(\varepsilon_0 - \varepsilon')^2 + \varepsilon''^2}{(\varepsilon' - \varepsilon_\infty)^2 + \varepsilon''^2} = (j\omega\tau_0)^{2(1-\alpha)} \quad (5.4)$$

The molecular relaxation time calculated using the equation by substituting the value of τ_0

$$\tau = [(2\varepsilon_s + \varepsilon_\infty)/3\varepsilon_s]\tau_0 \quad (5.5)[20].$$

The Cole-Cole plots corresponding to the samples are plotted in Figure 5.5.

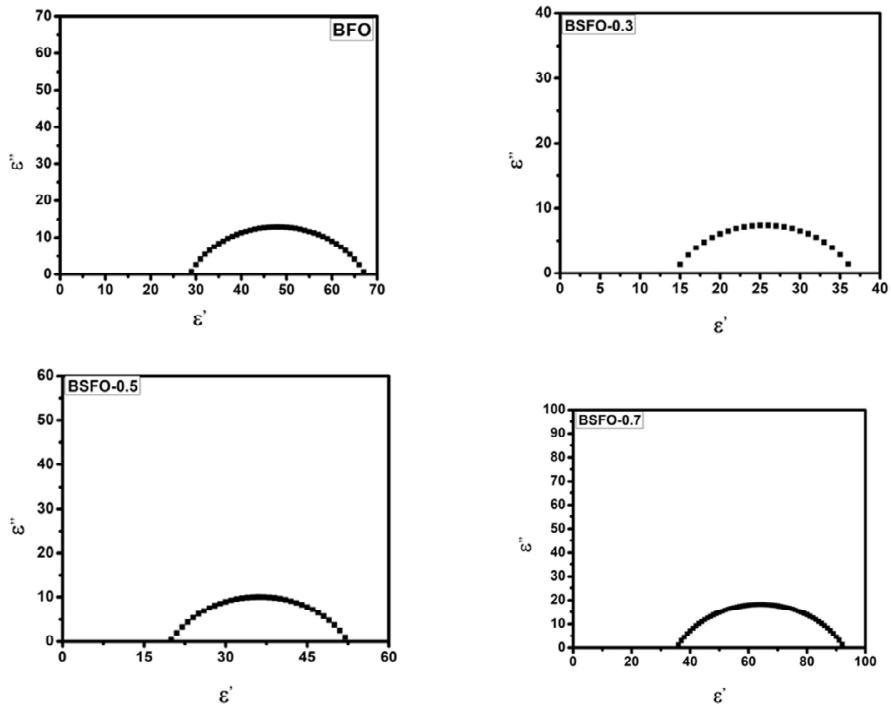

Fig 5.5: Cole-Cole plots of all samples

[19] S et al. 2022
[20] Sagar et al. 2006

The values of dispersion parameters obtained from the Cole-Cole plot analysis are given in Table 5.2[21].

Table 5. 2. Dispersion parameters from Cole-Cole analysis.

Sr content in sample (x)	ε_s	ε_∞	A	ε''	$\tau_0(10^{-8}s)$	$\tau(10^{-8}s)$
0	67.352	28.611	0.256	12.802	1.12	0.912
0.3	36.739	14.293	0.263	7.335	0.994	0.791
0.5	52.547	19.835	0.299	10.029	0.795	0.630
0.7	92.733	35.369	0.280	18.177	1.92	1.53

The dispersion parameters like ε_s (static dielectric constant), ε_α (optical dielectric constant), α(spreading factor), τ_0 (average relaxation time), and τ(molecular relaxation time) of all samples are evaluated and are tabulated and their variation with composition is analyzed (Figure 5.6).

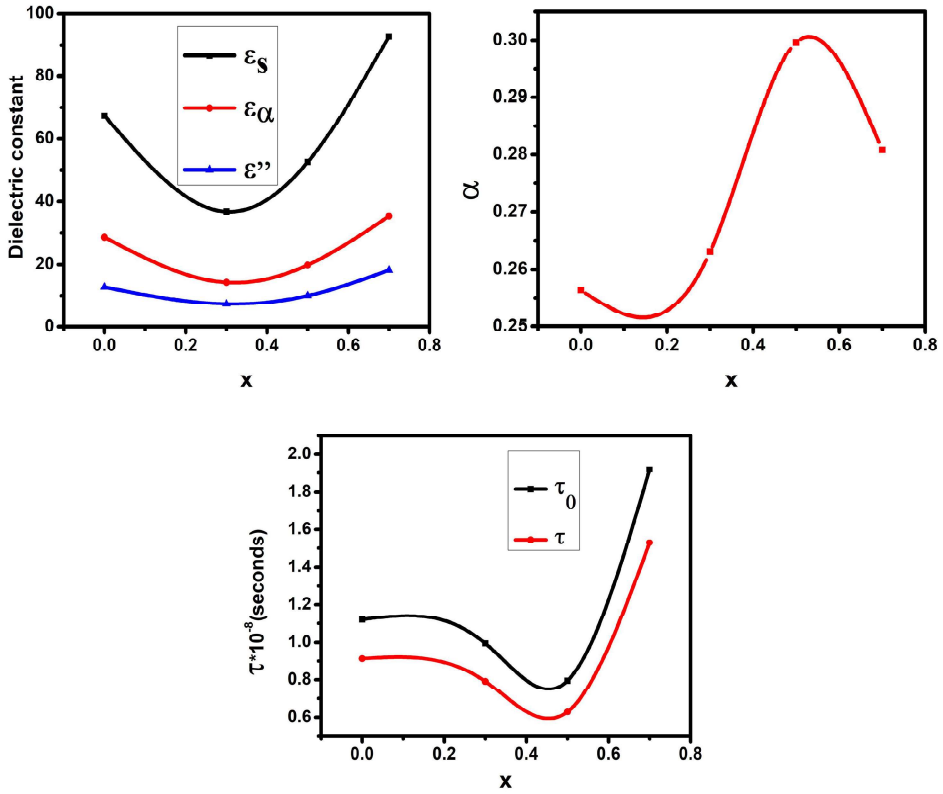

Fig 5.6: The ε_s (static dielectric constant),ε_α(optical dielectric constant),α(spreading factor),τ_0 (average relaxation time),τ(molecular relaxation time) of all the samples

The optical dielectric constant (ε_α) and static dielectric constant (ε_s) first

[21] S et al. 2022

decreased for x=0.3 and further addition of strontium increases their values which is similar to that of Figure 5.8. This is because the dielectric constant of a material is linearly proportional to the average value of grain size [22]. Therefore the decrease in dielectric constant for x=0.3 is due to a decrease in grain size. For x=0.5 & 0.7 the grain size increases and also dielectric constant increases. This indicates that there is a relation between the conduction process, dielectric polarization, and the grain size in Sr doped BFO samples. The grain boundary mobility decreases with Sr doping due to the segregation of defects induced by doping at the grain boundaries [23]. The spreading factor is the measure of the broadening of the relaxation time. The average relaxation time is the effectual time constant for the relaxation involved and the molecular relaxation time is the time constant for the instantaneous molecular dipole relaxation[24]. The spreading factor increases with Sr doping up to x=0.5 which may be attributed to the increase in disordering in BSFO nanoparticles as a result of doping. It is clear from the table that both the relaxation times (i.e., average and molecular) decreases up to x=0.5 and increases for x=0.7. This may be because by increasing doping up to x=0.5, disorders in the nanoparticles increase, thereby decreasing the relaxation time. For the sample x=0.7, the spreading factor decreases and the relaxation time increases because of disorder in the structure decreases and also there is a structural transition from Pm-3m to Fd-3m[25]. Analyzing the relaxation behavior of molecules in a material by observing the shape and position of the Cole-Cole plot, which can reveal information about the molecular structure and interactions.

5.3.3.3 Variation of ac conductivity

The variation of ac conductivity with frequency were also studied for all the samples and the variation is plotted in Figure 5.7.

[22] Rayssi et al. 2018
[23] Rayssi et al. 2018
[24] Veena Gopalan et al. 2009
[25] Chawla et al. 2014; S et al. 2022

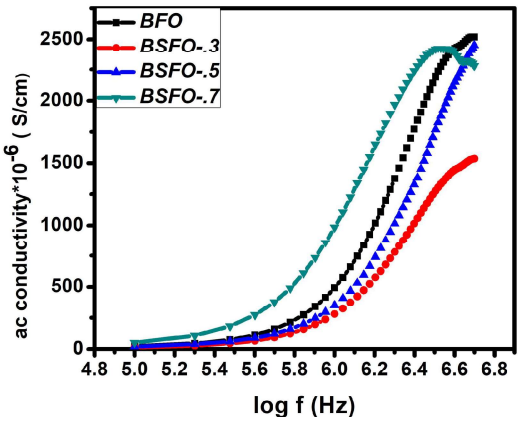

Fig 5.7: Dependence of ac conductivity on frequency of all samples

It is observed that ac conductivity increases with increasing frequency. This is because of the hopping of electrons from Fe^{2+} to Fe^{3+} ions. The decreasing dielectric constant with frequency is also linked with the hopping of electrons from Fe^{2+} to Fe^{3+} ions. The hopping electrons require a large amount of energy. At low frequency these electrons could not get enough energy from the electric field but as we increase the frequency of the electric field electrons get sufficient energy and at a particular point the hopping of electrons begins from Fe^{2+} to Fe^{3+}. This is the reason for the enhancement of conductivity of dielectric material with increasing frequency and the decrement in dielectric constant[26].

5.3.3.4 Effect of strontium substitution on dielectric properties

Variation in dielectric constant and conductivity with Sr content for the prepared samples are plotted in Figure 5.8 and Figure 5.9.

[26] S et al. 2022

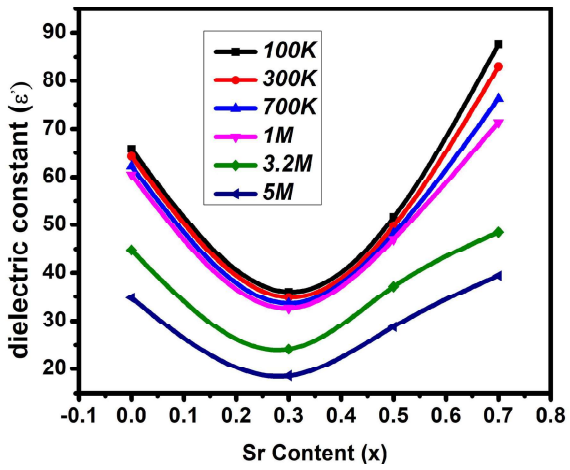

Fig 5.8. Variation of dielectric constant with Sr content in BFO

The decreasing dielectric constant (x=0.3) may be due to two phenomena. The substitution of Sr ions in BFO induces more oxygen vacancies for charge compensation which increases the hopping conduction mechanism. The second reason may be due to the substitution of higher radii strontium ion and the presence of traces of secondary phase which reduces grain sizes (increased grain boundaries) and the inhomogeneity which gives restriction to the charge movement. Strontium-substitution has a considerable effect on the dielectric properties of BSFO[27].

Doping with more strontium increases the dielectric constant (x>0.3) due to leakage current. The high conductivity and leakage current are caused by the part of the impurity phase so that even a very small amount of impurities separated to the boundaries can have a doping effect and change the dielectric to semiconductor [28]. In pure BFO samples, the spontaneous change in oxidation state from Fe^{3+} to Fe^{2+} results in the formation of oxygen vacancies to maintain the electrical neutrality which causes thermally activated hopping conduction. For our samples, the presence of oxygen vacancies contributes to the increase in conductivity (0.3<x<0.7) when $0 < x \leq 0.3$, the Fe^{3+} ions become donors and the number of Fe^{2+} ions changed from Fe^{3+} becomes less which reduces the conductivity. Strontium doping with x=0.5 and 0.7

[27] Kaur et al. 2016a; S et al. 2022
[28] Wang et al. 2004

increases the conductivity and hence the dielectric constant due to the structural transition. By doping, we can modify the dielectric properties to suit application requirements[29]. The measurement of dielectric constant and ac conductivity of BSFO samples suggests the leakage current plays an important role [30].

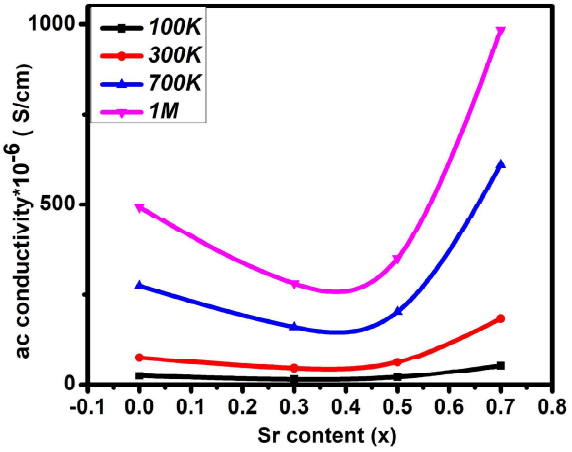

Fig 5.9 Variation of ac conductivity with Sr content in BFO

5.3.4 Magnetic Properties

The magnetic hysteresis loop for all the samples was drawn at 300K. The magnetic hysteresis loop at 300K is shown in Figure 5.10. The hysteresis loop for all the samples point towards superparamagnetic and some ferromagnetic in nature. The Fe^{3+} ions change to Fe^{4+} ions at Bi-site with the increasing concentration of divalent Sr^{2+} ions. This substitution introduces some oxygen vacancies to compensate for the charge for doped samples [31].

[29] Mostafa et al. 2019
[30] Chang et al. 2007; S et al. 2022
[31] Hussain et al. 2013; S et al. 2022

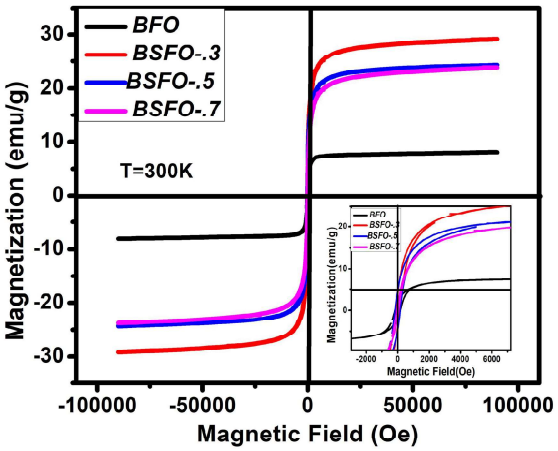

Fig 5.10: *M-H* loops for the samples

Variation of saturation magnetization and magnetic moment with Sr content is also plotted and is shown in Figure 5.11.

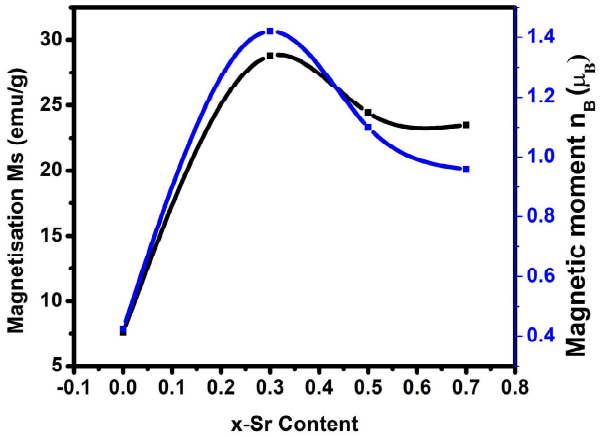

Fig 5.11: Magnetization, magnetic moment of all the samples

Table 5.3. Magnetic properties of BSFO samples

Sr content in sample (x)	M_s (emu/g)	M_r (emu/g)	M_r/M_S	H_C (Oe)	K (erg/g)	Magnetic moment n_B (μ_B)
0	7.58	2.6	0.34	24.43	192	0.424
0.3	28.76	3.64	0.12	70.68	2117	1.42
0.5	24.44	4.84	0.19	24.43	622	1.10
0.7	23.52	1.0	0.04	15.24	373	0.959

The substitution of strontium at the bismuth site restores its antiferromagnetic behavior and also compresses the spins because of a change in ionic radius of strontium and bismuth. This has been reported to result in increased magnetization in Sr doped BFO[32]. BFO displays distorted rhombohedral structure and collinear anti-parallel spin arrangement of Fe ions, following zero macroscopic magnetization[33] because of the magnetic moment with spin cycloid, and the Fe^{3+} to Fe^{2+} reductions produce the oxygen vacancies and leakage current. For minimizing this leakage current the substitution of rare earth and transitional metal atoms is attempted at the bismuth ferrite A and B sites. Spin canting of magnetic moments at the nanoparticle exterior is the origin of weak ferromagnetic or (anti)ferromagnetic systems. The weak ferromagnetism in BFO (x=0) is due to the spin canting of magnetic moments. For x=0.3 saturation magnetization is found to be nearly four times larger than bismuth ferrite. This enhancement of magnetization points towards grain size dependence of magnetization. The size of $Bi_{0.7}Sr_{0.3}FeO_3$ nanoparticles is much small (10.03nm) compared to BFO nanoparticles (48.39nm) which would increase the spin canting of magnetic moments and hence the Dzyaloshinskii-Moriya (DM) interaction thus magnetization increases. The increase in remnant magnetization (M_r) and coercive field (H_c) also established the spin canting of magnetic moments. For x=0.5 a decrease in magnetization is because of the structural transition to the pseudo-cubic (Pm3m) phase. The Fe ions in this structure (Pm3m) are present in an anti-parallel collinear configuration with a Fe-O-Fe bond angle is 180 and hence a decreased saturation magnetization. For x=0.7 there is also a decrease in magnetization due to the structural transition from Pm-3m to Fd-3m phase. The magnetic moment of all samples is calculated using the equation[34].

$$n_B = \frac{M.M_S}{N_A.\mu_B} \tag{5.6}$$

where M is molecular weight, M_S is the saturation magnetization and $N_A * \mu_B$ is a constant and equal to 5585.

[32] Hussain et al. 2013
[33] Anju et al. 2017
[34] Anju et al. 2017; S et al. 2022

Magnetic coercivity (H_c) of the Bi-Sr ferrite nanoparticles as a function of strontium content x as shown in Figure 5.12. It is seen that initially with the increase in strontium content i.e. for x=0.3 the magnetic coercivity increases from the initial value 24.43Oe to 70.08Oe due to the structural transition and then the value decreases for x=0.5 and 0.7. In general magnetic coercivity depends upon the domain wall energy, magneto-crystalline anisotropic constant, average grain size, and other factors[35]. The initial increasing coercivity value is due to an increase in magneto-crystalline anisotropy. There exist a relation of anisotropy constant K on the Sr^{2+} ion concentration x which can be calculated using the relation[36].

$$H_C = \frac{0.96}{M_S} \tag{5.7}$$

The calculated anisotropic constant for our samples is listed in Table 5.3[37]. From the above relation, for the greater the values of anisotropy constant, the coercivity will also increase. The observed increase in coercivity values is probably due to a decrease in the grain size. For x=0.5 and 0.7, the size increases and the coercivity decreases. The inverse relation between the coercivity and the grain size is reported in the literature [38].

[35] Kurmude et al. 2014
[36] S et al. 2022
[37] Gabal et al. 2012
[38] Gabal et al. 2012; S et al. 2022

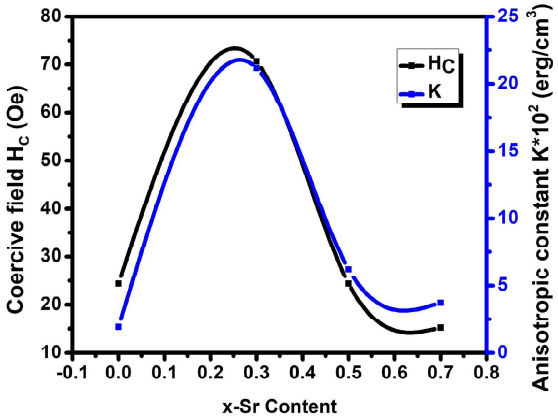

Fig 5.12: Coercive field and anisotropic constant with Sr content all the samples

The squareness ratio (SQR), M_r/M_s, is an important property in memory device applications (~1). A small value of SQR shows the isotropic nature. SQR shows how to square the M-H hysteresis loop is. In the Stoner-Wohlfarth model, M_r/M_s is 0.34 for BFO nanoparticles and it is very good agreement with the reported values[39]. The low value of remanent magnetization and coercive field indicates the superparamagnetic behavior of all the samples. All the samples exhibit superparamagnetic nature due to suppression of spin cycloid magnetic moment [40]. The observed value of saturation magnetization of all the samples in the present work is greater than the reported value 0.4 emu/g and 0.867 emu/g for x=0 and 0.3 respectively[41].

5.3.5 Optical Studies

The photoluminescent (PL) emission spectrum of the as-prepared samples is shown in Figure 5.13. It presents the luminescent response of bismuth ferrite and doped samples. For the sample with x = 0.0, the emission peak is observed at 863 nm for an excitation wavelength of 570 nm. For x = 0.3 and x = 0.5, the emission peaks appear at 842 nm and 858 nm for excitation wavelengths of 422 nm and 430 nm, respectively. In the case of x = 0.7, the emission peak is seen at 730 nm when excited at 366 nm.

[39] Rhaman et al. 2020; Sarkar et al. 2015
[40] Sarkar et al. 2015
[41] Hussain et al. 2013; S et al. 2022

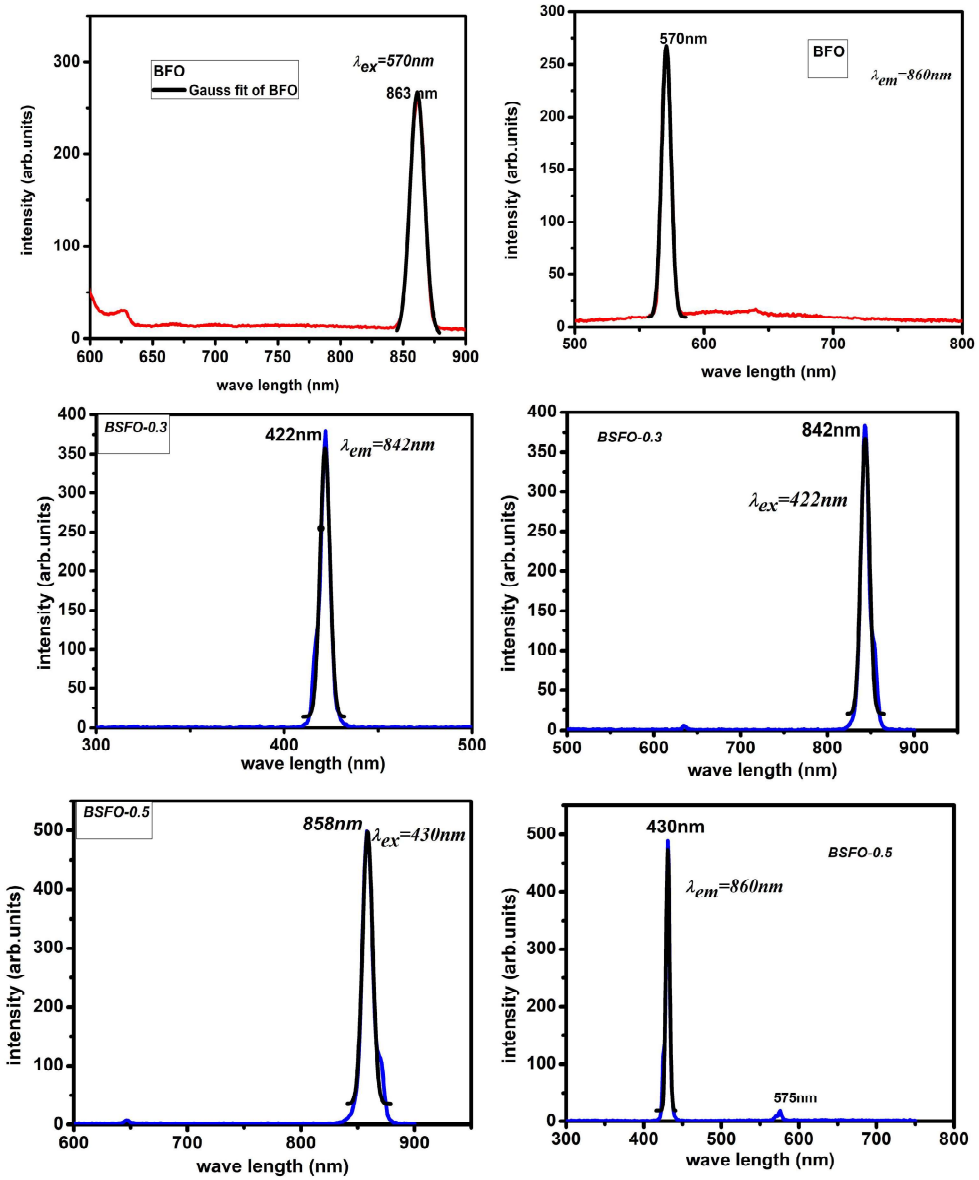

Fig 5.13. Deconvoluted peak profiles for the PL spectrum $BiFeO_3$, $Bi_{0.7}Sr_{0.3}FeO_3$, $Bi_{0.5}Sr_{0.5}FeO_3$

Greater than 780 nm emission spectrum belongs to infrared area. Evaluation of its optical characteristics aids in determining its use in photoconductive and photocatalytic processes[42]. Most of the optical studies reported on BFO –based systems have been based on UV-vis or limited optical range PL studies. But there is

[42] Van Minh & Gia Quan 2011

no detailed PL study in the IR region of the spectrum. This range is interesting because of O-vacancies-induced luminescence [43]. Strong luminescence lines are found in the IR region for all the samples due to the O-vacancies. The wavelength around this region can be used for optical communication[44]. A systematic study in the lines in the IR region may lead to some interesting application possibilities for these materials.

5.3.6 Photocatalytic Activity Studies:

The photocatalytic activity of bismuth ferrite strontium doped samples is evaluated by the degradation of methylene blue (MB) dye under sunlight irradiation. UV vis absorption spectra of the methylene blue solution containing bismuth ferrite and strontium doped bismuth ferrite samples in the wavelength range 200 to 750 nm with time step of 60 min is given in Figure 5.14. The preparation methods are given in section 2.10 of Chapter 2.

The MB solution which is bright blue color in the initial condition, on exposure to sunlight, showed a steady drop in the color with increasing irradiation time. According to Beer Lambert's law, dye concentration and absorbance maxima are directly correlated. Time-dependent absorption spectra of the MB dye solution are displayed in Figure 5.14 when BSFO-0.5 and BFO had the absorbance peaks at 664 nm and the secondary peaks at 610 nm and 290 nm. The intensity of absorbance peak was found to be decreases with increasing irradiation time without change in shape or position. The elimination of chromophoric group is the reason for the decrease in the intensity at 664 nm. That no additional chromophore molecule was created as a byproduct was proven by the absence of additional peaks in the UV-VIS spectra[45].

[43] Boccuzzi et al. 1990
[44] Kaur et al. 2016b
[45] N et al. 2023

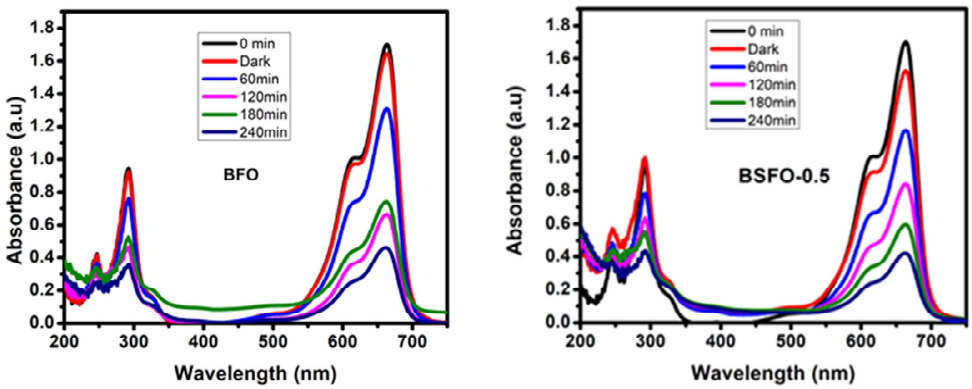

Fig 5.14 Time-dependent absorption spectra of the MB dye solution under visible light for BFO and BSFO-0.5

The degradation of MB can be defined by the degradation efficiency, $(C_0\text{-}C)/C_0$, where C is the change in dye's concentration at predetermined intervals of time, and C_0 is the initial dye concentration at time t = 0. This can also be expressed in terms of absorbance as $(A_0\text{-}A)/A_0$ where A is the absorbance of the MB solution containing the sample after photocatalytic degradation.

Percentage dye degradation was studied for all the catalysts and is plotted in Figure 5.15. The recombination of photo-induced e^-/h^+ pairs limits the photocatalytic activity of bismuth ferrite. To avoid recombination rate of bismuth ferrite by doping with Sr^{2+} ions for improve photocatalytic activity. The inhibition of e^-/h^+ pairs recombination and the creation of Fermi energy levels below the conduction band are the causes of the increasing photodegradation. The degradation percentage is calculated using the equation $(\frac{C_0-C}{C_0}) * 100$. The dye degradation percentage of all the samples under the present study is also given in Table 5.4. From the table the following inference can be obtained. The degradation of BFO and BSFO-0.5 reached 72% and 75% respectively. It is also evident that the strontium doping has little effect on the catalytic activity of bismuth ferrite.

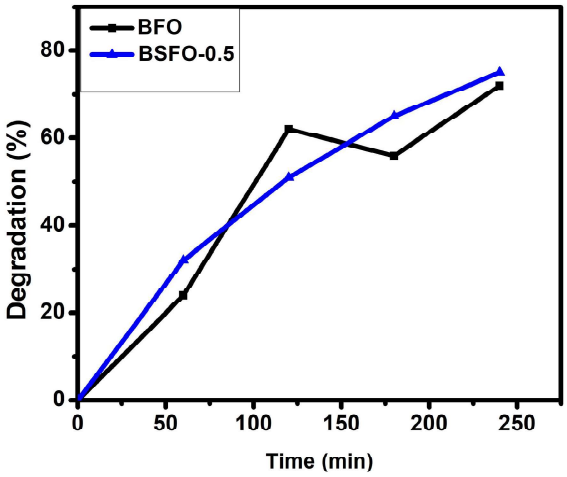

Fig 5.15. photocatalytic activity for BFO and BSFO-0.5 samples.

Table 5.4: Dye Degradation percentage for the BFO and BSFO-0.5 samples

Time of irradiation in minutes	BFO	BSFO-0.5
0	0	0
60	24	32
120	62	51
180	56	65
240	**72**	**75**

5.3.6.1 Kinetic Study of Photodegradation

Using the Langmuir-Hinshelwood model, the kinetic performance of BSFO samples for MB degradation was computed and fitted. This model explains the MB photodegradation rate constant as seen in Figure 5.16, where the pseudo-first order kinetic model fits the chemical kinetics of MB dye degradation.

$$\ln\frac{c_0}{c_t} = kt \qquad (5.8)$$

The slope of the linear fit plot of $\ln\frac{c_0}{c_t}$ v/s irradiation time gives degradation rate constant. All graphs of $\ln\frac{c_0}{c_t}$ v/s time were fitted linearly and the fitted curves are

given in Figure 5.16. Slope of the linear fit was obtained and these are called the rate constant are tabulated in Table 5.5. Under visible light irradiation, the photocatalytic activity for doped samples shows superior activity when compared to pure bismuth ferrite. The photocatalytic activity increases with doping. Efficiency of photocatalyst decreases because of the fast recombination of e^-/h^+ pairs after reaching its optimal limit. After crossing the optical limit of strontium doping the space charge barrier become greater. Hence recombination of photo-generated e^-/h^+ pairs become more easier this is the reason for the efficiency of photodegradation decreases. In the photocatalytic process deformation generated is more for doped samples compared to pure bismuth ferrite[46].

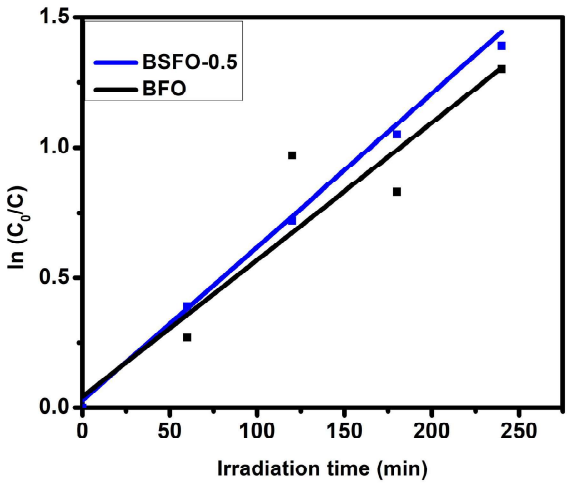

Fig 5.16 Kinetic plots and Linear fit for dye degradation by BFO and BSFO-0.5.

Table 5.5: Rate constant of MB dye in the presence of bismuth ferrite as photocatalyst

Sample	Rate constant ($k*10^{-2}$ min^{-1})
BFO	0.52
BSFO 0.5	0.57

[46] Madhukara Naik et al. 2019

5.4. Conclusions

$BiFeO_3$ and Sr doped BFO samples are successively synthesized by a modified Sol-gel auto-combustion process. The XRD pattern confirms the formation of the samples. The XRD analysis point towards a structural transition from rhombohedral- to cubic beyond x=0.3 which confirms the successful replacement of Bi with Sr. The dielectric constant decreases with increasing frequency. The dielectric constant, as well as ac conductivity, can be altered/tuned by the addition of dopants. Cole-Cole plots are drawn and various parameters are tabulated. The average relaxation time and molecular relaxation time are calculated and they are approximately the same order (~10^{-8} s). The magnetic studies confirm that this is a simple cost-effective method to prepare bismuth ferrite with improved magnetic characteristics. Saturation magnetization and remnant magnetization were found to increase with Sr-content. Magnetic measurements showed that for x=0.3, saturation magnetization (28.76emu/g) is nearly four times more than BFO (7.58emu/g), which can be attributed to spin canting of magnetic moments and grain size of the prepared samples. For x=0.5 and x=0.7 a decrease in magnetization is because of the structural transition to the pseudo-cubic (Pm3m) phase and to Fd-3m phase respectively. Magnetic moment and anisotropic constant are also studied. Sr-substituted BFO nanoparticles show characteristics of both superparamagnetic and ferromagnetic phases so these materials are promising for future magnetic device applications. O-vacancy induced strong and sharp photoluminescence activity is observed in the IR region and is useful in optical communication applications which open new avenues for these materials' applications. Bismuth ferrite can act as an efficient photocatalyst when compared to spinel ferrites. However, the result also indicate that the amount of strontium substituted in bismuth ferrite does not have any significant effect on the dye degradation efficiency. Thus we conclude that ferrite nanoparticles are "efficient photocatalytic semiconductor" for degradation of organic pollutants. The advantage of using these as photocatalyst is that after dye degradation the catalyst can be removed easily by using a magnetic field.

References

Ahlawat, A., Satapathy, S., Bhartiya, S., Singh, M. K., Choudhary, R. J., & Gupta, P. K. (2014). BiFeO3/poly(methyl methacrylate) nanocomposite films: A study on magnetic and dielectric properties. *Applied Physics Letters*, *104*(4), 042902. https://doi.org/10.1063/1.4863228

Ahmad, R., Hussain Gul, I., Zarrar, M., Anwar, H., Khan Niazi, M. B., & Khan, A. (2016). Improved electrical properties of cadmium substituted cobalt ferrites nano-particles for microwave application. *Journal of Magnetism and Magnetic Materials*, *405*, 28–35. https://doi.org/10.1016/j.jmmm.2015.12.019

Andhare, D. D., Patade, S. R., Kounsalye, J. S., & Jadhav, K. M. (2020). Effect of Zn doping on structural, magnetic and optical properties of cobalt ferrite nanoparticles synthesized via. Co-precipitation method. *Physica B: Condensed Matter*, *583*. https://doi.org/10.1016/j.physb.2020.412051

Anju, Agarwal, A., Aghamkar, P., & Lal, B. (2017). Structural and multiferroic properties of barium substituted bismuth ferrite nanocrystallites prepared by sol–gel method. *Journal of Magnetism and Magnetic Materials*, *426*, 800–805. https://doi.org/10.1016/j.jmmm.2016.09.103

Boccuzzi, F., Ghiotti, G., Chiorino, A., & Marchese, L. (1990). Pt/ZnO System: IR study of the vibrational and electronical effects induced by heating in CO atmosphere. *Surface Science*, *233*(1–2), 141–152. https://doi.org/10. 1016/0039-6028(90)90185-B

Chang, F., Zhang, N., Yang, F., Wang, S., & Song, G. (2007). Effect of Cr substitution on the structure and electrical properties of BiFeO3 ceramics. *Journal of Physics D: Applied Physics*, *40*(24), 7799–7803. https://doi.org/10.1088/0022-3727/40/24/031

Chawla, M., Shekhawat, N., Aggarwal, S., Sharma, A., & Nair, K. G. M. (2014). Cole-cole analysis and electrical conduction mechanism of N+ implanted polycarbonate. *Journal of Applied Physics*, *115*(18), 184104. https://doi.org/10.1063/1.4876123

Costa, L. V., Ranieri, M. G., Cilense, M., Longo, E., & Simões, A. Z. (2014). Evidence of magnetoelectric coupling on calcium doped bismuth ferrite thin films grown by chemical solution deposition. *Journal of Applied Physics*, *115*(17), 17D910. https://doi.org/10.1063/1.4867123

Dielectric relaxation [by] Vera V. Daniel. (Book, 1967) [WorldCat.org]. (n.d.). Retrieved March 3, 2021, from https://www.worldcat.org/title/dielectric-relaxation-by-vera-v-daniel/oclc/859841181

Gabal, M. A., El-Shishtawy, R. M., & Al Angari, Y. M. (2012). Structural and magnetic properties of nano-crystalline NiZn ferrites synthesized using egg-white precursor. *Journal of Magnetism and Magnetic Materials*, *324*(14), 2258–2264. https://doi.org/10.1016/j.jmmm.2012.02.112

Hegab, A. F., Ahmed Farag, I. S., El-Shabiny, A. M., Nassaar, A. M., Ramadan, A. A., & Moustafa, A. M. (2017). Role of Sr doping on transport and magnetic properties of bismuth ferrite in correlation with defect formation. *Journal of Materials Science: Materials in Electronics*, *28*(19), 14460–14470. https://doi.org/10.1007/s10854-017-7308-5

Hegab, A. F., Farag, I. S. A., El-Shabiny, A. M., Nassaar, A. M., & Ramadan, A. A. (2015). Synthesis and rietveld whole-pattern analysis of Sr-doped perovskite bismuth ferrite. *Journal of Ovonic Research*, *11*(5), 235–241.

Hussain, T., Siddiqi, S. A., Atiq, S., & Awan, M. S. (2013). Induced modifications in the properties of Sr doped BiFeO3 multiferroics. *Progress in Natural Science: Materials International*, *23*(5), 487–492. https://doi.org/10.1016/j. pnsc.2013. 09.004

Iqbal, S., Fakhar-e-Alam, M., Atif, M., Amin, N., Alimgeer, K. S., Ali, A., Aqrab-ul-Ahmad, Hanif, A., & Aslam Farooq, W. (2019). Structural, morphological, antimicrobial, and in vitro photodynamic therapeutic assessments of novel Zn+2-substituted cobalt ferrite nanoparticles. *Results in Physics*, *15*(July), 102529. https://doi.org/10.1016/j.rinp.2019.102529

Kaur, B., Singh, L., Annapu Reddy, V., Jeong, D. Y., Dabra, N., & Hundal, J. S. (2016a). AC impedance spectroscopy, conductivity and optical studies of sr doped bismuth ferrite nanocomposites. *International Journal of Electrochemical Science*, *11*(5), 4120–4135. https://doi.org/10.20964/110353

Kaur, B., Singh, L., Annapu Reddy, V., Jeong, D. Y., Dabra, N., & Hundal, J. S. (2016b). AC impedance spectroscopy, conductivity and optical studies of sr doped bismuth ferrite nanocomposites. *International Journal of Electrochemical Science*, *11*(5), 4120–4135. https://doi.org/10.20964/110353

Khomchenko, V. A., Kiselev, D. A., Selezneva, E. K., Vieira, J. M., Lopes, A. M. L., Pogorelov, Y. G., Araujo, J. P., & Kholkin, A. L. (2008). Weak ferromagnetism in diamagnetically-doped Bi1 - xAxFeO3 (A = Ca, Sr, Pb, Ba) multiferroics. *Materials Letters*, *62*(12–13), 1927–1929. https://doi.org/10.1016/j. matlet. 2007.10.044

Kurmude, D. V., Kale, C. M., Aghav, P. S., Shengule, D. R., & Jadhav, K. M. (2014). Superparamagnetic behavior of zinc-substituted nickel ferrite nanoparticles and its effect on mossbauer and magnetic parameters. *Journal of Superconductivity and Novel Magnetism*, *27*(8), 1889–1897. https://doi.org/10.1007/s10948-014-2535-y

Ma, W., Sun, Q., Sun, M., Bai, L., Liu, Y., Zhang, J., & Yang, J. (2022). Structural Evolution-Enabled BiFeO3 modulated by strontium doping with enhanced magnetic and photoelectric performance. *Applied Surface Science*, *571*, 151130. https://doi.org/10.1016/j.apsusc.2021.151130

Madhukara Naik, M., Bhojya Naik, H. S., Nagaraju, G., Vinuth, M., Vinu, K., & Viswanath, R. (2019). Green synthesis of zinc doped cobalt ferrite nanoparticles: Structural, optical, photocatalytic and antibacterial studies. *Nano-Structures and Nano-Objects*, *19*, 100322. https://doi.org/10.1016/j.nanoso.2019.100322

Mostafa, M., Rahman, M. J., & Choudhury, S. (2019). Enhanced dielectric properties of BaTiO 3 ceramics with cerium doping, manganese doping and Ce-Mn co-doping. *Science and Engineering of Composite Materials*, *26*(1), 62–69. https://doi.org/10.1515/secm-2017-0177

N, A., Philip, R. S., & Mathew, M. (2023). Photocatalytic activities of SnS thin films deposited at room temperature. *Applied Surface Science Advances*, *13*(September 2022), 100374. https://doi.org/10.1016/j.apsadv.2023.100374

Rayssi, C., El Kossi, S., Dhahri, J., & Khirouni, K. (2018). Frequency and temperature-dependence of dielectric permittivity and electric modulus studies of the solid solution Ca0.85Er0.1Ti1-: XCo4 x /3O3 ($0 \leq x \leq 0.1$). *RSC Advances*, *8*(31), 17139–17150. https://doi.org/10.1039/c8ra00794b

Rhaman, M. M., Matin, M. A., Hossain, M. N., Khan, M. N. I., Hakim, M. A., & Islam, M. F. (2020). Ferromagnetic, electric, and ferroelectric properties of samarium and cobalt co-doped bismuth ferrite nanoparticles. *Journal of Physics and Chemistry of Solids*, *147*(July 2019), 109607. https://doi.org/10.1016/j.jpcs.2020.109607

S, S. V., E, V. G., & A, M. K. (2022). Structural Evolution–Enabled BiFeO 3 modulated by strontium doping with enhanced dielectric, optical and superparamagnetic properties by modified sol-gel method . *Chinese Physics B*, *32*. https://doi.org/10.1088/1674-1056/ac785b

Sagar, S., Saravanan, S., Suresh Kumar, S., Venkatachalam, S., & Anantharaman, M. R. (2006). Evidence for the existence of multiple equilibrium states in cobalt phthalocyanine tetramer: A study by dielectric spectroscopy. *Journal of Physics D: Applied Physics*, *39*(8), 1678–1683. https://doi.org/10.1088/0022-3727/39/8/030

Sarkar, K., Mukherjee, S., & Mukherjee, S. (2015). Structural, electrical and magnetic behaviour of undoped and nickel doped nanocrystalline bismuth ferrite by solution combustion route. *Processing and Application of Ceramics*, *9*(1), 53–60. https://doi.org/10.2298/PAC1501053S

Singh, R., & Ulrich, R. K. (1999). High and low dielectric constant materials. *Electrochemical Society Interface*, *8*(2), 26–30.

Soibam, I., & Devadatta Mani, A. (2018). Optimisation and the Effect of Addition of Extra Bismuth on the Dielectric and Optical Properties of Bismuth Ferrite (BFO). *Materials Today: Proceedings*, *5*(1), 2064–2073. https://doi.org/10.1016/j.matpr.2017.09.202

Van Minh, N., & Gia Quan, N. (2011). Structural, optical and electromagnetic properties of Bi 1-xHoxFeO3 multiferroic materials. *Journal of Alloys and Compounds*, *509*(6), 2663–2666. https://doi.org/10.1016/j.jallcom.2010.12.033

Veena Gopalan, E., Malini, K. A., Sakthi Kumar, D., Yoshida, Y., Al-Omari, I. A., Saravanan, S., & Anantharaman, M. R. (2009). On the dielectric dispersion and absorption in nanosized manganese zinc mixed ferrites. *Journal of Physics Condensed Matter*, *21*(14). https://doi.org/10.1088/0953-8984/21/14/146006

Wang, Y. P., Zhou, L., Zhang, M. F., Chen, X. Y., Liu, J. M., & Liu, Z. G. (2004). Room-temperature saturated ferroelectric polarization in BiFeO3 ceramics synthesized by rapid liquid phase sintering. *Applied Physics Letters*, *84*(10), 1731–1733. https://doi.org/10.1063/1.1667612

Chapter 6

STRUCTURAL AND ELECTRICAL STUDIES ON NANOCOMPOSITES BASED ON FERRITES AND BARIUM TITANATE

STRUCTURAL AND ELECTRICAL STUDIES ON NANOCOMPOSITES BASED ON FERRITES AND BARIUM TITANATE

This chapter discusses the detailed analysis of various multiferroic composites prepared using different materials and ratios. The systems studied include composites of bismuth ferrite, bismuth strontium ferrite, nickel ferrite, nickel zinc ferrite, cobalt ferrite and cobalt zinc ferrite with barium titanate. The components were taken in various weight ratios of 1:1, 1:2 and 2:1 and the structural, electrical and ferroelectric properties of multiferroic composites prepared were studied. The structural properties were examined using XPS and XRD techniques, while the electrical properties were investigated through frequency-dependent dielectric constant and ac conductivity analysis. The ferroelectric nature was confirmed through a ferroelectric studies using P-E loop tracer. This chapter provides some aspects about the various properties leading to different applications of these multiferroic composites.

Part of this chapter have been published in

Synthesis and characterization of bismuth ferrite-barium titanate nano composites, Sharon, V S; Malini, K A; Arun, KJ, IOP Conference Series: Materials Science and Engineering 1263 (1), 012028, https://10.1088/1757-899X/1263/1/012028

Multiferroic and magnetic characterization of Nickel Ferrite- Barium Titanate nanocomposites Sharon V.S, Swapna S Nair, Nandakumar Kalarikkal, Malini K A Materials Today: Proceedings, https://doi.org/10.1016/j.matpr.2023.12.018)

6.1 Introduction

Natural multiferroic single-phase materials are very rare and their magneto electric coupling (ME) is relatively weak and hence their application prospects is very low[1]. The composites based on multiferroics have gained importance because of their uniqueness to possess both ferroelectric and ferromagnetic phases(2). The multiferroic nanocomposites are expected to show good magnetoelectric coupling response above room temperature, which makes these materials useful for industrial applications[2]. The advantage of the sintered ME composites is the ease and cost effectiveness of fabrication. The ME coupling has application in the field of magnetic field probes, novel actuators, tetrahertz radiation sensors, transducers, capacitive/inductive passive filters for communications, etc[3]. Electrically written and magnetically read new memory devices are developed based on these ME materials[4].

The forms of ceramics, thin films, and multilayers are the most researched ME composite materials. Barium titanate ($BaTiO_3$) is usually used for ferroelectric (FE) component, whereas ferrites are mainly used for the magnetic module in the ME composites[5]. $BaTiO_3$ (BTO) has been a major topic of research because of their low dielectric loss, high dielectric constant, fine tunability, elevated resistivity and for being not harmful to the environment[6]. $BaTiO_3$ with a high dielectric constant is more attractive for miniaturing communication devices[7]. The spontaneous electric polarization is generated because of the movement of Ti^{4+} ions along the crystallographic c-axis[8]. Because of the ferroelectric and piezoelectric properties tetragonal polymorph (t-$BaTiO_3$) is more attractive. The cubic polymorph (c-$BaTiO_3$) possess paraelectric properties[9]. BTO compounds have the application in non-volatile memories, multi-layer ceramic capacitors, dielectric resonators, chemical sensors,

[1] Chauhan & Srivastava 2016
[2] Chauhan & Srivastava 2016
[3] Chauhan & Srivastava 2016
[4] Scott 2007
[5] Chauhan & Srivastava 2016
[6] Y. Slimani et al. 2020; Yassine Slimani et al. 2021
[7] Y. Slimani et al. 2019
[8] Y. Slimani et al. 2020
[9] Leonel et al. 2011

actuators, transducers, etc[10]. The ferroelectric-ferrite composites can be synthesized cost effectively and they can be used in the application of electromagnetic devices, optical active systems, memory storage, logic operators, and in many multifunctional electronic components[11]. Since the ferrite phase's resistivity is lower than that of FE materials, the amount of ferrite phase in such ME composites is essential. As ferrite content increases, these materials' employment is restricted because it gets more difficult to apply high voltages, which are required to record the FE hysteresis P-E loops[12]. Nickel ferrite is an important ferrite possessing moderate saturation magnetization and mechanical hardness and it has diverse applications in magnetic storage systems, site-specific drug delivery, catalysts, and microwave devices[13]. $BaTiO_3$-$NiFe_2O_4$ composites are expected as a fascinating magnetoelectric material because of the individual applications of their components. Among other nano-ferrites, cobalt ferrite have also gained much attention due to their unusual characteristics, which include electrical insulation, high coercivity, moderate saturation magnetization, and cubic magneto-crystalline anisotropy[14]. The $BaTiO_3$-$CoFe_2O_4$ magnetoelectric composites are of great interest to researchers because of their applications in controlled drug delivery, Alzheimer's- Parkinson's disease treatment, sensors, data storage, etc[15]. These composites are artificially prepared multiferroic material that exhibits two distinct ferroic properties, ferroelectricity of $BaTiO_3$ and ferromagnetism of $NiFe_2O_4$ and $CoFe_2O_4$. Bismuth ferrite ($BiFeO_3$) belongs to the multiferroic family, possesses the structure of rhombohedral perovskite with the space group of R3c and exhibits multiferroic properties at room temperature[16]. $BiFeO_3$ is an eco-friendly material as it does not contain lead and is also used for high-temperature piezoelectric applications due to its high Curie temperature (1100K).

[10] Y. Slimani et al. 2020
[11] Y. Slimani et al. 2020
[12] Chauhan & Srivastava 2016
[13] Schuster et al. 2004
[14] Sugimoto 1999
[15] De Leo et al. 2021
[16] Basantakumar Sharma 2017; Pakalniškis et al. 2020

In this study, we examined the structural and electrical properties of various composites of ferrites and barium titanate in different proportions. The details of the samples prepared and the sample IDs are given in Table 6.1.

Table 6.1 Details of the sample ID

Sl No	Components	Weight Ratio	Sample label
1	$NiFe_2O_4$- $BaTiO_3$	1:1	NFO:BTO-1:1
2	$NiFe_2O_4$- $BaTiO_3$	1:2	NFO:BTO-1:2
3	$NiFe_2O_4$- $BaTiO_3$	2:1	NFO:BTO-2:1
4	$Ni_{0.7}Zn_{0.3}Fe_2O_4$- $BaTiO_3$	2:1	NZFO-0.3:BTO-2:1
5	$Ni_{0.5}Zn_{0.5}Fe_2O_4$- $BaTiO_3$	2:1	NZFO-0.5:BTO-2:1
6	$Ni_{0.3}Zn_{0.7}Fe_2O_4$- $BaTiO_3$	2:1	NZFO-0.7:BTO-2:1
7	$ZnFe_2O_4$- $BaTiO_3$	2:1	ZFO:BTO-2:1
8	$CoFe_2O_4$- $BaTiO_3$	2:1	CFO:BTO-2:1
9	$Co_{0.7}Zn_{0.3}Fe_2O_4$- $BaTiO_3$	2:1	CZFO-0.3:BTO-2:1
10	$Co_{0.5}Zn_{0.5}Fe_2O_4$- $BaTiO_3$	2:1	CZFO-0.5:BTO-2:1
11	$Co_{0.3}Zn_{0.7}Fe_2O_4$- $BaTiO_3$	2:1	CZFO-0.7:BTO-2:1
12	$BiFeO_3$- $BaTiO_3$	1:2	BFO:BTO-1:2
13	BiFeO3- BaTiO3	2:1	BFO:BTO-2:1
14	$Bi_{0.7}Sr_{0.3}FeO_3$- $BaTiO_3$	2:1	BSFO-0.3:BTO-2:1
15	$Bi_{0.5}Sr_{0.5}FeO_3$- $BaTiO_3$	2:1	BSFO-0.5:BTO-2:1
16	$Bi_{0.3}Sr_{0.7}FeO_3$- $BaTiO_3$	2:1	BSFO-0.7:BTO-2:1

6.2 Synthesis

Nickel ferrite with zinc doped ($Ni_{1-x}Zn_xFe_2O_4$), cobalt ferrite with zinc doped ($Co_{1-x}Zn_xFe_2O_4$) and bismuth ferrite with strontium doped ($Bi_{1-x}Sr_xFeO_3$) were synthesized by the modified sol-gel technique. The ferroelectric phase $BaTiO_3$ with a tetragonal structure is directly purchased from Nano Research Elements. The required amounts of the ferrites and barium titanate are used to prepare composites in the weight ratio 1:2 and 2:1. Then these are mixed well using a mortar and pestle with acetone as a homogenizing medium. The samples are then calcinated at 1000°C for three hours and slowly cooled to room temperature.

6.3 Results and Discussion

6.3.1 X-ray diffraction analysis

The structural characterization of synthesized composites was done by XRD. The wavelength of 1.54Å is used for the X-ray diffraction. The average crystallite size is calculated using Scherrer formula.

$$D = \frac{0.9\lambda}{\beta \cos\theta} \tag{6.1}$$

where β is full-width at half-maxima of the strongest intensity diffraction peak, λ is the wavelength of the radiation and θ the angle of the strongest characteristic peak.

The lattice parameters of the $BaTiO_3$ samples were calculated using the formula

$$\frac{1}{d^2} = \frac{(h^2+k^2)}{a^2} + \frac{l^2}{c^2} \tag{6.2}$$

The lattice parameters of the $NiFe_2O_4$ and $CoFe_2O_4$ samples were analysed using the equation

$$a = d(h^2+k^2+l^2)^{1/2} \tag{6.3}$$[17]

where a, b, c: lattice constants, d: Inter planar distance, (h,k,l) : the miller indices

The lattice parameters of the $BiFeO_3$ samples are analyzed by the formula

$$d = \frac{a}{\sqrt{\frac{4(h^2+k^2+hk)}{3} + \frac{a^2 l^2}{c^2}}} \tag{6.4}$$

$$d = \frac{1}{\sqrt{\frac{h^2}{a^2} + \frac{k^2}{b^2} + \frac{l^2}{c^2}}} \tag{6.5}$$

The XRD results of samples of $NiFe_2O_4$, $BaTiO_3$, $NiFe_2O_4$- $BaTiO_3$ with the ratios (1:1), (1:2), (2:1) and $Ni_{1-x}Zn_xFe_2O_4$- $BaTiO_3$ (x=0.3, 0.5, 0.7, 1) with the ratio 2:1 are presented in Figure 6.1. The formation of nickel ferrite with cubic spinel structure and barium titanate with tetragonal crystal structure was identified by the characteristic diffraction peaks according to the JCPDS file No. 10-0325 and 05-0626 respectively[18]. In the XRD pattern of barium titanate, some extra peaks are

[17] Krishna et al. 2012
[18] Vijatovic Petrovic et al. 2020

also observed. The peak observed at $2\theta=24.19^0$ is assigned to the orthorhombic structure of barium carbonate as confirmed by the JCPDS card (pdf 41-0373). The peak at $2\theta=25.36^0$ attributed to the anatase phase of titanium oxide having a tetragonal structure as confirmed by card (pdf-89-4921)[19]. The lattice constant is tabulated in Table 6.2. The lattice constant for the individual phase does not differ much. The c/a ratio ~ 1 confirms the tetragonality of barium titanate component of the samples[20]. The tetragonality (c/a ratio) for barium titanate is 1.016 and composites of barium titanate with pure $NiFe_2O_4$ in various proportions show a constant but slightly decreased c/a ratio of 1.006. It was also observed that the composites of barium titanate with zinc doped nickel ferrite showed variations for c/a value with the amount of zinc doping in nickel ferrite. The c/a values matches with the previous reported values[21]. The lattice constant enhances with zinc substitution in ferrite phase because the Zn^{2+} ions possess larger ionic radius (0.83 Å) in comparison on with Ni^{2+}(0.74 Å) and Fe^{3+}(0.65 Å) ions[22]. The average crystallite size of the samples were obtained by the Debye- Scherrer formula[23] and are tabulated in Table 6.2.

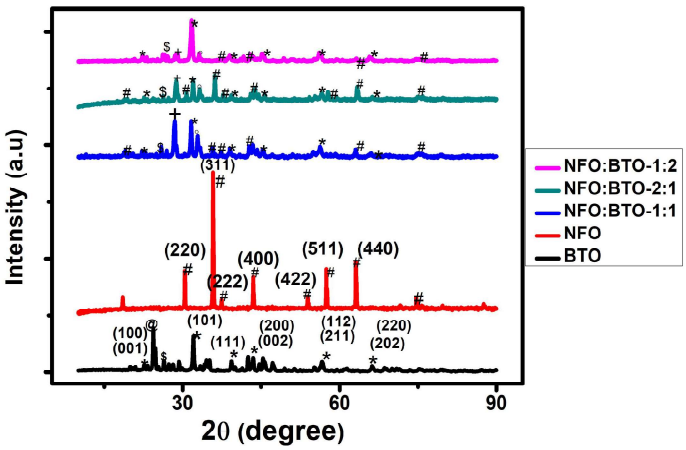

[19] Humera et al. 2016
[20] Zali et al. 2014
[21] de Andrade et al. 2014
[22] Khan et al. 2019
[23] Hussain et al. 2013

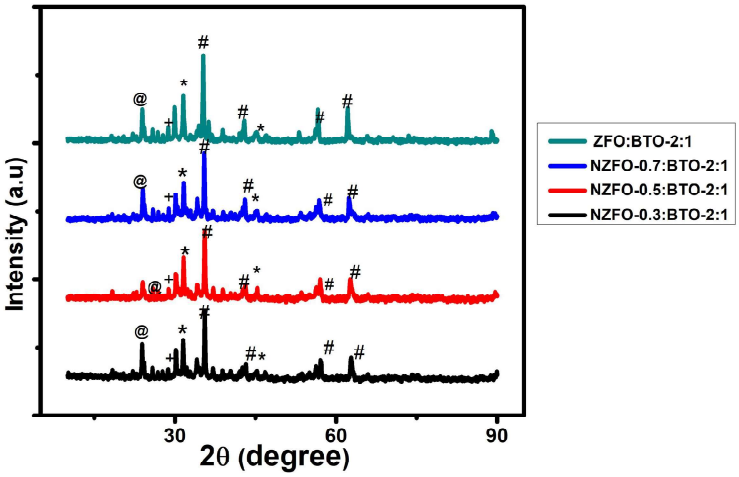

*# ---$NiFe_2O_4$ spinel: *---$BaTiO_3$ tetragonal @---$BaCO_3$ +---gamma phase of $BaCO_3$ $--$TiO_2$*

Fig 6.1 : X-ray diffractograms of all the samples

Table 6.2. Parameters obtained from the XRD analysis of the samples.

Composition	Crystallite Size D (nm)		Lattice parameter (Å)		c/a
	Ferrite Phase	Ferroelectric phase	Ferrite phase	Ferroelectric phase	
NFO	9		a = 8.269	-	-
NFO:BTO-(1:1)	5	32	a = 8.32	a = 3.988 c = 4.012	1.006
NFO:BTO-(2:1)	7	32	a = 8.349	a = 3.985 c = 4.012	1.006
NFO:BTO-(1:2)	7	32	a = 8.32	a = 3.988 c = 4.012	1.006
NZFO-0.3:BTO-(2:1)	38	12	a =8.367	a = 3.917 c =4.031	1.029
NZFO-0.5:BTO-(2:1)	34	13	a =8.367	a = 3.923 c =4.009	1.021
NZFO-0.7:BTO-(2:1)	38	12	a =8.388	a = 3.933 c =3.949	1.004
ZFO:BTO-(2:1)	35	12	a =8.42	a = 4.001 c = 3.847	0.961
BTO		31	-	a = 3.949 c = 4.012	1.016

The XRD results presented in Figure 6.2 confirms the formation of $Co_{1-x}Zn_xFe_2O_4$- $BaTiO_3$ (x=0,0.3,0.5,0.7,1) heterogenous composites. The XRD pattern contain some additional peak which may be due to impurities present in $BaTiO_3$ phase. The formation of cobalt ferrite with cubic spinel structure and barium titanate with tetragonal structure was identified by the characteristic peaks according to the JCPDS file No.(22-1086) and (05-0626) respectively [24].

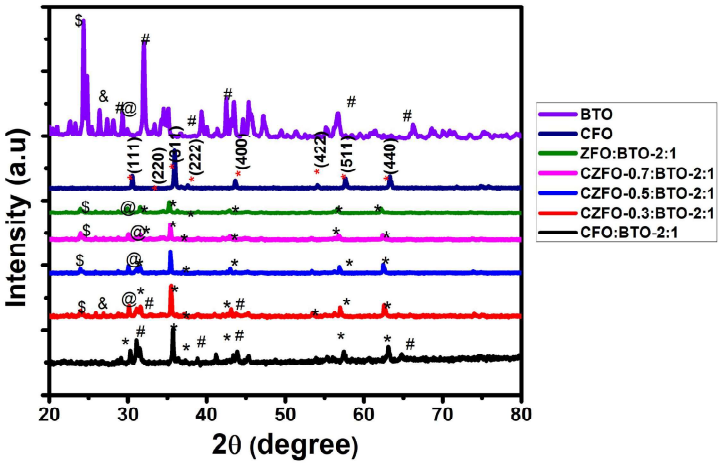

* *---$CoFe_2O_4$ spinel: #---$BaTiO_3$ tetragonal $---$BaCO_3$ @---gamma phase of $BaCO_3$ &--TiO_2*

Fig 6.2 : X-ray diffractograms of all the samples

Table 6.3. Parameters obtained from the XRD analysis of the samples.

Composition	**Crystallite Size D(nm)**		**Lattice parameter (Å)**		c/a
	$CoFe_2O_4$	**$BaTiO_3$**	**Ferrite phase**	**Ferroelectric phase**	
CFO	52		8.33		
CFO:BTO	40	11	a = 8.324	a = 4.044 c = 3.915	0.968
CZFO-0.3:BTO	48	10	a = 8.379	a = 4.030 c = 3.922	0.973
CZFO-0.5:BTO	50	11	a = 8.395	a = 4.030 c = 3.988	0.989
CZFO-0.7:BTO	43	22	a = 8.402	a = 4.003 c = 4.052	1.01
ZFO:BTO	38	25	a = 8.429	a = 3.974 c = 4.065	1.02
$BaTiO_3$		31	-	a = 3.949 c = 4.012	1.016

[24] Kawamura et al. 2019; Vijatovic Petrovic et al. 2020

Table 6.3 provides the lattice characteristics and average crystallite size for both phases. The crystallite size of barium titanate remains smaller than cobalt ferrite nanoparticles. The lattice parameters c and a are used to calculate the degree of tetragonality of the barium titanate phase. It is found that as zinc content rises, the lattice constant (a) for the CFO phase of the nanocomposite decreases. This could be the result of a small diffusion of Ti ions within the lattice and a shift in the spinel lattice's inversion degree brought on by the nanocomposite's ionic redistribution[25]. When Co^{2+} ion is replaced by Zn^{2+} ions the lattice parameter is significantly increased from 8.32 Å to 8.42 Å as listed in Table 6.3. The increase in lattice constant is due to the greater the ionic radius Zn^{2+} (0.74Å) compared to Co^{2+} (0.72Å) ions[26].

The XRD pattern of $BaTiO_3$ (BTO) and $BiFeO_3$ (BFO) in the ratio 1:2 and 2:1 as well as $BaTiO_3$ with $Bi_{1-x}Sr_xFeO_3$ in the ratio 1:2 are shown in Figure 6.3. The diffraction peaks shown in the standard PCPDF file (86-1518) and JCPDS file (05-0626) confirm the synthesis of bismuth ferrite with rhombohedral structure and space group R3c and barium titanate with tetragonal structure and space group P4mm[27] respectively. The lattice constant is tabulated in Table 6.4. The c/a ratio yields information on the samples' tetragonal phase [28]. c/a ratio for the bismuth ferrite phase increases with strontium doping because of the higher ionic radius of Sr^{2+} (1.18Å) compared to Bi^{3+} (1.03Å) ions. Debye-Scherrer formula is used to calculate the average crystallite size of the samples and are tabulated in Table 6.4[29].

[25] Corral-Flores et al. 2010
[26] Lin et al. 2018
[27] Vijatovic Petrovic et al. 2020
[28] Zali et al. 2014
[29] Hussain et al. 2013

Table 6.4. Parameters obtained from the XRD analysis of the samples.

Composition	Crystallite Size D(nm)		Lattice parameter (Å)		c/a ratio	
	$BiFeO_3$	$BaTiO_3$	$BiFeO_3$ phase	$BaTiO_3$ Phase	$BaTiO_3$ Phase	$BiFeO_3$ phase
BFO:BTO-2:1	20	33	a =5.66 c =13.06	a =4.005 c =3.808	0.950	2.307
BFO:BTO-1:2	20	32	a =5.92 c =13.98	a =4.054 c =4.029	0.993	2.361
BSFO-0.3:BTO-2:1	25	33	a =5.64 c =13.8	a =3.988 c =4.15	1.04	2.446
BSFO-0.5:BTO-2:1	15	22	a =5.64 c =13.8	a =3.959 c =4.070	1.03	2.446
BSFO-0.7:BTO-2:1	17	8	a =5.56 c =13.88	a =3.931 c =4.004	1.01	2.496
$BaTiO_3$		31		a = 3.949 c = 4.012	1.016	

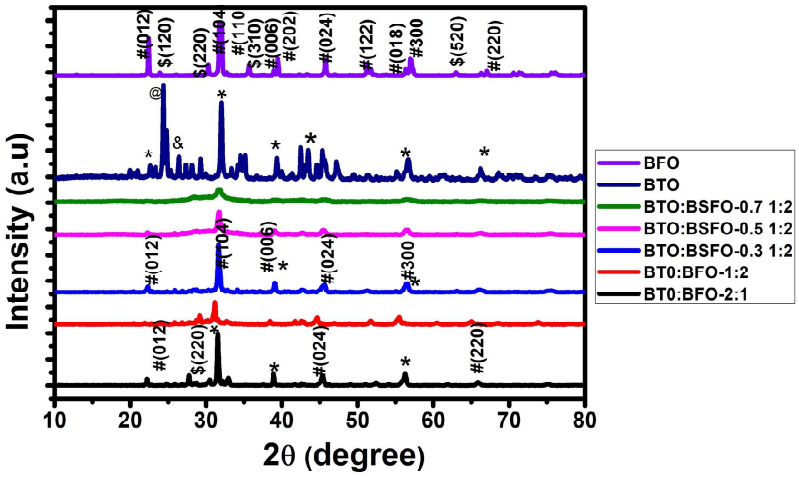

Fig 6.3.XRD pattern of all samples
*# ---$BiFeO_3$ $---$BiFe_4O_9$ *---$BaTiO_3$ tetragonal @---$BaCO_3$ &--TiO_2*

6.3.2 XPS analysis

Initially, each element in the formula was checked for presence using XPS analysis, which also confirmed the element's chemical state of oxidation. The survey spectra of NZFO-0.5:BTO seen here closely resemble those in the published literature and is shown in Figure 6.4. From the survey spectra, it can be seen that the Ti2p peaks'intensity is much lower than the Ba3d and O1s peaks. The Figure 6.4(e) shows the Ni2p core level which have the binding energy of 853.48 eV. It may be classified as typical for metallic nickel – the main photoemission $Ni2p_{3/2}$ line and its satellite. The Zn2p spectrum is displayed in Figure 6.4(b). For pure metallic zinc, the peaks fitted at 1014.53 and 1038.06 eV correspond to $Zn2p_{3/2}$ and $Zn2p_{1/2}$ respectively. Fe = O double metal cation bonding could be the cause of the signal at 525 eV. The Figure 6.4(f) shows the fitted peaks for the 2p lines namely $Fe2p_{3/2}$ (BE = 705.92 eV) and $Fe2p_{1/2}$ (BE = 719.02 eV) which are characteristic of pure metallic iron. The Ba3d peak can be divided into two components, $Ba3d_{5/2}$ and $Ba3d_{3/2}$, as shown in Figure 6.4(g). Barium in $BaTiO_3$ is represented by these peaks, which are located at 775.30 eV and 790.15 eV, respectively. The Ti2p peak is divided into two components ($Ti2p_{3/2}$ and $Ti2p_{1/2}$), as shown in Figure 6.4(c). These components can be deconvoluted into two peaks using Gaussian functions; two of these peaks are compatible with the $Ti2p_{3/2}$ and $Ti2p_{1/2}$ peaks of Ti^{4+} in $BaTiO_3$ and are positioned at approximately 455.27 eV and 469.29 eV [30].

[30] Nayak et al. 2014

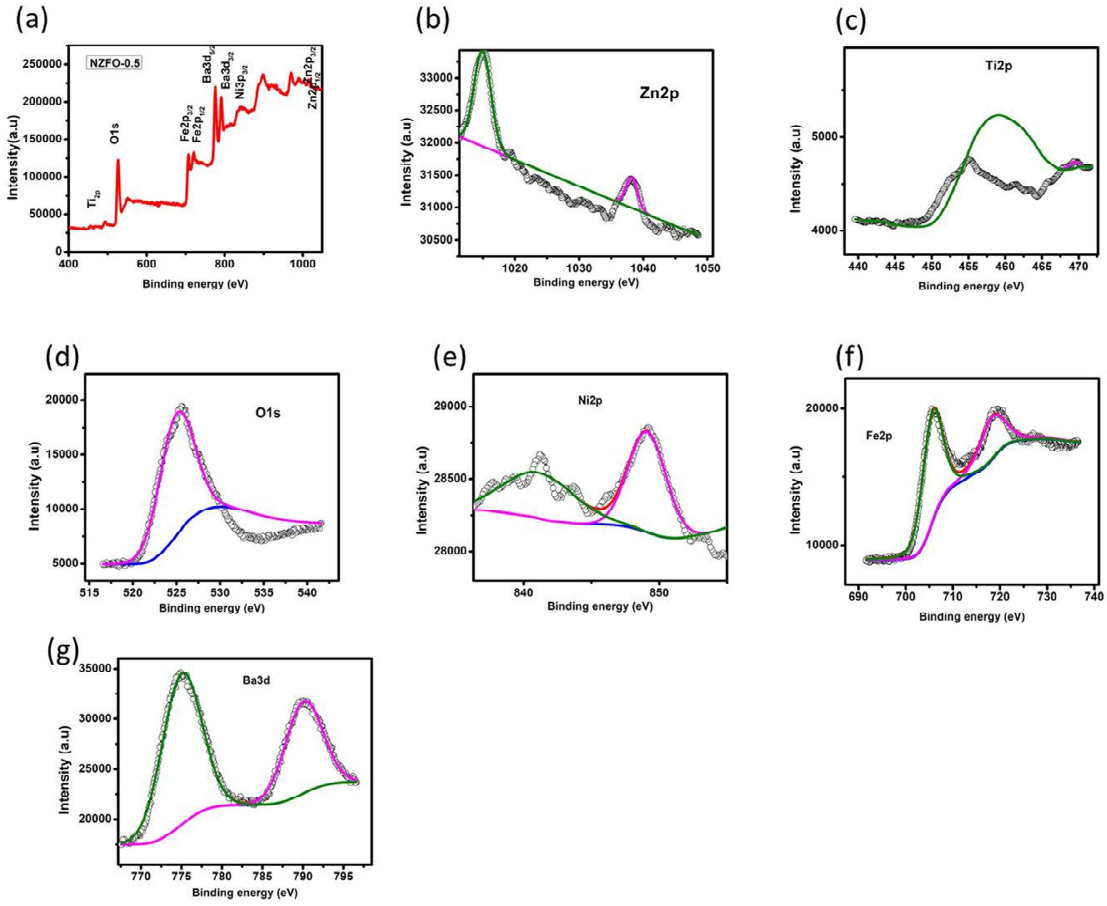

Fig 6.4.(a) XPS full spectra and high resolution spectra for the NZFO composite (b) Zn2p (c) Ti2p (d) O1s (e) Ni2p (f) Fe2p (g) Ba3d

Figure 6.5 displays the typical XPS core level spectra for the CZFO-0.5:BTO composite. The binding energies of Co2p and Zn2p are attributed to the Co^{2+} and Zn^{2+} ionic states in the samples. The conformed spinel crystalline structure (AB_2O_4) contains metal atoms in tetrahedral and octahedral sites. CoO phase's $Co2p_{1/2}$ and $Co2p_{3/2}$ spin-orbit peaks are represented by binding energies of 795.71 and 780.89 eV, respectively, in Figure 6.5(c) which depicts the Co2p XPS spectrum. The Figure 6.5(g) shows that Zinc exhibits binding energies of 1020.58 and 1043.33 eV, which are equivalent to $Zn2p_{3/2}$ and $Zn2p_{1/2}$ electrons in the Zn^{2+} oxidation state, respectively. The Figure 6.5(i) shows the peaks of $Fe2p_{3/2}$ and $Fe2p_{1/2}$ states which

are observed at 705.92 eV and 719.02 eV respectively[31]. The Ba3d peak is divided into two components ($Ba3d_{5/2}$ and $Ba3d_{3/2}$) in Figure 6.5(b). Barium in $BaTiO_3$ is represented by these peaks, which are located at 780.52 eV and 795.70 eV, respectively. The Ti2p peak is divided into two components ($Ti2p_{3/2}$ and $Ti2p_{1/2}$) in Figure 6.5(f). These components may be deconvoluted into two peaks using Gaussian functions, and they are roughly 457.96 eV and 463.53 eV, respectively, corresponding with the $Ti2p_{3/2}$ and $Ti2p_{1/2}$ peaks of Ti^{4+}in $BaTiO_3$[32]. The Figure 6.5(h) shows that the $Ba3p_{3/2}$ is positioned at 1062.01 eV.

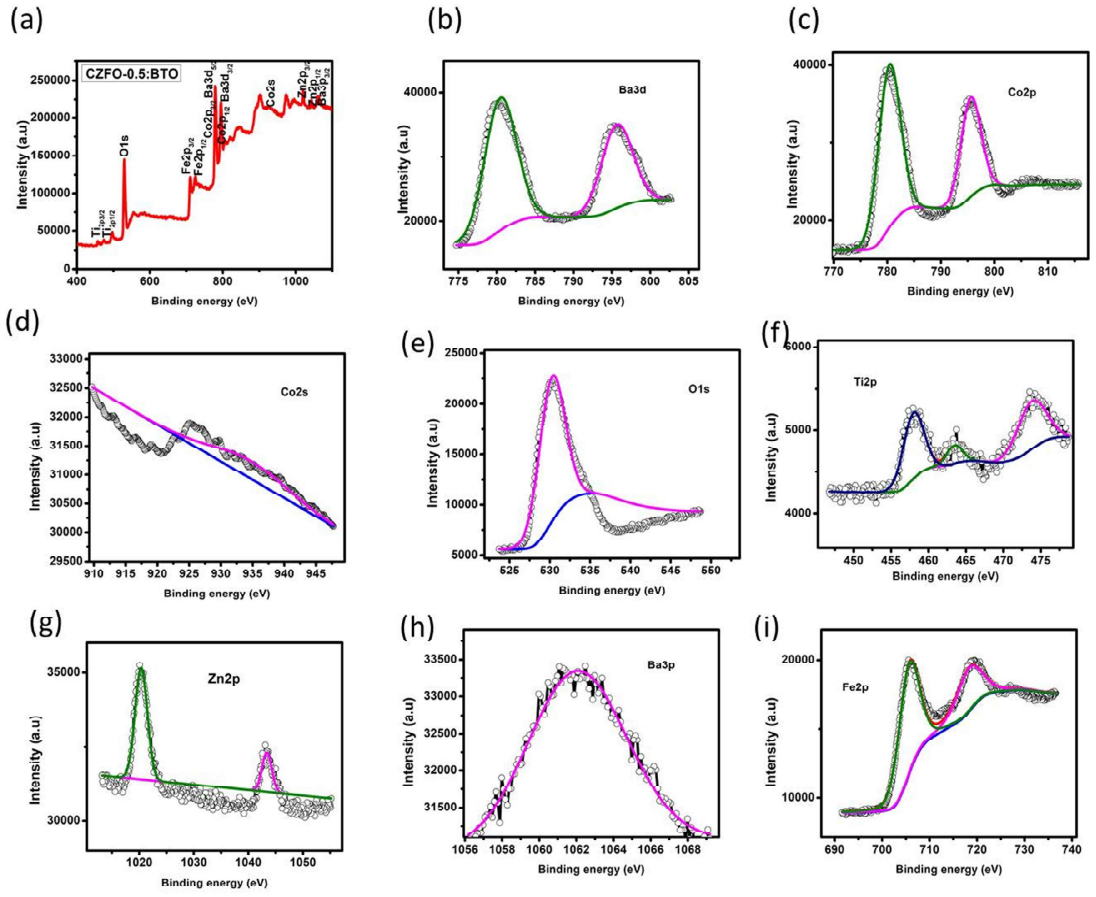

Fig 6.5. (a) XPS full spectra and high resolution spectra for the CZFO composite (b) Ba3d (c) Co2p (d) Co2s (e) O1s (f) Ti2p (g) Zn2p (h) Ba3p (i) Fe2p

[31] Vinuthna et al. 2019
[32] Erbe et al. 2018

Figure 6.6(a) displays the typical XPS full spectra for the BFO:BTO composite. The narrow scan spectra of the Bi4f, Fe2p, and O1s peaks were fitted using the software XPS PEAK 4.1, and the binding energies were adjusted using the C1 s peak at 284.5 eV after accounting for charge effects. The core level spectra for Bi4f are at 158.44 eV and 164.02 eV for 7/2 and 5/2 spin orbit doublet components, respectively, indicating that the bismuth ion has an oxidation state of +3. The peak around 525 eV may be related to double metal cation bonding Fe = O. Fitted peaks for the 2p line characteristic of pure metallic iron are $Fe2p_{3/2}$ (BE = 707.08 eV) and $Fe2p_{1/2}$ (BE = 719.85 eV). The Ba3d peak can be divided into two components, $Ba3d_{5/2}$ and $Ba3d_{3/2}$, as shown in Figure 6.6(b). Barium in $BaTiO_3$ is represented by these peaks, which are located at 775.97 eV and 791.69 eV, respectively. The Ti2p peak may be divided into two components ($Ti2p_{3/2}$ and $Ti2p_{1/2}$), as shown in Figure 6.6(f). These components can then be deconvoluted into two peaks using Gaussian functions; two of these peaks are compatible with the $Ti2p_{3/2}$ and $Ti2p_{1/2}$ peaks of Ti^{4+} in $BaTiO_3$ and are positioned at approximately 458.31 eV and 463.81 eV[33]. The Figure 6.6(g) shows the Ti2s is positioned at 554.3 eV[34]

[33] Erbe et al. 2018
[34] Bhuwal & Shelke 2013

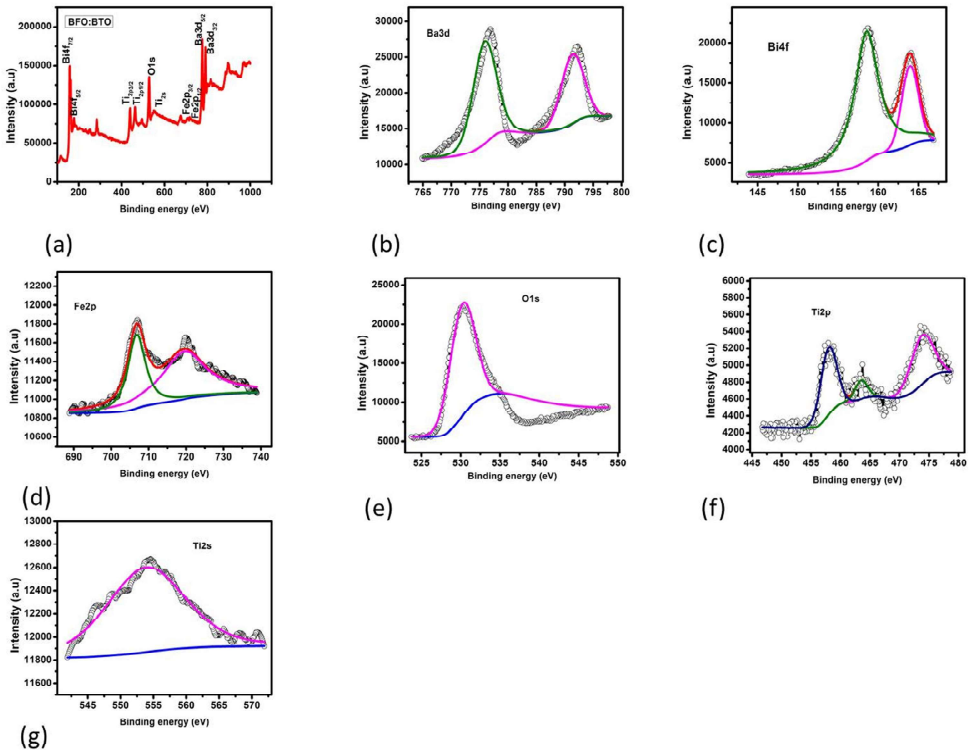

Fig 6.6.(a) XPS full spectra and high resolution spectra for the BFO composite (b) Ba3d (c) Bi4f (d) Fe2p (e) O1s (f) Ti2p (g) Ti2s

6.4 Dielectric Properties

Pellets of the prepared samples are used to study the dielectric properties. HP 4285A LCR meter is used to study the variation of dielectric constant (έ) and ac conductivity with frequency at room temperature in the range of 100kHz-5MHz[35].

Figure 6.7 shows the frequency variation of dielectric constant for the samples $NiFe_2O_4$- $BaTiO_3$ (2:1) and (1:2) and $Ni_{1-x}Zn_xFe_2O_4$- $BaTiO_3$ (x=0.3, 0.5, 0.7, 1) in the ratio 2:1. It is evident from the Figure that as frequency increases, the dielectric constant decreases.

[35] V.S et al. 2022

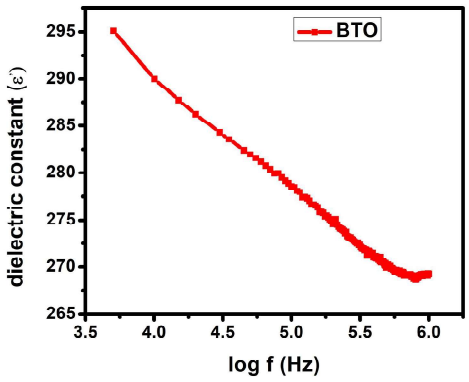
BTO
dielectric constant (ε')
log f (Hz)

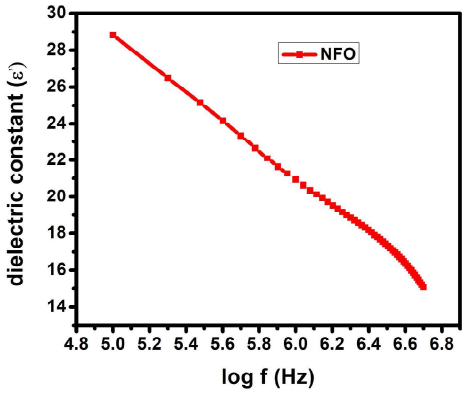
NFO
dielectric constant (ε')
log f (Hz)

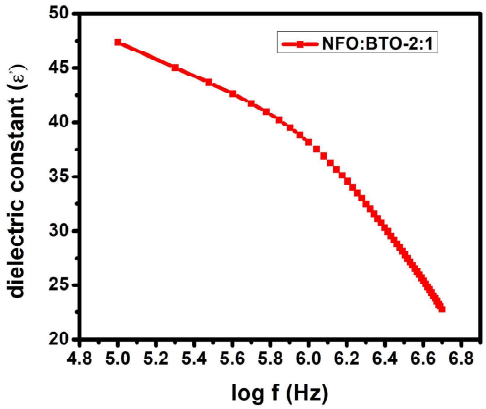
NFO:BTO-2:1
dielectric constant (ε')
log f (Hz)

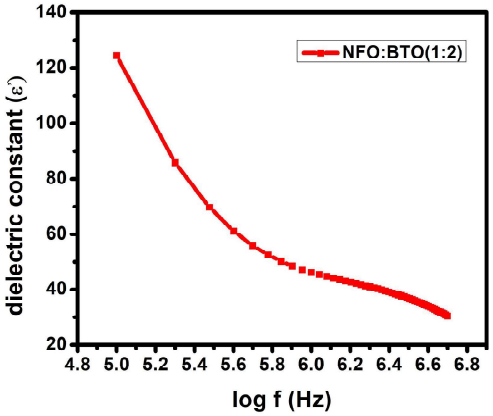
NFO:BTO(1:2)
dielectric constant (ε')
log f (Hz)

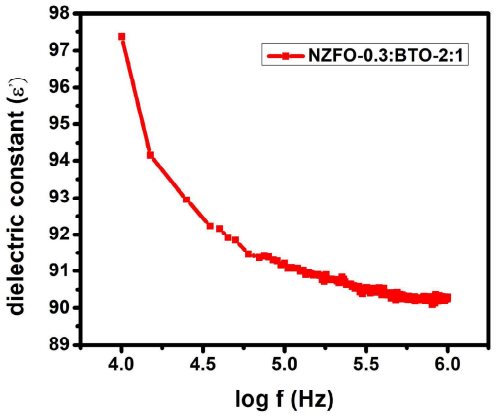
NZFO-0.3:BTO-2:1
dielectric constant (ε')
log f (Hz)

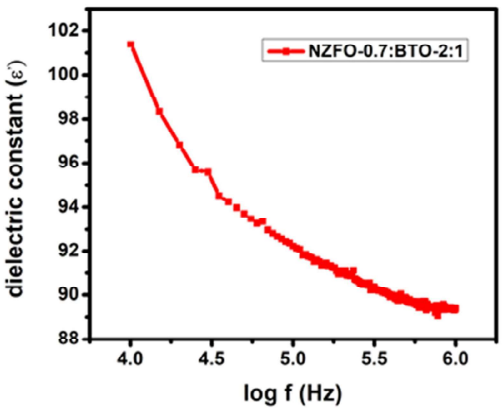
NZFO-0.7:BTO-2:1
dielectric constant (ε')
log f (Hz)

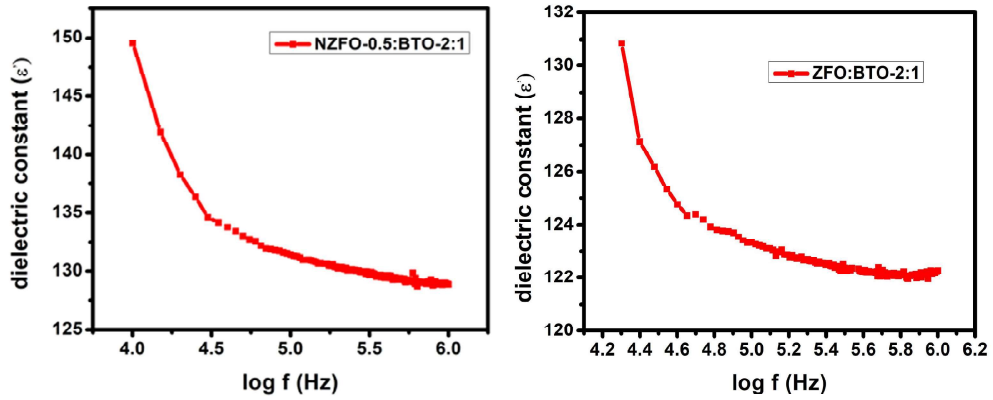

Fig 6.7 Variation of dielectric constant with frequency for the samples $BaTiO_3$, $NiFe_2O_4$-$BaTiO_3$(2:1),(2:1) and $Ni_{1-x}Zn_xFe_2O_4$- $BaTiO_3$ (x=0.3,0.5,0.7,1) with the ratio (2:1)

The dielectric dispersion can be explained based on Maxwell-Wagner polarization theory and Koop's two-layer model. The dielectric constant naturally falls as the frequency of the reversal field increases because the group of space charge carriers in the inhomogeneous dielectric structure set at a predetermined time to align their axes parallel to an alternating electric field. The decrease in the dielectric constant can be explained by the electron exchange between Fe^{2+} and Fe^{3+} ions. These ions cannot follow the alternate electric field after a certain critical frequency. The high value of the dielectric constant at lower frequencies is ascribed to space charge polarization due to inhomogeneous dielectric structure. The presence of two different phases is verified from X-ray diffraction studies and crystallite size confirmed formation of nanocomposite. These nanocomposites have phases of orientation or facets in the direction of growth with minimum energy guiding to thermodynamic phase stability. So the dielectric polarization of the composite samples would be influenced by structures and phases of the components. In the present case, ferromagnetic and ferroelectric-based materials are surrounding each other or in contact with each other. These two components have different permittivity, conductivity, and structure. By applying an electric field varying with frequency, the space charge produced by one could be impeded by the other phase of the nanocomposite. As a consequence of this interfacial polarization arises which follows the Maxwell-Wagner type of interfacial polarization[36].

[36] Mukherjee 2017

The value of the dielectric constant of all sample shows that they are high-K- dielectric materials and these materials can be used in gate dielectrics, capacitor dielectrics, and photoelectrochemical cells. Ferroelectric random access memory (FeRAM), which is non-volatile, is made using the high K-dielectrics. The fabrication of inexpensive field-effect transistors is a significant additional use for high-K gate dielectrics[37]. The dielectric constant found to be higher for composites with zinc doped and also increases with barium titanate content. So, we can modify dielectric constant by zinc doping or barium titanate content. The maximum value of dielectric constant was found to be NZFO-0.5: BTO composites.

Figures 6.8 show the variation of the real part of the permittivity versus frequency of the $Co_{1-x}Zn_xFe_2O_4$- $BaTiO_3$ (x=0, 0.3, 0.5, 0.7, 1) samples. These figures show that the dielectric permittivity values exhibit a feature of Maxwell-Wagner type interfacial polarization, where they decrease at lower frequencies and remain constant at higher frequencies. The electric dissipation happens at lower frequency ranges specifying the interfacial polarization of Maxwell Wagner type for all samples based on Koop's phenomenological theory. The dissipation energy occurring at lower frequencies is because of all types of polarization mechanisms that happen. At higher frequencies, the phenomenon of space charge polarization is shown because of the inhomogenous dielectric structure, which are confirmed by the higher value of the dielectric constant[38]. The value of the dielectric constant shows the samples are High-K- dielectric materials and these materials are used in gate dielectrics, capacitor dielectrics, and photoelectrochemical cells[39].

[37] Singh & Ulrich 1999; V.S et al. 2022
[38] Mahalakshmi et al. 2019
[39] Singh & Ulrich 1999

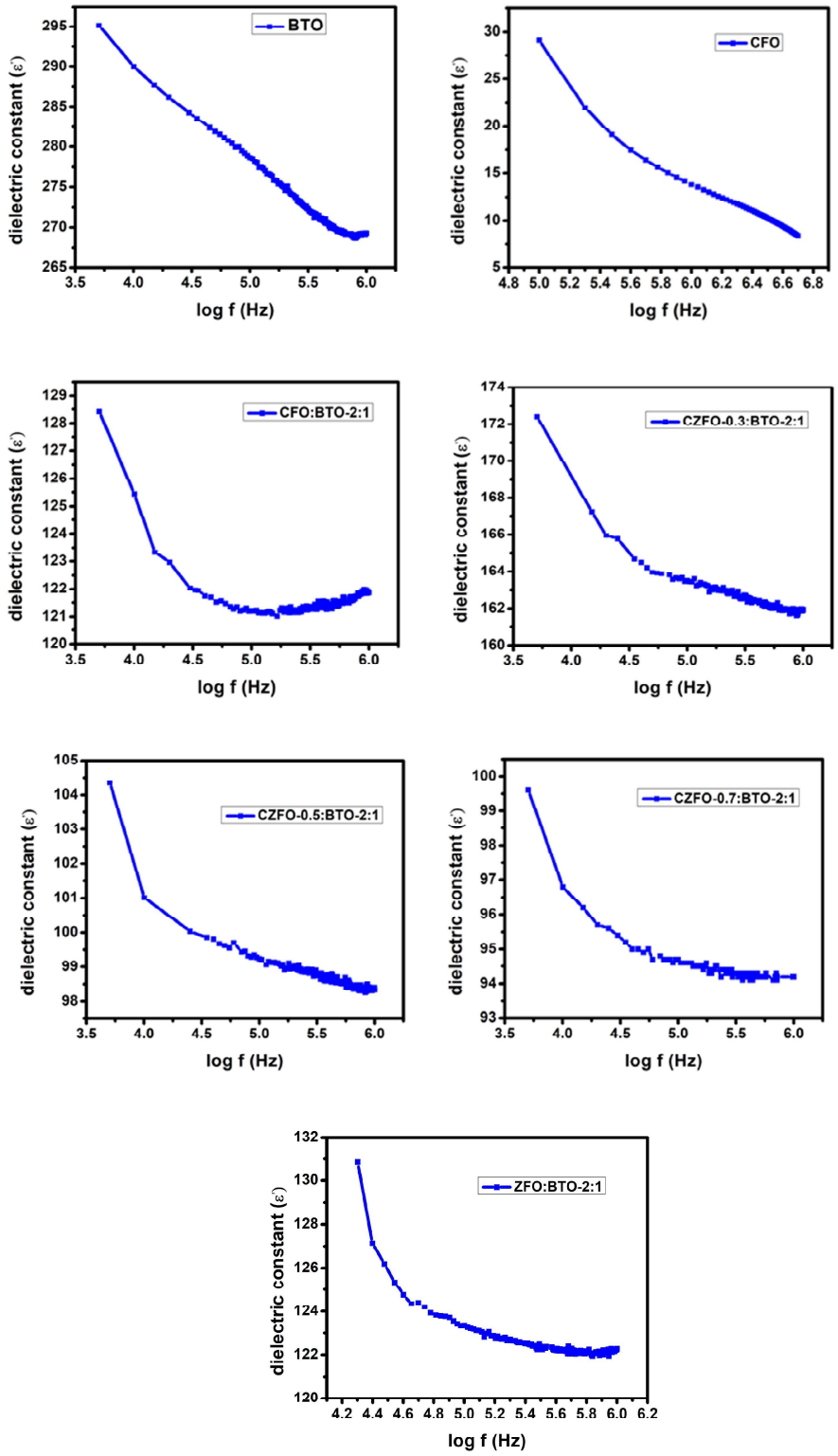

Fig 6.8. Variation of dielectric constant with frequency for the CZFO samples.

The variation of dielectric constant with frequency for composites of $Bi_{1-x}Sr_xFeO_3$ with $BaTiO_3$ samples are shown in Figure 6.9. The Maxwell-Wagner type interfacial polarization is the reason of the decrement in dielectric constant with increasing frequency[40] and space charge polarization and is in agreement with the Koop's phenomenological theory[41]. The dielectric constant value is in close agreement with the published values[42].

[40] Spies et al. 1992
[41] Meaz et al. 2003
[42] Baji & Abtahi 2013

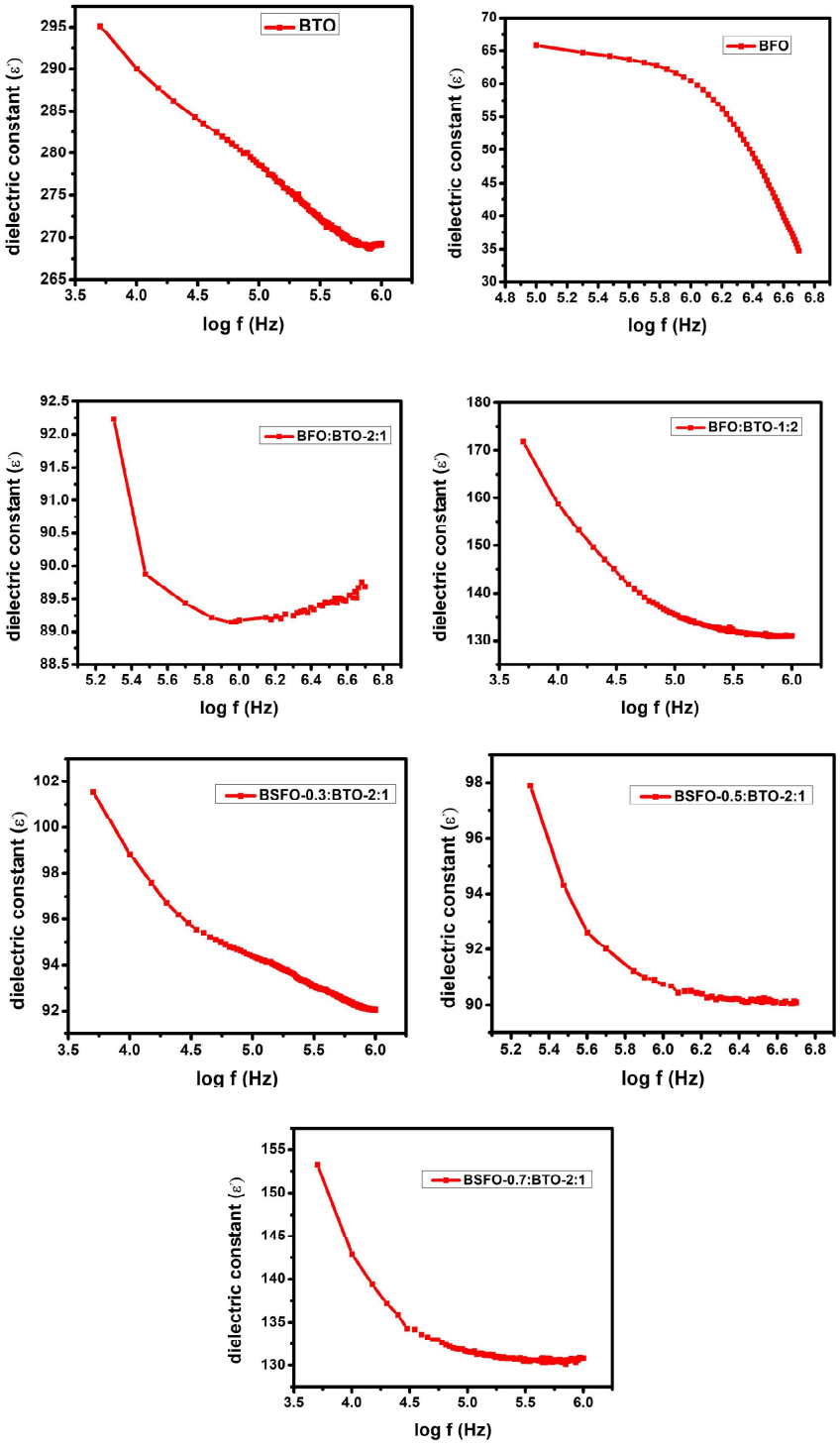

Fig 6.9. Variation of dielectric constant with frequency for the BSFO composites.

The value of dielectric constant is found to depend greatly on the composition of ferrite component present in it. The dielectric constant value is found to be very high for BSFO-0.7: BTO samples. It is consistent with the values of dielectric constant obtained and provided in Chapter 5. When the strontium is doped into the bismuth ferrite samples the value of the dielectric constant increases and a maximum value of dielectric constant is obtained for BSFO-0.7: BTO sample as expected. These results indicate that these materials can be used to tailor materials with specific dielectric constant values and can be used in capacitor dielectrics[43]. At larger frequencies the hopping electrons cannot follow the applied field and this is the cause of the decrement in the dielectric parameters.

6.4.1 Tuning of Dielectric Constant Composites

The main observation from the dielectric studies of the composites is that the dielectric constant of the composites except a few obeys an empirical relation as given below.

$$\boldsymbol{\varepsilon_{composite} = w_1 * \varepsilon_1 + w_2 * \varepsilon_2}$$

Where w_1 is the weight fraction of the component one, ε_1 is the dielectric constant of the component one and w_2 is the weight fraction of the component two, ε_2 is the dielectric constant of the component two.

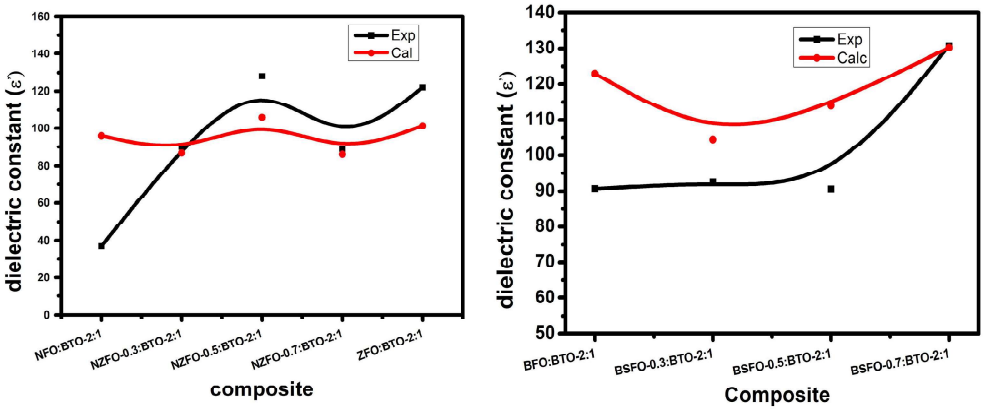

[43] Singh & Ulrich 1999

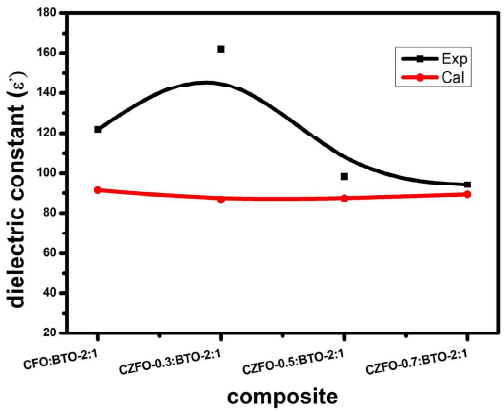

Fig 6.10. Variation of dielectric constant with composition (experimental and calculated).

The variation in some samples may be due to the slight difference in weight fraction. This result is very significant in tuning the dielectric constant for various applications.

6.5 Ferroelectric properties

Ferroelectric properties were studied by measuring the polarization (P) against the electric field (E). Figure 6.11 shows the polarization versus electric field (P-E) loops of all nickel-zinc ferrite composites. From the ferroelectric hysteresis loop, the ferroelectric behavior of the composite is evident. The value is almost same for all composites because of the similar crystallite size and tetragonality. The low value of polarization is due to the paraelectric effect of the nickel ferrite phase[44]. From the figure, it is clear that all nickel-zinc ferrite-barium titanate compositions possessed similar electrical stability since the breakdown field obtained for $Ni_{0.7}Zn_{0.3}Fe_2O_4$-$BaTiO_3$, $Ni_{0.5}Zn_{0.5}Fe_2O_4$- $BaTiO_3$, and $Ni_{0.3}Zn_{0.7}Fe_2O_4$- $BaTiO_3$(2:1) was 50 kV/cm, 49.57 kV/cm and 49.33 kV/cm respectively. $NiFe_2O_4$- $BaTiO_3$(1:1), $NiFe_2O_4$-$BaTiO_3$(2:1) and $NiFe_2O_4$- $BaTiO_3$(1:2) nanoparticles are suppressed the leakage current, so these materials achieve a saturated polarization[45]. $Ni_{0.7}Zn_{0.3}Fe_2O_4$-

[44] Liu et al. 2013
[45] Naganuma et al. 2008

$BaTiO_3$(2:1), $Ni_{0.5}Zn_{0.5}Fe_2O_4$- $BaTiO_3$(2:1), $Ni_{0.3}Zn_{0.7}Fe_2O_4$- $BaTiO_3$(2:1) and $ZnFe_2O_4$-$BaTiO_3$(2:1) shows an expanded shape because of the high leakage current density[46].

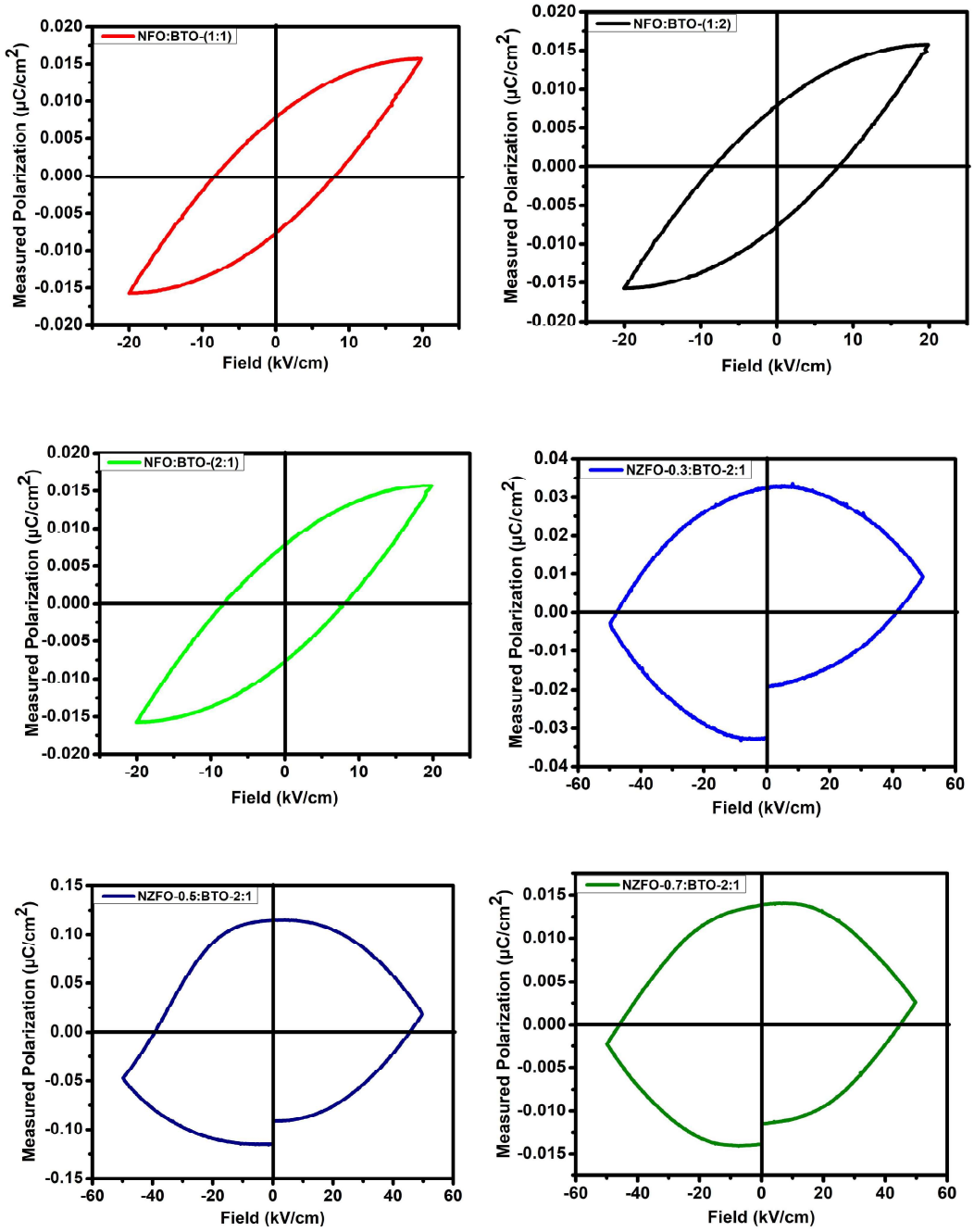

[46] Naganuma et al. 2010

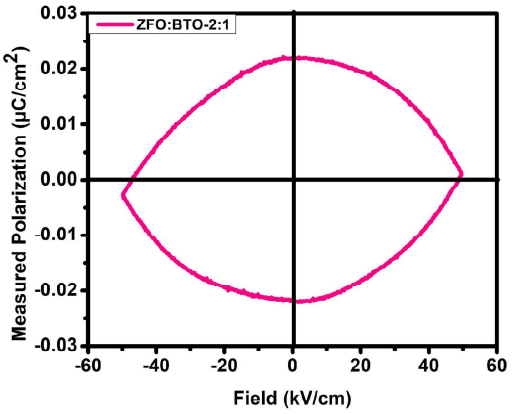

Fig 6.11. Polarization (P) against electric field(E) for all composites

The ferroelectric measurements for zinc ferrite-barium titanate composites are reported for the first time. The zinc ferrite is a multiferroic material and has a narrow P-E loop. But for the composite have a roundish P-E loop can be observed due to the involvement of high leakage current[47]. It is observed that the ferroelectric parameters obtained are small in comparison to the reported values. The obtained result falls much less than 1 μC/cm^2. Ferroelectric properties are tabulated in Table 6.5.

Table 6.5. Saturation polarization, Remanent Polarization and Coercive Field for all compositions

Composition	Saturation polarization (μC/cm^2)	Remanent Polarization μC/cm^2)	Coercive Field(kV/cm)
NFO:BTO-(1:1)	0.0159	0.0078	8.64
NFO:BTO (1:2)	0.0156	0.0080	8.34
NFO:BTO (2:1)	0.0157	0.0079	8.24

Figure 6.12 shows that the cobalt ferrite:barium titanate composite nanoparticles also exhibit ferroelectric nature. Ferroelectric properties were studied by measuring the polarization(P) against the electric field(E) up to 50KV/cm. From the Figure, it is clear that the breakdown field obtained for $CoFe_2O_4$- $BaTiO_3$, $Co_{0.5}Zn_{0.5}Fe_2O_4$- $BaTiO_3$, and $Co_{0.3}Zn_{0.7}Fe_2O_4$- $BaTiO_3$(2:1) was 49.81 kV/cm, 49.57 kV/cm and 49.81 kV/cm

[47] Kumar et al. 2021; Zheng & Wu 2016

respectively. All the ferroelectric loops shows an expanded shape which specifies the high leakage current density[48]. The low value of polarization is due to the paraelectric effect of the cobalt ferrite phase.

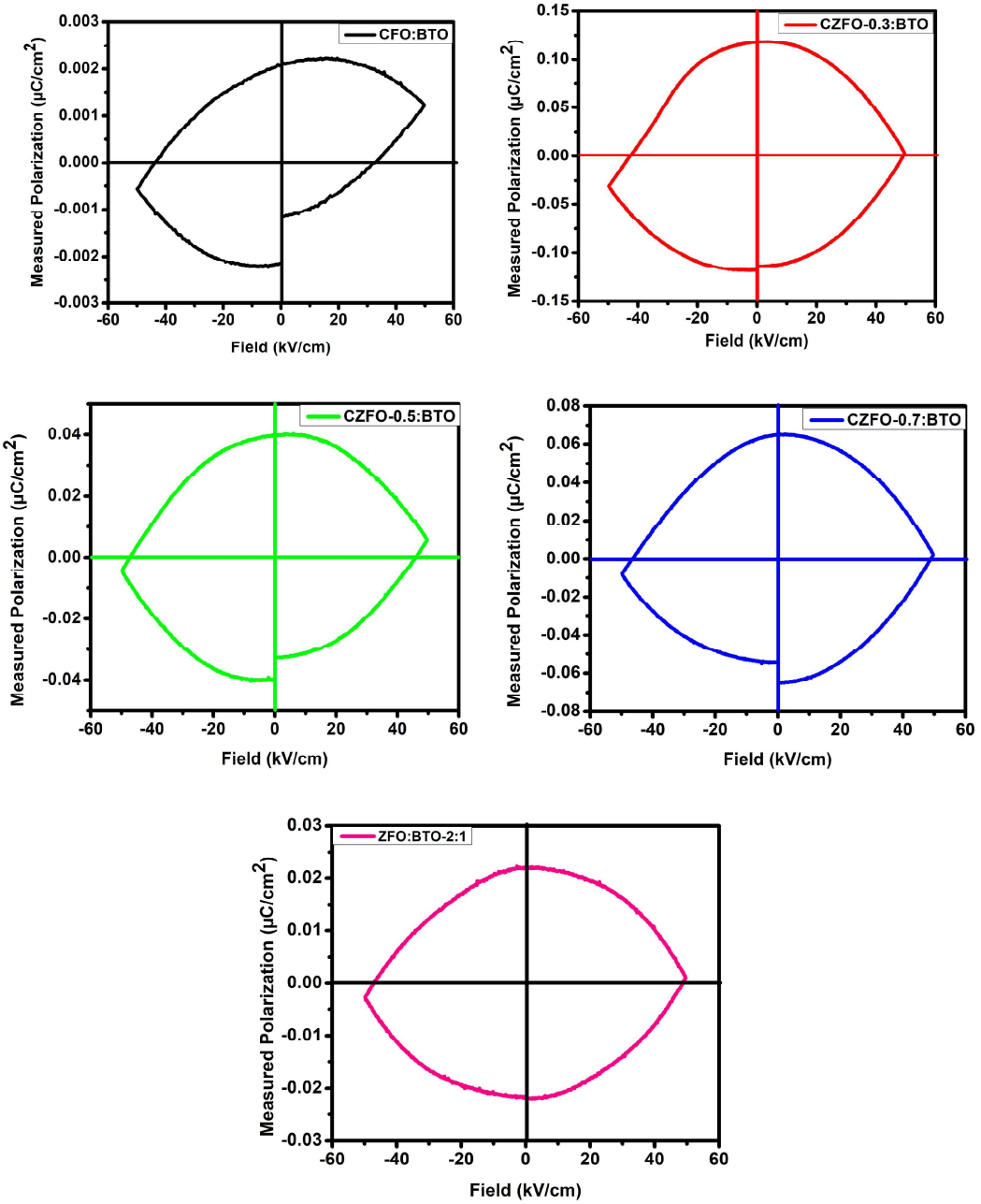

Fig 6.12. Polarization (P) against electric field(E) for all composites

[48] Naganuma et al. 2010

Fig 6.13 represents the polarization with the electric field (P-E) loops for $BaTiO_3$ with $Bi_{1-x}Sr_xFeO_3$ samples. Ferroelectric properties are explained by measuring the polarization (P) against the electric field(E) up to 20KV/cm.

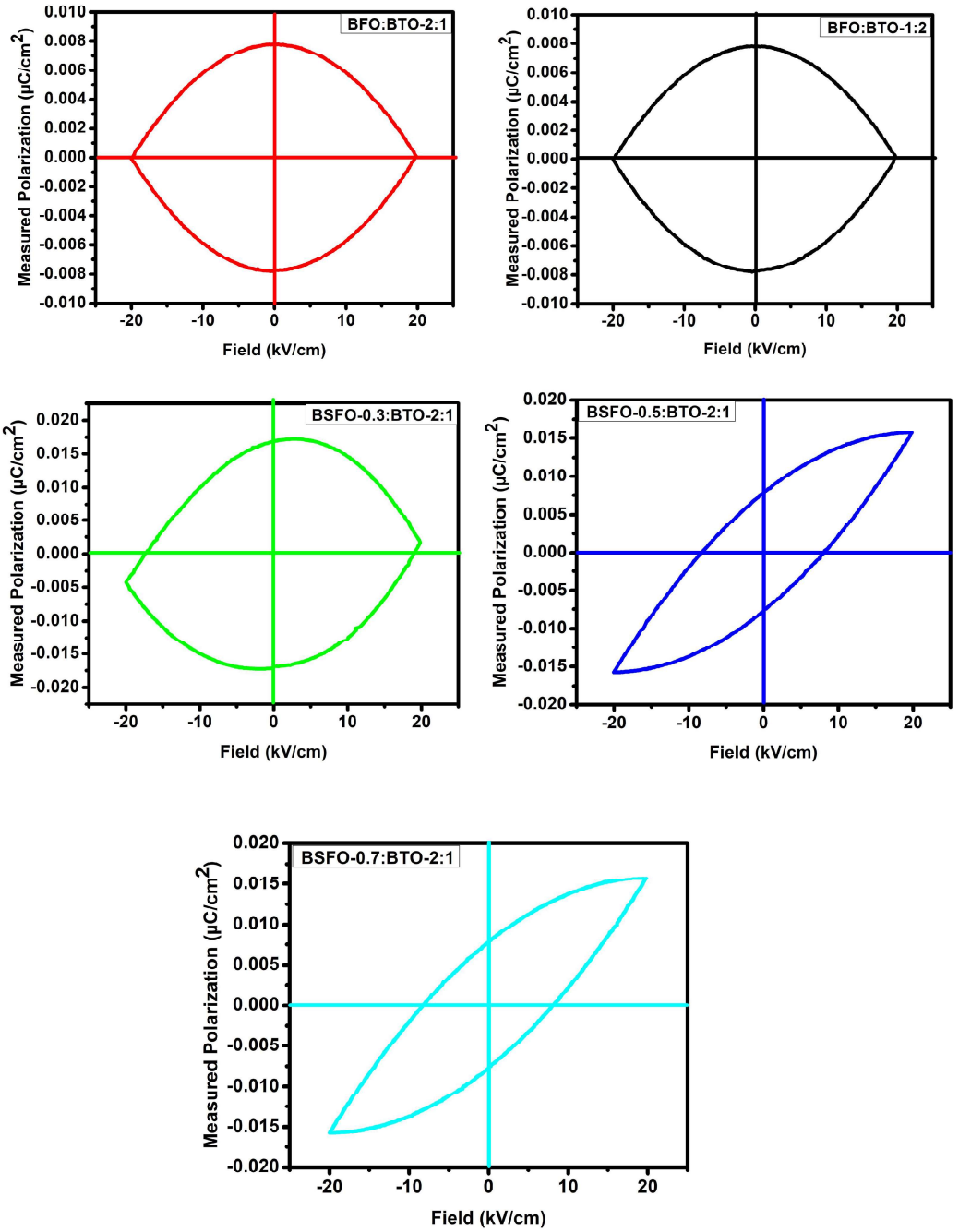

Fig 6.13. Polarization (P) against electric field (E) for all composites

From the above ferroelectric hysteresis loop, it is clear that all samples show the ferroelectric behavior. From the XRD, it is clear that the secondary phase of bismuth ferrite $Bi_2Fe_4O_9$ are present for BFO: BTO (2:1), BFO:BTO(1:2) and BSFO-0.3:BTO samples. The secondary phase lead to increase the conductivity and leakage current. BFO: BTO (2:1) and BSFO-0.3: BTO show an enlarge shape which assigns to high leakage current density[49]. But for BSFO-0.5: BTO and BSFO-0.7:BTO have suppressed the leakage current because there is no presence of secondary phase $Bi_2Fe_4O_9$ [50]. The value of measured polarization value is smaller than the reported values. The reported value of saturation magnetization is ~22 $\mu C/cm^2$ [51]. Ferroelectric properties are tabulated in Table 6.6.

Table 6.6. Saturation polarization, Remanent Polarization and coercive field for all compositions.

Composition	Saturation polarization($\mu C/cm^2$)	Remanent Polarization($\mu C/cm^2$)	Coercive Field(kV/cm)
BSFO-0.5:BTO-2:1	0.0158	0.0081	8.22
BSFO-0.7:BTO-2:1	0.0156	0.0081	8.43

6.6 Conclusion

A series of $BaTiO_3$- and $NiFe_2O_4$ (NF: BTO) in various proportions such as (1:1, 1:2, 2:1), $Ni_{1-x}Zn_xFe_2O_4$- $BaTiO_3$ (x=0.3,0.5,0.7,1) with the ratio 2:1 has been successfully prepared using nickel ferrite and barium titanate. The composite's material formation was confirmed by XRD. XRD confirms the tetragonal perovskite structure of $BaTiO_3$ and the cubic spinel structure of $Ni_{1-x}Zn_xFe_2O_4$ phases. The c/a ratio confirms the tetragonality of all $BaTiO_3$ samples. The dielectric studies showed that the dielectric constant decreases with increasing frequency. The high value of the dielectric constant was observed for all samples and this can be utilized for application in capacitor dielectrics and gate dielectrics. Observation of ferroelectric hysteresis loops indicates that ferroelectric properties exist at room temperature in the nickel ferrite-barium

[49] Naganuma et al. 2010
[50] Naganuma et al. 2008
[51] Zheng & Wu 2016

titanate composites. The presence of highly conductive and non-ferroelectric ferrite phases has resulted in the decay of ferroelectric characteristics, as demonstrated by roundish hysteresis ferroelectric loops.

$Co_{1-x}Zn_xFe_2O_4$- $BaTiO_3$ (x=0, 0.3, 0.5, 0.7, 1) with the ratio 2:1 was successfully prepared by solid-state reaction method. XRD pattern confirms the cubic spinel structure of cobalt ferrite nanoparticles and barium titanate with tetragonal structure. The dielectric studies reveal that dielectric constant decreases with increasing frequency. Ferroelectric hysteresis loops shows the existence of ferroelectric properties in room temperature. This work offers a new method for improving the characteristics of ferroelectric materials devoid of lead.

A series of $BiFeO_3$-$BaTiO_3$ (BFO: BTO) in various proportions such as (1:2, 2:1), $Bi_{1-x}Sr_xFeO_3$ - $BaTiO_3$ (x=0.3,0.5,0.7) with the ratio 2:1 is successfully prepared. XRD studies confirms pure tetragonal perovskite structure of $BaTiO_3$ and rhombohedral structure for pure bismuth ferrite as well as for strontium doped samples. The dielectric studies reveal that with increasing frequency the dielectric constant value decreases. Developed the empirical formula for tuning the dielectric constant.

In Summary, for the samples CZFO-0.3: BTO, BFO: BTO-1:2, and NZFO-0.5: BTO, a high dielectric constant is found. The dielectric constant can be modified by doping with strontium and zinc.

References

Baji, A., & Abtahi, M. (2013). Fabrication of barium titanate-bismuth ferrite fibers using electrospinning. *Advances in Nano Research*, *1*(4), 183–192. https://doi.org/10.12989/ANR.2013.1.4.183

Basantakumar Sharma, H. (2017). Multiferroic bismuth ferrite thin film and bismuth ferrite-cobalt ferrite nanocomposites. *Ferroelectrics*, *516*(1), 90–97. https://doi.org/10.1080/00150193.2017.1362289

Bhuwal, D., & Shelke, V. (2013). Synthesis of single phase BiFeO3 by one step method. *AIP Conference Proceedings*, *1536*(January 2017), 817–818. https://doi.org/10.1063/1.4810478

Chauhan, R., & Srivastava, R. C. (2016). Various properties of the 0.6BaTiO3-0.4Ni0.5Zn0.5Fe2O4 multiferroic nanocomposite. *Pramana - Journal of Physics*, *87*(4), 2–7. https://doi.org/10.1007/s12043-016-1263-1

Corral-Flores, V., Bueno-Baqués, D., & Ziolo, R. F. (2010). Synthesis and characterization of novel CoFe2O4-BaTiO3 multiferroic core-shell-type nanostructures. *Acta Materialia*, *58*(3), 764–769. https://doi.org/10. 1016/j. actamat.2009.09.054

de Andrade, M. C., Carneiro, G. N., Moreira, E. L., Araújo, J. C., & Moraes, V. C. A. (2014). Synthesis and characterization of barium titanate by solid-state reaction. *Materials Science Forum*, *802*(December), 285–290. https://doi.org/10.4028/www.scientific.net/MSF.802.285

De Leo, C. T., Dannangoda, G. C., Hobosyan, M. A., Held, J. T., Samghabadi, F. S., Khodadadi, M., Litvinov, D., Mkhoyan, K. A., & Martirosyan, K. S. (2021). Carbon combustion synthesis of Janus-like particles of magnetoelectric cobalt ferrite and barium titanate. *Ceramics International*, *47*(4), 5415–5422. https://doi.org/10.1016/J.CERAMINT.2020.10.123

Erbe, A., Nayak, S., Chen, Y. H., Niu, F., Pander, M., Tecklenburg, S., & Toparli, C. (2018). How to probe structure, kinetics, and dynamics at complex interfaces in situ and operando by optical spectroscopy. *Encyclopedia of Interfacial Chemistry: Surface Science and Electrochemistry*, 199–219. https://doi.org/10.1016/B978-0-12-409547-2.14061-2

Humera, S. N., Noor, H., Riaz, S., & Naseem, S. (2016). Dielectric and structural analysis of barium titanate nanoparticles prepared by nano ball milling technique. *World Congress on Adv. Civ. Envir. Mat. Res*, *September*.

Hussain, T., Siddiqi, S. A., Atiq, S., & Awan, M. S. (2013). Induced modifications in the properties of Sr doped BiFeO3 multiferroics. *Progress in Natural Science: Materials International*, *23*(5), 487–492. https://doi.org/10.1016/j. pnsc. 2013. 09.004

Kawamura, G., Oura, K., Tan, W. K., Goto, T., Nakamura, Y., Yokoe, D., Deepak, F. L., Hajraoui, K. El, Wei, X., Inoue, M., Muto, H., Yamaguchi, K., Boccaccini, A. R., & Matsuda, A. (2019). Nanotube array-based barium titanate–cobalt ferrite composite film for affordable magnetoelectric multiferroics. *Journal of Materials Chemistry C*, *7*(32), 10066–10072. https://doi.org/10.1039/C9TC02442E

Khan, S. B., Irfan, S., & Lee, S. L. (2019). Influence of Zn+2 doping on ni-based nanoferrites; (Ni1−x ZnxFe2O4). *Nanomaterials*, *9*(7). https://doi.org/10.3390/nano9071024

Krishna, K. R., Kumar, K. V., & Ravinder, D. (2012). Structural and Electrical Conductivity Studies in Nickel-Zinc Ferrite. *Advances in Materials Physics and Chemistry*, *02*(03), 185–191. https://doi.org/10.4236/ampc.2012.23028

Kumar, V., Kumar, N., Bhushan Das, S., Singh, R. K., Sarkar, K., & Kumar, M. (2021). Sol-gel assisted synthesis and tuning of structural, photoluminescence, magnetic and multiferroic properties by annealing temperature in nanostructured zinc ferrite. *Materials Today: Proceedings*, *47*(May), 6242–6248. https://doi.org/10.1016/j.matpr.2021.05.215

Leonel, L. V., Righi, A., Mussel, W. N., Silva, J. B., & Mohallem, N. D. S. (2011). Structural characterization of barium titanate–cobalt ferrite composite powders. *Ceramics International*, *37*(4), 1259–1264. https://doi.org/10.1016/J.CERAMINT.2011.01.017

Lin, Q., Xu, J., Yang, F., Lin, J., Yang, H., & He, Y. (2018). Magnetic and Mössbauer spectroscopy studies of zinc-substituted cobalt ferrites prepared by the sol-gel method. *Materials*, *11*(10), 1–12. https://doi.org/10.3390/ma11101799

Liu, Y., Wu, Y., Li, D., Zhang, Y., Zhang, J., & Yang, J. (2013). A study of structural, ferroelectric, ferromagnetic, dielectric properties of NiFe2O4-BaTiO3 multiferroic composites. *Journal of Materials Science: Materials in Electronics*, *24*(6), 1900–1904. https://doi.org/10.1007/s10854-012-1032-y

Mahalakshmi, S., Jayasri, R., Nithiyanatham, S., Swetha, S., & Santhi, K. (2019). Magnetic interactions and dielectric behaviour of cobalt ferrite and barium titanate multiferroics nanocomposites. *Applied Surface Science*, *494*, 51–56. https://doi.org/10.1016/J.APSUSC.2019.07.096

Meaz, T. M., Attia, S. M., & Abo El Ata, A. M. (2003). Effect of tetravalent titanium ions substitution on the dielectric properties of Co-Zn ferrites. *Journal of Magnetism and Magnetic Materials*, *257*(2–3), 296–305. https://doi.org/10.1016/S0304-8853(02)01212-X

Mukherjee, S. (2017). *Studies on Dielectric , P-E Loop Measurements and Pl Spectra Analysis Prepared by Solution Method*. *7*(2), 413–420.

Naganuma, H., Inoue, Y., & Okamura, S. (2008). Dependence of ferroelectric and magnetic properties on measuring temperatures for polycrystalline BiFeO3 films. *IEEE Transactions on Ultrasonics, Ferroelectrics, and Frequency Control*, *55*(5), 1046–1050. https://doi.org/10.1109/TUFFC.2008.754

Naganuma, H., Inoue, Y., & Okamura, S. (2010). Evaluation of ferroelectric hysteresis loops of leaky multiferroic BiFeO3 films using a system with a high driving frequency of 100 kHz system. *Journal of the Ceramic Society of Japan*, *118*(1380), 656–658. https://doi.org/10.2109/jcersj2.118.656

Nayak, S., Sahoo, B., Chaki, T. K., & Khastgir, D. (2014). Facile preparation of uniform barium titanate (BaTiO3) multipods with high permittivity: Impedance and temperature dependent dielectric behavior. *RSC Advances*, *4*(3), 1212–1224. https://doi.org/10.1039/c3ra44815k

Pakalniškis, A., Lukowiak, A., Niaura, G., Głuchowski, P., Karpinsky, D. V., Alikin, D. O., Abramov, A. S., Zhaludkevich, A., Silibin, M., Kholkin, A. L., Skaudžius, R., Strek, W., & Kareiva, A. (2020). Nanoscale ferroelectricity in pseudo-cubic sol-gel derived barium titanate - bismuth ferrite (BaTiO3– BiFeO3) solid solutions. *Journal of Alloys and Compounds*, *830*, 1–22. https://doi.org/10.1016/j. jallcom. 2020.154632

Schuster, H., Barter, P. J., Stender, S., Cheung, R. C., Bonnet, J., Morrell, J. M., Watkins, C., Kallend, D., & Raza, A. (2004). Effects of switching statins on achievement of lipid goals: Measuring Effective Reductions in Cholesterol Using Rosuvastatin Therapy (MERCURY I) study. *American Heart Journal*, *147*(4), 705–712. https://doi.org/10.1016/j.ahj.2003.10.004

Scott, J. F. (2007). Multiferroic memories. *Nature Materials 2007 6:4*, *6*(4), 256–257. https://doi.org/10.1038/nmat1868

Singh, R., & Ulrich, R. K. (1999). High and low dielectric constant materials. *Electrochemical Society Interface*, *8*(2), 26–30.

Slimani, Y., Almessiere, M. A., Güner, S., Tashkandi, N. A., Baykal, A., Sarac, M. F., Nawaz, M., & Ercan, I. (2019). Calcination effect on the magneto-optical properties of vanadium substituted NiFe 2 O 4 nanoferrites. *Journal of Materials Science: Materials in Electronics*, *0123456789*. https://doi.org/10.1007/s10854-019-01243-x

Slimani, Y., Almessiere, M. A., Shirsath, S. E., Hannachi, E., Yasin, G., Baykal, A., Ozçelik, B., & Ercan, I. (2020). Investigation of structural, morphological, optical, magnetic and dielectric properties of (1-x)BaTiO3/xSr0. 92Ca0. 04Mg0. 04Fe12O19 composites. *Journal of Magnetism and Magnetic Materials*, *510*(January). https://doi.org/10.1016/j.jmmm.2020.166933

Slimani, Yassine, Shirsath, S. E., Hannachi, E., Almessiere, M. A., Aouna, M. M., Aldossary, N. E., Yasin, G., Baykal, A., Ozçelik, B., & Ercan, I. (2021). (BaTiO3)1-x + (Co0.5Ni0.5Nb0.06Fe1.94O4)x nanocomposites: Structure, morphology, magnetic and dielectric properties. *Journal of the American Ceramic Society*, *104*(11), 5648–5658. https://doi.org/10.1111/jace.17931

Spies, W., Maller, A., Linkemann, J., Frank, A., Wagner, M., Kozhuharov, C., Franzke, B., Beckert, K., Bosch, F., Eickhoff, H., Jung, M., Klepper, O., König, W., Mokler, P. H., Moshammer, R., Nolden, F., Schaaf, U., Spädtke, P., Steck, M., … Badnell, N. R. (1992). Dielectronic and radiative recombination of lithiumlike gold. *Physical Review Letters*, *69*(19), 2768–2771. https://doi.org/ 10.1103/ PhysRevLett.69.2768

Sugimoto, M. (1999). The Past, Present, and Future of Ferrites. *Journal of the American Ceramic Society*, *82*(2), 269–280. https://doi.org/10.1111/j.1551-2916.1999. tb20058.x

V.S, S., Gopalan, V. E., Al-Omari, I. A., & Malini, K. A. (2022). Superparamagnetic Nickel Ferrite Nanoparticles Doped with Zinc by Modified Sol–gel Method. *Journal of Superconductivity and Novel Magnetism 2021*, 1–10. https://doi.org/10.1007/S10948-021-06110-7

Vijatovic Petrovic, M. M., Dzunuzovic, A., Bobic, J. D., Ilic, N., Stijepovic, I., & Stojanovic, B. D. (2020). Study of barium titanate/nickel-zinc ferrite based composites: Electrical and magnetic properties and humidity sensitivity. *Processing and Application of Ceramics*, *14*(1), 9–18. https://doi.org/ 10.2298/ PAC2001009V

Vinuthna, C. H., Chandra Babu Naidu, K., Chandra Sekhar, C., & Dachepalli, R. (2019). Magnetic and antimicrobial properties of cobalt-zinc ferrite nanoparticles synthesized by citrate-gel method. *International Journal of Applied Ceramic Technology*, *16*(5), 1944–1953. https://doi.org/10.1111/ijac.13276

Zali, N. M., Mahmood, C. S., Mohamad, S. M., Foo, C. T., & Murshidi, J. A. (2014). X-ray diffraction study of crystalline barium titanate ceramics. *AIP Conference Proceedings*, *1584*(January), 160–163. https://doi.org/10.1063/1.4866124

Zheng, T., & Wu, J. (2016). Quenched bismuth ferrite-barium titanate lead-free piezoelectric ceramics. *Journal of Alloys and Compounds*, *676*, 505–512. https://doi.org/10.1016/j.jallcom.2016.03.205

Chapter 7

MAGNETIC AND MULTIFERROIC STUDIES ON NANOCOMPOSITES

MAGNETIC AND MULTIFERROIC STUDIES ON NANOCOMPOSITES

The magnetic and multiferroic properties of composites of nickel ferrite and barium titanate ($NiFe_2O_4$-$BaTiO_3$) in the ratio 1:1, 1:2, 2:1 as well as composites of nickel zinc ferrite and barium titanate ($Ni_{1-x}Zn_xFe_2O_4$-$BaTiO_3$) in the ratio 2:1, multiferroic $Co_{1-x}Zn_xFe_2O_4$- $BaTiO_3$ (x=0,0.3,0.5,0.7,1) with the ratio 2:1 samples and bismuth ferrite and barium titanate in the ratio 2:1 and $Bi_{1-x}Sr_xFeO_3$ – $BaTiO_3$ (x=0.3,0.5,0.7) with the ratio 2:1, were prepared by solid-state reaction method are discussed in detail in this chapter. Magnetization measurement indicates a weak ferromagnetism for all composites. Through magneto-electric (M-E) coupling measurement, the coexistence of ferroelectric and ferromagnetic orders is verified.

Part of this chapter have been published as

Synthesis and characterization of bismuth ferrite-barium titanate nano composites, Sharon, V S; Malini, K A; Arun, KJ, IOP Conference Series: Materials Science and Engineering 1263 (1), 012028, https://10.1088/1757-899X/1263/1/012028

Multiferroic and magnetic characterization of Nickel Ferrite- Barium Titanate nanocomposites Sharon V.S, Swapna S Nair, Nandakumar Kalarikkal, Malini K A Materials Today: Proceedings, https://doi.org/10.1016/j.matpr.2023.12.018)

7.1 Introduction

Multiferroic materials (MF) which show the magnetoelectric effect as a combination of electrical and magnetic properties[1]. They can be used in multipurpose devices including sensors, transducers, memory, and spintronics because of the coexistence and coupling of ferroelectric, piezoelectric, and magnetic orders and phases. Few materials have been shown to naturally exhibit magnetoelectricity, but at low temperatures. There are reports of various composites such as $BaTiO_3$–$CoFe_2O_4$, $BaTiO_3$–$NiFe_2O_4$, $BaTiO_3$–$(NiZn)Fe_2O_4$, $Ba(Zr,Ti)O_3$–$Ni(Fe,Mn)_2O_4$ exhibiting ME characteristics[2].

This chapter discusses the magnetic and multiferroic properties of various composites listed in Table 7.1.

Table 7.1 Details of the sample ID

Sl No	Components	Ratio	Sample label
1	$NiFe_2O_4$- $BaTiO_3$	1:1	NFO:BTO-1:1
2	$NiFe_2O_4$- $BaTiO_3$	1:2	NFO:BTO-1:2
3	$NiFe_2O_4$- $BaTiO_3$	2:1	NFO:BTO-2:1
4	$Ni_{0.7}Zn_{0.3}Fe_2O_4$- $BaTiO_3$	2:1	NZFO-0.3:BTO-2:1
5	$Ni_{0.5}Zn_{0.5}Fe_2O_4$- $BaTiO_3$	2:1	NZFO-0.5:BTO-2:1
6	$Ni_{0.3}Zn_{0.7}Fe_2O_4$- $BaTiO_3$	2:1	NZFO-0.7:BTO-2:1
7	$ZnFe_2O_4$- $BaTiO_3$	2:1	ZFO:BTO-2:1
8	$CoFe_2O_4$- $BaTiO_3$	2:1	CFO:BTO-2:1
9	$Co_{0.7}Zn_{0.3}Fe_2O_4$- $BaTiO_3$	2:1	CZFO-0.3:BTO-2:1
10	$Co_{0.5}Zn_{0.5}Fe_2O_4$- $BaTiO_3$	2:1	CZFO-0.5:BTO-2:1
11	$Co_{0.3}Zn_{0.7}Fe_2O_4$- $BaTiO_3$	2:1	CZFO-0.7:BTO-2:1
12	$BiFeO_3$- $BaTiO_3$	1:2	BFO:BTO-1:2
13	BiFeO3- BaTiO3	2:1	BFO:BTO-2:1
14	$Bi_{0.7}Sr_{0.3}FeO_3$- $BaTiO_3$	2:1	BSFO-0.3:BTO-2:1
15	$Bi_{0.5}Sr_{0.5}FeO_3$- $BaTiO_3$	2:1	BSFO-0.5:BTO-2:1
16	$Bi_{0.3}Sr_{0.7}FeO_3$- $BaTiO_3$	2:1	BSFO-0.7:BTO-2:1

[1] Vijatovic Petrovic et al. 2020
[2] Augustine et al. 2021

7.2 Synthesis

The zinc doped nickel ferrite ($Ni_{1-x}Zn_xFe_2O_4$), zinc doped cobalt ferrite and strontium doped bismuth ferrite ($Bi_{1-x}Sr_xFeO_3$) samples were prepared by the modified sol-gel method. The ferroelectric phase $BaTiO_3$ with a tetragonal structure is directly purchased from Nano Research Elements. The required amounts of the ferrites and barium titanate are used to prepare composites in the molecular mass ratio 1:2 and 2:1. doped ferrites and barium titanate are taken in the ratio 2:1. Then these are mixed well using a mortar and pestle with acetone as a homogenizing medium. The samples are then calcinated at 1000°C for three hours and slowly cooled to room temperature.

7.3 Results and Discussion

7.3.1 Magnetic studies

Magnetic properties of the samples were evaluated using a VSM in a Physical Properties Measurement System (PPMS) from Quantum Design at 300K (Central University of Kerala) for NZFO: BTO and CZFO: BTO samples. PPMS from central instrumentation facility Pondicherry University (Make: Lakeshore: Model: 7404) were used for the evaluation of BSFO: BTO samples. The magneto-crystalline anisotropic constant (K) were calculated by employing the given formula in equations 7.1.

$$H_C = \frac{0.96K}{M_S} \tag{7.1}$$

where H_C is Coercivity and M_S is saturation magnetization.

Magnetization results are tabulated and presented in Figure 7.1 and Table 7.2. The magnetization increases with zinc doping in both spinel ferrite: barium titanate composites. This is in accordance with the magnetisation variation in the magnetic component in the composites. The decrease in magnetisation for composites is due to the non-magnetic barium titanate phase[3]. The presence of a non-magnetic barium titanate phase would act as pores and influence the magnetic properties. The very

[3] V.S et al. 2022

narrow and well-saturated hysteresis loops indicate the ordered magnetic structure and soft magnetic characteristic of all samples.

The results of VSM measurements for all samlpes are shown in Figure 7.1. The magnetic hysteresis loop of the BFO:BTO (1:2) and BFO:BTO (2:1) samples shows the paramagnetic nature, with a small fraction amount of ferromagnetic materials. The saturation magnetization was found to be small compared to the pure samples; this is because of the presence of non-magnetic barium titanate phase. With strontium doping, the magnetization was observed to vary in the same manner as the component magnetic phase. Anisotropic constant shows continuous enhancement through doping which is beneficial for biomedical applications like magnetic resonance imaging, among others.

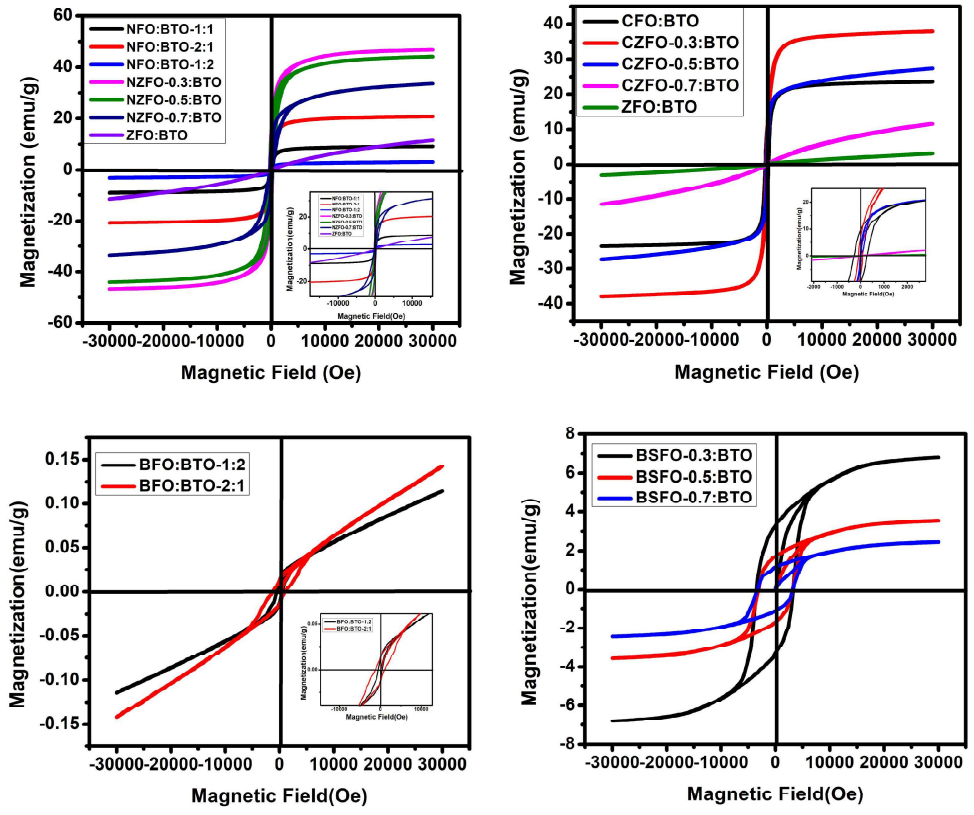

Fig 7.1. Magnetic hysteresis loops at 300K for all composites

Table 7.2 Saturation magnetization (M_S), Remanent magnetization (M_r), Coercive Field (H_C), M_r/M_S ratio and anisotropic constant (K) for all composites

Sl No	Composition	M_S(emu/g)	M_r (emu/g)	M_r/M_S	K(erg/g)	Coercive Field (Oe)
1	NFO:BTO-(1:1)	9.25	3.8	0.41	963	100
2	NFO:BTO (1:2)	3.11	0.9	0.28	511	158
3	NFO:BTO (2:1)	21.09	9.44	0.44	1999	91
4	NZFO-0.3:BTO-2:1	46.49	21.40	0.46	12784	264
5	NZFO-0.5:BTO-2:1	43.57	14.17	0.32	7488	165
6	NZFO-0.7:BTO-2:1	33.55	12.66	0.37	8981	257
7	ZFO:BTO-2:1	3.08	0.155	0.05	219	68
8	CFO:BTO-2:1	23.54	9.95	0.42	7160	292
9	CZFO-0.3:BTO-2:1	38.19	13.80	0.36	4137	104
10	CZFO-0.5:BTO-2:1	27.29	3.79	0.13	402	14.15
11	CZFO-0.7:BTO-2:1	11.69	0.23	0.01	114	9.59
12	ZFO:BTO-2:1	3.08	0.155	0.05	219	68
13	BFO:BTO-1:2	0.11	0.022	0.2	57	505
14	BFO:BTO-2:1	0.14	0.013	0.09	214	1287
15	BSFO-0.3:BTO-2:1	6.87	3.44	0.50	26067	3447
16	BSFO-0.5:BTO-2:1	3.56	1.79	0.50	21917	2993
17	BSFO-0.7:BTO-2:1	2.53	1.21	0.47	22817	3289
18	NFO	42.84	5.43	0.13	4748	106.42
19	CFO	38.5	12.77	0.33	48485	1209
20	BFO	7.58	2.6	0.34	192	24.43

The anisotropic constant and squareness of the hysteresis loop are tabulated in Table 7.2. The low value of M_r/M_S indicates the soft magnetic nature of the material. These soft magnetic characteristics of the composites can be used in the development of multifunctional devices capable of developing magnetization with a small magnetic field[4]. The low value of remanent magnetization and coercive field indicate the

[4] Padmapriya et al. 2021

superparamagnetic nature of the CZFO-0.5: BTO, CZFO-0.7: BTO and ZFO:BTO samples.

The magnetization data is fitted with the Langevin function in order to further investigate the nature of magnetic characteristics,which is characterised by

$$M = M_S \left[\coth\left(\frac{\mu H}{K_B T}\right) - \left(\frac{K_B T}{\mu H}\right)\right] \quad (7.2)$$

where μ is the reduced magnetic moment, K_B is the Boltzman constant, H is the applied magnetic field, T is the temperature and M_S is the saturation magnetization. Magnetization data fitted with Langevin function for ZFO: BTO sample is given in Figure 7.2.

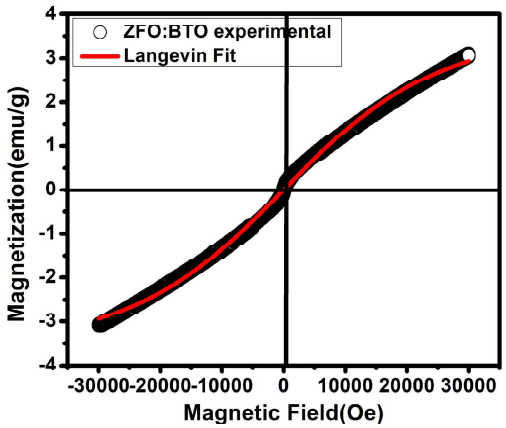

Fig 7.2 Fitting of magnetization data of ZFO:BTO using Langevin function

It can be clearly visible that Langevin function fits well with ZFO: BTO sample. The goodness of fitting parameter was found to be R^2=0.99528 and χ^2=0.01206 respectively. The R^2value's proximity to one confirms that the sample's experimental data and Langevin function suit each other well. The sample's superparamagnetic nature is confirmed by the Langevin function's excellent fitting of experimental data[5].

[5] Devi & Singh 2021

7.3.1.1 Prediction of saturation magnetization composites

The main observation from the magnetic studies of the composites is that the saturation magnetization of the composites except a few obeys an empirical relation as given below.

$$M_s = w_1 * m_1 + w_2 * m_2$$

where $w_1$is the weight fraction of the component one, m_1 is the saturation magnetization of the component one and w_2 is the weight fraction of the component two, m_2 is the saturation magnetization of the component two. The Figure 7.3 shows the variation of saturation magnetization with the empirical formula.

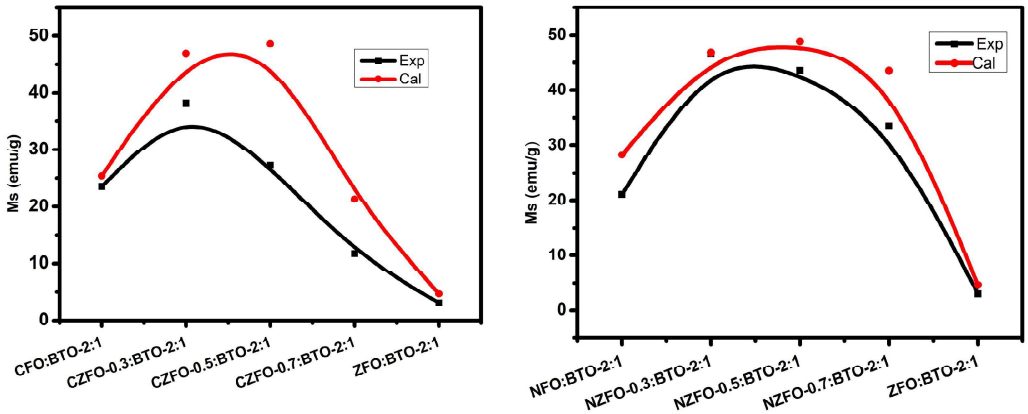

Fig 7.3 Variation of saturation magnetization with the empirical formula

The deviation in some samples may be due to the slight difference in weight fraction. This result is very significant in tuning the magnetic properties for various applications.

7.3.2 Multiferroic studies

The magnetoelectric voltage coefficient of all composites was measured using dynamic lock-in amplifier setup at MG University, Kottayam. The ME effect can be explained as the ability to control polarization through an applied magnetic field or inducing magnetization by an applied electric field, which is studied using magnetoelectric voltage coefficient (α_{ME}). ME effect depends on the applied magnetic field, the relative mass ratio of the constituent phases (ferroelectric and ferrite), and

their connection. Additionally, both magneto-mechanical resonance in the ferrite phase and electromechanical resonance in the ferroelectric phase might also affect ME response. When a magnetic field is supplied to an M-E material, the stress-induced strain causes the electric dipoles to reorient, which results in M-E coupling and an AC voltage on the top and bottom surfaces of the material. The magnetoelectric coupling coefficient is evaluated by using the formula,

$$\alpha_{ME} = \frac{V_{out}}{h_0 t} \tag{7.3}$$

where V_{out} is the AC magnetoelectric voltage across the sample surface,h_0 is the magnitude of the AC magnetic field and t is the thickness of the pellet.

The dependence of M-E voltage with the applied ac and dc magnetic fields at room temperature is shown in Figure 7.4. The M-E voltage shows a linear variation with the applied ac field and from the slope, the coupling coefficient (α) is calculated and shown in Table 7.3. Additionally, equation 7.3 is used to compute the ME coefficient. It is discovered that the value and slope are comparable. Based on the observed value of α, the composite materials are appropriate options for magnetoelectric devices. We can enhance magnetoelectric coupling coefficient by doping[67].

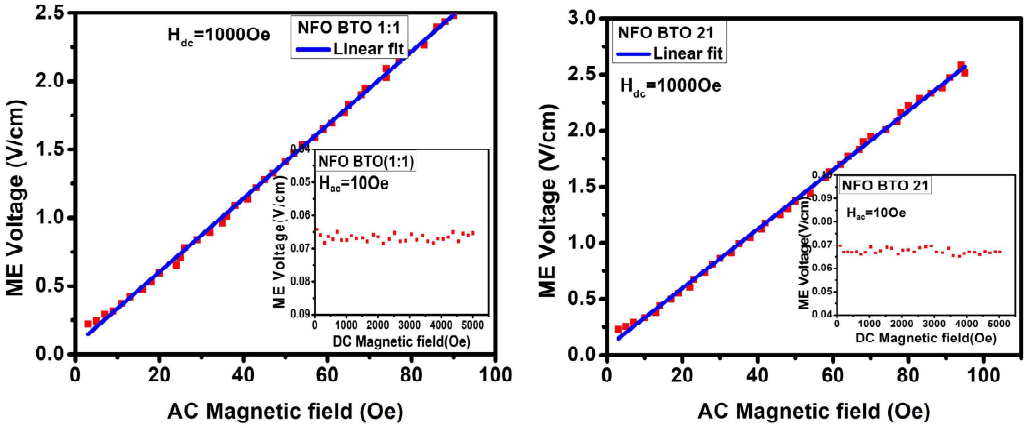

[6] Padmapriya et al. 2021
[7] **8)**

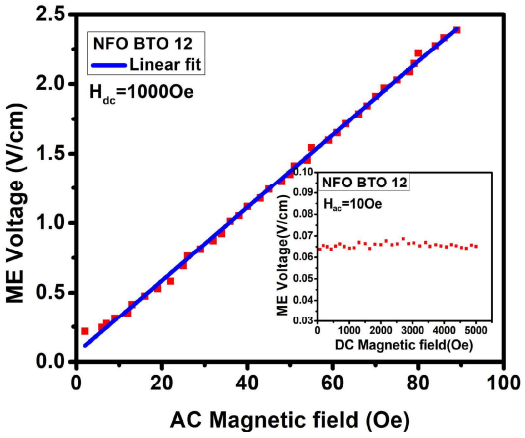
NFO BTO 12
Linear fit
H_dc=1000Oe
ME Voltage (V/cm)
AC Magnetic field (Oe)
NFO BTO 12
H_ac=10Oe
ME Voltage(V/cm)
DC Magnetic field(Oe)

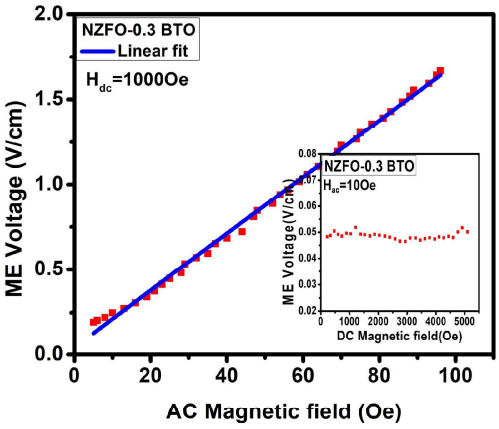
NZFO-0.3 BTO
Linear fit
H_dc=1000Oe
ME Voltage (V/cm)
AC Magnetic field (Oe)
NZFO-0.3 BTO
H_ac=10Oe
ME Voltage(V/cm)
DC Magnetic field(Oe)

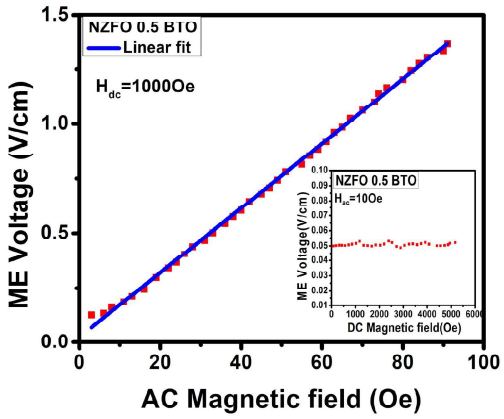
NZFO 0.5 BTO
Linear fit
H_dc=1000Oe
ME Voltage (V/cm)
AC Magnetic field (Oe)
NZFO 0.5 BTO
H_ac=10Oe
ME Voltage(V/cm)
DC Magnetic field(Oe)

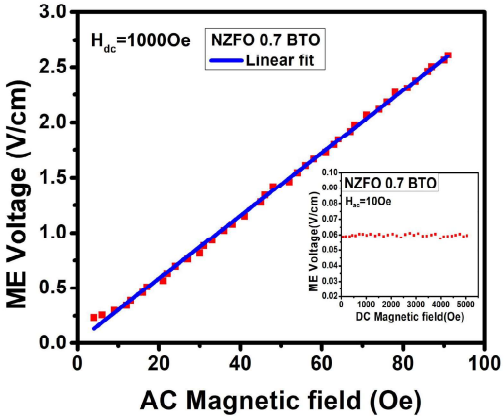
H_dc=1000Oe
NZFO 0.7 BTO
Linear fit
ME Voltage (V/cm)
AC Magnetic field (Oe)
NZFO 0.7 BTO
H_ac=10Oe
ME Voltage(V/cm)
DC Magnetic field(Oe)

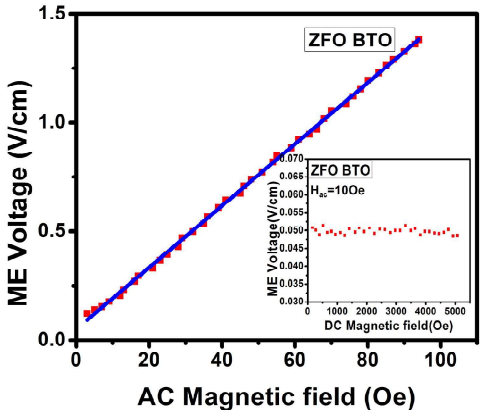
ZFO BTO
ME Voltage (V/cm)
AC Magnetic field (Oe)
ZFO BTO
H_ac=10Oe
ME Voltage(V/cm)
DC Magnetic field(Oe)

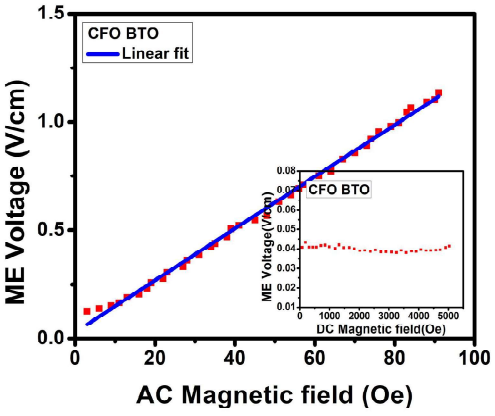
CFO BTO
Linear fit
ME Voltage (V/cm)
AC Magnetic field (Oe)
CFO BTO
ME Voltage(V/cm)
DC Magnetic field(Oe)

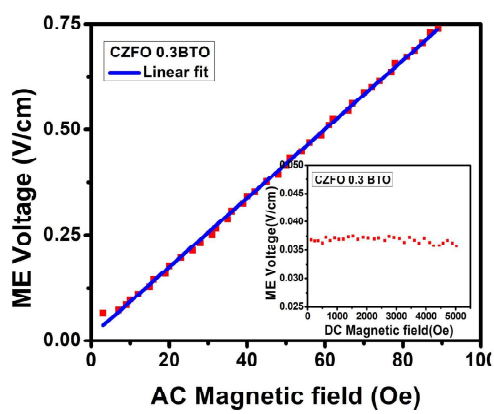
CZFO 0.3BTO
Linear fit
ME Voltage (V/cm)
AC Magnetic field (Oe)
CZFO 0.3 BTO
ME Voltage(V/cm)
DC Magnetic field(Oe)

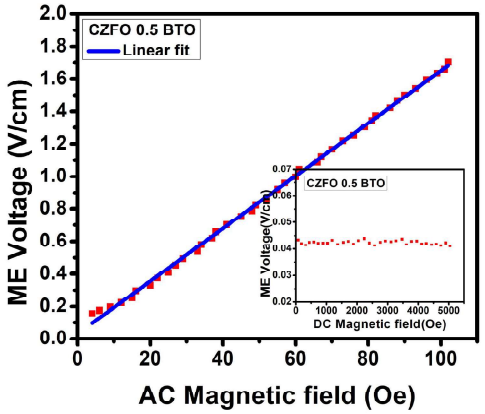
CZFO 0.5 BTO
Linear fit
ME Voltage (V/cm)
AC Magnetic field (Oe)
CZFO 0.5 BTO
ME Voltage(V/cm)
DC Magnetic field(Oe)

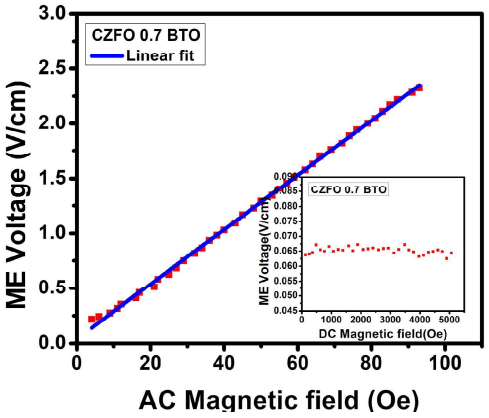
CZFO 0.7 BTO
Linear fit
ME Voltage (V/cm)
AC Magnetic field (Oe)
CZFO 0.7 BTO
ME Voltage(V/cm)
DC Magnetic field(Oe)

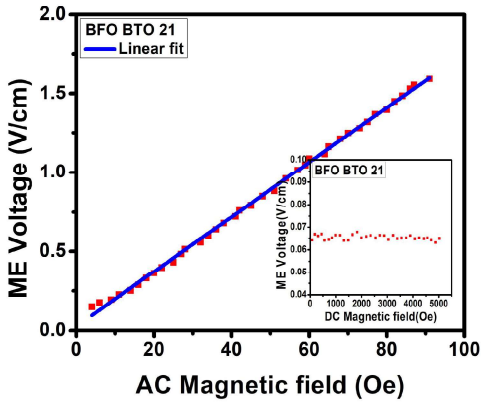
BFO BTO 21
Linear fit
ME Voltage (V/cm)
AC Magnetic field (Oe)
BFO BTO 21
ME Voltage(V/cm)
DC Magnetic field(Oe)

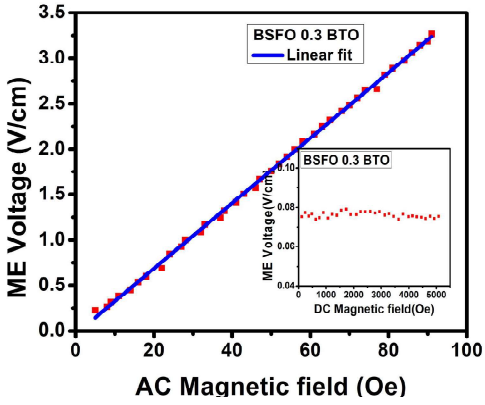
BSFO 0.3 BTO
Linear fit
ME Voltage (V/cm)
AC Magnetic field (Oe)
BSFO 0.3 BTO
ME Voltage(V/cm)
DC Magnetic field(Oe)

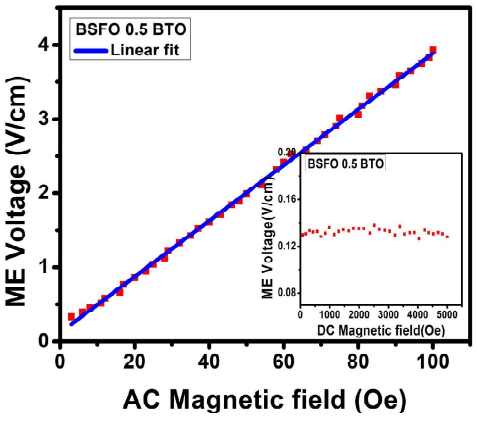
BSFO 0.5 BTO
Linear fit
ME Voltage (V/cm)
AC Magnetic field (Oe)
BSFO 0.5 BTO
ME Voltage(V/cm)
DC Magnetic field(Oe)

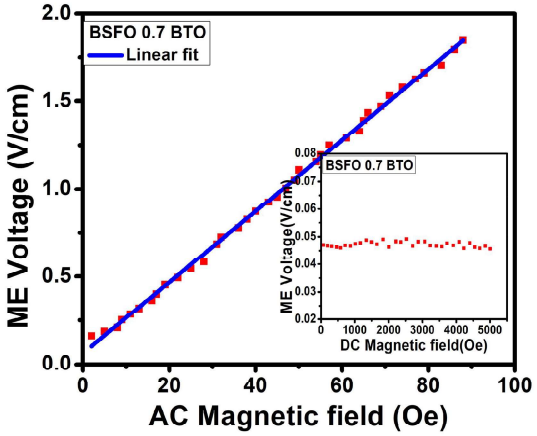

Fig 7.4. Variation of M-E voltage with magnetic field for all composites

Table 7.3. Comparison of magnetoelectric coupling coefficient from the slope and equation

Sl No	Composition	Coupling coefficient (α) from slope (V/cm.Oe)	Coupling coefficient (α) using equation (V/cm.Oe)
1	$NiFe_2O_4$- $BaTiO_3$(1:1)	0.0269	0.028
2	$NiFe_2O_4$- $BaTiO_3$(1:2)	0.0262	0.0274
3	$NiFe_2O_4$- $BaTiO_3$(2:1)	0.0263	0.0276
4	$Ni_{0.7}Zn_{0.3}Fe_2O_4$- $BaTiO_3$(2:1)	0.0166	0.0174
5	$Ni_{0.5}Zn_{0.5}Fe_2O_4$- $BaTiO_3$(2:1)	0.0147	0.0153
6	$Ni_{0.3}Zn_{0.7}Fe_2O_4$- $BaTiO_3$(2:1)	0.0283	0.0286
7	$ZnFe_2O_4$- $BaTiO_3$(2:1)	0.0141	0.0155
8	$BiFeO_3$- $BaTiO_3$	0.0173	0.0177
9	$Bi_{0.7}Sr_{0.3}FeO_3$- $BaTiO_3$	0.0359	0.0352
10	$Bi_{0.5}Sr_{0.5}FeO_3$- $BaTiO_3$	0.0376	0.0394
11	$Bi_{0.3}Sr_{0.7}FeO_3$- $BaTiO_3$	0.0203	0.0221
12	$CoFe_2O_4$- $BaTiO_3$	0.0119	0.0124
13	$Co_{0.7}Zn_{0.3}Fe_2O_4$- $BaTiO_3$	0.0081	0.0083
14	$Co_{0.5}Zn_{0.5}Fe_2O_4$- $BaTiO_3$	0.0161	0.0166
15	$Co_{0.3}Zn_{0.7}Fe_2O_4$- $BaTiO_3$	0.0248	0.0257

7.4 Conclusion

The magnetic measurements leads to the conclusion that, the presence of barium titanate phase in the composite ceramics is responsible for the lower magnetism observed in contrast to pure samples of nickel zinc ferrite, cobalt zinc ferrite, and bismuth ferrite. This decrease in magnetisation for composites is due to magnetic dilution. The saturation magnetization of the composites were found to vary with the amount of zinc and strontium content as in the case of the respective magnetic phases. We can modify the saturation magnetization by doping. The low value of the remanent magnetization and coercive field indicate the superparamagnetic behavior for CZFO-0.5: BTO, CZFO-0.7:BTO and ZFO:BTO samples. Developed the empirical formula for tuning the magnetic properties. The linear response of ME voltage with high value of coupling coefficient indicates the coexistence of electric and magnetic phases. These materials can be used in the fabrication of magnetoelectric devices.

References

Augustine, P., Narayana, Y., & Kalarikkal, N. (2021). An effective strategy for the development of multiferroic composite nanostructures with enhanced magnetoelectric coupling performance: a perovskite-spinel approach. *Nanoscale Advances*, *3*(16), 4866–4877. https://doi.org/10.1039/d1na00376c

Devi, E. C., & Singh, S. D. (2021). Manifestation of Magnetic Characteristics of Zinc Ferrite Nanoparticles Using the Langevin Function. *Journal of Superconductivity and Novel Magnetism*, *34*(2), 617–622. https://doi.org/ 10.1007/s10948-020-05732-7

Francis, P. N., Dhanuskodi, S., Jayalakshmy, M. S., Muneeswaran, M., Philip, J., & Giridharan, N. V. (2018). Optical limiting and magnetoelectric coupling in multiferroic BiFeO3 nanoparticles. *Materials Chemistry and Physics*, *216*, 93–101. https://doi.org/10.1016/j.matchemphys.2018.05.062

Padmapriya, D., Dhayanithi, D., Rahul, M. T., Kalarikkal, N., & Giridharan, N. V. (2021). Study of room-temperature magnetoelectric coupling in (1 − x)BaTiO3 and (x)NiFe2O4 multiferroic composites. *Applied Physics A: Materials Science and Processing*, *127*(4), 1–10. https://doi.org/10.1007/s00339-021-04431-x

V.S, S., Gopalan, V. E., Al-Omari, I. A., & Malini, K. A. (2022). Superparamagnetic Nickel Ferrite Nanoparticles Doped with Zinc by Modified Sol–gel Method. *Journal of Superconductivity and Novel Magnetism 2021*, 1–10. https://doi.org/ 10.1007/S10948-021-06110-7

Vijatovic Petrovic, M. M., Dzunuzovic, A., Bobic, J. D., Ilic, N., Stijepovic, I., & Stojanovic, B. D. (2020). Study of barium titanate/nickel-zinc ferrite based composites: Electrical and magnetic properties and humidity sensitivity. *Processing and Application of Ceramics*, *14*(1), 9–18. https://doi.org/ 10.2298/ PAC2001009V

Chapter 8

CONCLUSION AND FUTURE RECOMMENDATION

CONCLUSION AND FUTURE RECOMMENDATION

8.1 CONCLUSION

This chapter provides a comprehensive overview of the entire research detailed in preceding chapters and outlines future directions. The thesis focuses on the structural, dielectric, magnetic, ferroelectric, magnetoelectric, and optical studies on the nanoparticles containing spinel and perovskite ferrites, as well as their composites with barium titanate. The objective is to develop heterogeneous composites with a wide range of properties. The synthesis and examination of multiferroic particulates and composites are thoroughly detailed, encompassing structural, microstructural, dielectric, ferroelectric, magnetic, magnetoelectric (ME), and optical properties of nanoparticles. Spinel and perovskite ferrites are chosen for the magnetic phase of the multiferroic composites, while $BaTiO_3$ is selected for the ferroelectric phase. Multiferroics, which exhibit multiple primary ferroic orders such as ferroelectricity, ferroelasticity, and ferromagnetism within a single phase, are investigated. In addition to these ferroic properties, some multiferroics demonstrate unique optical and magnetoelectric characteristics. The synthesis of constituent magnetic phases is achieved using the sol-gel technique, and these phases are combined in various weight ratios before being sintered at high temperatures to create the composites via solid-state reaction methods. The research aims to identify compositions with diverse properties and classify them for various applications. The thesis is divided into two parts: the first part focusing on the synthesis and characterization of ferrite constituents, and the second centering on the synthesis and characterization of composites. This comprehensive approach enables a thorough exploration of the multifaceted properties and potential applications of the studied materials.

The thesis work, drawing on the insights and analyses presented in each chapter, culminates as follows. Chapters 3, 4, and 5 focus on the synthesis and characterization of spinel ferrites, encompassing nickel zinc ferrite, cobalt zinc ferrite, and perovskite structured bismuth strontium ferrite. Subsequent chapters

(Chapters 6 and 7) delve into composites incorporating these ferrites along with barium titanate.

Super paramagnetic nickel zinc ferrite $Ni_{1-x}Zn_xFe_2O_4$ (x=0.0,0.3,0.5,0.7,1) nanoparticles were prepared by modified Sol-gel auto-combustion method. The synthesised samples, according to Rietveld refinement, exhibit a cubic spinel structure with an Fd-3m space group and a slight fluctuation in the lattice constant as the concentration of zinc increases. The dielectric studies reveal that the dielectric constant can be changed by doping with zinc. The high value of dielectric constant for the prepared samples points towards it use in gate and capacitor dielectric applications. The superparamagnetic characteristics as well as the variation of magnetic parameters with zinc concentration are also studied. The low remanence ratio (M_r/M_S) values of all samples indicate that they are less anisotropic containing a major fraction of superparamagnetic nanoparticles and show pronounced spin canting effects. The conclusion that, nickel ferrites' magnetic and dielectric properties can be changed using the very straightforward, cost-effective technique of zinc doping, can enhance its tailored use in various magnetic devices. The absorption intensities of methylene blue solutions with ferrite photocatalysts were measured after sun exposure to assess the degradation of methylene blue by NZFO catalysts. It appears that the photocatalyst nickel zinc ferrite demonstrates efficient functionality, while zinc ferrite, in contrast, and shows the least amount of dye degradation activity.

Single phase cubic spinel nanoparticles of zinc substituted cobalt ferrite nanoparticles are also prepared by modified sol-gel method and the structural properties are evaluated. Rietveld refinement established that the samples synthesized have a cubic spinel structure with an *Fd-3m* space group and small variation in the lattice constant with the increasing the zinc concentration. The Maxwell-Wagner two-layer model explains the normal behaviour of the frequency-dependent dielectric response. All samples showed a high value for the dielectric constant, which can be applied to capacitor dielectrics, gate dielectrics, and epitaxial dielectrics. The saturation magnetization values increase with increase in Zn content

initially and beyond x=0.5 the value is found to decrease. Magnetic studies reveal superparamagnetic nature except for cobalt ferrite which has relatively larger crystalline size and all zinc doped cobalt samples contain superparamagnetic component in them. Dependence of coercivity on grain size is very evident in this set of samples. The ZFC-FC curve of CZFO-0.7 and hysteresis loops ZFO samples indicate the superparamagnetic behavior. The lower value Mr/M_s shows the uniaxial anisotropy and this material can be used for biomedical applications. Overall, this study evaluate that cobalt ferrite nanoparticles has potential cytotoxic and photoctalytic activity.

$BiFeO_3$ and strontium doped $BiFeO_3$ samples are successively synthesized by a modified Sol-gel auto-combustion process. The XRD studies reveal a structural transition from rhombohedral- to cubic beyond x=0.3. The studies reveal that dielectric constant, as well as ac conductivity, can be altered/tuned by the addition of dopants. The magnetic studies confirm that this is a simple cost-effective method to prepare bismuth ferrite with improved magnetic characteristics. Strontium doping can enhance the saturation magnetization and remnant magnetization to a large extend which improve its application potential in magnetic devices.

The sixth and seventh chapters of this thesis provide the various properties of the composites based the spinel and perovskite ferrites with barium titanate.

Composites of $Ni_{1-x}Zn_xFe_2O_4$ -$BaTiO_3$, $Co_{1-x}Zn_xFe_2O_4$ -$BaTiO_3$ and $Bi_{1-x}Sr_xFeO_3$ -$BaTiO_3$ were successfully synthesized with different weight ratios. Structural, dielectric, magnetic and magnetoelectric characteristics of these composites were analyzed. The individual and composite phase formation was validated by X-ray diffraction (XRD) studies. The dielectric study examines how frequency affect the dielectric constant (ε') and ac conductivity of the composite samples. Dielectric dispersion is seen at low frequencies for all composite samples, and this phenomenon can be attributed to Maxwell-Wagner interfacial polarization. Furthermore, at ambient temperature, all of the composite samples show loops that indicate ferroelectric and magnetic characteristics simultaneously: magnetization (M)

vs. magnetic field (H) and polarisation (P) vs. electric field (E).

The dielectric constant values at 1 M Hz for all composites are show in Table 8.1.

Table 8.1. The dielectric constant values at 1 M Hz for all composites.

Sample	**Diel Const. at 1MHz**	**Sample**	**Diel Const.at 1MHz**
BTO	248	NFO:BTO-1:2	46
NFO	20	NFO:BTO-2:1	37
NZFO-0.3	6	NZFO-0.3:BTO-2:1	90
NZFO-0.5	35	NZFO-0.5:BTO-2:1	128
NZFO-0.7	5	NZFO-0.7:BTO-2:1	89
ZFO	28	ZFO:BTO-2:1	122
CFO	13	CFO:BTO-2:1	121.85
CZFO-0.3	6	CZFO-0.3:BTO-2:1	161.95
CZFO-0.5	7	CZFO-0.5:BTO-2:1	98.32
CZFO-0.7	10	CZFO-0.7:BTO-2:1	94.2
BFO	60.42	BFO:BTO-2:1	90.63
BSFO-0.3	32.61	BSFO-0.3:BTO-2:1	92.5
BSFO-0.5	47.01	BSFO-0.5:BTO-2:1	90.55
BSFO-0.7	71.35	BSFO-0.7:BTO-2:1	130.8
		BFO:BTO-1:2	131.12

The major observation from the dielectric studies of the composites is that the dielectric constant of the composites except a few obeys an empirical relation as given in chapter 6. The deviation in some samples may be due to the slight difference in weight fraction. This result is very significant in tuning the dielectric constant for various applications.

Values of various magnetic parameters for all samples are given in Table 8.2.

Table 8.2: Magnetic parameters for all samples

Sample	Ms (emu/g)	Hc(Oe)	K (erg/g)	Mr (emu/g)	Mr/Ms
NFO	42.84	106.42	4748	5.43	0.13
NZFO-0.3	71	46.43	3433	3.66	0.05
NZFO-0.5	74	46.43	3578	3.66	0.04
NZFO-0.7	66	22.43	1542	1	0.01
ZFO	7.06	4.17	30.6	0.124	0.02
NFO:BTO-1:1	9.25	100	963	3.8	0.41
NFO:BTO-1:2	3.11	158	511	0.9	0.28
NFO:BTO-2:1	21.09	91	1999	9.44	0.44
NZFO-0.3:BTO-2:1	46.49	264	12784	21.4	0.46
NZFO-0.5:BTO-2:1	43.57	165	7488	14.17	0.32
NZFO-0.7:BTO-2:1	33.55	257	8981	12.66	0.37
ZFO:BTO-2:1	3.08	68	219	0.155	0.05
CFO	38.5	1209	48485	12.77	0.33
CZFO-0.3	71.07	230	17027	15.55	0.21
CZFO-0.5	73.72	219	16817	19.51	0.26
CZFO-0.7	32.27	89	2991	2.59	0.08
CFO:BTO-2:1	23.54	292	7160	9.95	0.42
CZFO-0.3:BTO-2:1	38.19	104	4137	13.8	0.36
CZFO-0.5:BTO-2:1	27.29	14.15	402	3.79	0.13
CZFO-0.7:BTO-2:1	11.69	86	1047	0.23	0.01
BFO	7.58	24.43	192	2.6	0.34
BSFO-0.3	28.76	70.68	2117	3.64	0.12
BSFO-0.5	24.44	24.43	622	4.84	0.19
BSFO-0.7	23.52	15.24	373	1	0.04
BFO:BTO-2:1	0.11	543	79	0.022	0.12
BFO:BTO-1:2	0.14	1287	214	0.013	0.11
BSFO-0.3:BTO-2:1	6.87	3447	26067	3.68	0.5
BSFO-0.5:BTO-2:1	3.56	2993	21917	1.79	0.5
BSFO-0.7:BTO-2:1	2.53	3289	22817	1.21	0.47

The observed values of various parameters lead to the following conclusions

- NZFO-0.3 and NZFO-0.5 exhibit the maximum saturation magnetization values among the nickel zinc ferrite samples, accompanied by higher coercive field and anisotropic constant.

- The composites demonstrate the larger values for coercive field, anisotropic constant and squareness ratio in comparison to other materials but the saturation magnetisation and remanent magnetisation values are lower than the component magnetic phase.
- Maximum value for coercive field and anisotropic constant were observed for CFO and CZFO samples compared to the other composites.
- In the nickel zinc ferrite barium titanate composites, saturation magnetization reaches its maximum, while composites containing cobalt zinc ferrite display maximum coercivity and anisotropy.
- Bismuth ferrite - barium titanate composites have large coercivity, anisotropy constant and their squareness ratio is also high.
- The composites with larger weight fraction of nonmagnetic component exhibited higher coercivity and anisotropy.
- Furthermore, the consistent dielectric constant values ranging from 50 to 300 across BFO, BSFO-0.7, and all composite materials suggest their suitability for applications in gate dielectrics and photo-electrochemical cells.
- With dielectric constant values falling within the range of 25 to 50, NZFO-0.5, ZFO, BSFO-0.3, BSFO-0.5, NFO:BTO-1:2, and NFO:BTO-2:1 exhibit promising potential for utilization in capacitor dielectrics, indicating their suitability for various electronic applications.
- NZFO-0.3, NZFO-0.7, CZFO-0.3, and CZFO-0.5 materials demonstrate favourable characteristics for applications in epitaxial dielectrics, suggesting their potential in advancing thin film technology and electronic device miniaturization.
- Due to their high coercive field exceeding 1000 Oe, CFO and BSFO composites are ideal candidates for memory device applications, offering reliable data retention and stability in various electronic systems.
- With a dielectric constant ranging between 17-20, NFO materials present favourable properties for application in gate dielectrics specifically designed

for organic transistors, showcasing their potential in enhancing the performance and efficiency of such electronic devices.

- The substantial hysteresis exhibited by BSFO composites makes them particularly suitable for use in magnetic field sensors, providing reliable detection and measurement capabilities across various applications requiring precise sensing of magnetic fields.
- Cobalt ferrite is a promising candidate for biomedical applications, particularly in in-vitro cytotoxicity studies, showcasing its potential in advancing medical research and diagnostics.
- From these observation we can conclude that by manipulating the amount of non-magnetic component as well as by selecting the appropriate magnetic phase we can design new materials for various applications.

The ME coefficient was measured and observed maximum for BSFO-0.5: BTO sample.

In conclusion, the thesis outlines a comprehensive series of experiments and characterizations related to various metal oxide composite materials. These materials' structural, dielectric, and magnetic properties were meticulously studied and manipulated to serve diverse technological applications, ranging from electronics to magnetism and device fabrication. The findings collectively contribute to a broader understanding of how these materials can be tailored for specific purposes.

During the course of this research, the prepared samples were characterised by some additional studies aiming at exploring the application of the materials in diverse areas. The studies include the photocatalytic dye degradation studies, spectral studies for evaluating the band gap and photoluminescence in some selected samples. Attempts were also made to study the cytotoxicity study of cobalt ferrite to explore its application in cancer therapy, which is a recent spin-off of novel applications of ferrites.

In summary, the study presents a systematic approach to synthesizing and characterizing metal oxide composite materials with tunable properties. The findings

have significant implications for diverse applications, ranging from dielectrics and magnetism to potential use in magnetic and magnetoelectric devices.

8.2 FUTURE RECOMMENDATION

With possible uses as memory devices, transducers, magnetic field sensors, and other devices, multiferroic laminated composites exhibit better ME responsiveness than single phase and particle composites.

- Optimization of properties for device fabrication involves fine-tuning and enhancing specific characteristics, such as dielectric properties, magnetic properties to achieve the desired performance and functionality in the manufacturing process
- Materials engineering through the incorporation of various doping elements and control of their ratios plays a crucial role in tailoring the physical, chemical, and electronic properties of materials.
- Explore the application of these in various fields
- Study the long-term Stability
- Measurements of the isothermal magneto-capacitance and magnetic field-dependent dielectric constant may be used to accurately determine the precise order of magneto-electric coupling in these compounds, which is a crucial component of any multiferroic material.
- $BiFeO_3$ nanoparticles are promising for photocatalysis, including hydrogen generation from water splitting and organic contaminant degradation. This process can address Kerala's energy and environmental issues. Developing a new photocatalyst for direct water splitting under visible light is essential for hydrogen production and is a significant challenge for academia and industry.